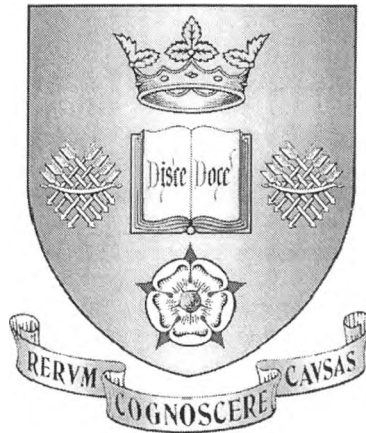


Dispersion due to Surcharged Manholes



By

Robert O'Brien

M.Eng (Hons)

Thesis submitted in partial fulfilment of the requirements for the
Degree of Doctor of Philosophy

University of Sheffield

Department of Civil and Structural Engineering

(November 1997)

Revised July 1999

Summary

The modelling of urban drainage systems has, in the past, focused on the systems ability to convey a maximum discharge. More recently, the design of drainage systems has adopted a more environmentally aware outlook. With increasing numbers of sewer overflows discharging into natural water courses, there is an ever present need to quantify the magnitude of the pollutants entering the environment.

To enable accurate predictions of pollutant discharges from sewer systems into the environment, the transport of a pollutant within the sewer system must first be elucidated. As a pollutant travels through a sewer system it will be diluted in the surrounding flow, thus causing a general spread in both the temporal and spatial domains. Studies measuring the spread of a pollutant as it passes through a pipeline have already been conducted. However, no such study has yet been undertaken to quantify the effects of the ancillary structures within the sewer system. This thesis examines the effects on a pollutant as it passes through the most commonly occurring of these ancillary structures, the manhole.

Through the construction of a scale laboratory model, data has been acquired from a variety of manhole chambers that are subjected to a range of surcharges and discharges. By utilising, and expanding upon, two existing numerical modelling techniques, the changes that occur in the distribution of pollutant as it passes through these structures has been quantified within a temporal field of reference. From these results, a set of general equations that represent the passage of a pollutant have been derived. Through the comparison of predictions made using the derived equations, the most effective predictive tool has been identified.

Acknowledgements

This research project was conducted at the University of Sheffield within the Department of Civil and Structural Engineering. The research was funded by the UK Science and Engineering Research Council.

The utmost thanks is given to Dr Ian Guymer for his role as supervisor and his endless support and advice over the last 7 years. His persistent motivation has been the driving force behind the final submission of this thesis.

The author would also like to thank the technical staff within the department, especially Mr G. Brawn, Mr S. Richards, Mr M. Moore and Mr A. Lumby. Their diligent work within the laboratory ensured that the test rig ran smoothly, and most leaks were caught before they became floods.

The author is also grateful to Mr R. Potter and Mr J. Pearson for both their academic assistance and support in times of evading academia.

A final acknowledgement is made to my Parents, whose invaluable support at all times makes any venture worthwhile.

'Good morning,' said Deep Thought at last.

'Er...Good morning, O Deep Thought,' said Loonquawl nervously, 'do you have... er, that is ...'

'An answer for you?' interrupted Deep Thought majestically. 'Yes I have.'

The two men shivered with expectancy. Their waiting had not been in vain.

'There really is one?' breathed Phouchg.

'There really is one,' confirmed Deep Thought.

'To Everything? To the great Question of Life, the Universe and Everything?'

'Yes.'

Both of the men had been trained for this moment, their lives had been a preparation for it, they had been selected at birth as those who would witness the answer, but even so they found themselves gasping and squirming like excited children.

'And you're ready to give it to us?' urged Loonquawl.

'I am.'

'Now?'

'Now,' said Deep Thought.

They both licked their dry lips.

'Though I don't think,' added Deep Thought, 'that you're going to like it.'

'Doesn't matter!' said Phouchg. 'We must know it! Now!'

'Now?' inquired Deep Thought.

'Yes! Now...'

'Alright,' said the computer and settled into silence again. The two men fidgeted. The tension was unbearable.

'You're really not going to like it,' observed Deep Thought.

'Tell us!'

'Alright,' said Deep Thought. 'The Answer to the Great Question...'

'Yes...!'

'Of Life, the Universe and Everything...' said Deep Thought.

'Yes...!'

'Is... ' said Deep Thought, and paused.

'Yes...!'

'Is...'

'Yes...!!!...?'

'Forty-two,' said Deep Thought with infinite majesty and calm.

It was a long time before anyone spoke.

The Hitch Hiker's Guide to the Galaxy
Douglas Adams

Contents

Summary	ii
Acknowledgements	iii
Contents	v
Notation	viii
List of tables	xi
List of figures	xii
Introduction	xix

Chapter 1 Mixing Processes

1.1 Effects of Mixing	1
1.2 Mixing Through Molecular Diffusion	1
1.2.1 Mixing in Laminar Flow	2
1.2.2 Mixing in Turbulent Flow	5
1.2.3 One Dimensional (Depth Averaged) Dispersion	7
1.2.4 Application of the Taylor Advective Dispersive Equation	9
1.2.5 Evaluation of the Shear Flow Dispersion Coefficient	13
1.3 Non-Fickian Dispersion Models	16
1.3.1 Cells in Series Model	16
1.3.2 Aggregated Dead Zone Model	18
1.4 Summary of Mixing Processes	21

Chapter 2 Collection and Analysis of Data

2.1 Fluorometry	23
2.2 Fluorometer Modification	25
2.3 Calibration of the Modified Fluorometer	26
2.4 Laboratory System	29
2.5 Data Acquisition	32

2.5.1 Equipment Calibration	32
2.5.2 Data Analysis	33
2.6 Results	40

Chapter 3 Discussion

3.1 Headlosses	52
3.1.1 Introduction	52
3.1.2 Determining Headloss Coefficients	52
3.1.3 Headlosses in Pipes	53
3.1.4 Headlosses in Manholes	54
3.2 Results to the Advective Dispersion Model	60
3.2.1 Straight Pipe	60
3.2.2 Manholes	62
3.3 Results to the Aggregated Dead Zone Model	74
3.3.1 Straight Pipe	74
3.3.2 Manholes	75
3.4 Alternative Analysis – Optimal Iteration Study	83
3.4.1 Analysis Technique	83
3.4.2 Optimal Iterative ADE Analysis	85
3.4.3 Optimal Iterative ADZ Analysis	94

Chapter 4 Comparison Between Observed and Predicted Data

4.1 Data Selection	103
4.2 Summary of Standard ADE and ADZ Predictions for all Manhole Diameters	116
4.3 Summary of Optimised ADE and ADZ Predictions for all Manhole Diameters	119
4.4 Summary of ADE and ADZ Predictions for the Straight Pipe	122

Chapter 5 Conclusions

5.1 Introduction	123
------------------	-----

5.2 Standard ADE and ADZ Predictions	123
5.3 Optimised ADE and ADZ predictions	124
5.4 Synopsis	126
References	131

Notation

$A(z^{-1})$	=	Backward shift polynomial
a	=	Aggregated dead zone parameter
$B(z^{-1})$	=	Backward shift polynomial
b	=	Aggregated dead zone parameter
C	=	Tracer concentration within a cell (CIS)
C_0	=	Mass of injected tracer (ADE)
$C_n(t)$	=	Tracer concentration in n^{th} cell at time t (CIS)
$C(x,t)$	=	Concentration at position x and time t (ADE)
c	=	Concentration
\bar{c}	=	Time averaged concentration
$\overline{\bar{c}}$	=	Depth averaged concentration
c'	=	Turbulent concentration fluctuation
c''	=	Concentration fluctuation about a depth average
$c_i(t)$	=	Concentration at time t in profile i (ADE)
D_m	=	Manhole chamber diameter
d	=	Pipe diameter
e_k	=	Area mean shear flow diffusion coefficient
e_m	=	Molecular diffusion coefficient
e_t	=	Turbulent diffusion coefficient
f	=	Friction factor
g	=	Acceleration due to gravity
h_L	=	Headloss
J_0	=	Sum of residuals
J_m	=	Tracer flux
J_x	=	Tracer flux in x direction
J_y	=	Tracer flux in y direction
K	=	Dispersion coefficient due shear flow (ADE)

$K_{(\text{Post-threshold})}$	=	Dispersion coefficient in a manhole with a post-threshold surcharge
$K_{(\text{Pre-threshold})}$	=	Dispersion coefficient in a manhole with a pre-threshold surcharge
K_{HL}	=	Headloss coefficient
k	=	Discrete time step (ADZ)
M_0	=	Total mass of tracer (CIS)
M_t	=	Mass of tracer at time t
P^*	=	Peizometric pressure
Q	=	Mean discharge
Q	=	Volumetric discharge from a cell (CIS)
Re	=	Reynolds number
R_T^2	=	Coefficient of determination
r	=	Pipe radius
s	=	Tracer concentration in dead zone
T	=	Residence time
t	=	Time
\bar{t}	=	Centre of mass travel time (ADZ)
\bar{t}_i	=	Centre of mass of profile i (ADE)
U	=	Mean streamwise velocity (ADE)
U_x	=	Velocity in the x direction
U_y	=	Velocity in the y direction
\bar{U}_x	=	Time averaged velocity in the x direction
$\bar{\bar{u}}$	=	Depth averaged streamwise velocity
u''	=	Streamwise velocity fluctuation about a depth average
u'_x	=	Turbulent velocity fluctuation in the x direction
u'_y	=	Turbulent velocity fluctuation in the y direction
u^*	=	Shear velocity
V	=	Dead zone volume (ADZ)
V	=	Cell volume (CIS)
V_e	=	Effective dead zone volume (ADZ)
v	=	Area mean velocity

$W(t)$	=	Tracer entering a cell during the discrete time interval t
x	=	Co-ordinate in the longitudinal direction
y	=	Co-ordinate in the vertical direction
y_k	=	Observed data at a k^{th} location along a dimensionless abscissa
z^p	=	Backward shift operator of p^{th} order
α	=	Volumetric travel time (CIS)
δ	=	Advective time delay (ADZ)
γ	=	Dispersive fraction (ADZ)
Γ_c	=	Volumetric mass transfer coefficient from a main flow into a dead zone
Γ_s	=	Volumetric mass transfer coefficient from a dead zone into a main flow
μ	=	Fluid viscosity
μ	=	Skewness
ρ	=	Fluid density
σ_s^2	=	Spatial variance (ADE)
σ_t^2	=	Temporal variance (ADE)
τ	=	Delay time (ADZ)
τ	=	Dummy temporal variable of integration (ADE)
τ_0	=	Shear stress
ξ	=	Dummy spatial variable of integration (ADE)

Subscripts

1	=	Upstream data
2	=	Downstream data

Note:

In the interest of preserving notation from original derivations, some notation may be duplicated with alternative definitions. To avoid confusion, case specific notation has been annotated using the following convention:

ADE - Advective dispersion equation.

ADZ - Aggregated dead zone.

CIS - Cells in series

List Of Tables

2.1	Summary of acquired data.	34
4.1	Summary of ADE and ADZ predictions.	117

List of Figures

1.1	The spread of tracer in laminar flow.	2
1.2	Mechanisms of turbulent diffusion.	6
1.3	Mechanisms of depth averaged turbulent diffusion.	7
1.4	Development of a skewed temporal distribution from a Gaussian spatial distribution.	11
1.5	Temporal and spatial distributions at station x_1 and time t_1 respectively.	13
1.6	Required measurements for calculation of temporal variance.	15
1.7	Illustration of ADZ travel and residence time parameters.	21
2.1	Schematic showing the operation of a fluorometer.	23
2.2	Diagram of fluorometer and cut away flow through section.	24
2.3	Section through modified fluorometer flow through.	25
2.4	Calibration of standard flow through fluorometer.	27
2.5	Calibration of modified fluorometer.	27
2.6	Calibration of two fluorometers extending beyond the linear range.	28
2.7	Calibration of two fluorometers within the linear range.	29
2.8	Configuration of test facility.	30
2.9	Typical variations in surcharge during a 300s test.	31
2.10	Comparison between errors in cumulative concentration and second moments.	35
2.11	Typical data set used to determine average voltage / time distribution.	37
2.12(a)	Typical averaged voltage / time data.	38
2.12(b)	Typical filtered voltage / time data.	38
2.13	Straight pipe, variation in dispersion coefficient (K) with discharge.	40
2.14	Straight pipe, variation of travel time (\bar{t}) and delay time (τ) with discharge.	41
2.15	Straight pipe, variation of headloss (h_L) with discharge.	41
2.16	400mm chamber, variation of dispersion coefficient (K) with surcharge for a range of discharges.	42

2.17	400mm chamber, variation of travel time (\bar{t}) with surcharge for a range of discharges.	42
2.18	400mm chamber, variation of delay time (τ) with surcharge for a range of discharges.	43
2.19	500mm chamber, variation of dispersion coefficient (K) with surcharge for a range of discharges.	43
2.20	500mm chamber, variation of travel time (\bar{t}) with surcharge for a range of discharges.	44
2.21	500mm chamber, variation of delay time (τ) with surcharge for a range of discharges.	44
2.22	500mm chamber, variation of headloss (h_L) with surcharge for a range of discharges.	45
2.23	600mm chamber, variation of dispersion coefficient (K) with surcharge for a range of discharges.	45
2.24	600mm chamber, variation of travel time (\bar{t}) with surcharge for a range of discharges.	46
2.25	600mm chamber, variation of delay time (τ) with surcharge for a range of discharges.	46
2.26	600mm chamber, variation of headloss (h_L) with surcharge for a range of discharges.	47
2.27	800mm chamber, variation of dispersion coefficient (K) with surcharge for a range of discharges.	47
2.28	800mm chamber, variation of travel time (\bar{t}) with surcharge for a range of discharges.	48
2.29	800mm chamber, variation of delay time (τ) with surcharge for a range of discharges.	48
2.30	800mm chamber, variation of headloss (h_L) with surcharge for a range of discharges.	49
2.31	400mm chamber control test, variation of dispersion coefficient (K) with surcharge for a range of discharges.	49

2.32	400mm chamber control test, variation of travel time (\bar{t}) with surcharge for a range of discharges.	50
2.33	400mm chamber control test, variation of delay time (τ) with surcharge for a range of discharges.	50
2.34	400mm chamber control test, variation of headloss (h_L) with surcharge for a range of discharges.	51
3.1	Measured headlosses for a straight perspex pipe over a distance of 2.7m.	53
3.2	Measurements of hydraulic gradient.	56
3.2(a)	Location of pressure tappings for previous and present study.	56
3.2(b)	Method of determining hydraulic gradient from previous studies.	56
3.2(c)	Method of determining hydraulic gradient within present study.	56
3.2(d)	Possible source of errors within present study.	56
3.3	Variations in total headloss with velocity head for different chamber diameters.	57
3.4	Comparison of present headloss data with previous studies.	59
3.5	Variation of dispersion coefficient with discharge.	60
3.6	Increase in surcharge threshold with chamber diameter.	64
3.7	Composite image of dispersive mechanisms in a pre surcharge threshold manhole.	67
3.8	Composite image of dispersive mechanisms in a post surcharge threshold manhole.	68
3.9	Dispersion coefficients for 400mm diameter chamber, before and after surcharge threshold.	69
3.10	Dispersion coefficients for 500mm diameter chamber, before and after surcharge threshold.	70
3.11	Dispersion coefficients for 600mm diameter chamber, before and after surcharge threshold.	70
3.12	Dispersion coefficients for 800mm diameter chamber, before and after surcharge threshold.	71
3.13	Summary of all dispersion coefficients for all chamber diameters.	73

3.14	ADZ Coefficients, travel time (\bar{t}) and delay time (τ) for a straight pipe.	75
3.15	ADZ Coefficients, travel time (\bar{t}) and delay time (τ) for the 400mm chamber.	76
3.16	ADZ Coefficients, travel time (\bar{t}) and delay time (τ) for the 500mm chamber.	77
3.17	ADZ Coefficients, travel time (\bar{t}) and delay time (τ) for the 600mm chamber.	77
3.18	ADZ Coefficients, travel time (\bar{t}) and delay time (τ) for the 800mm chamber.	78
3.19	Variation of predicted time delay with discharge.	78
3.20	Variation of predicted travel time with discharge.	79
3.21	Variation of dispersive fraction (γ) with discharge for all chamber diameters.	80
3.22	Variation of unified dispersive fraction with discharge.	81
3.23	Variation of normalised travel time (\bar{t}/D_m^2) with discharge.	82
3.24	Variation in optimised travel time with surcharge for the 400mm chamber diameter.	86
3.25	Variation in optimised dispersion coefficient with surcharge for the 400mm chamber diameter.	86
3.26	Variation in optimised travel time with surcharge for the 500mm chamber diameter.	87
3.27	Variation in optimised dispersion coefficient with surcharge for the 500mm chamber diameter.	87
3.28	Variation in optimised travel time with surcharge for the 600mm chamber diameter.	88
3.29	Variation in optimised dispersion coefficient with surcharge for the 600mm chamber diameter.	88
3.30	Variation in optimised travel time with surcharge for the 800mm chamber diameter.	89
3.31	Variation in optimised dispersion coefficient with surcharge for the 800mm chamber diameter.	89
3.32	Surcharge averaged travel time prior to surcharge threshold.	91
3.33	Normalised surcharge averaged travel time prior to surcharge threshold.	91
3.34	Surcharge averaged travel time after the surcharge threshold has been reached.	92

3.35	Variation of dispersion coefficient with discharge.	93
3.36	Variation in travel time with surcharge for the 400mm diameter chamber.	95
3.37	Variation in delay time with surcharge for the 400mm diameter chamber.	95
3.38	Variation in travel time with surcharge for the 500mm diameter chamber.	96
3.39	Variation in delay time with surcharge for the 500mm diameter chamber.	96
3.40	Variation in travel time with surcharge for the 600mm diameter chamber.	97
3.41	Variation in delay time with surcharge for the 600mm diameter chamber.	97
3.42	Variation in travel time with surcharge for the 800mm diameter chamber.	98
3.43	Variation in delay time with surcharge for the 800mm diameter chamber.	98
3.44	Surcharge averaged travel time prior to the surcharge threshold.	99
3.45	Normalised surcharge averaged travel time prior to the surcharge threshold.	100
3.46	Surcharge averaged travel time after the surcharge threshold has been reached.	100
3.47	Surcharge averaged delay time.	101
4.1	Standard ADE and ADZ predictions for a 400mm chamber with a pre-threshold surcharge presented with measured data.	104
4.2	Optimised ADE and ADZ predictions for a 400mm chamber with a pre-threshold surcharge, presented with measured data.	104
4.3	Standard ADE and ADZ predictions for a 400mm chamber with a post-threshold surcharge, presented with measured data.	105
4.4	Optimised ADE and ADZ predictions for a 400mm chamber with a post-threshold surcharge, presented with measured data.	105
4.5	Standard ADE and ADZ predictions for a 500mm chamber with a pre-threshold surcharge, presented with measured data.	106
4.6	Optimised ADE and ADZ predictions for a 500mm chamber with a pre-threshold surcharge, presented with measured data.	106
4.7	Standard ADE and ADZ predictions for a 500mm chamber with a post-threshold surcharge, presented with measured data.	107
4.8	Optimised ADE and ADZ predictions for a 500mm chamber with a post-threshold surcharge, presented with measured data.	107

4.9	Standard ADE and ADZ predictions for a 600mm chamber with a pre-threshold surcharge, presented with measured data.	108
4.10	Optimised ADE and ADZ predictions for a 600mm chamber with a pre-threshold surcharge, presented with measured data.	108
4.11	Standard ADE and ADZ predictions for a 600mm chamber with a post-threshold surcharge, presented with measured data.	109
4.12	Optimised ADE and ADZ predictions for a 600mm chamber with a post-threshold surcharge, presented with measured data.	109
4.13	Standard ADE and ADZ predictions for a 600mm chamber with a pre-threshold surcharge, presented with measured data.	110
4.14	Optimised ADE and ADZ predictions for a 600mm chamber with a pre-threshold surcharge, presented with measured data.	110
4.15	Standard ADE and ADZ predictions for a 600mm chamber with a post-threshold surcharge, presented with measured data.	111
4.16	Optimised ADE and ADZ predictions for a 600mm chamber with a post-threshold surcharge, presented with measured data.	111
4.17	Standard ADE and ADZ predictions for a 600mm chamber with a pre-threshold surcharge, presented with measured data.	112
4.18	Optimised ADE and ADZ predictions for a 600mm chamber with a pre-threshold surcharge, presented with measured data.	112
4.19	Standard ADE and ADZ predictions for a 600mm chamber with a post-threshold surcharge, presented with measured data.	113
4.20	Optimised ADE and ADZ predictions for a 600mm chamber with a post-threshold surcharge, presented with measured data.	113
4.21	Standard ADE and ADZ predictions for a 800mm chamber with a pre-threshold surcharge, presented with measured data.	114
4.22	Optimised ADE and ADZ predictions for a 800mm chamber with a pre-threshold surcharge, presented with measured data.	114
4.23	Standard ADE and ADZ predictions for a 800mm chamber with a post-threshold surcharge, presented with measured data.	115

4.24	Optimised ADE and ADZ predictions for a 800mm chamber with a post-threshold surcharge, presented with measured data.	115
4.25	Observed and predicted data for a straight pipe with an average discharge.	116
5.1	Comparison between spread of a tracer traveling through a straight pipe and an 800mm manhole chamber.	129

Introduction

Since construction of the first sewer systems, the main goal in their design has been to convey an adequate discharge from their source to a point of disposal. During the 19th century storm drains, used to convey precipitation away from built up areas, were modified to carry domestic effluent (Hammer (1991)). These sewers are commonly referred to as combined sewers due to their conveyance of both storm and domestic effluent. Originally these drains were constructed to transport effluent to natural water courses. However, with the increase in both domestic and industrial effluent, public health became a priority and sewage treatment became a necessity before the effluent could be re-introduced into the natural environment. Through this development, the modern sewer systems with all its ancillary structures (e.g. manholes, gully pots, overflows etc.) has evolved. By far the most common of the sewerage structures, beyond the pipes themselves, are the manhole chambers. These structures are commonly placed no more than 150m apart, enabling inspection of the sewer systems, with further chambers being placed at every change in sewer sizes, direction, gradient and at junctions between multiple sewers.

Within the UK, the majority of the sewers that are currently in service are combined. As such, they typically convey domestic and industrial effluent as well as storm water and water that 'infiltrates / inflows' into the sewer system. Metcalf and Eddy, Inc. (1991) define these flow categories as follows -

- ◆ Domestic effluent: Inflow from sources such as residential, commercial, recreational and institutional areas. Generally design guides exist, enabling the prediction of flows from these sources. Typically, discharge of domestic effluent will fluctuate on a diurnal basis.
- ◆ Industrial effluent: The product of manufacturing industries. In some cases pre treatment may be carried out prior to the effluents discharge into the sewer system. Industrial effluent can be the source of toxic discharges into the sewer system such as Ammonia (Saul & Thornton (1989)).
- ◆ Infiltration / inflow: Infiltration is the passage of ground water into the sewer system through leaks and porous materials used in construction (i.e. through pipe and manhole walls).

Inflow is the surface runoff from non porous land (e.g. roads, forecourts etc.) that enters into the sewer system. Inflow can enter the sewer system through storm drains.

- ◆ Storm water: Inflow from non porous areas of land as a result of precipitation. Storm water enters the sewer systems through storm drains.

The total flow within a sewer system at any one time can be calculated from the sum of these discharges. However, due to the unpredictable nature of storm flow (both in its intensity and duration) there is always the probability of exceeding the maximum discharge that can be conveyed by the sewer system. An economic method of avoiding failure of the sewer systems at these times of excess flow is to introduce overflow structures. These structures, called combined sewer overflows (CSO's), divert surplus flow from the sewer system into natural water courses. Consequently effluent may be diverted into natural water courses before it has been treated.

Originally CSO's were designed solely for their conveyance of excess flow from sewer systems. However, in recent times, political and public pressure has meant that the design of these structures has had to take on a more environmentally conscious role. To this end, within Europe, directives have been issued stipulating guidelines for the design of sewer systems and limits on the effluent discharged into natural water courses (Council of the European Communities, (1991)). Within the UK, the EC directives are reflected in the AMP2 guidelines, National Rivers Authority, (1993), which governs both the constant and intermittent effluent discharges from the perspective of the natural water courses. In conjunction with these guidelines the Urban Pollution Management Manual, Foundation for Water Research, (1994), dictates the management of discharges from both sewer systems and sewage treatment works from the perspective of the sewerage system. With respect to the intermittent discharges from sewer systems, the guidelines cover overflows from new sewer systems and the upgrading of those already in existence. The limits governing the discharges from overflow structures are primarily dictated by the nature of the water course into which they flow.

The main goal of the current guidelines is to address the aesthetic problem of reducing the gross particulate discharged from the sewer systems during times of overflow. However, within the near future, water industries will have to address the potentially more critical problem of chemical and bacterial discharges during times of overflow. To prevent these pollutants from having any major detrimental effects on the natural environment, limits will

have to be enforced on BOD levels as well as the discharge levels of heavy metals, ammonia, and other toxins into natural waterways. Although the overflow structures cannot directly remove these water borne pollutants, selective discharging from overflows can minimise their impact on the receiving waters.

To determine how the magnitude of pollutants vary within the discharge from an overflow, the source of the pollutant must first be elucidated. It has been shown by many authors (including Beck, Adeloye, Lessard, Finney & Simon (1986), Thornton & Saul (1989), Payne, Moys, Hutchings & Henderson (1989) and Larson, Berndtsson, Hogland, Spångberg & Bennerstedt (1990)) that there is a temporal fluctuation in the pollutant concentration at times of increased flow (normally coincident with storm events). An initial peak in concentration, commonly referred to as the first flush, is seen during these times (especially when preceded by a long dry weather period). The source of this peak pollutant load is sediment that has settled out of the main flow during the slower dry weather flows, and its associated solutes. The rapid increase in the flow that is characteristic of a storm event, quickly entrains the settled pollutants back into the main flow. To accommodate for this increase in concentration, storage tanks are often built into the sewer system, thus, in theory, the portion of the flow containing the highest pollutant load is retained within the sewer system. The design of such structures however, is very site specific and their optimum design is based on the minimum required storage volume and cost of construction (Crabtree, Gent & Garsdal (1994)).

Numerical and computational models are becoming increasingly widespread in the design of optimal sewer systems. Numerical modelling techniques of existing sewer systems and overflows are continually under development and can be used to assist in the design and location of storage tanks with respect to overflow structures (Gupta & Saul (1996)). However, these techniques often require site specific measurements, rather than being purely hypothetical.

Computer models allow for insight into the behaviour of sewer systems before they are even constructed. However, to enable the accurate numerical modelling of concentrated pollutants flowing through sewer systems, the factors affecting their transport and temporal variations must be assessed. Pollutants that are in transit will not travel as a plug flow, but will spread into the surrounding flow. This in turn will assist in the dilution of the pollutants, but will also temporally retard their passage through the sewer system. If a model were to assume that

pollutant transport was purely through plug flow, it would result in an over estimation of the peak concentration, but an underestimation of the travel time and spread (incorrect assessment of the travel time will have further repercussions in the calculation of both chemical and BOD decay). Consequently, to accurately model the transport of a pollutant load, the effects of the sewer system and all its ancillary structures must be taken into account. Extensive studies have been conducted regarding the flow and spread of pollutants within pipes (Taylor (1953 and 1954)). However, beyond these studies, no account has been made to assess the effects of the ancillary structures.

As has been previously mentioned, the most common structure within sewer systems are manholes. At times of increased flow, these structures will often become surcharged. The cause of this surcharge is the pressure head that is built up in the sewer system when the pipes are flowing full. At ancillary structures, such as manholes, where atmospheric conditions exist, the effluent will rise into the chamber to balance the pressure head and maintain free flow conditions. As a result, the manhole will act as an additional storage volume, consequently causing additional dilution of the pollutant and also retarding its progress through the sewer system. Until now, little or no effort has been made to take account of these structures, yet as the current research will show, they cause excessive divergence from pipe flow.

The current research will quantify the change in temporal characteristics of a transient pollutant as it passes through a manhole structure. It will examine the effects of manhole diameter, surcharge (within the manhole) and discharge (through the manhole) on a soluble tracer. In conclusion, the study will supply a numerical model that describe the change in temporal distribution of a pollutant as it passes through a manhole. Such a solution would lend itself to more complex computer modelling techniques that can simulate entire sewer systems (e.g. MouseTrap (Danish Hydraulic Institute, Denmark) or HydroWorks (HR Wallingford, UK)). With this increase in the accuracy of travel time and dispersion predictions, these modelling tools can be more reliably used in the optimal design of sewer systems, taking both conveyance and environmental impact into consideration.

Chapter 1

Mixing Processes

1.1 Effects of Mixing

The effects of one fluid mixing into another can be seen within the every day environment. When a traceable fluid "a" is added to a second stationary fluid "b", the tracer will often be seen to continue mixing until it has become uniformly diluted throughout the second fluid. A common examples of this can be seen when steeping tea in water. This example can illustrate how one fluid will mix into another, although it is not an entirely perfect example because the tracer movements will, to some degree, be influenced by convection currents.

For two inert fluids to thoroughly combine by diffusion, two conditions must be observed, namely that the fluids have comparable densities and viscosities. Significant differences in either of these parameters will inhibit the mixing processes. With a difference in densities, stratification between the fluids will be observed, whilst a difference in the viscosities can retard the mixing processes to the point where the fluids remain segregated. A tracer that exhibits properties similar to the fluid into which it has been placed is referred to as being neutrally buoyant.

If a true neutrally buoyant tracer was added to a second fluid, it would, if unhindered, spread spatially into the volume of the containing fluid. The rate at which a tracer spreads into its surrounding environment is governed by a process called Molecular Diffusion (or Brownian Motion). Molecular diffusion was first identified by Fick in 1855. It was shown that a tracer moved from a high concentration to a low concentration at a rate proportional to the concentration gradient between the tracer and its surrounding environment.

1.2 Mixing Through Molecular Diffusion

Fick deduced that the movement of the tracer in any one orthogonal direction could be defined in terms of a one dimensional diffusion equation -

$$J_m = -e_m \left(\frac{\partial c}{\partial x} \right) \quad (1.1)$$

Where,

- J_m = Tracer flux in the x direction. i.e. $J_m = (dc/dt)$,
- c = Tracer concentration,
- t = Time,
- e_m = Molecular diffusion coefficient,
- $\frac{\partial c}{\partial x}$ = Tracer concentration gradient in the x direction.

1.2.1 Mixing in Laminar Flow

In a two dimensional fluid continuum, Figure 1.1, a mean velocity U has been considered planar to the page, and it is assumed that this velocity has no effect perpendicular to the page. Within the continuum a small cell of dimensions Δx and Δy can be considered, moving with the same mean velocity U (Holley (1969), French (1986), Rutherford (1994)).

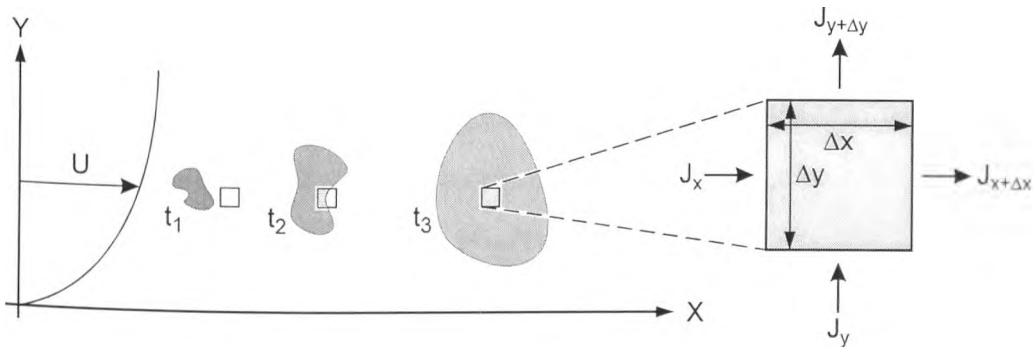


Figure 1.1 The spread of tracer in laminar flow

If a tracer was introduced into the continuum in the vicinity of the cell at a time t_0 , over a period of time it would spread out relative to the cell, as if both were located in a stationary continuum. Thus the tracer would spread through the cell. From Figure 1.1 it can be seen that the tracer flux entering the cell in the x direction could be written J_x , whilst the flux leaving the cell would be $J_{x+\Delta x}$. Similarly in the y direction the tracer flux entering and leaving the cell could be written J_y and $J_{y+\Delta y}$ respectively. If the time taken for the flux to travel through the cell was Δt then the average mass of tracer within the cell during this time would be,

$$\frac{M_t - M_{t+\Delta t}}{\Delta t} = (J_x - J_{x+\Delta x})\Delta y + (J_y - J_{y+\Delta y})\Delta x \quad (1.2)$$

where,

- M_t = Mass of tracer at time t ,
- J_i = Tracer flux at i , where $i = x$ or y ,
- Δx = Width of cell,
- Δy = Height of cell.

The above equation relates to the time average mass of tracer as it would appear in an Eulerian environment. However, in a Lagrangian frame of reference, the change in the mass of tracer present within the cell over the same period of time, Δt , can be represented by the initial mass present within the cell plus the change in mass that has occurred over the period Δt .

$$M_{t+\Delta t} = M_t + \left(\frac{dM}{dt} \right)_t \Delta t \quad (1.3)$$

where,

- M_t and $M_{t+\Delta t}$ = Mass of tracer in cell at time t and $t+\Delta t$,
- dM/dt = Rate of change in tracer mass with time.

If the continuum is considered spatially, the total mass of tracer within the cell can be expressed in terms of the area mean concentration and the volume of the cell -

$$M = c\Delta x\Delta y \quad (1.4)$$

where,

- M = Total mass of tracer in cell,
- c = Area mean concentration of tracer.

The change in the spatial mass of tracer within the cell over at period Δt can therefore be related to the rate of change in the concentration within the cell by substituting for the mass term in the right hand side of equation 1.3 with the concentration term in equation 1.4.

Therefore the time averaged mass of tracer within the cell over the period Δt is found to be -

$$\frac{M_{t+\Delta t} - M_t}{\Delta t} = \left(\frac{dc}{dt} \right)_t \Delta x\Delta y \quad (1.5)$$

Instead of considering the change in mass of the tracer within the cell, it is also possible to regard the change in flux across the cell. It can be seen that the flux leaving the cell can be

written in terms of that entering plus the change that occurs as it passes through the cell.

Therefore in both the x and y directions, it holds that the flux leaving the cell can be written -

$$J_{x+\Delta x} = J_x + \left(\frac{\partial J_x}{\partial x} \right)_x \Delta x \quad (1.6)$$

$$J_{y+\Delta y} = J_y + \left(\frac{\partial J_y}{\partial y} \right)_y \Delta y \quad (1.7)$$

Obviously, from equations 1.6 and 1.7, the net change in flux across the cell is the difference between that entering, and that leaving. This change in flux can be expressed in terms of concentration by substituting Ficks one dimensional diffusion equation (equation 1.1) in place of the rate of change of flux with distance.

$$(J_x - J_{x+\Delta x}) = \frac{\partial}{\partial x} \left(e_m \frac{\partial c}{\partial x} \right) \Delta x \quad (1.8)$$

$$(J_y - J_{y+\Delta y}) = \frac{\partial}{\partial y} \left(e_m \frac{\partial c}{\partial y} \right) \Delta y \quad (1.9)$$

Similarly the net change in the mass of tracer within the cell over the period Δt can be expressed in terms of concentration by substituting equations 1.8 and 1.9 into 1.2, giving -

$$\frac{M_t - M_{t+\Delta t}}{\Delta t} = e_m \left(\frac{\partial^2 c}{\partial x^2} \right) \Delta x \Delta y + e_m \left(\frac{\partial^2 c}{\partial y^2} \right) \Delta x \Delta y \quad (1.10)$$

Therefore the change in the concentration with respect to distance can be expressed in terms of the temporal change in concentration by substituting for the average mass term in equation 1.5.

$$\left(\frac{dc}{dt} \right)_t = e_m \left(\frac{\partial^2 c}{\partial x^2} \right) + e_m \left(\frac{\partial^2 c}{\partial y^2} \right) \quad (1.11)$$

If two relative spatial points 'A' and 'B' are now considered within the continuum, and the tracer is not fully mixed throughout the continuum, then the tracer concentration can be assumed to vary with position (Douglas, Gasiorek & Swaffield (1987)). From Ficks model it is also possible to assume that the concentration at any one point within the continuum will vary with time. Therefore the change in the tracer concentration as it moves through a distance δs (where $\delta s = (\delta x^2 + \delta y^2)^{0.5}$) from A to B in a given time δt is given by -

$$\text{Total change in tracer concentration} = \text{Difference in tracer concentration between A and B at a given instant} + \text{Change in tracer concentration at B occurring in time } \delta t$$

In other words -

$$dc = \frac{\partial c}{\partial t} \delta t + \frac{\partial c}{\partial x} \delta x + \frac{\partial c}{\partial y} \delta y \quad (1.12)$$

The temporal rate of change in the tracer concentration relative to the cell can be found by differentiating (1.12) with respect to time. If $\lim(\delta t) \rightarrow 0$ this differential can be written,

$$\left(\frac{dc}{dt} \right)_t = \frac{\partial c}{\partial t} + \frac{\partial c}{\partial x} \frac{dx}{dt} + \frac{\partial c}{\partial y} \frac{dy}{dt} \quad (1.13)$$

Clearly both dx/dt and dy/dt can be represented by velocities in the x and y direction respectively, U_x and U_y .

$$\left(\frac{dc}{dt} \right)_t = \frac{\partial c}{\partial t} + U_x \frac{\partial c}{\partial x} + U_y \frac{\partial c}{\partial y} \quad (1.14)$$

However, as seen in Figure 1.1, the flow in the continuum is laminar and in the x direction, therefore there is no y component to the flow regime and U_y will be zero. Equating 1.11 and 1.14 gives rise to the two dimensional molecular diffusion equation that will satisfy dispersion within laminar flow. This equation is commonly referred to as Ficks 2nd law of molecular diffusion.

$$\frac{\partial c}{\partial t} + U_x \frac{\partial c}{\partial x} = e_m \left(\frac{\partial^2 c}{\partial x^2} + \frac{\partial^2 c}{\partial y^2} \right) \quad (1.15)$$

1.2.2 Mixing in Turbulent Flow

If the same continuum is considered, but now with a turbulent flow in the x direction an analogous equation to 1.15 can be used.

$$\frac{\partial c}{\partial t} + U_x \frac{\partial c}{\partial x} + U_y \frac{\partial c}{\partial y} = e_m \left(\frac{\partial^2 c}{\partial x^2} + \frac{\partial^2 c}{\partial y^2} \right) \quad (1.16)$$

Where,

U_x and U_y = Instantaneous turbulent velocity component in the x and y directions respectively.

The advective term $U_y(\partial c/\partial y)$ has been included because within a turbulent flow there will be a y component as a result of the shear velocities. The terms U_x , U_y and c are instantaneous and will vary with both time and location. In practice actually obtaining instantaneous values is not a practical solution. As an alternative, time averaged values are used to replace the instantaneous values.

$$U_x = \bar{U}_x + u'_x \quad (1.17a)$$

$$U_y = u'_y \quad (1.17b)$$

$$c = \bar{c} + c' \quad (1.17c)$$

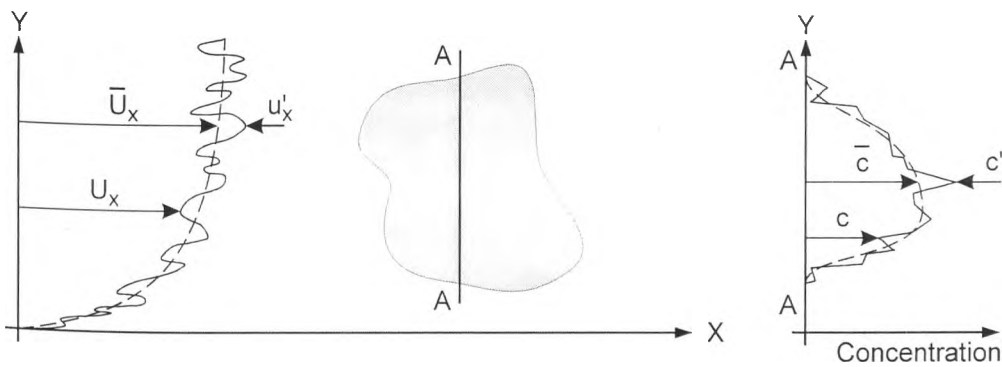


Figure 1.2 Mechanisms of turbulent diffusion.

Time averaged values are shown with over bars, whilst the terms with primes indicate turbulent fluctuations about the time average (Figure 1.2). As can be seen there is no time average for the U_y term. This is because any velocity perpendicular to the main flow is due to the shear velocity which by its nature is a turbulent fluctuation, thus a time average of U_y would be zero. Substituting the above time averaged terms into equation 1.16 yields -

$$\frac{\partial \bar{c}}{\partial t} + \frac{\partial c'}{\partial t} + \bar{U}_x \frac{\partial \bar{c}}{\partial x} + \bar{U}_x \frac{\partial c'}{\partial x} + u'_x \frac{\partial \bar{c}}{\partial x} + u'_x \frac{\partial c'}{\partial x} + u'_y \frac{\partial \bar{c}}{\partial x} + u'_y \frac{\partial c'}{\partial y} = e_m \left\{ \frac{\partial^2 \bar{c}}{\partial x^2} + \frac{\partial^2 c'}{\partial x^2} + \frac{\partial^2 \bar{c}}{\partial y^2} + \frac{\partial^2 c'}{\partial y^2} \right\} \quad (1.18)$$

If equation 1.18 is itself time averaged, all the terms containing a single turbulent fluctuation will reduce to zero because they are only fluctuations about a mean. Thus 1.18 will simplify to the form -

$$\frac{\partial \bar{c}}{\partial t} + \bar{U}_x \frac{\partial \bar{c}}{\partial x} + \frac{\partial \overline{c'u'_x}}{\partial x} + \frac{\partial \overline{c'u'_y}}{\partial y} = e_m \frac{\partial^2 \bar{c}}{\partial x^2} + e_m \frac{\partial^2 \bar{c}}{\partial y^2} \quad (1.19)$$

Rearranging 1.19 to the form -

$$\frac{\partial \bar{c}}{\partial t} + \bar{U}_x \frac{\partial \bar{c}}{\partial x} = e_m \frac{\partial^2 \bar{c}}{\partial x^2} + e_m \frac{\partial^2 \bar{c}}{\partial y^2} + \frac{\partial(-\overline{c'u'_x})}{\partial x} + \frac{\partial(-\overline{c'u'_y})}{\partial y} \quad (1.20)$$

generates terms that are analogous to the Fickian molecular diffusion equation (equation 1.1), where -

$$\overline{c'u'_x} = -e_t \left(\frac{\partial \bar{c}}{\partial x} \right) \quad (1.21)$$

$$\overline{c'u'_y} = -e_t \left(\frac{\partial \bar{c}}{\partial y} \right) \quad (1.22)$$

$\overline{c'u'_x}$ and $\overline{c'u'_y}$ = turbulent flux,

e_t = turbulent diffusion coefficient.

therefore, substituting the turbulent diffusion terms into equation 1.20 gives -

$$\frac{\partial \bar{c}}{\partial t} + \bar{U}_x \frac{\partial \bar{c}}{\partial x} = e_m \frac{\partial^2 \bar{c}}{\partial x^2} + e_m \frac{\partial^2 \bar{c}}{\partial y^2} + e_t \frac{\partial^2 \bar{c}}{\partial x^2} + e_t \frac{\partial^2 \bar{c}}{\partial y^2} = (e_m + e_t) \frac{\partial^2 \bar{c}}{\partial x^2} + (e_m + e_t) \frac{\partial^2 \bar{c}}{\partial y^2} \quad (1.23)$$

This equation provides a two dimensional dispersion equation that accounts for both molecular diffusion as well as turbulent diffusion in a two dimensional shear flow.

1.2.3 One Dimensional (Depth Averaged) Dispersion

If it is now assumed that the tracer has had time to disperse throughout the entire depth of the continuum, (Rutherford, 1994) it would now be possible to produce a depth average of equation 1.23.

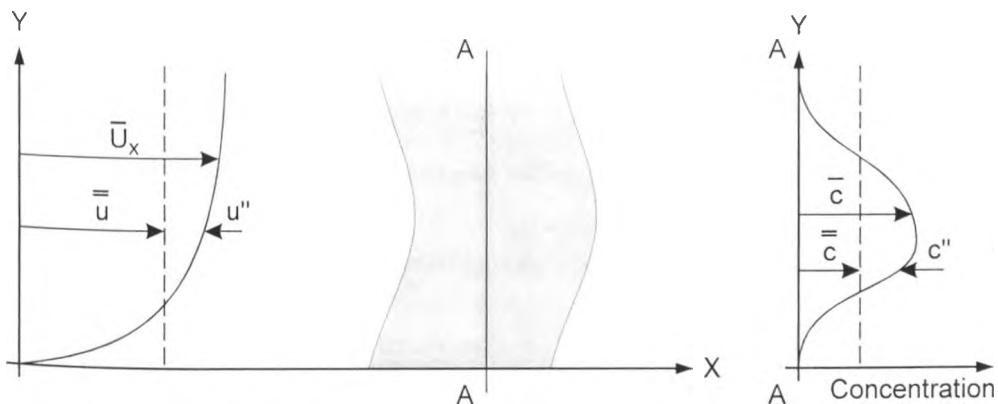


Figure 1.3 Mechanisms of depth averaged turbulent diffusion.

$$\overline{\overline{c}} = \overline{\overline{c}} + c'' \quad (1.24)$$

$$\overline{U_x} = \overline{\overline{u}} + u'' \quad (1.25)$$

As with the time averaged solution, variables can be replaced with a depth averaged value plus a fluctuation about the average. The double over bar indicates a depth averaged value whilst double prime indicates fluctuations about the depth average throughout the entire depth. The apparent mixing caused by the spatial averaging of tracer concentrations within a continuum is termed 'shear flow dispersion'. To obtain a one dimensional, depth averaged shear flow dispersion equation, 1.24 and 1.25 can be substituted into 1.23 giving -

$$\frac{\partial(\overline{\overline{c+c''}})}{\partial t} + (\overline{\overline{u+u''}}) \frac{\partial(\overline{\overline{c+c''}})}{\partial x} = (e_m + e_t) \frac{\partial^2(\overline{\overline{c+c''}})}{\partial x^2} + (e_m + e_t) \frac{\partial^2(\overline{\overline{c+c''}})}{\partial y^2} \quad (1.26)$$

However, if a tracer is considered fully cross-sectionally mixed, the variation of concentration in the y direction becomes negligible, and therefore the last right hand term in equation 1.26 can be ignored. If equation 1.26 is averaged over the depth of the continuum, then, as with equation 1.18, all terms containing a solitary double prime reduce to zero. Thus equation 1.26 becomes -

$$\frac{\partial \overline{\overline{c}}}{\partial t} + \overline{\overline{u}} \frac{\partial \overline{\overline{c}}}{\partial x} + \frac{\partial(\overline{\overline{c''u''}})}{\partial x} = (e_m + e_t) \frac{\partial^2 \overline{\overline{c}}}{\partial x^2} \quad (1.27)$$

Again the analogy to equation 1.1 can be assumed to develop a diffusion coefficient due to the effects of shear flow (e_k), where -

$$-\overline{\overline{c''u''}} = e_k \left(\frac{\partial \overline{\overline{c}}}{\partial x} \right) \quad (1.28)$$

Therefore a one dimensional longitudinal dispersion equation for a tracer that is fully cross sectionally mixed within a continuum, and travelling with a mean velocity U in the x direction can be found by substituting equation 1.28 into 1.27.

$$\frac{\partial \overline{\overline{c}}}{\partial t} + U \frac{\partial \overline{\overline{c}}}{\partial x} = (e_m + e_t + e_k) \frac{\partial^2 \overline{\overline{c}}}{\partial x^2} \quad (1.29)$$

To simplify the above equation the coefficients e_m , e_t , and e_k can be replaced by a general, bulk, dispersion coefficient, K . However, it should be noted that $e_k \gg e_m + e_t$, therefore $K \approx e_k$.

The resulting equation is commonly referred to as the Taylor advective dispersion equation as it is the result found from his work, Taylor (1954).

$$\frac{\partial c}{\partial t} + U \frac{\partial c}{\partial x} = K \frac{\partial^2 c}{\partial x^2} \quad (1.30)$$

1.2.4 Application of the Taylor Advective Dispersive Equation

Many authors have supplied practical solutions to equation 1.30 (Taylor (1954), French (1986), Barnett (1983)), allowing a concentration profile of a tracer to be routed from an upstream location to a new downstream site. Taking both K and U to be constant, the solution to a second order differential can be found by specifying the initial and boundary conditions.

Given the initial spatial conditions -

$$C(x,t) = C(x,0) = 0 \text{ for } x > 0$$

$$\text{and } C(x,t) = C(x,0) = C_0 \text{ for } x < 0$$

the solution to equation 1.30 can be shown to be (Taylor (1953), Barnett(1983)) -

$$C(x,t) = \frac{C_0}{2} \left[1 - \operatorname{erf} \left(\frac{x - Ut}{\sqrt{4Kt}} \right) \right] \quad (1.31)$$

Where

$C(x,t)$ = Tracer concentration at a distance x and time t from the injection

C_0 = Mass of injected tracer

By specifying C_0 as a delta function, equation 1.31* can be written -

$$C(x,t) = \frac{C_0}{2\sqrt{\pi Kt}} \exp \left[-\frac{(x - Ut)^2}{4Kt} \right] \quad (1.32)$$

Convolution principles can be used to provide a solution for any spatially distributed input (Barnett 1983). If, rather than a single delta function, an upstream concentration profile is now considered, the profile can be divided into a series of discrete delta functions. Using equation 1.32 these individual delta functions can be routed to a downstream location, where, by superposition the overall downstream concentration profile can be found (Rutherford, 1994).

*The solution to an error function of x is taken as $\operatorname{erf}(x) = \frac{2}{\sqrt{\pi}} \int_0^x e^{-t^2} dt$, and the complimentary error function as $\operatorname{erfc}(x) = 1 - \operatorname{erf}(x)$.

$$C(x_2, t_2) = \int_{\xi=-\infty}^{\infty} \frac{C(\xi_1, t_1)}{\sqrt{4\pi K(t_2 - t_1)}} \exp \left\{ -\frac{[x_2 - \xi - U(t_2 - t_1)]^2}{4K(t_2 - t_1)} \right\} d\xi \quad (1.33)$$

Where

$C(x_i, t_i)$ = Concentration at location x and time t , $i = 1$ or 2 , corresponding to up or downstream locations respectively,

t_1 & t_2 = Relative temporal centroids of up and downstream profiles.

ξ = Dummy spatial variable of integration.

Equation 1.33 can be used to route a spatial distribution of a tracer profile. Derived from Taylors (1954) work it describes the spatial propagation of a distribution that starts as a delta function and tends towards a Gaussian distribution as it travels downstream. From studies carried out in the natural environment, several drawbacks to this approach become evident. Tracer profiles are rarely obtained as an instantaneous spatial distribution. To obtain a spatial distribution would require taking some form of "snap shot" of the data. The alternative is to acquire a temporal distributions at a fixed location. Measurements of the concentration of a tracer within a flow can readily be monitored by the abstraction of samples, or by insitu methods.

Within the environment, tracer profiles have rarely been shown to be Gaussian. There are numerous reasons for this to be the case. Taylor (1954) observed that the increase in the spread of a tracer would, at some point downstream from its injection become linear. This region commonly referred to as the equilibrium zone is where an equilibrium between the velocity shear and the turbulent diffusion has been developed. However, it was shown by Fischer (1966) that any skewness imparted into the tracer profile prior to the equilibrium zone through the velocity profile or even through the injection method would remain well into the equilibrium zone.

As has been previously stated, in practice most data is acquired as a temporal distribution. This process in itself will result in the observation of a skewed distribution, even if the spatial distribution is truly Gaussian. The cause of this observed skewness is that the dispersion of a tracer is proportional to time, therefore if a tracer profile is measured temporally at a fixed spatial location, the tailing edge of the data will have had a longer time in which to disperse, as

opposed to the leading edge. The result of observing a temporal distribution from a fixed spatial location would be that the distribution would appear skewed. This effect is illustrated in Figure 1.4. The dashed line represents the spread of a single spatial distribution of a tracer (at several locations within the reach) as it travels downstream. In contrast, the solid line represents the observed temporal distribution of the same tracer as it passes a station at a distance of 80 metres downstream.

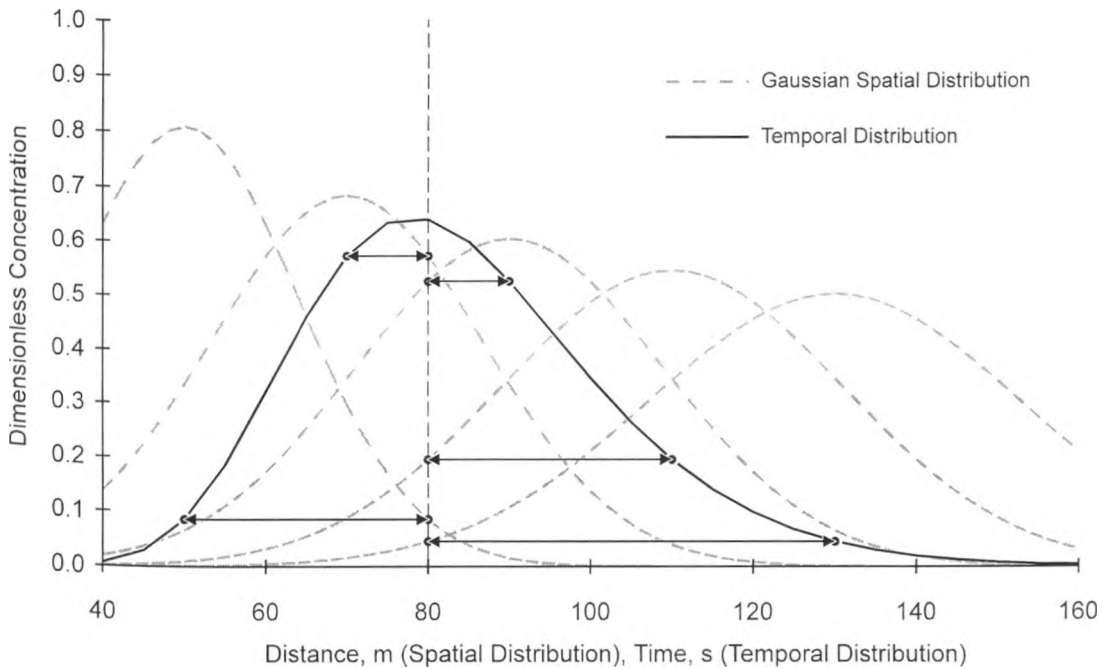


Figure 1.4 Development of a skewed temporal distribution from a Gaussian spatial distribution.

From the problems that arise when considering spatial tracer distributions it can be seen that a temporal solution would prove more useful. One such solution can be found if the boundary and initial conditions are -

$$C(x,t) = C(0,t) = C_0 \text{ for } 0 < t < \infty$$

$$\text{and } C(x,t) = C(x,0) = 0 \text{ for } 0 < x < \infty$$

in which case the solution to equation 1.30 can be shown to be (French 1986, Barnett 1983) -

$$C(x,t) = \frac{C_0}{2} \left[\operatorname{erfc} \left(\frac{x - Ut}{\sqrt{4Kt}} \right) + \operatorname{erfc} \left(\frac{x + Ut}{\sqrt{4Kt}} \right) \exp \left(\frac{Ux}{K} \right) \right] \quad (1.34)$$

For the tracer inlet condition where C_0 is a delta function, equation 1.34 will reduce to the form,

$$C(x, t) = \frac{C_0 x}{2Ut\sqrt{\pi Kt^3}} \exp\left[-\frac{(x - Ut)^2}{4Kt}\right] \quad (1.35)$$

and again by using convolution principles (Rutherford 1994) the general solution of equation 1.35 can be determined.

$$C(x_2, t) = \int_{\tau=-\infty}^{\infty} \frac{C(x_1, \tau)(x_2 - x_1)}{\sqrt{4\pi K(t - \tau)^3}} \exp\left[-\frac{[x_2 - x_1 - U(t - \tau)]^2}{4K(t - \tau)}\right] d\tau \quad (1.36)$$

Historically the temporal solution, equation 1.36, actually predates that of the spatial solution, equation 1.30 (Barnett 1983). This temporal solution was actually developed to describe the propagation of a flood wave rather than the transport of a tracer, although its application within both scenarios is valid.

Another solution to the Taylor advective dispersive equation (equation 1.30) is the so called "Frozen Cloud Approximation" (Fischer 1968, Barnett 1983, Rutherford 1994). This approach assumes that the time taken for the advection of a tracer past a fixed spatial measuring station is much greater than the rate of temporal dispersion. Therefore the dispersion that occurs as the tracer passes the station is negligible. With this assumption, a temporal profile can be transcribed to spatial profile (Rutherford 1994) with its centroid at the upstream measuring station x_1 .

$$C(x, t_1) = C\left(x_1, t_1 + \frac{x_1 - x}{U}\right) \quad (1.37)$$

Once in a spatial format, the profile can be routed downstream to a second station using equation (1.33), where upon, the profile can be transcribed back to a temporal distribution by simply reversing equation 1.37.

$$C(x_1, t) = C(x_1 + U(t_1 - t), t_1) \quad (1.38)$$

An illustration of the process used to transcribe between temporal and spatial data can be seen if figure 1.5.

The actions of transcribing and routing the data have been summarised into a single equation (Fischer 1968), that can be applied directly to temporal data when routing it downstream.

$$C(x_2, t) = \int_{\tau=-\infty}^{\infty} \frac{C(x_1, \tau)U}{\sqrt{4\pi K(\bar{t}_2 - \bar{t}_1)}} \exp\left[-\frac{U^2(\bar{t}_2 - \bar{t}_1 - t + \tau)^2}{4K(\bar{t}_2 - \bar{t}_1)}\right] d\tau \quad (1.39)$$

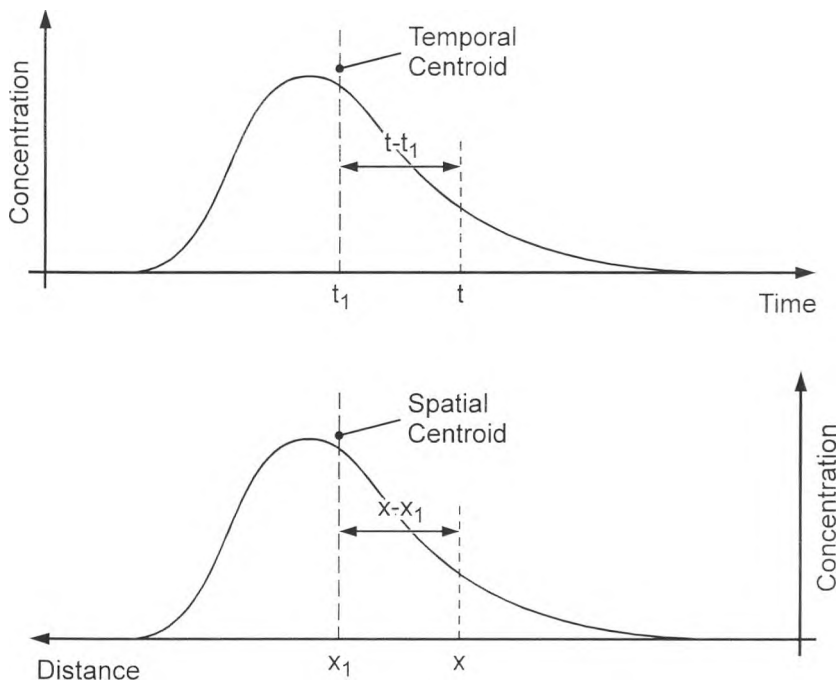


Figure 1.5 Temporal and spatial distributions at station x_1 and time t_1 respectively.

1.2.5 Evaluation of the Shear Flow Dispersion Coefficient

Once a method of routing a tracer through a reach has been determined, the evaluation of a suitable dispersion coefficient must be undertaken. From the initial straight pipe studies carried out by Taylor (1954), an approximate, theoretical relationship between the value of the dispersion coefficient, shear velocity and pipe radius was determined.

$$K = 10.1ru^* \quad (1.40)$$

Where -

K = Turbulent dispersion coefficient (m^2s^{-1}),

r = Pipe radius (m),

u^* = Shear velocity (ms^{-1}).

However, the coefficient, 10.1, was found to be very case specific, and in results presented by Taylor (1954) for varying pipe roughness and curvature this coefficient was seen to vary between 10.0 and 21.9.

Although Taylor (1954) identified that there was an increase in the spread of a tracer during its passage downstream, no attempt was made to quantify this increase. As an alternative, and due to the relative symmetry observed within the results, the width of the concentration profile was simply measured at the point where the measured concentration was at 50 per-cent of the peak concentration.

Further work undertaken by Aris (1956) showed that the spread of a tracer could be calculated in terms of the variance (second moment of area) about its centre of mass. These findings showed that the growth of the variance, from to point of injection of the tracer, rapidly tended towards a constant. Through calculation of the change in variance about an origin located at the centre of mass of the distribution, and moving spatially in a streamwise direction with the average cross-sectional velocity, Aris (1956) concluded that -

$$\lim_{t \rightarrow \infty} \frac{1}{2} \frac{d\sigma_s^2}{dt} = K \quad (1.41)$$

Where -

$$\sigma_s^2 = \text{Spatial variance (m}^2\text{),}$$

$$t = \text{Time (s).}$$

As a result of further studies undertaken by Fischer (1966), the spatial variance seen in equation 1.41 was found to be directly proportional to the temporal variance, with the following relationship -

$$\partial\sigma_s^2 = U^2\partial\sigma_t^2 \quad (1.42)$$

where -

$$\sigma_t^2 = \text{Temporal variance (s}^2\text{),}$$

$$U = \text{Mean velocity (ms}^{-1}\text{).}$$

In both the temporal and spatial cases, the variances have been normalised by dividing throughout by the area under the concentration distributions. Figure 1.6 illustrates the variables that are required to calculate the temporal variance (equation 1.43). It should be noted that the temporal distribution is analogous to a spatial distribution through the substitution of time with distance.

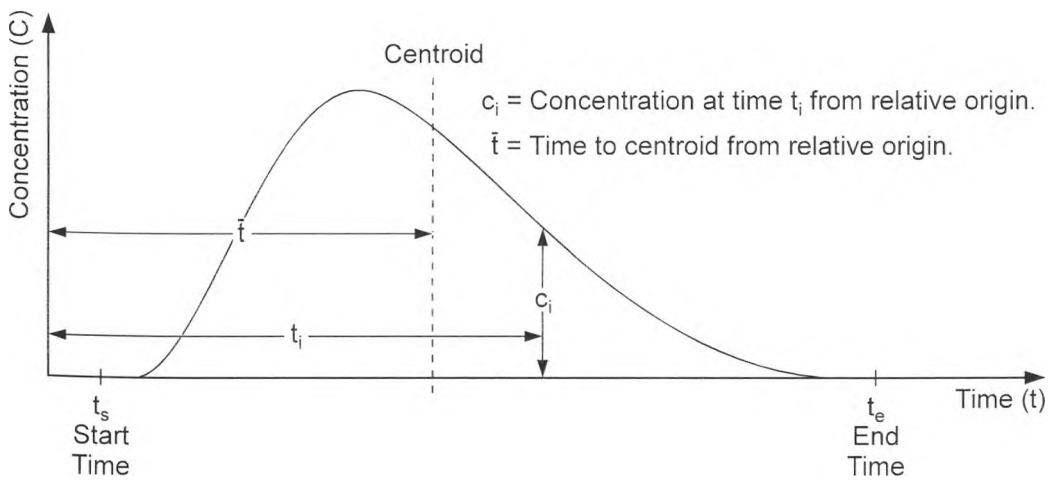


Figure 1.6 Required measurements for calculation of temporal variance.

$$\sigma_t^2 = \frac{\int_{t_s}^{t_e} c_i (t_i - \bar{t})^2 dt}{\int_{t_s}^{t_e} (c_i t_i) dt} \quad (1.43)$$

In addition, it was also proposed that a dispersion coefficient could be calculated from the rate of change of temporal variance, irrespective of the injection conditions. By substituting equation 1.42 into 1.41 and discretising the resultant equation, the dispersion coefficient, K , can be calculated from just two temporal concentration distributions. If the subscripts 1 and 2 are used to denote the relative up and downstream distributions respectively, the discretised representation of the rate of change in variance would take the form -

$$K = \frac{1}{2} U^2 \frac{(\sigma_{t_2}^2 - \sigma_{t_1}^2)}{\bar{t}_2 - \bar{t}_1} \quad (1.44)$$

where -

σ_i^2 = Temporal variance of tracer distribution at i , where i represents relative up and downstream measuring stations (s^2),

t_i = Temporal centroid of tracer distribution at i , where i represents relative up and downstream measuring stations (s).

Fischer (1966) found that this representation of the dispersion coefficient held even if markedly skewed data was observed.

1.3 Non-Fickian Dispersion Models

1.3.1 Cells in Series Model

Within river mixing it has long been acknowledged that although the standard advective dispersive equation (ADE) can reliably predict the travel times of a dispersing media, there can often be large discrepancies in the skewness of predicted concentration / time profiles, and thus a poor correlation between observed and predicted downstream profiles (Thackston & Schnelle (1970), Stefan & Demetrapoulos (1981)). As has been previously shown, it is the nature of ADE predictions to tend toward a Gaussian distribution. In the context of the research undertaken by Taylor (1953 & 1954) where "the cross-section was independent of both distance and time", and "the turbulence was statistically stationary in time" (Chatwin, (1980)), the ADE provided a good approximation to the observed trend in the data. However, when a more complex flow regime is considered (Beer & Young (1984), Nordin & Troutman (1980), Stefan & Demetrapoulos (1981)) a persistence in the skewness of the data has been observed. Through riverine studies, attempts have been made to include the observed skewness in predictions by the inclusion of dead zones (Pedersen (1977), Valentine & Wood (1977)). However, these solutions have often proved to be complicated and difficult to calibrate.

In a departure from the classic ADE, Stefan & Demetrapoulos (1981) have developed a method that no longer depends on the Fickian analogy. This method divides the flow into a number of sub-reaches of equal volume, called cells. When a tracer is entered into the flow it will travel from cell to cell as it travels downstream. Upon entering into any individual cell, the mass of the tracer is assumed to becoming completely well mixed throughout the cell before it moves on to the next cell. In essence, it is the discretisation of the flow that causes the dispersion to take place within the model. It can be shown (Stefan & Demetrapoulos (1981)) that for a conservative tracer, an expression for the mass transport of a tracer through a single cell will be -

$$V \frac{dC}{dt} = W(t) - QC, \quad (1.45)$$

where,

- V = Cell volume,
 C = Tracer concentration with cell,
 Q = Volumetric flow away from the cell,
 $W(t)$ = Mass of tracer entering into the cell over a discrete time period t ,
 either by advection from a neighbouring cell or by direct injection into
 the cell.

If an instantaneous injection in the form of a delta function was applied to the first cell within the reach then the discrete time expression for the concentration present within this cell would be expressed as -

$$C_1(t) = \frac{M_0}{V} e^{-\alpha t}, \quad (1.46)$$

where,

- t = Discrete time interval,
 M_0 = Total mass of tracer injection,
 α = Volumetric travel time (Q/V),

and the general solution for the n^{th} cell (where n is an integer) would be -

$$C_n(t) = \frac{Q^{n-1} t^{n-1}}{V^{n-1} (n-1)!} \frac{M_0}{V} e^{-\alpha t} = \frac{Q^{n-1} t^{n-1}}{(n-1)!} \frac{M_0}{V^n} e^{-\alpha t} \quad (1.47)$$

Stefan & Demetrapoulas (1981) showed that for a concentration / time distribution predicted from equation 1.47 (mathematically termed a gamma function), the first moment of area or centroid (\bar{t}), the second moment or spread (σ^2) and the third moment or skewness (μ) could respectfully be defined as -

$$\bar{t} = \frac{n}{\alpha} \quad (1.48)$$

$$\sigma^2 = \frac{n}{\alpha^2} \quad (1.49)$$

$$\mu = \frac{2n}{\alpha^3} \quad (1.50)$$

where n is the number of cells downstream of the injection point. From this model it can be shown that the injected mass will be advected further downstream as the number of cells is increased whilst at the same time the concentration / time profile will be dispersed in the longitudinal direction leading to increases in the centroid, spread and variation in skewness. As with Taylors advective dispersive equation (within the equilibrium zone, Fischer (1966)) the spread will be directly proportional to the travel time. However, as the above equations show, the cells in series model forces the travel time, spread and skewness to be directly proportional to the number of cells used within the model. Thus these variables cannot vary independently to one another removing site specific variations in each variable. The cells in series model is compromised by this lack of independence, and as a result it has been shown by Stefan & Demetracopoulos (1981) that although the model provides adequate prediction of travel time calculations, there is no improvement in the concentration / time prediction between the cells in series model and the advective dispersive equation.

1.3.2 Aggregated Dead Zone Model

An improvement on the cells in series model is that of the aggregated dead zone. Beer and Young (1984) demonstrated that a standard advective model could be modified to include a segregated mixing / retention zone. With the inclusion of this zone (Thackston & Schnelle (1970), Pedersen (1977), Nordin & Troutman (1980)) the advective dispersive equation would take the form -

$$\frac{\partial c}{\partial t} + U \frac{\partial c}{\partial x} = K \frac{\partial^2 c}{\partial x^2} + \Gamma_c (s - c) \quad (1.51a)$$

which describes the dispersion within the main flow, and

$$\frac{\partial s}{\partial t} = \Gamma_s (c - s) \quad (1.51b)$$

which describes the retention of a tracer within a dead zone, where,

c and s = Tracer concentration entering and leaving the dead zone respectively,

Γ_c and Γ_s = Volumetric mass transfer coefficient in the main channel and dead zone respectively.

From these two equations it can be seen that even if the Taylor dispersion coefficient, K , were zero, dispersion would still take place due to the retention within the dead zone. With this assumption, and through observation of riverine studies, it was postulated that the combined effect of all the dead zones within a reach provided a majority of the observed dispersion, whilst the shear flow dispersion was only secondary. The difference in the model derived by Beer and Young (1984) and that of the cells in series, is that instead of considering a chain of linked cells, this model assumes that a tracer is advected through the entire reach by a plug flow (i.e. advection with no dispersion) after which it passes through a single mixing cell that has the aggregated effect of all the dead zones within the reach (i.e. dispersion with no advection). A description of the temporal change in concentration within a single dead zone can be written -

$$\frac{dc_2(t)}{dt} = \frac{1}{T}(c_1(t) - c_2(t)) \quad (1.52)$$

where,

$dc_2(t)/dt$ = Rate of change in net temporal concentration,

$c_1(t)$ and $c_2(t)$ = Net input and output concentration in time interval t respectively,

T = Residence time within the dead zone, $T=(V/Q)$ where V is the volume of the dead zone and Q is the mean discharge within the reach.

To simulate an entire reach using the above model, the tracer must be advected through the reach prior to it entering into the dead zone. This can be done by simply entering a pure time delay (τ) into the input concentration term. To use equation 1.52 as a representation of all the dead zones within a reach, the net effect of the individual dead zones within the reach are conglomerated into one effective dead zone volume, V_e . By introducing these change to the equation of a single dead zone, a model for an entire reach can be formed.

*The term dead zone is often misunderstood, although it implies a form of pocket that is separated from the main flow, it should be considered in a wider context as a bulk parameter that not only describes the effect of segregated regions of flow, but also other dispersive catalysts such as eddies, viscose sub layers and velocity profile (Wallis, Young & Beven 1989)

$$\frac{dc_2(t)}{dt} = \alpha(c_1(t - \tau) - c_2(t)) \quad (1.53)$$

Where,

$dc_2(t)/dt$ = Rate of temporal change in net concentration,

α = T^{-1} , where $T = V_e/Q$.

In practice, data is often acquired at discrete sampling times rather than as a continuous time varying fluctuation. It is therefore advantageous to discretise equation 1.53, where each discrete step has a time interval of Δt . The resulting discretised equation is of the form -

$$c_{2,k} = -ac_{2,k-1} + bc_{1,k-\delta} \quad (1.54)$$

where,

$c_{1,i}$ and $c_{2,i}$ = Input and output concentrations of the reach at discrete time step i respectively,

k = Discretised time step, where $k = t/\Delta t$ and t = time,

δ = Discretised advective time delay,

a and b = Aggregated dead zone coefficients.

Wallis, Young and Beven (1989) illustrated that if δ is taken to be the integer value of $\tau/\Delta t$, where τ is the time delay within the reach and Δt the discrete time interval, (Figure 1.6) then -

$$a = -\exp(\Delta t / T), \quad (1.55a)$$

$$b = 1 + a. \quad (1.55b)$$

The values of travel time (\bar{t}), time delay (τ) and residence time (T) can be determined from the variation in temporal concentration distributions within a reach, where -

$$T = \bar{t} - \tau \quad (1.56)$$

Within Figure 1.7, the dashed line represents the actual concentration / time distribution of a tracer at two locations (up and downstream) within a reach. Superimposed over these temporal fluctuations are bars that illustrate the discrete time representation of the data set. It is a discretised data set of this form that is used when applying the aggregated dead zone model.

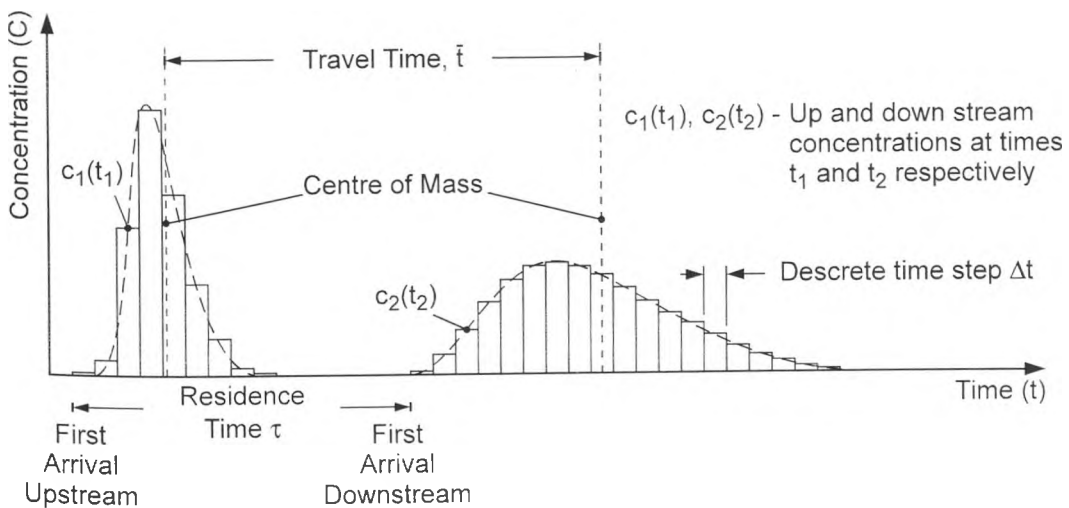


Figure 1.7 Illustration of ADZ travel and residence time parameters.

1.4 Summary of Mixing Processes

Throughout the current chapter, two approaches to dispersion modelling have been examined, namely Fickian and non-Fickian processes. The Fickian approach, known as the advective dispersion equation (ADE), is derived from the cross sectionally averaged shear flow dispersion, and is represented by a second order differential equation (equation 1.30). Through observation of this second order differential it can be seen that the spread of a tracer within a flow (either a temporal or spatial domain) is governed by both the streamwise area mean velocity, U , and a shear flow dispersion coefficient, K . It has been shown that the shear flow dispersion coefficient can be calculated for any reach, from the concentration distributions of a tracer measured at two locations within the reach (equations 1.42 and 1.44).

To enable application of the second order differential to either temporal or spatial data, a solution to the equation must first be sort. In the case of temporal data collected at a fixed measuring location, a solution to the second order differential has been found in the form of the 'Frozen Cloud Approximation' (equation 1.39). Through application of this equation, a temporal concentration distribution located at an upstream site can be projected to a new downstream location.

The non-Fickian approaches discussed within the chapter concentrate on both the cells in series (CIS) and aggregated dead zone (ADZ) models. Both of these models supply discretised solutions to the temporal passage of a tracer through a reach. However, of these

two approaches, the ADZ (equation 1.54) has been shown to be the superior modelling technique. The nature of the ADZ is to assume that all mixing processes influencing the spread of a tracer are the result of discrete mixing cells. When modelling a reach, a tracer is first advected from a known upstream site, to a new, relative, downstream location. The effects of all the mixing cells within the reach are then applied to the tracer distribution in the form of a single aggregated dead zone.

Data presented within the current study will be modelled using both the ADE and ADZ approaches. From application of both model types, the ideal modelling approach will be elucidated.

Chapter 2

Collection and Analysis of Data

2.1 Fluorometry

To measure the mixing characteristics within a hydraulic system, a tracer must be introduced into the flow. By monitoring the cross-sectionally averaged changes in the tracer distribution at points downstream of its injection an assessment of the general mixing processes within the flow can be deduced. A variety of tracers are available, each requiring different methods of detection (e.g. salts can be introduced into a flow as a tracer and detected at a site downstream of its injection through the use of a conductivity probe). The choice of tracer is generally dictated by the nature of experiments. For the experiments carried out within this research a fluorescent dye tracer was opted for. The reasoning for this being the ease of detection and the availability of test equipment. Once dye has been introduced into a flow, it can be detected using a process called fluorometry.

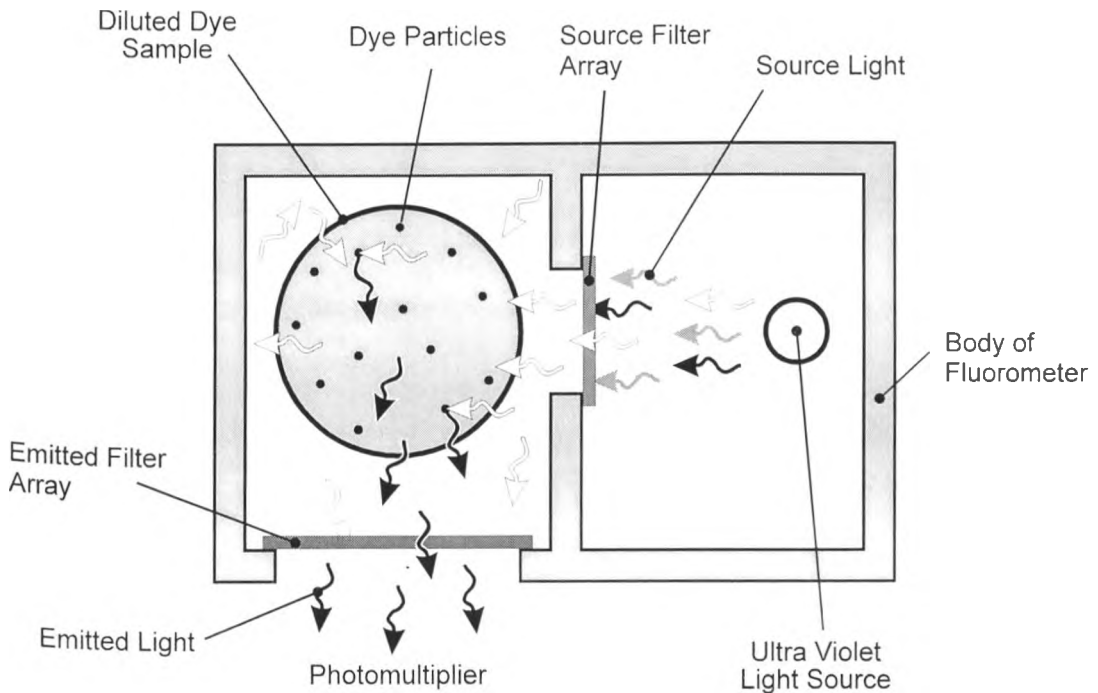


Figure 2.1 Schematic showing the operation of a fluorometer.

The process of fluorometry works by relating the concentration of a diluted dye to its relative fluorescence. Throughout this research, Rhodamine WT was used as the tracer and Turner Design Series 10 fluorometers were employed as detectors. A fluorometer operates by illuminating a dye with a light source of known wavelength, and measuring the intensity of the light fluoresced by the dye (Figure 2.1). To achieve the specific wavelength of illuminating light, a broad band ultra violet source is passed through a 546nm band pass filter (Filter Selection Guide, Turner Designs). It is known that when Rhodamine WT is illuminated using a 550nm source, it will fluoresce with a mean wavelength of 580nm. The fluoresced light from the Rhodamine is passed through a second band pass filter, 570-700nm, removing any stray excitation light before it passes into a photomultiplier which emits an output voltage proportional to the light intensity.

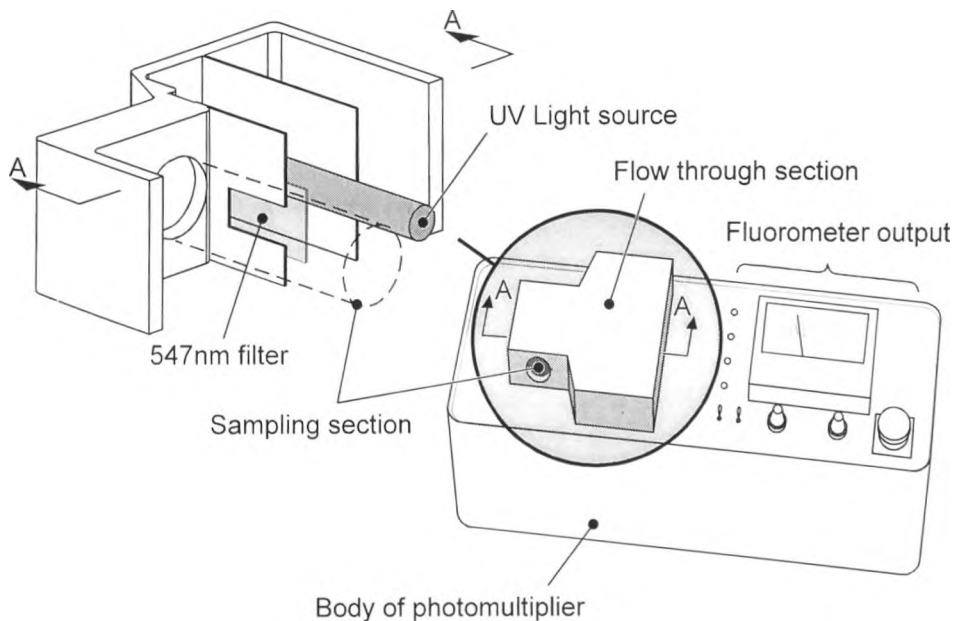


Figure 2.2 Diagram of fluorometer and cut away flow through section.

To ensure that there is no degeneration in the fluorometer signal due to fluctuations in the source light or response of the photomultiplier, a reference signal is taken from the source light directly to the photomultiplier. Via a rotating shutter ("light chopper"), a "dynamic stability" is applied to the output signal of the fluorometer 13 times per second (Operating and Service Manual, Model 10 Series Fluorometers). Firstly the background voltage of the photomultiplier (i.e. when no light is present) is subtracted from the measured output voltage. A correction

factor is then applied to the output voltage using a reference signal taken directly from the illuminating light.

2.2 Fluorometer Modification

The standard Series 10 fluorometer can operate in two modes. Either analysing discrete samples using a 25ml test tube that can be placed inside the sampling section of the fluorometer, or continuous sampling via a 13mm (internal diameter) flow through tube. For this research neither of the above (standard) options for sampling were deemed suitable. The discrete sampling method can only be carried out through the use of abstraction points (i.e. removing discrete samples from the flow). For the scale of model that could be constructed within the laboratory, this method of sampling would adversely influence the flow within the model, thus affecting the accuracy of the results. Also, a large number of samples would have to be abstracted in order to develop an accurate dye concentration distribution. The continuous flow through method of sampling can be used in two ways. Either via a continuous abstraction point, which has already been shown to be unsuitable, or by a non intrusive method on a small scale model.

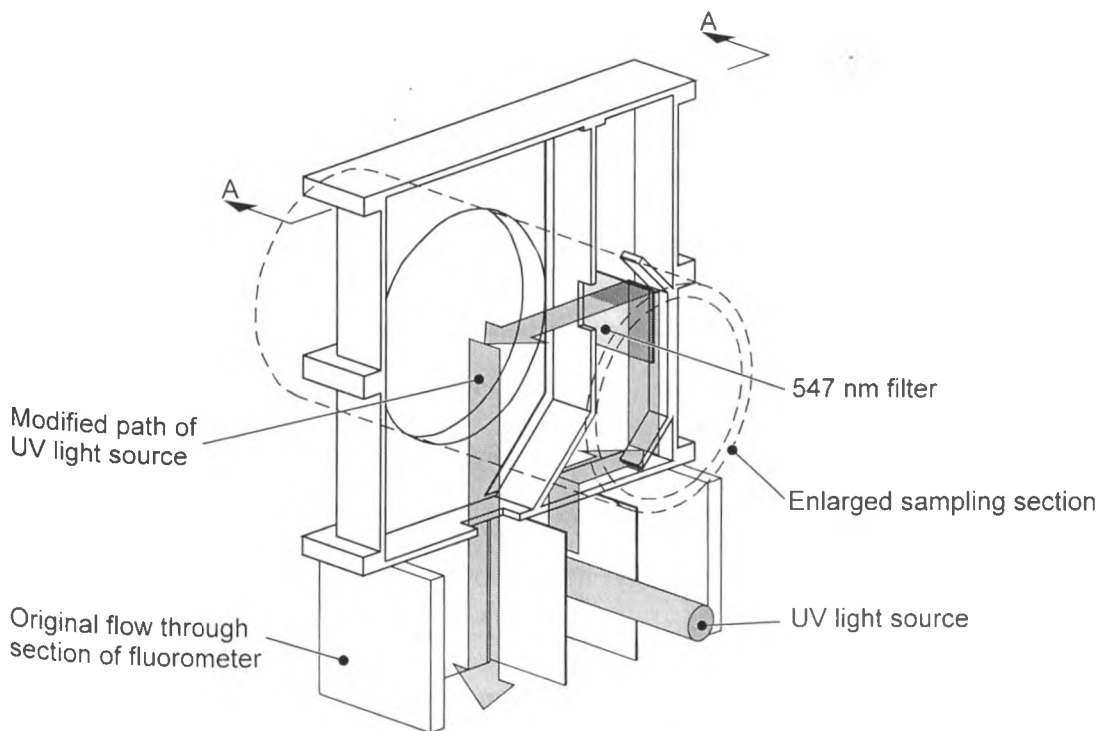


Figure 2.3 Section through a modified fluorometer flow through

With the non intrusive method, the pipes within the drainage model would have to be small enough to pass through the sampling section of the fluorometers. This method was also rejected because the model would have to be of such a small scale it would be unrepresentative of the hydraulic parameters such as surface tension and viscosity.

As an alternative method of sampling, a modification to the standard fluorometer was designed. The modification rode "piggy back" on the standard fluorometer flow through section (Figure 2.3), thus minimising the changes that needed to be made to any individual fluorometer (O'Brien (1993)).

A new flow through with a sampling section that could accommodate a pipe with an external diameter of 100mm, was mounted above the centre line of the original flow through section. Source light was directed from it's original location to a plane level with the centre of the new flow through via a periscope arrangement. As with an unmodified fluorometer, the light entering the new sampling section was perpendicular to the plane of the photomultiplier. The modified region of the fluorometer was then enclosed in a light proof box to prevent any stray light from entering the photomultiplier. The location of the source filter was moved from its original location within the body of the flow through section of the fluorometer to a point adjacent to the new sampling section, on the modified plane of the source light.

2.3 Calibration of the Modified Fluorometer

Once constructed the response of the modified fluorometer was compared to that of a standard design (Figure 2.4). Both a modified and standard flow through fluorometer were set up in series with a 100 litre recirculating water supply. Rhodamine WT was injected into the supply and the output of the fluorometers was monitored. When both fluorometers maintained constant outputs it was assumed that the dye had become well mixed throughout the water supply. The outputs were then logged for a short period of time to enable a time averaged output to be determined. This procedure was repeated for a range of concentrations, the result of which was used to determine the relative response between a modified fluorometer (Figure 2.5) and that of the standard design.

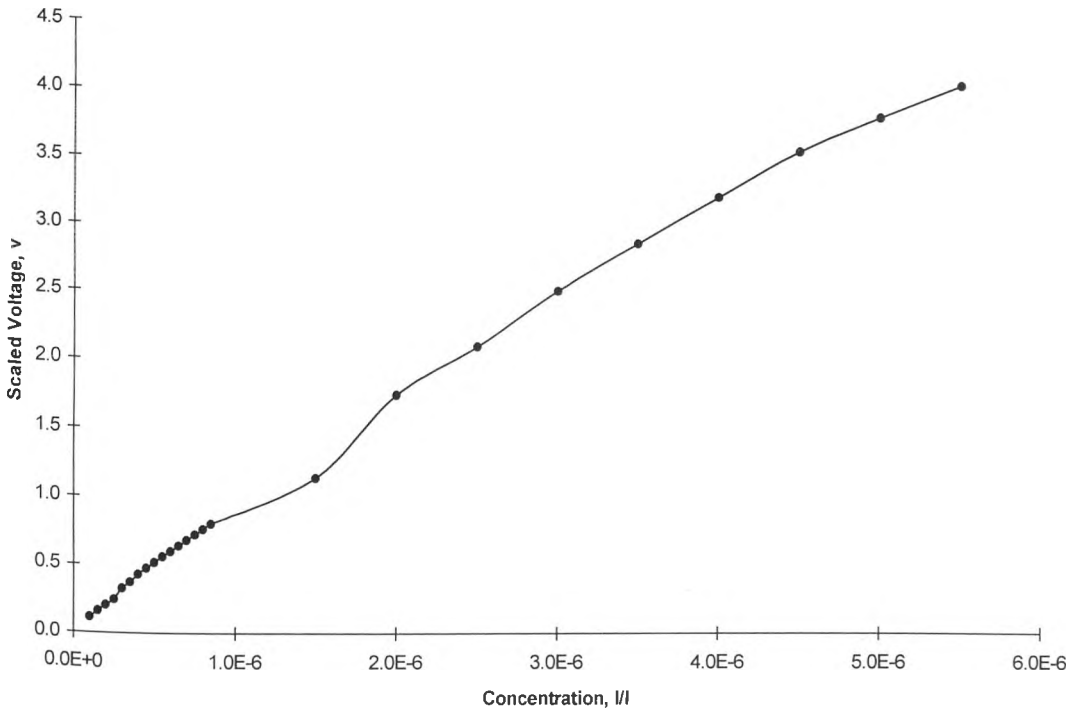


Figure 2.4 Calibration of a standard flow through fluorometer.

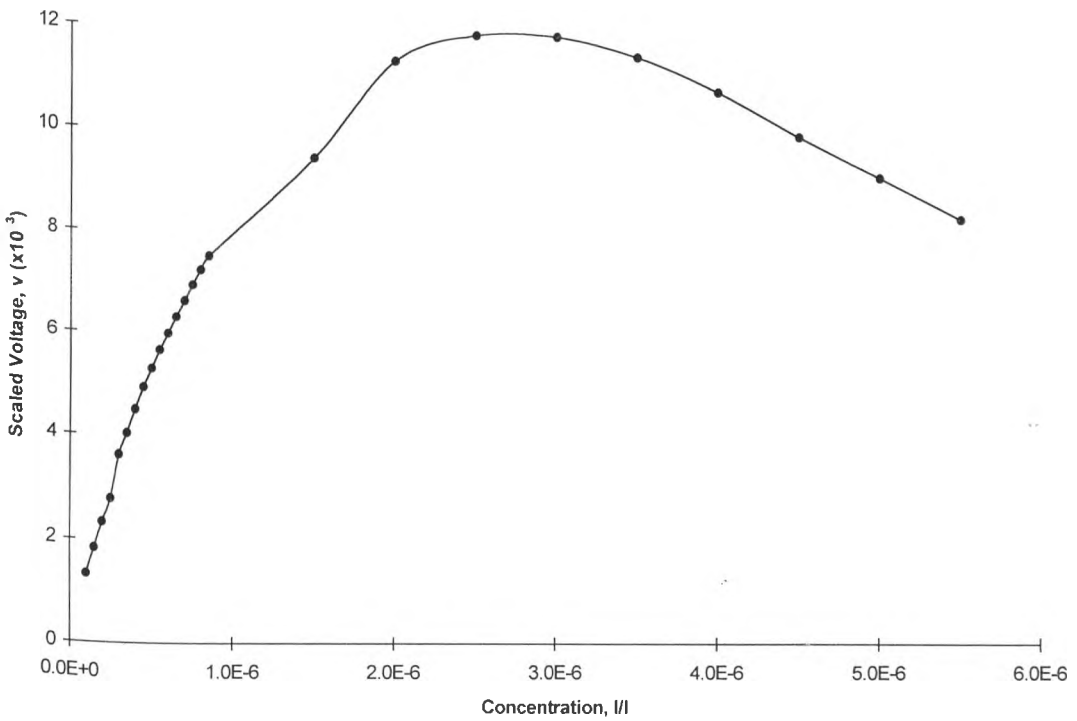


Figure 2.5 Calibration of a modified fluorometer.

From the results it was evident that the standard fluorometer provided a linear response for the range of concentrations tested (Figure 2.4). In contrast, the modified fluorometer appeared to greatly deviate from a linear response (Figure 2.5). However, for concentrations up to $8.5 \times 10^{-7} \text{ l/l}$ a linear response was observed (O'Brien (1993)). From this calibration, the limitations of the modified fluorometer were deduced. It was also deemed unwise to operate the beyond the linear response. The reason for the observed decay in the signal from the modified fluorometer at high concentrations was assumed to be due to the dye in solution acting as a filter and blocking out some of the fluoresced light.

Once the modified fluorometer had been shown to operate with a linear calibration up to concentrations of $8.5 \times 10^{-7} \text{ l/l}$, a second test calibration was carried out. Two modified fluorometers were set up with a 100 litre recirculating system and the relative response between two modified fluorometers was determined (Figure 2.6).

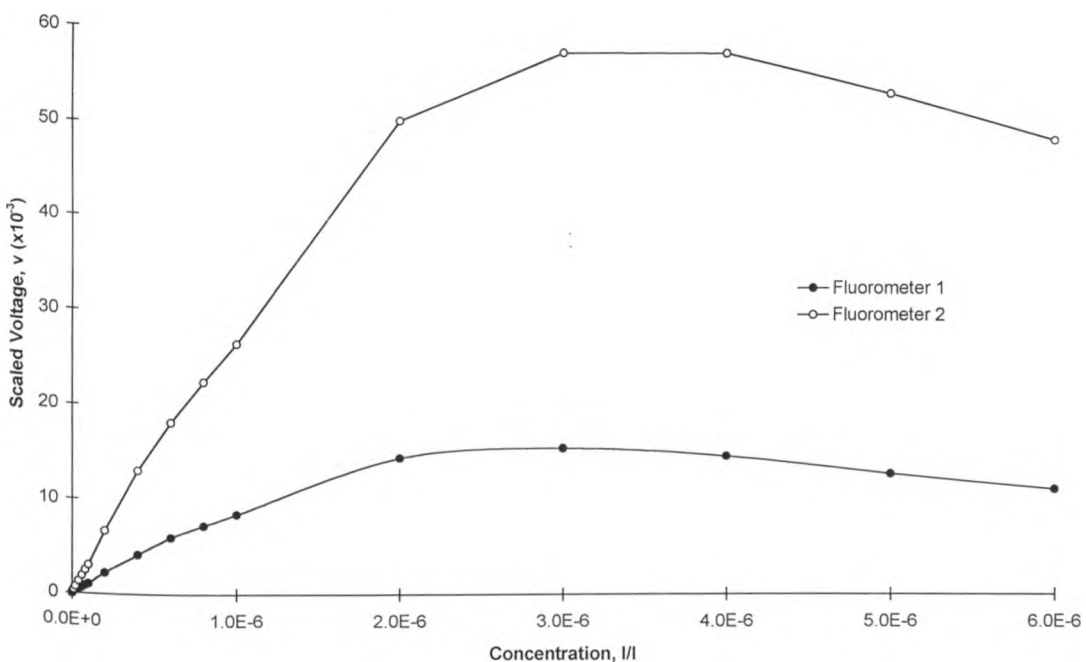


Figure 2.6 Calibration of two fluorometers extending beyond the linear range

The difference in the output of the two fluorometers shown in Figure 2.6 is due to the individual calibrations of the fluorometers. The plot shows a calibration that has gone beyond the linear range of both fluorometers. It can be seen that both fluorometers deviate from a

* Scaled voltages are determined by dividing output voltages by the scale setting of the fluorometer.

linear response at approximately 1×10^{-6} l/l concentration. Figure 2.7 illustrates a calibration that remains within the working range of both fluorometers and thus retains a linear response.

The Turner Design Series 10 fluorometer has 8 scale settings that can either increase or decrease the sensitivity of the instrument, depending on the concentration of the dye being detected. Switching between the different scale settings can be done manually or automatically, however the switching process causes an approximate 2 second loss in data.

To prevent this from causing a problem, all tests were carried out on a single scale setting and the concentration of the dye is varied to maintain readings within the working range.

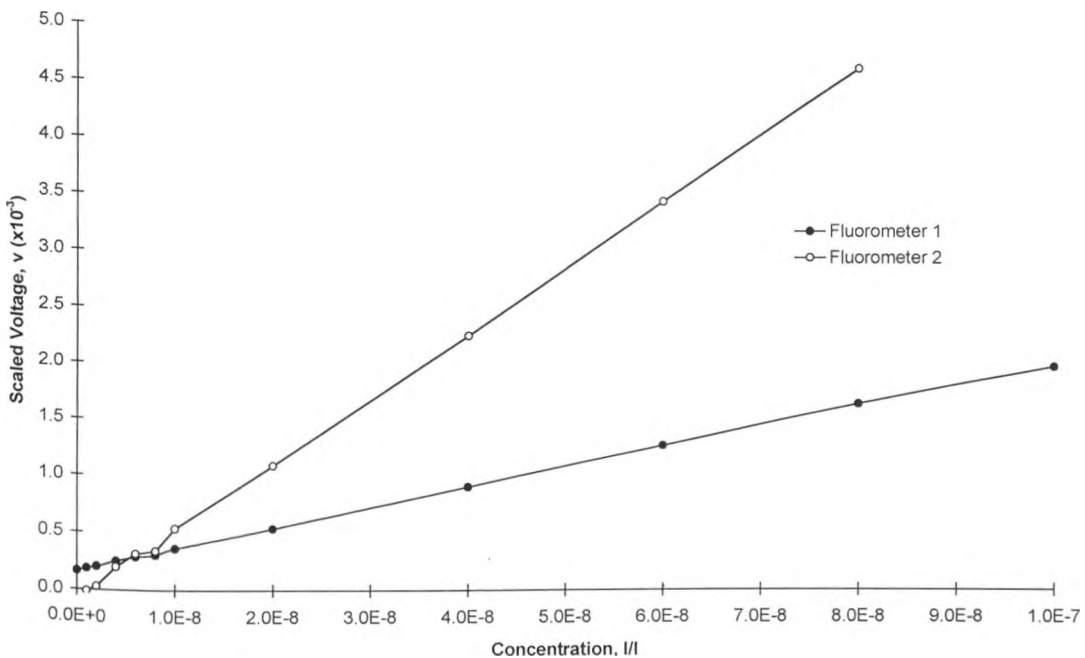


Figure 2.7 Calibration of two fluorometers within the linear range

2.4 Laboratory System

A self contained recirculating laboratory system was developed in which to undertake these studies. The head for the water supply was maintained at 6 metres by an upstream header tank which was fed up to 16 l/s via a submersible pump in the downstream sump. The test region consisted of two 3 metre lengths of 100mm external diameter (88mm internal diameter) clear perspex tubes, simulating sewers, either side of a model manhole chamber. Initially discharge through the system was controlled with an upstream gate valve, whilst the surcharge within the manhole was controlled by a downstream tank containing a second gate

valve. It was originally intended to control the surcharge by restricting the outflow from the downstream tank, thus the surcharge in the tank would increase until an equilibrium between inflow and outflow was obtained. This system was soon found to be inadequate because it required excessive time to achieve a stable flow throughout the system. In place of the second gate valve, a tailgate was installed. This proved to be more reliable because it depended on a free surface for its discharge. Therefore surcharge in the manhole was only a function of the tailgate level and the discharge through the system. To measure the discharge through the system, a 30° V-notch weir, designed to BS 3680, was installed downstream of the test section.

Throughout this research, the aim was to quantify the magnitude of the dispersion of a solute travelling through a surcharged manhole chamber. For this purpose two modified fluorometers were used, placed 1.35m up and downstream of the manhole chamber centre line (Figure 2.8). In the initial test runs of the system it was found that the fluorometers were sensitive to the slightest quantities of stray light. Consequently, the entire test section required blacking out and a lid was fitted to the top of the manhole chamber.

When testing commenced, the initial configuration of the test rig was a 400mm unbenched manhole chamber with a straight inlet and outlet pipe of 88mm (internal diameters). Surcharges were measured within the chamber using a vernier pointer gauge. All surcharges were measured from the soffit of the inlet pipe, thus when the inlet pipe was just flowing full

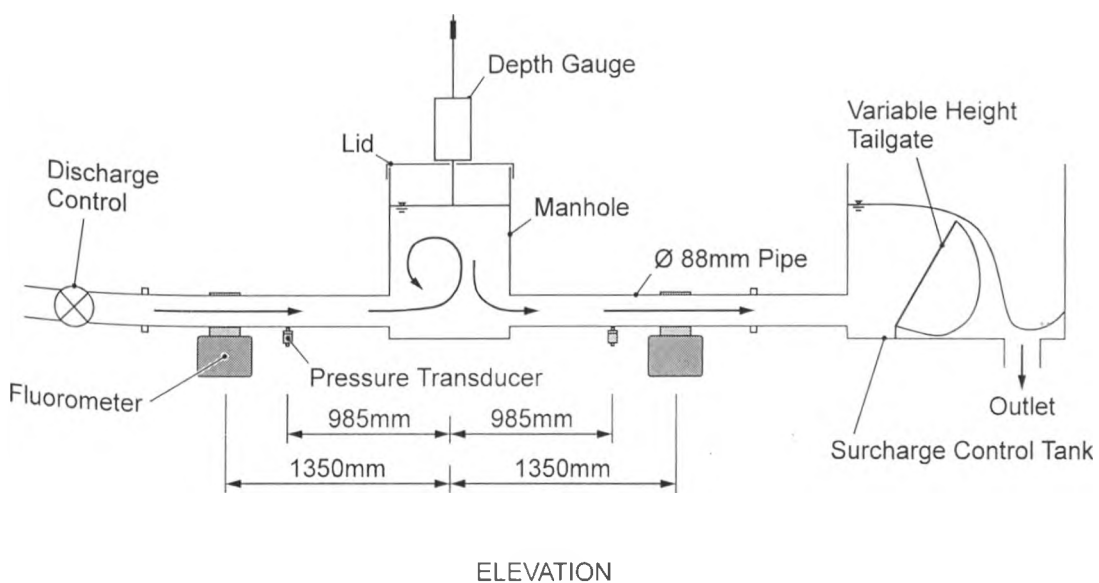


Figure 2.8 Configuration of test facility

there would be zero surcharge. Through observation it was seen that fluctuations in the surface level of the water within the manhole increased with flowrate. Also, these fluctuations were not just a to and fro "sloshing" motion, but also a vertical rise and fall. As a result, the single water surface measurements made using a vernier depth gauge that was initially fitted to the test facility became increasingly inaccurate with increase in the flow. To alleviate this problem from subsequent test configurations, the vernier depth gauge was replaced with an automatic depth follower. The follower emitted a variable voltage proportional to the surface level of the water in the manhole chamber (Figure 2.9). The advantage of this form of measurement was that instead of relying on a single measurement of surcharge, a time averaged value could now be determined.

Pressure transducers were also a modification to the initial manhole configuration. Although measuring headloss within the manhole chamber was not a goal of the research, it was postulated that the processes contributing to headloss could also dictate the level of dispersion within the manhole chamber. Thus for all subsequent test configurations after the initial 400mm chamber, two pressure transducers were fitted 985mm up and downstream of the manhole centre line (Figure 2.8).

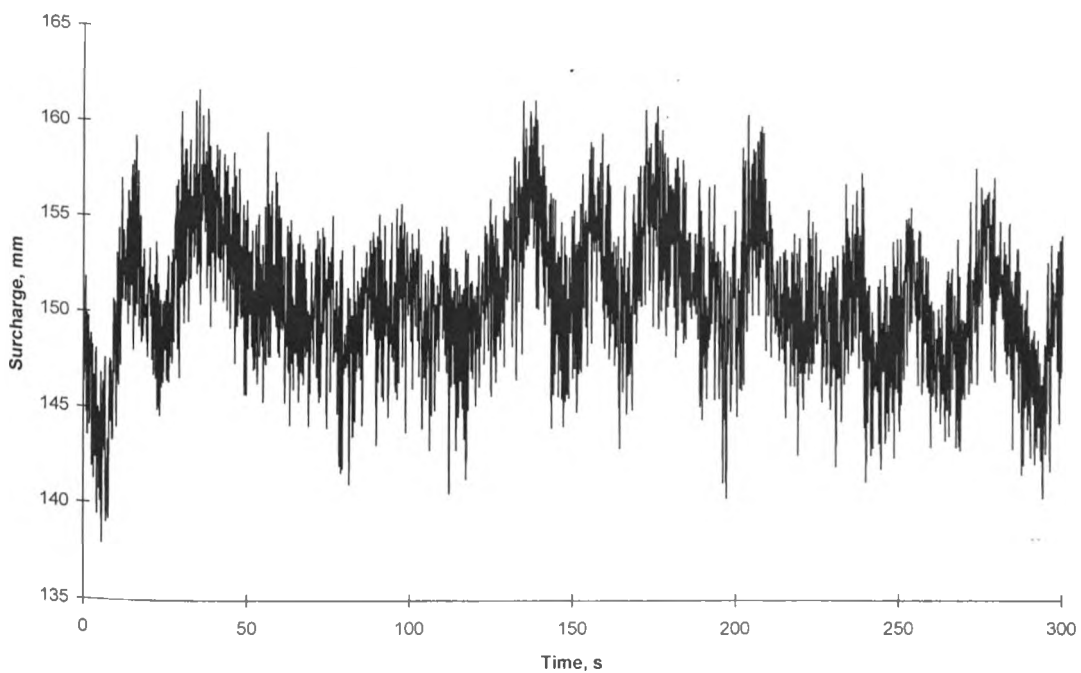


Figure 2.9 Typical variations in surcharge during a 300s test

2.5 Data Acquisition

2.5.1 Equipment Calibration

Data was collected using a CED 1401 (Cambridge Electronic Design) data logger. With this model of data logger, data files are written to a personal computer hard disk as *.smr files. These files contain the data in a compressed binary format. The data that was logged on the computer included output from two fluorometers (including their scale settings for future reference), a depth follower (after the substitution of the vernier gauge) for measuring the surcharge within the manhole and two pressure transducers.

Prior to the testing of any individual manhole configuration, all test equipment was calibrated insitu. For the fluorometers, this was done by forming an isolated recirculating zone which included the manhole section as well as the two fluorometers. A known volume of water was introduced into this region, and with the aid of a small pump the water was recirculated. A known quantity of dye was introduced into this isolated zone and the system was left recirculating until the dye had become uniformly mixed into the volume of water (i.e. the reading on the fluorometers tended to be constant as the water / dye mixture was recirculated through them). When this state had been attained, the output from the fluorometers was logged for approximately one minute. A time averaged output voltage for each fluorometer at a known concentration was then determined, thus eliminating any minor fluctuations in the fluorometer output. This procedure was carried out for a range of increasing dye concentrations. Over the period of the calibration, it was found that there was a noticeable increase in the temperature of the volume of water. The change in temperature was attributed to the recirculation pump and was seen to be unavoidable. To attempt to compensate for the temperature variation, a temperature dependant correction factor (Smart and Laydlaw (1977)) was applied to the observed response. A calibration equation was determined from a linear regression through the corrected results.

Although the Turner Design fluorometers can work on a range of scale settings, only a single setting was used. Two reasons for this are, firstly, as previously stated, if the scale setting was changed during a test, it would result in a loss of data as the fluorometer shifted between scale settings. Secondly, a single calibration equation is only truly valid for one specific scale

setting. Consequently, due to time constraints during the current research programme, multiple scale settings were not used.

Both the pressure transducers and the depth follower (when used) were calibrated concurrently. To enable their calibration, the outlet of downstream tank used to control the surcharge, and the upstream valve used to control the discharge through the manhole, were sealed off. Thus the region containing the manhole depth gauge and the pressure transducers was isolated. Water was introduced into the isolated section by filling the downstream tank, and thus generating a surcharge within the manhole, which was monitored by a manometer tube mounted on the downstream tank. After the isolated volume of water had been given time to settle, the output voltages from the pressure transducers and the depth follower were logged for approximately one minute using the CED 1401 and a time averaged voltage from each of the devices was ascertained. The level of the water in the isolated section was then lowered and the process was repeated. This process was carried out for a range of water levels and resulted in a data set that related the output voltages of each device to the hydrostatic pressure and surcharge above the inlet soffit for the pressure transducers and the depth follower respectively. Calibration equations were determined from linear regressions fitted to each data set.

Although the data acquisition software was capable of real time calibration of the acquired data, this was only done for the first two test configurations. All subsequent data was acquired uncalibrated, having the necessary calibrations applied during the data analysis. The main reasons for this strategy to be adopted are due to time constraints within the test programme, and also it allowed for a second calibration to be performed at the end of each manhole study. This second calibration acted as a check on the on the initial calibration, and where necessary compensated for any shift in the calibration that may have occurred.

2.5.2 Data Analysis

Once all the required test equipment had been calibrated, data was acquired for a range of flowrates and surcharges for each manhole configuration. A summary of all tests undertaken can be seen in Table 2.1.

Test Configuration	Pressure Transducers	Depth Follower	Range of Discharges (l/s)	Total No. Discharges Tested	Range of Surcharges [‡] (mm)	Total No. Surcharges Tested [†]	Manhole Parameters
Straight Pipe	✓	✗	2.06 → 10.31	7	N/A	N/A	
Manhole (D=400mm)	✗	✗	0.97 → 7.69	6	7.12 → 281.67	96	
Manhole (D=500mm)	✓	✓	0.92 → 7.54	6	9.64 → 268.05	60	
Manhole (D=600mm)	✓	✓	0.84 → 7.59	7	26.69 → 308.9	96	
Manhole (D=800mm)	✓	✓	0.86 → 8.84	5	27.49 → 331.57	94	
Manhole (D=400mm)*	✓	✓	1.99 → 7.68	3	48.04 → 251.31	14	

Note:

All dimensions are internal.

All inlet and outlet pipes have an internal diameter of 88mm.

Rhodamine WT used as dispersive media.

* Second set of 400mm diameter tests performed as control.

[‡] Surcharge measured from soffit of inlet pipe

[†] For each surcharge tested, five repeat tests were performed to obtain average results.

Table 2.1 Summary of acquired data

To ensure a continuity in the data collection and analysis, once all data for a test configuration had been gathered, an analysis was carried out using a purpose written Visual Basic programme. To aid this programme, and to provide complete data files, all information gathered manually (i.e. discharges, and in the case of the first test configuration, surcharges) was entered into an ASCII data file. For each manhole configuration, tests were carried out at a range of flowrates and surcharges. At any one surcharge / flowrate combination, five individual tests were performed. The reason being, to find the average solution at one surcharge / flowrate combinations, thus reduce the effects of background noise and any minor errors that may have occurred in any individual test. Errors in calculating the temporal duration of a data trace may, at first appear to have only a minor influence on the overall concentration / time profile. However, this error is greatly magnified when calculating second moments. This has been illustrated in Figure 2.10, where a normalised symmetrical Gaussian distribution has been shown along with its second moment. From the cumulative plots of these data it can be seen that if only 90 per-cent of the entire data trace is observed, the equivalent second moment of area will reduce to only 67 per-cent of that obtainable from the entire distribution. This error in second moment will causes an uncertainty in the determination of the dispersion coefficient (equation 1.44) used within the advective dispersion equation (equation 1.30).

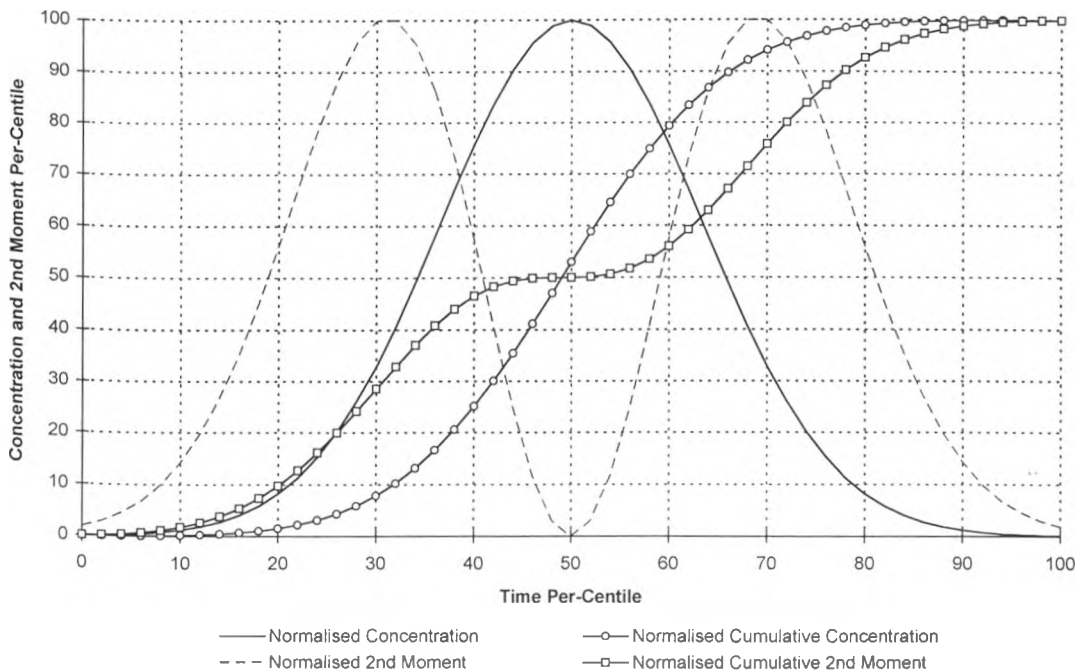


Figure 2.10 Comparison between errors in cumulative concentration and second moment.

To clarify the measured data, and to reduce any errors in the temporal duration of the concentration / time distribution, the analysis software applied the following steps to each individual surcharge / flowrate combination:

- Where required, the average surcharge and discharge (i.e. manually acquired data) were determined from the data file.
- The average fluorometer time series data was determined by superposition of all the data sets in the surcharge / flowrate combination. The peak value of each individual data set was used as a datum for this superposition (Figures 2.11 and 2.12(a)), and the average time difference between the up and down stream profiles was used to calculate the travel times of the peak values.

High frequency fluctuations present within the data were removed by implementing a low pass Fourier filter (Figure 2.11(b)). The filter used was the low pass Butterworth filter supplied with the Prosig (1994) 'Dats Plus 2 Spreadsheet Signal Processing Environment'. The cut-off frequency of the filter varied from one manhole configuration to the next, but was kept constant throughout any individual configuration, both for ease and to provide a consistency in the analysis technique. In all cases only a single pass of the filter was used. Due to the nature of Fourier filters, if the cut-off frequency was too low there would have been a marked attenuation in the data signal, whereas if the frequency was too high a large proportion of the unwanted noise would pass through the filter. To assess the lowest suitable pass frequency, a Fourier analysis was performed on the data with the highest flowrate but the lowest surcharge to obtain a frequency spectrum of the data. Through experience this was found to be the critical case, due to the short temporal duration of the data (as a result of the high flowrate) a high attenuation of the data was evident if the cut-off frequency was too low.

The cause of the high frequency noise, seen in Figure 2.11, that manifested itself in all the data collected was not ascertained, however it was attributed to electronic noise imparted to the data from the sampling equipment (e.g. fluorometers). This deduction was made due to of the regular nature of the noise as well as its extremely high frequency relative to the overall observed data profile.

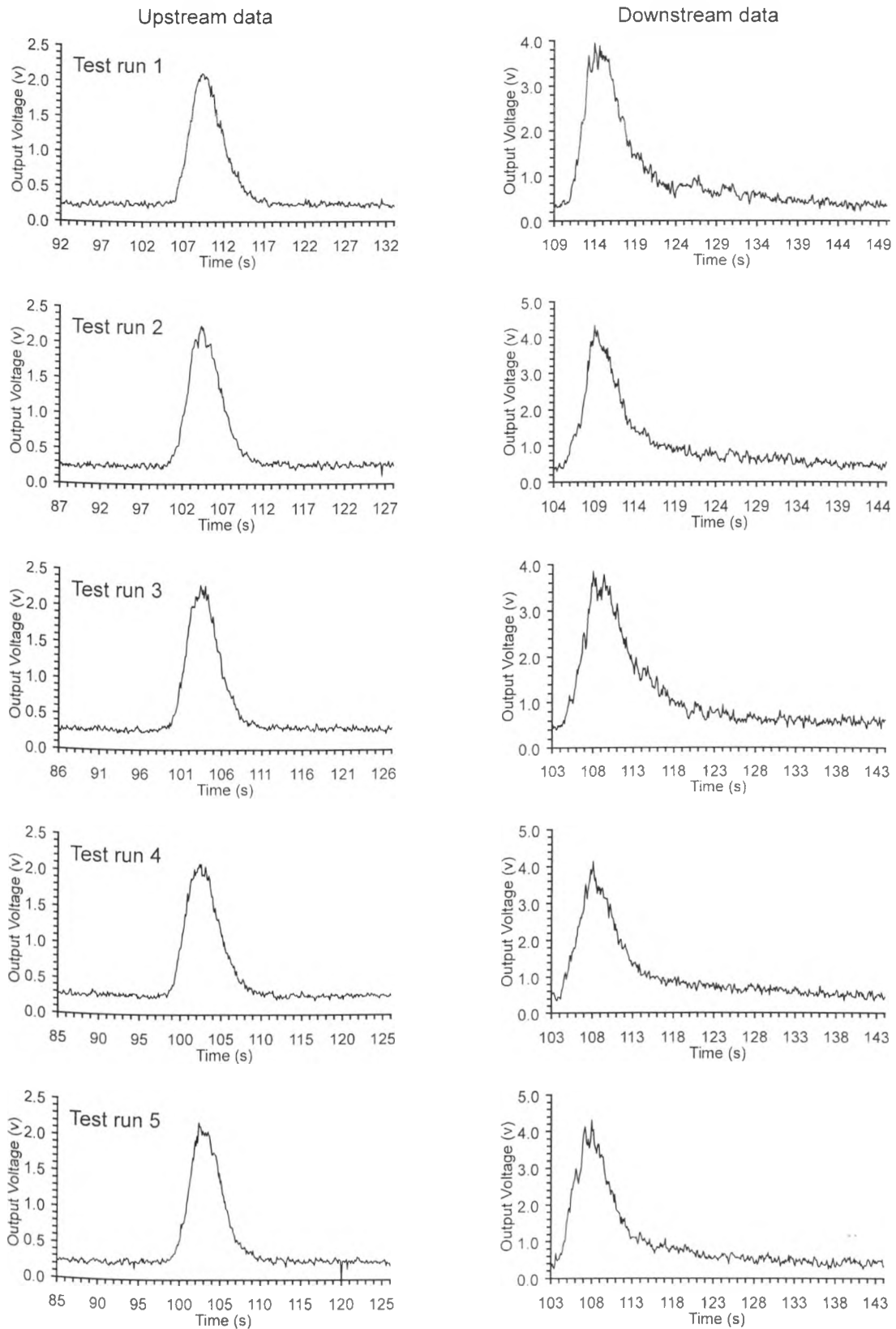


Figure 2.11 Typical data set used to determine average voltage / time distribution .

Data taken from 400mm diameter manhole with an average discharge of 3.46l/s and surcharge of 69.16mm

The noise was also present, even when there was no dye within the system, but was greatly reduced when the sampling equipment was turned off. Thus, all indication points towards the sampling equipment being the source of the noise.

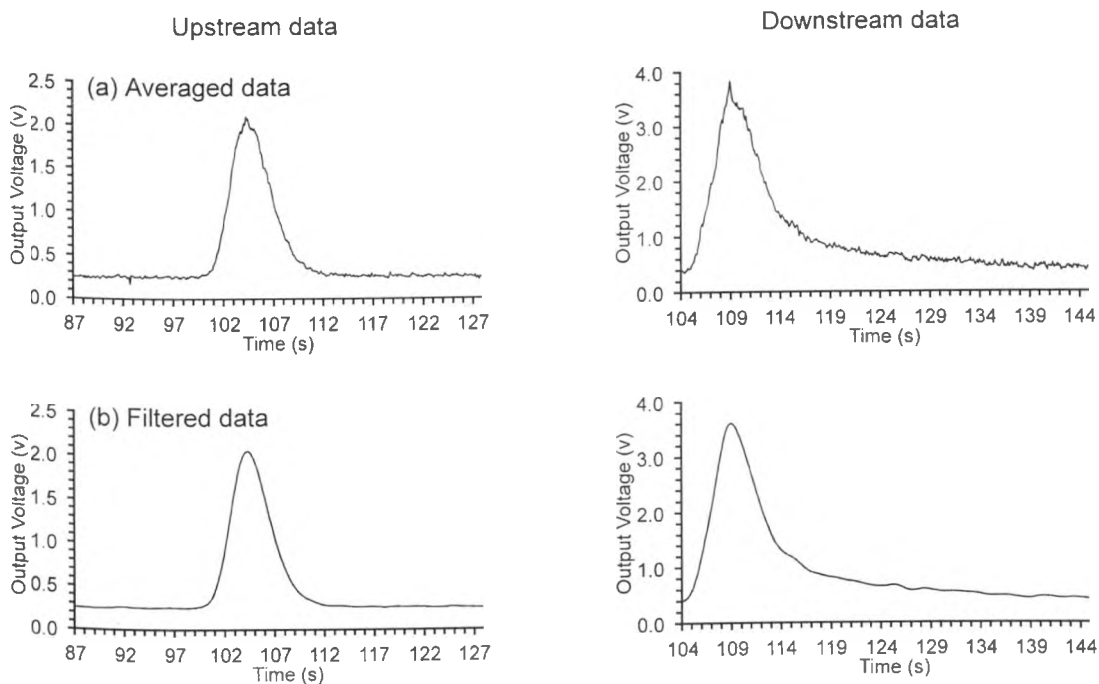


Figure 2.12 (a) Typical averaged voltage / time data. (b) Typical filtered voltage / time data.

- After filtering the data, the previously determined fluorometer calibration equations were applied (where appropriate).
- A time averaged surcharge and the up and downstream pressures were determined for all tests that included the depth follower and pressure transducers. Average values were used to eliminate any temporal fluctuations that occurred during the tests.
- Although all tests were logged to a data file for 300 seconds, the relevant experimental data only formed a fraction of this time. As a result the relevant up and downstream data had to be extracted from the data file to perform the analysis. An initial, temporary, start and end time were determined for the data sets. This was done by determining where the peak value of the time series data, and moving in discrete time intervals toward either the start or end of the data file (depending on whether a temporary start or end was being determined), calculating the mean and standard deviation of the data for each time interval. This process continued to step through the data until the mean plus standard deviation for the current time interval was greater than the mean of the previous interval. From this process

temporary start and end times were determined for the temporal distribution. A linear regression, fitted between the temporary start and end times was then subtracted from the data set, thus removing any background concentration from the data. Absolute start and end times were determined by again travelling through the data from the peak value in the direction of either the start or end of the distribution. In this case each data point was looked at individually, and the absolute start and end times of the relevant data were deemed to be the first negative point encountered in this manner. Although, with the presence of noise in the data this would tend to produce a late start and an early finish time, the errors were assumed to be minimised by the application of the Fourier filter. The reason for not pursuing data points beyond the first negative points was because of the errors they cause in calculating a reliable second moment. Although any negative values are only minor in comparison to the peak value of the data set, they would be located at the greatest lever arm from the centre of mass. Thus when determining second moments for calculation of the dispersion coefficient (equation 1.44) used within the advective dispersion equation (equation 1.30), the lever arm would be squared, resulting in excessively large negative moments.

- Once a discrete data set had been extracted from the data file for both the up and downstream fluorometers a recovery ratio was determined from the data by dividing the area under the upstream profile by that of the downstream profile. The downstream data was then mass balanced by dividing each data point by the total area under the downstream profile and then multiplying each by the area under the upstream profile. This was done to remove any small discrepancies that may have existed between the up and downstream data profiles caused by either errors in the calibrations or in the abstraction of the relevant data from the data file.
- The centre of mass of the profiles was determined using first moments, and second moments were calculated about the centre of mass. Aggregated dead zone parameters were determined from the centre of mass and the first arrival times of the up and downstream profiles, whilst advective dispersion parameters were determined from the travel time of the centres of mass of the up and down stream profiles and their associated second moments of area.

2.6 Results

Through the application of the previously mentioned Visual Basic program, data has been extracted from all the test summarised in Table 2.1. In the case of the manhole data, the results are presented as variations with surcharge, whilst the results of the straight pipe study are presented as variations with discharge. The following results include the Taylor dispersion coefficient (equation 1.44), K , aggregated dead zone parameters of travel time (Figure 1.7), \bar{t} , and delay time (Figure 1.7), τ (also known as residence time), and the measured headlosses (h_L). All error bars are calculated as \pm one sample standard deviation about the mean data point. Due to the nature of the data analysis used when calculating Taylors dispersion coefficient, extraction of the sample standard deviation must be carried out prior to the Fourier filters application. Therefore, the precision of these standard deviations can not be entirely relied upon. For this reason the error bars should only be used as an indication rather than an absolute measurement.

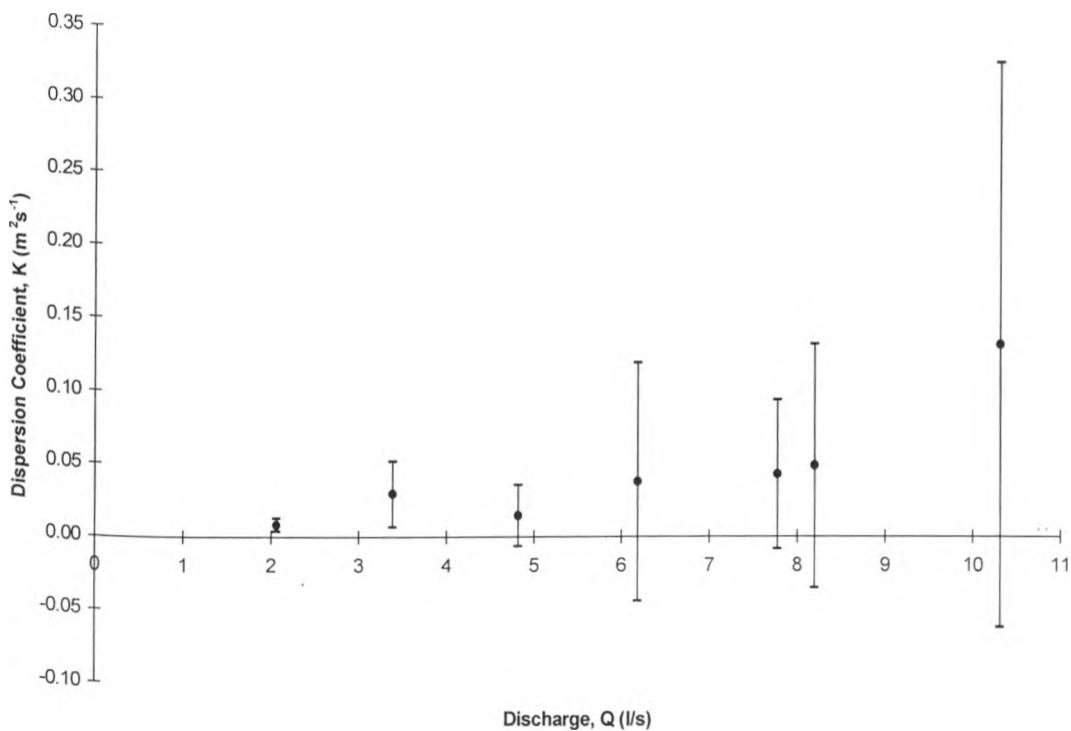


Figure 2.13 Straight pipe, variation of dispersion coefficient (K) with discharge.

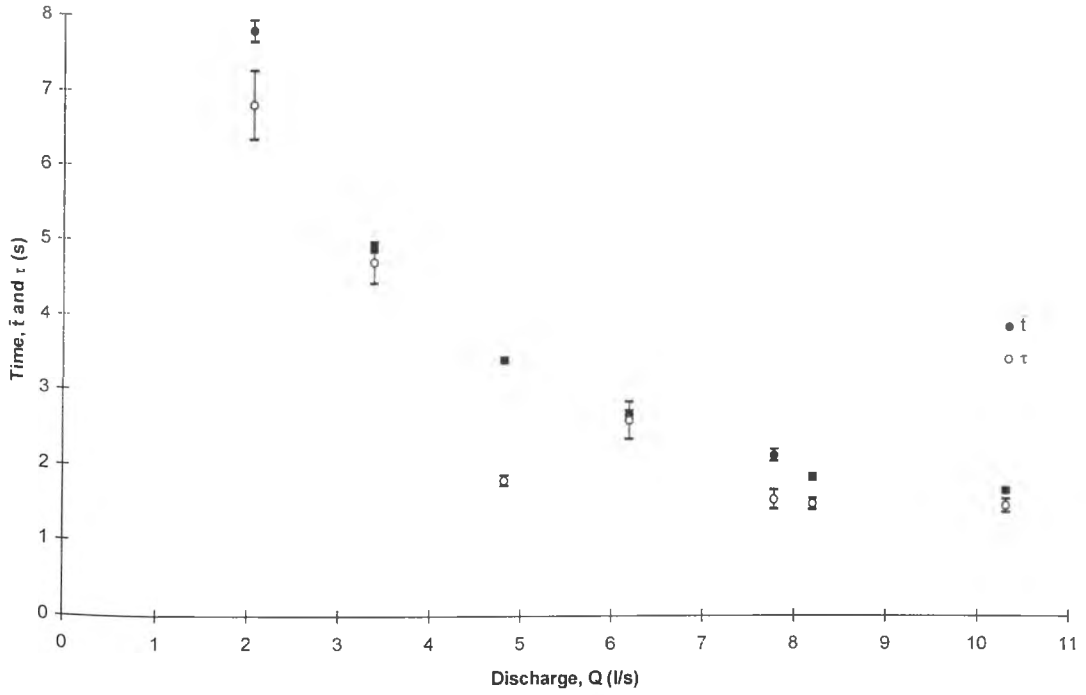


Figure 2.14 Straight pipe, variation of travel time (t) and delay time (τ) with discharge.

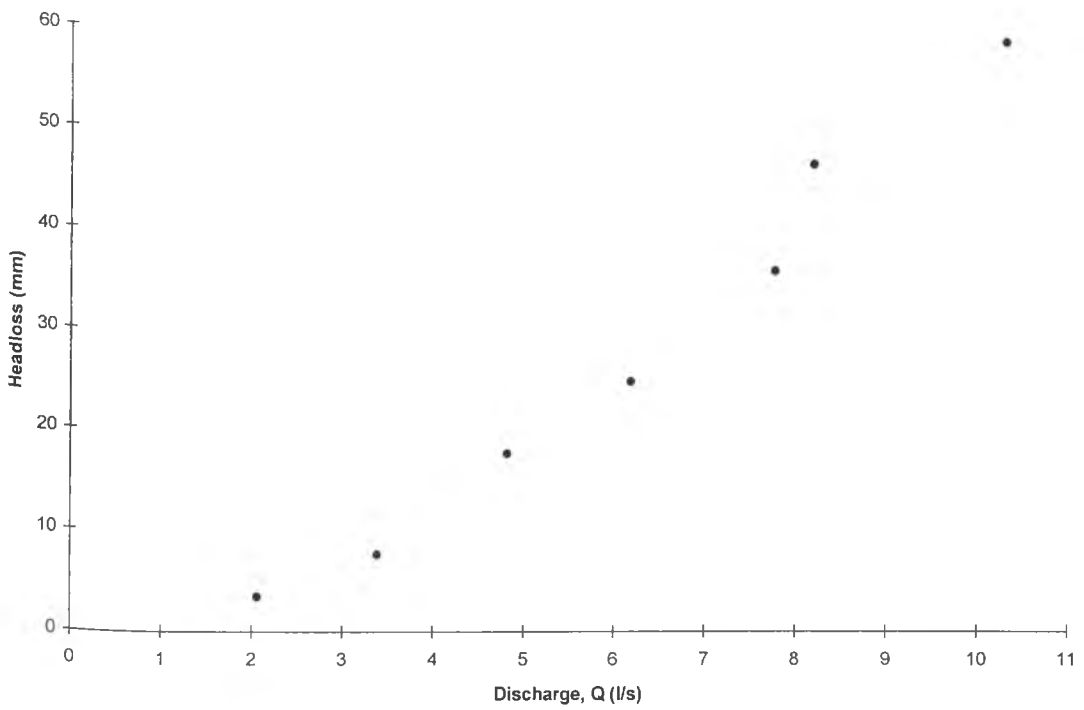


Figure 2.15 Straight pipe, variation of headloss (h_L) with discharge.

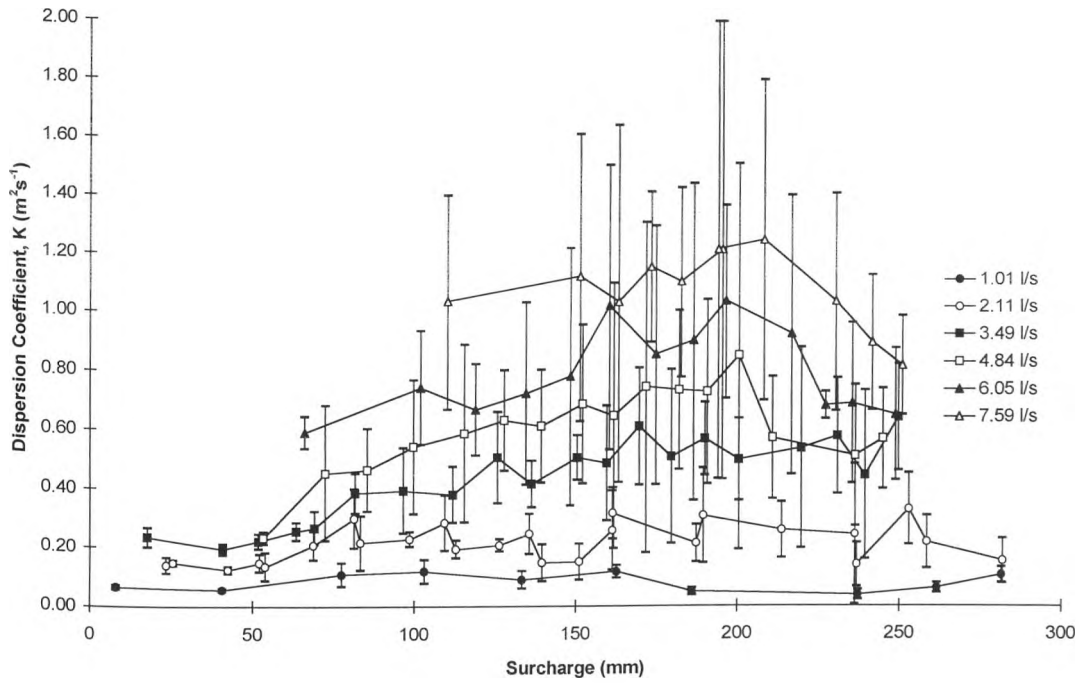


Figure 2.16 400mm chamber, variation of dispersion coefficient (K) with surcharge for a range of discharges.

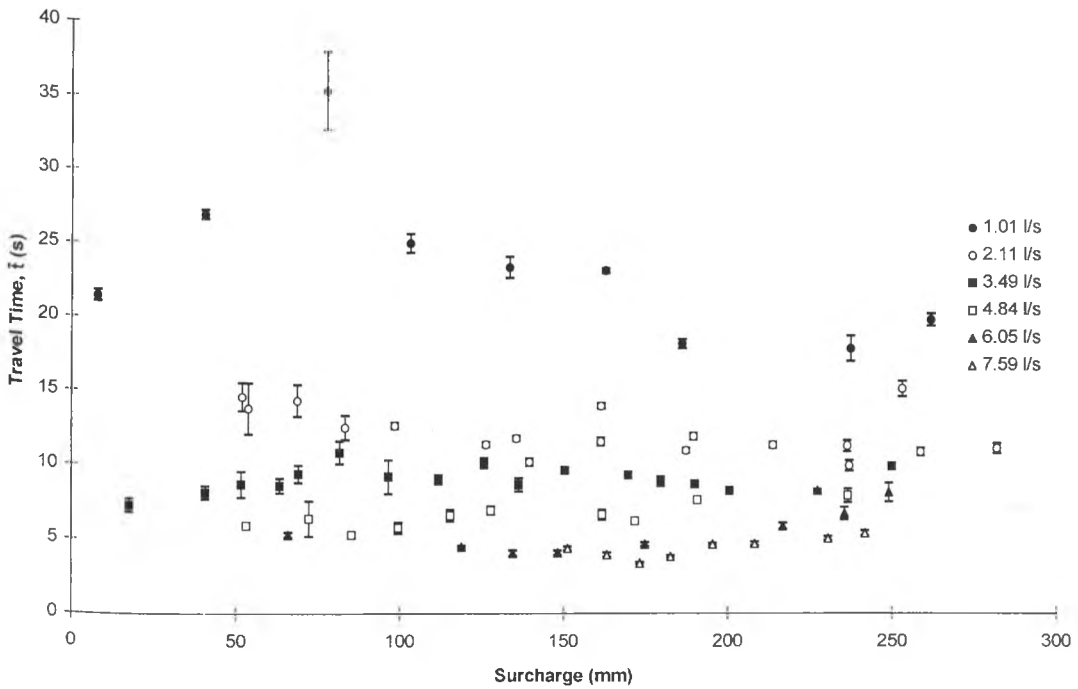


Figure 2.17 400mm chamber, variation of travel time (\bar{t}) with surcharge for a range of discharges.

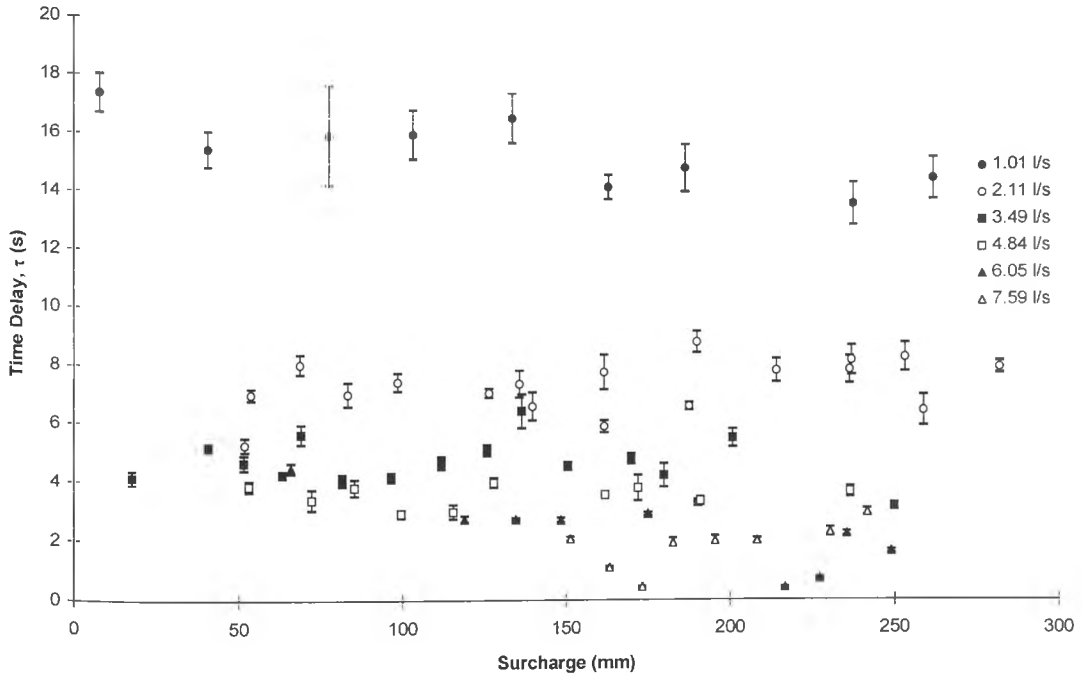


Figure 2.18 400mm chamber, variation of time delay (τ) with surcharge for a range of discharges.

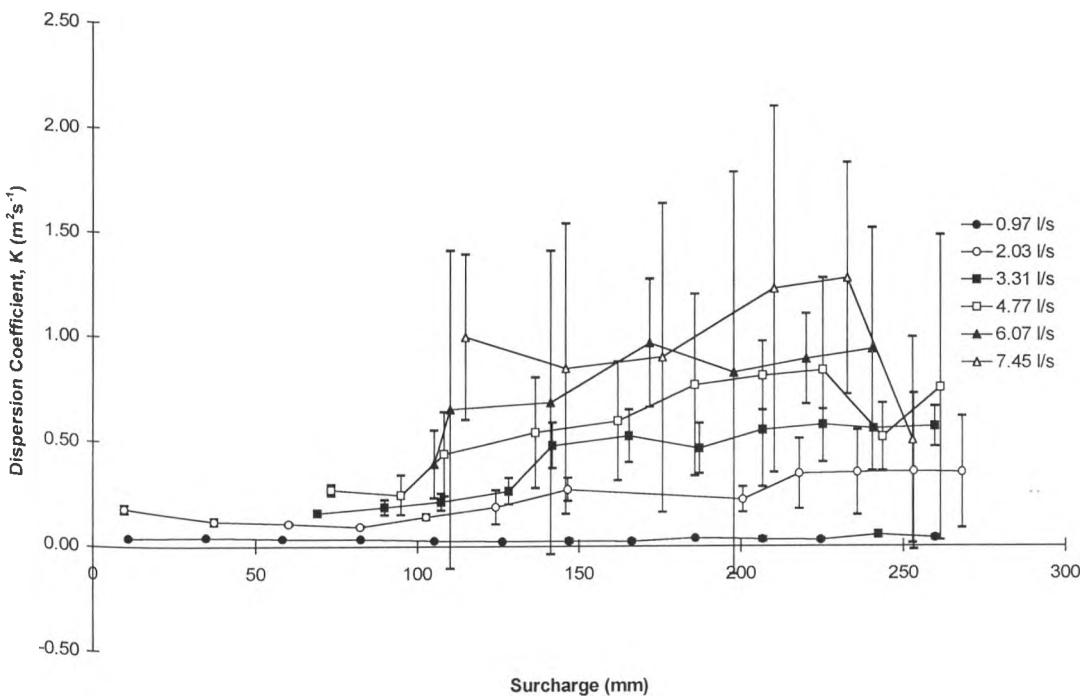


Figure 2.19 500mm chamber, variation of dispersion coefficient (K) with surcharge for a range of discharges.

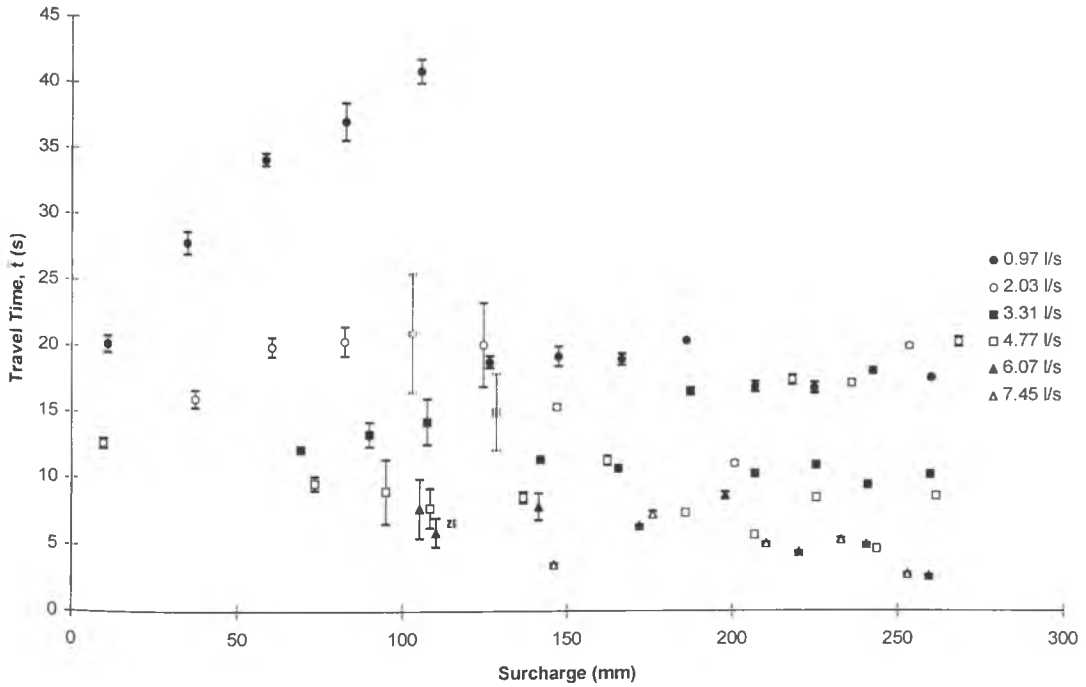


Figure 2.20 500mm chamber, variation of travel time (t) with surcharge for a range of discharges.

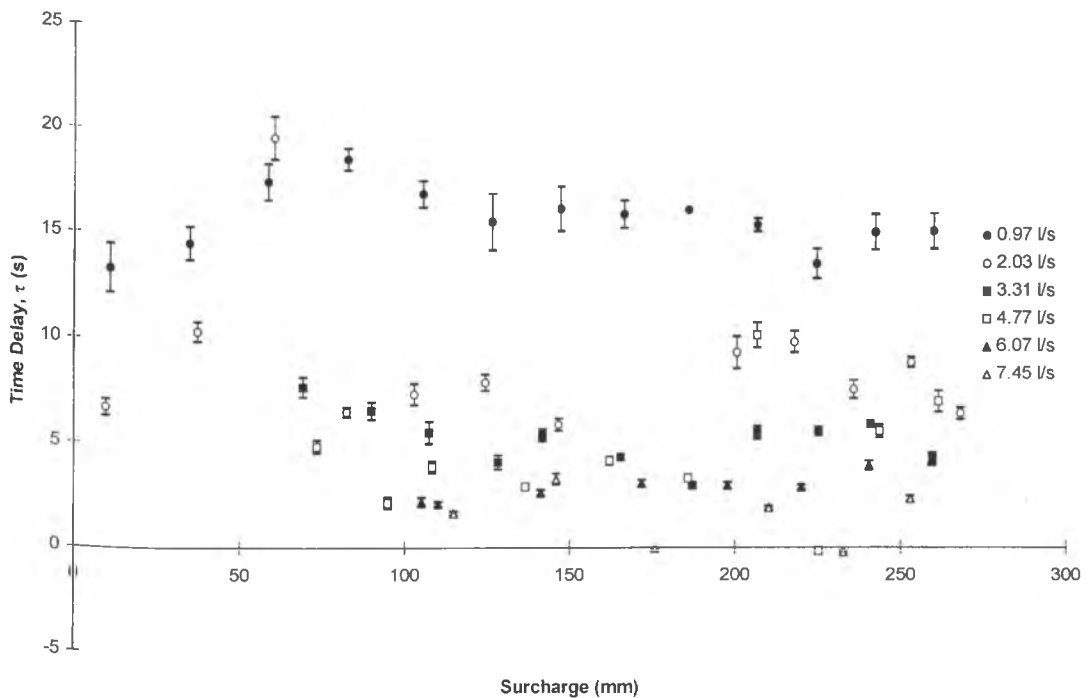


Figure 2.21 500mm chamber, variation of time delay (τ) with surcharge for a range of discharges.

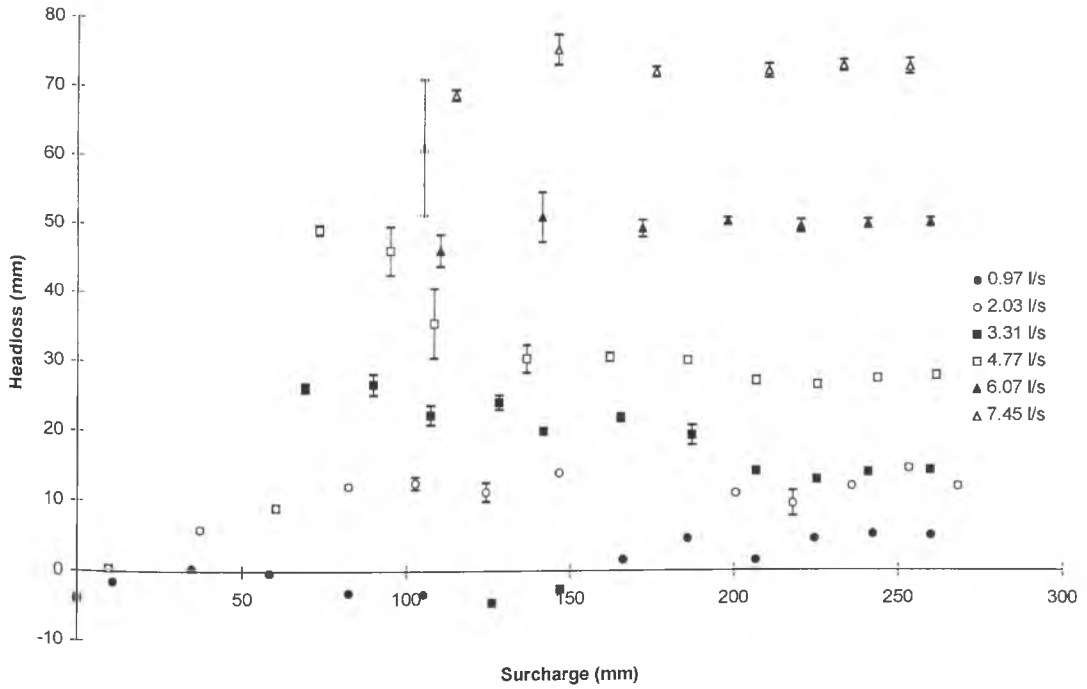


Figure 2.22 500mm chamber, variation of headloss (h_L) with surcharge for a range of discharges.

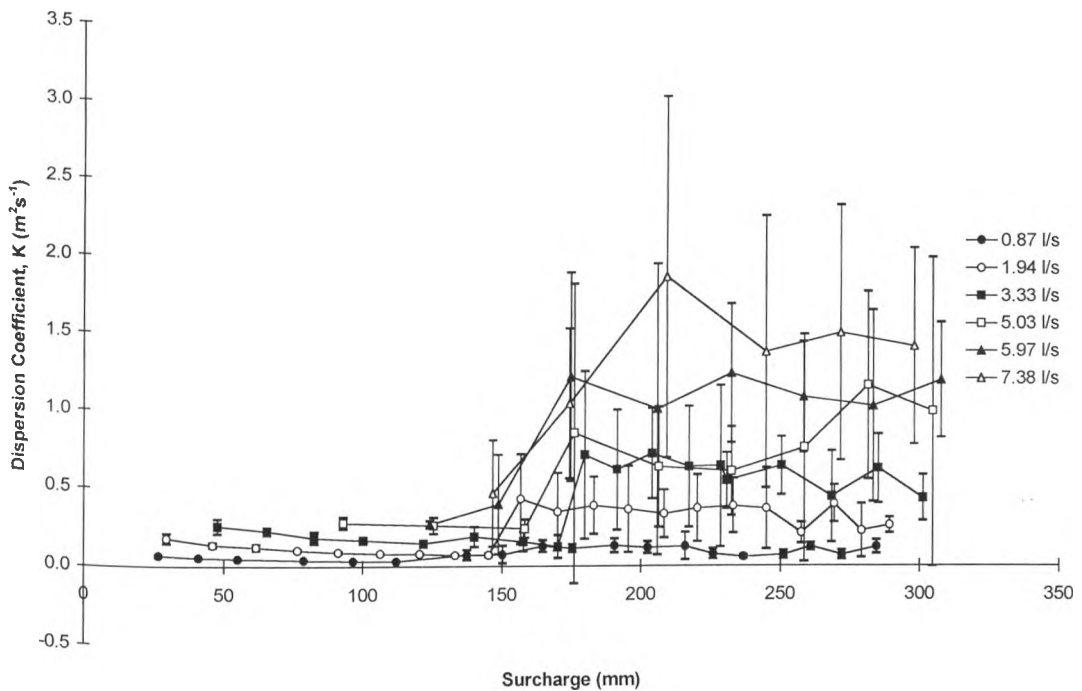


Figure 2.23 600mm chamber, variation of dispersion coefficient (K) with surcharge for a range of discharges.

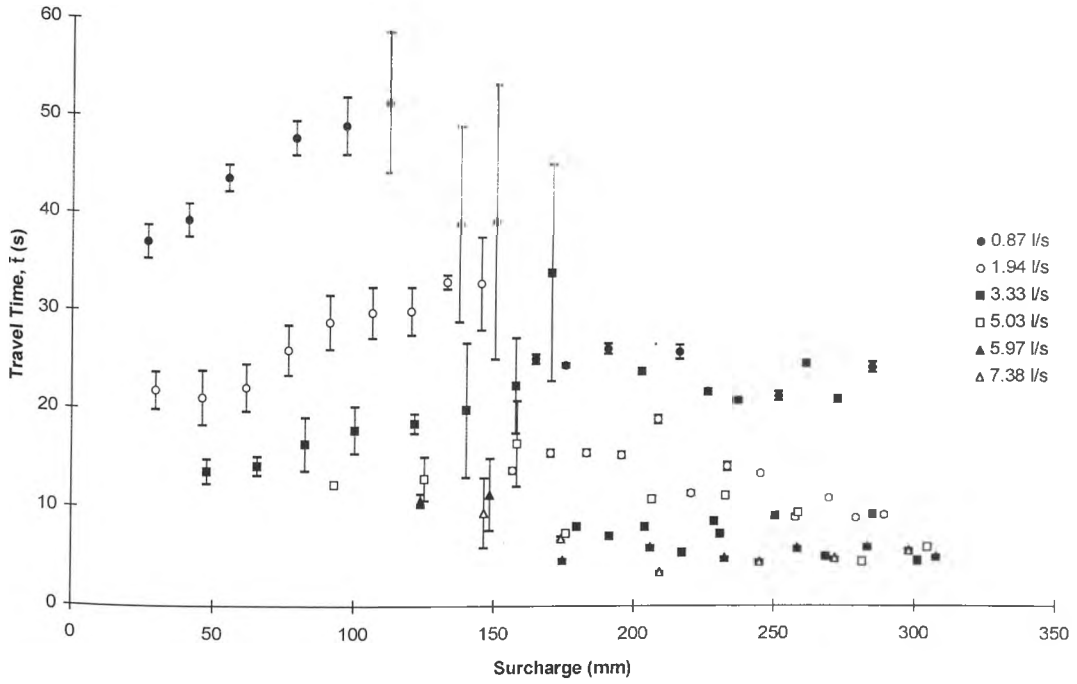


Figure 2.24 600mm chamber, variation of travel time (\bar{t}) with surcharge for a range of discharges.

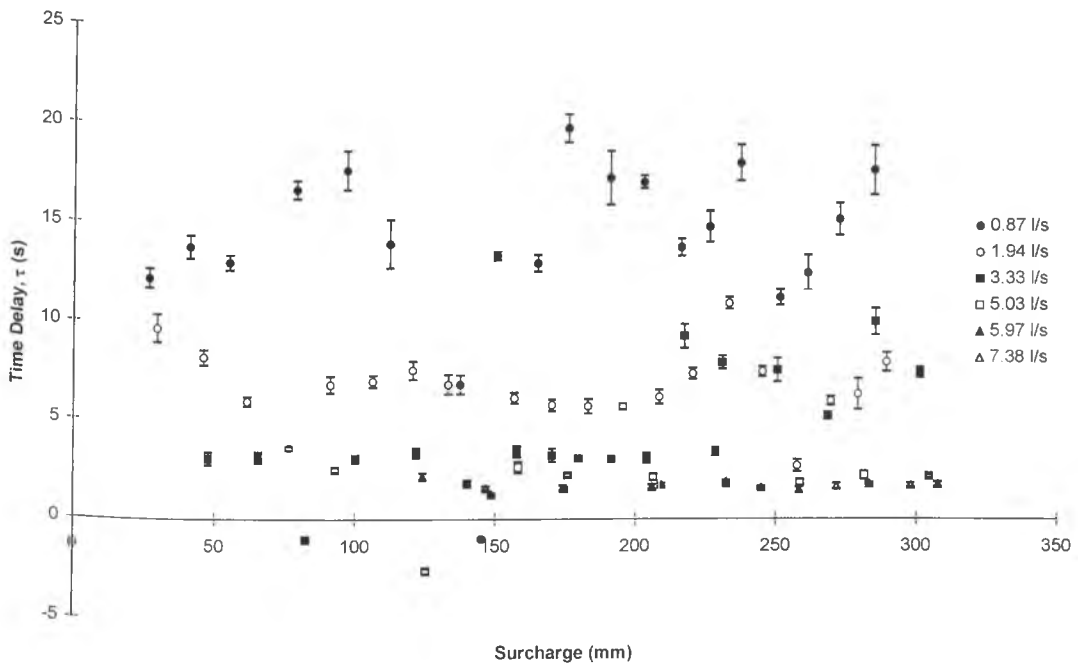


Figure 2.25 600mm chamber, variation of time delay (τ) with surcharge for a range of discharges.

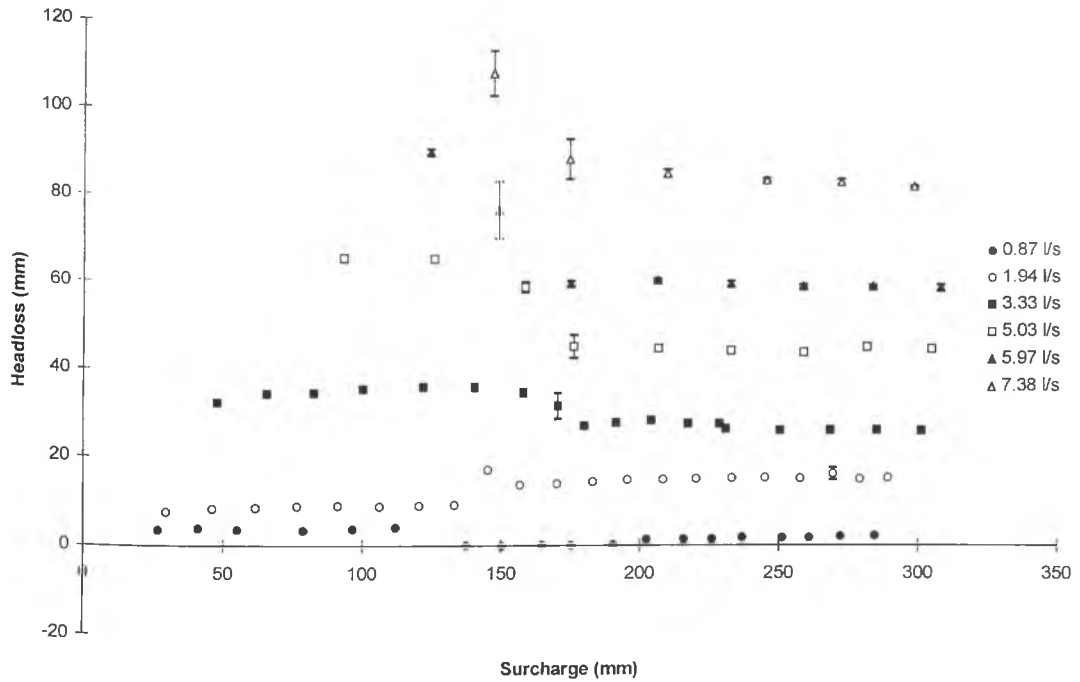


Figure 2.26 600mm chamber, variation of headloss (h_L) with surcharge for a range of discharges.

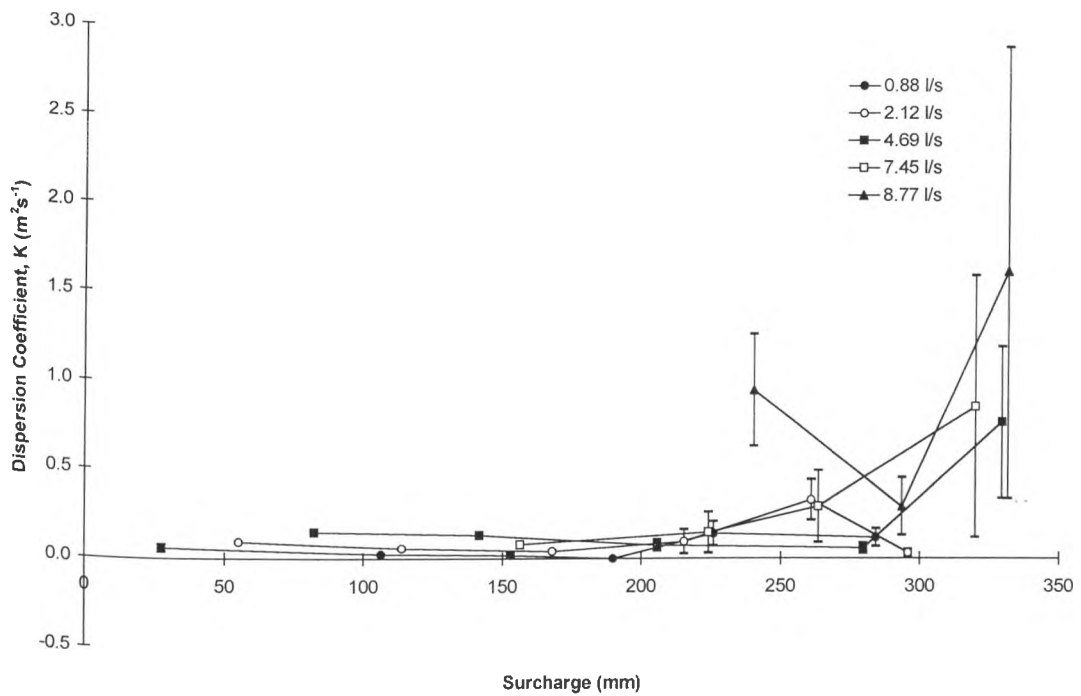


Figure 2.27 800mm chamber, variation of dispersion coefficient (K) with surcharge for a range of discharges.

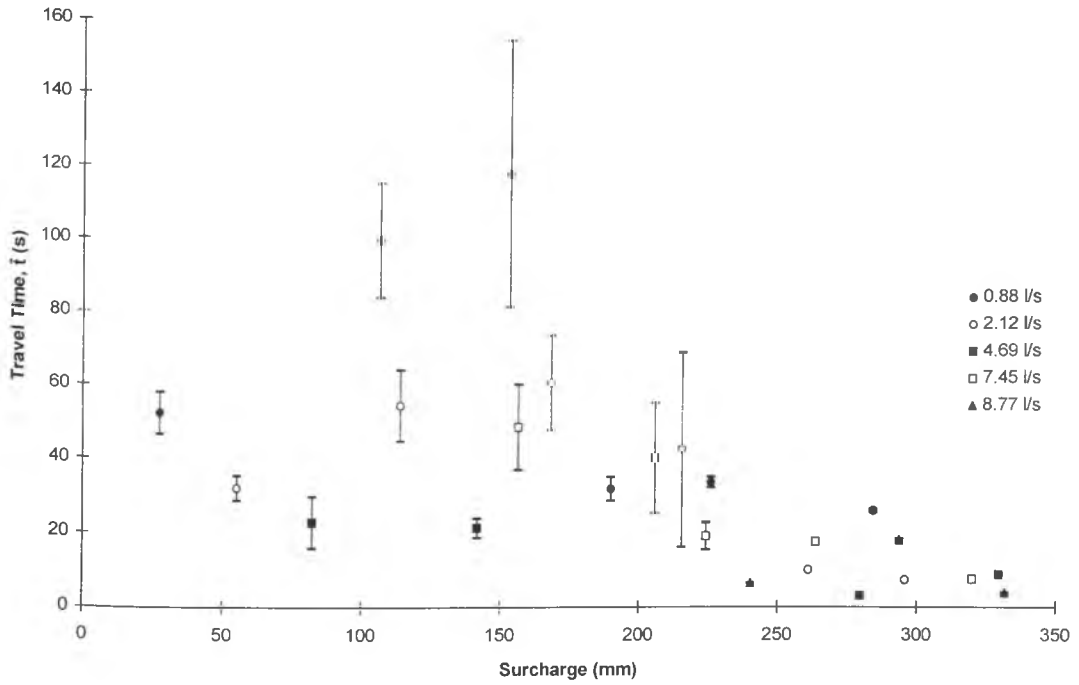


Figure 2.28 800mm chamber, variation of travel time (t) with surcharge for a range of discharges.

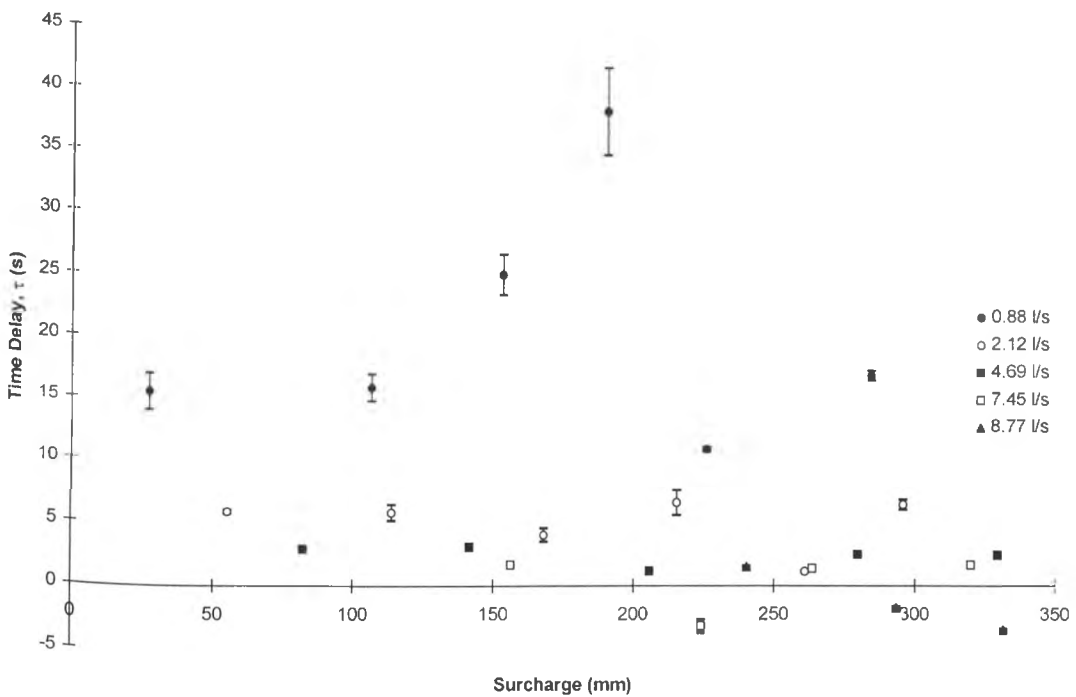


Figure 2.29 800mm chamber, variation of time delay (τ) with surcharge for a range of discharges.

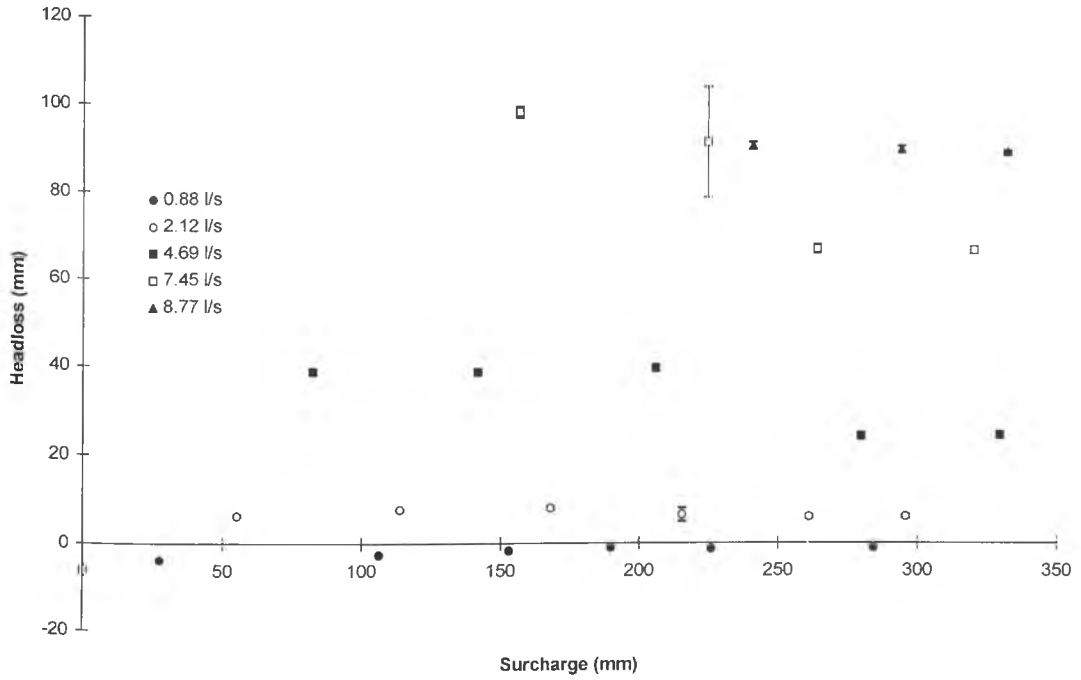


Figure 2.30 800mm chamber, variation of headloss (h_L) with surcharge for a range of discharges.

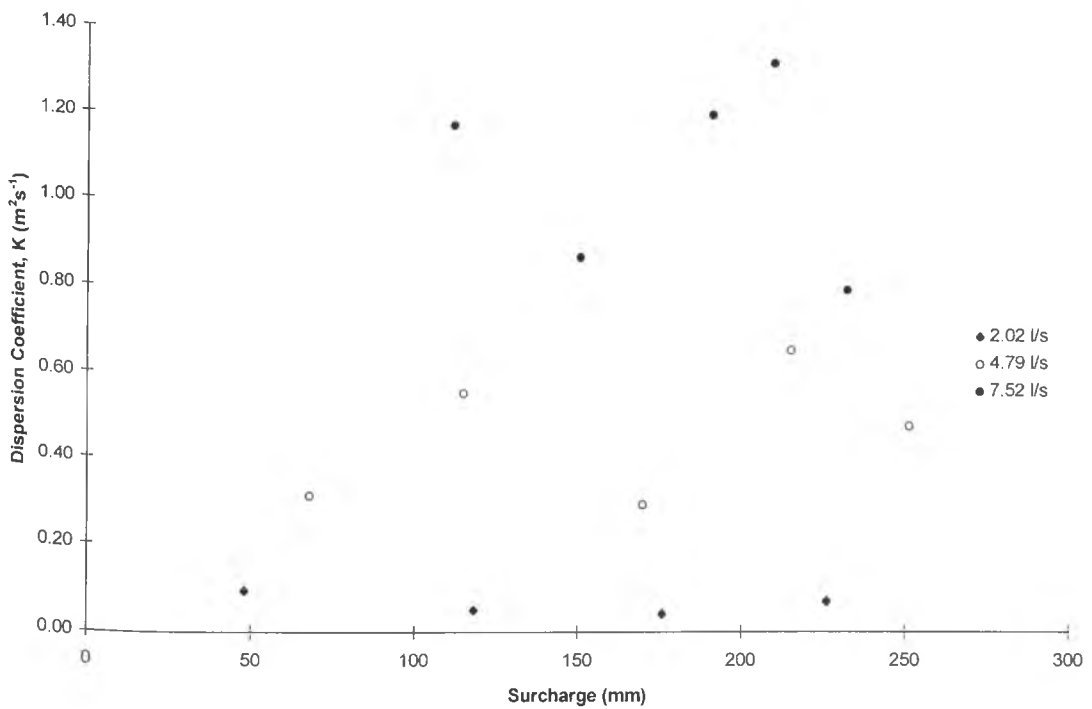


Figure 2.31 400mm chamber control test, variation of dispersion coefficient (K) with surcharge for a range of discharges.

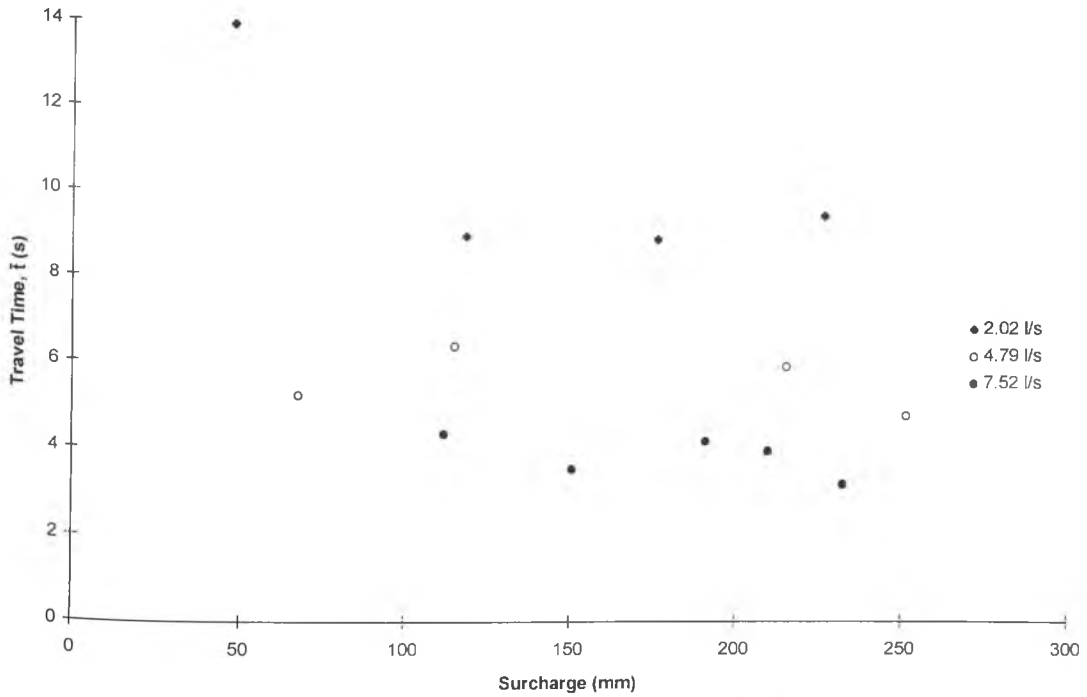


Figure 2.32 400mm chamber control test, variation of travel time (\bar{t}) with surcharge for a range of discharges.

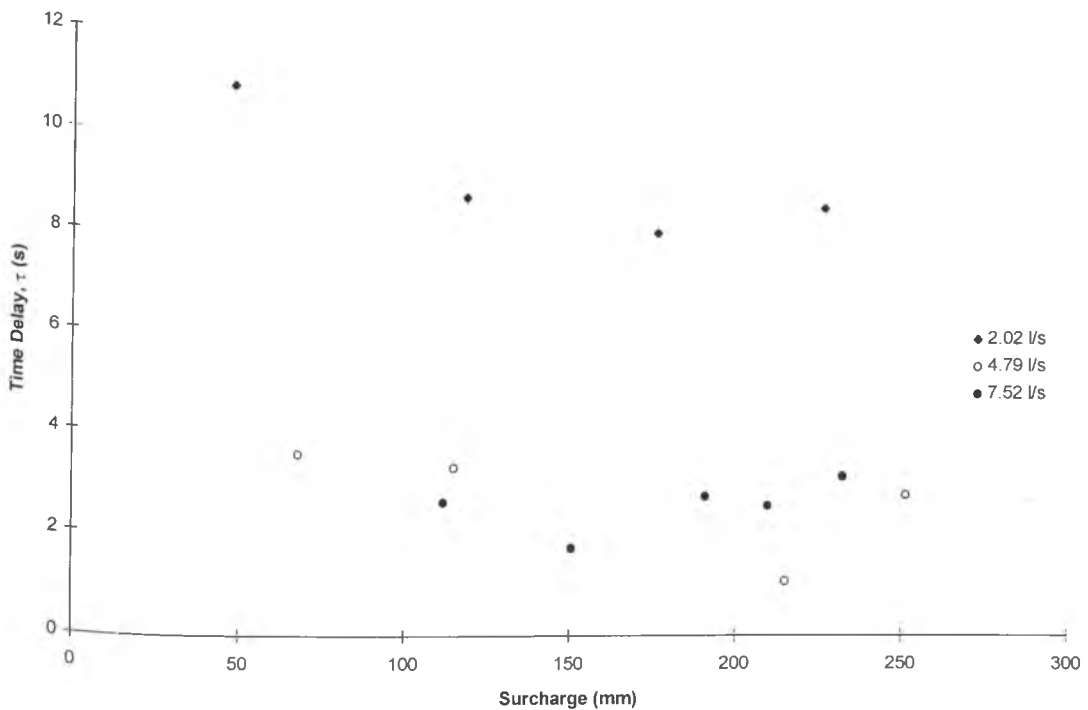


Figure 2.33 400mm chamber control test, variation of time delay (τ) with surcharge for a range of discharges.

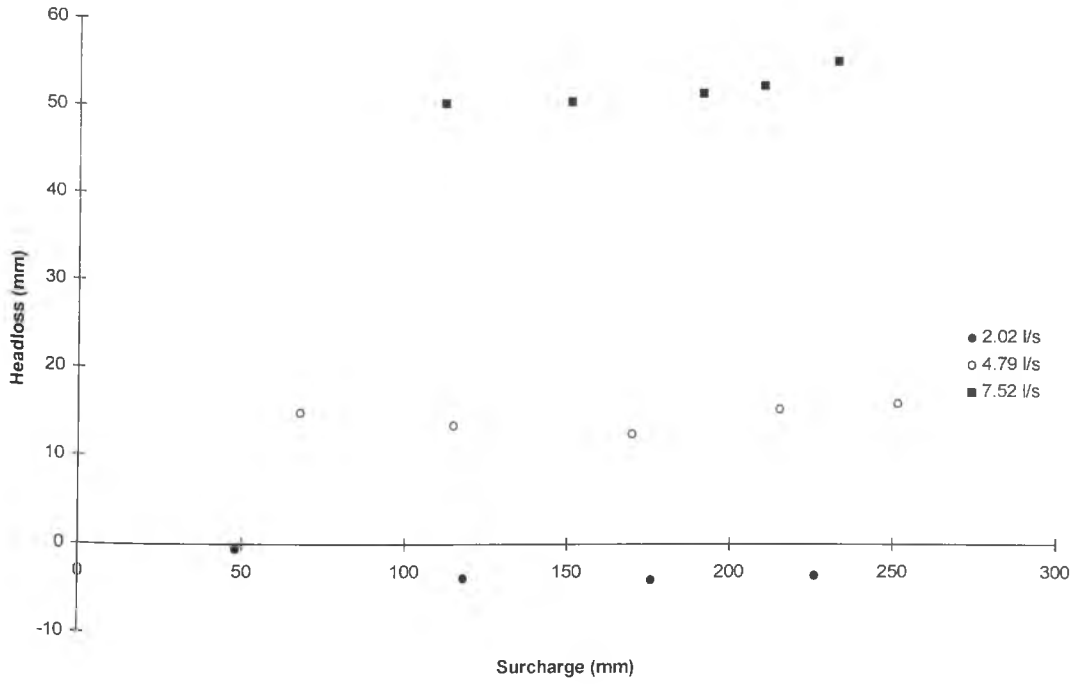


Figure 2.34 400mm chamber control test, variation of headloss (h_L) with surcharge for a range of discharges.

Chapter 3

Discussion

3.1 Headlosses

3.1.1 Introduction

In recent years an extensive range of studies have been undertaken to quantify the effect of manholes on the within sewer systems (Marsalek (1984), Johnston & Volker (1990) and Pedersen & Mark (1990)). These studies examined both a wide range of manhole geometry's and flow regimes.

The headloss measurements performed within the current study are similar to those of the previous studies. However, due to the apparent ease of gaining such information, and the obvious benefit of obtaining a greater understanding of the mechanisms at work within the manhole chamber, pressure transducers were fitted to the test facility.

Although a study of the headlosses has consequently been undertaken, this work is of secondary importance to the main theme of the current research, namely, to identify the effects of manhole structures on longitudinal dispersion. As a result, the level of analysis performed on the headloss data is less detailed.

Headloss data is available for all but the initial 400mm manhole tests (Table 2.1). However an additional 400mm manhole tests was later performed, thus allowing a comparison between all the examined manhole configurations.

3.1.2 Determining Headloss Coefficients

To enable a comparison with the previous studies, headloss is assumed to be directly proportional to the velocity head. The gradient of such a relationship is termed the headloss coefficient (K_{HL}). This coefficient can be used to predict headlosses from the area mean velocity by application of the Darcy equation.

$$h_L = K_{HL} \left(\frac{v^2}{2g} \right) \quad (3.1)$$

Where -

- K_{HL} = Headloss coefficient (-),
- h_L = Headloss (m),
- v = Area mean velocity (ms^{-1}),
- g = Acceleration due to gravity (ms^{-2}).

(Note: K_{HL} is a bulk parameter containing both the friction factor, f , and associated constants normally portrayed in the Darcy equation.)

3.1.3 Headloss in Pipes

The measured headlosses for a straight pipe are shown in Figure 3.1. By application of the previously illustrated approach for evaluating headloss coefficients, K_{HL} is determined by fitting a linear regression through the data set. This will yield a headloss coefficient of 0.4314. However this value has been calculated from two pressure transducers 1.97m apart (Figure 2.8). If this coefficient were expressed per metre length of pipe, the coefficient would become 0.217m^{-1} .

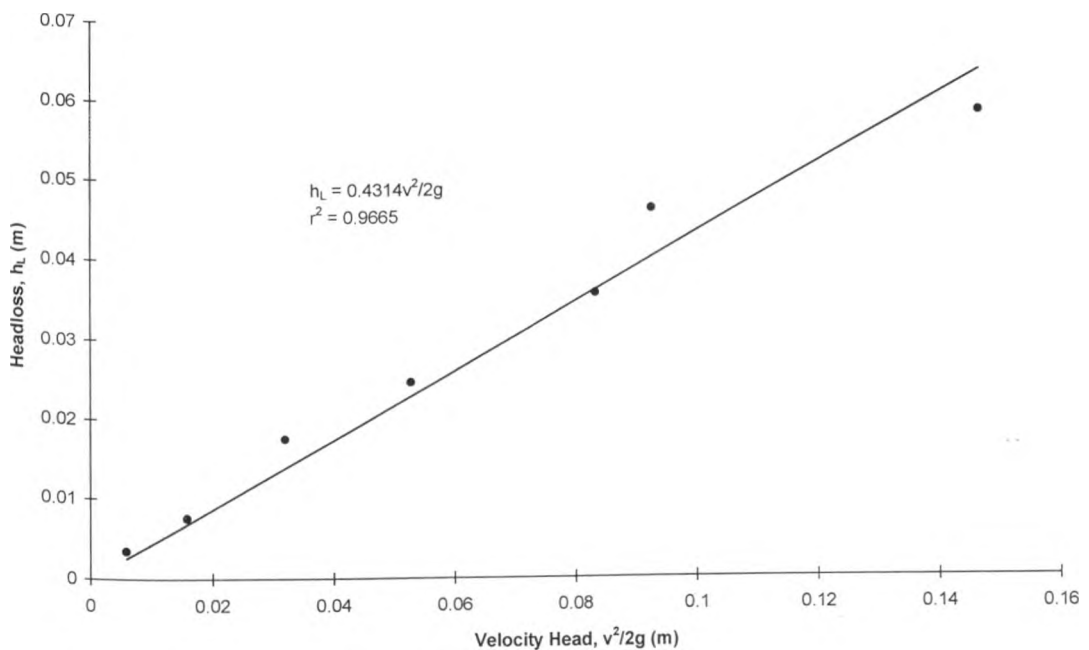


Figure 3.1 Measured headloss for a straight perspex pipe over a distance of 2.7m (88mm internal diameter)

Studies of headloss within a turbulent flow in smooth pipes was conducted by Blasius (Douglas, Gasiorek & Swaffield (1987)). From this work it was shown that for turbulent flow, the Reynolds number, Re , could be used to evaluate the pipe friction factor, f , within $\pm 5\%$.

$$f = 0.079/Re^{1/4} \quad (3.2)$$

The variation in the Reynolds number with area mean velocity can be calculated from the equation -

$$Re = \frac{\rho v d}{\mu} \quad (3.3)$$

Where -

- ρ = Fluid density (kgm^{-3}),
- v = Area mean velocity (ms^{-1}),
- d = Pipe diameter (m),
- μ = Fluid viscosity ($\text{kgm}^{-1}\text{s}^{-1}$).

The values of fluid density and viscosity for water at 20°C are 998.2 and 1.005 respectively.

Observation of the headloss coefficient, K_{HL} (equation 3.1), and the headloss expression found in the original Darcy equation, leads to the following relationship.

$$K_{HL} = \frac{4f}{d} \quad (3.4)$$

In which, the headloss coefficient is expressed per metre length of pipe.

Examination of headloss coefficients predicted when applying Blasius to the same range of discharges as the measured headlosses (Figure 2.13), show that the predicted headloss coefficient will vary between 0.274 and 0.183m^{-1} . The average predicted headloss coefficient over this range is found to be 0.217m^{-1} . Indeed, due to the relative simplicity of the straight pipe study, a high degree of accuracy would be expected.

3.1.4 Headlosses in Manholes

In general, unlike the present study, previous studies have been dedicated to examining headlosses due to the manhole chamber. Pressure measurements were taken at several locations in the pipes either side of the manhole (Marsalek (1984), Johnston & Volker (1990)

and Pedersen & Mark (1990)). From these measurements, the hydraulic gradients within the pipes up and downstream of the manhole section were determined. The total energy loss due to the manhole structure was taken as the offset between the up and downstream hydraulic gradients at a concurrent location. This was normally calculated by extrapolating the hydraulic gradients to the centre line of the manhole, or similar reference location (See Figure 3.2 (a) and (b)).

Due to the lack of pressure tappings used within the present study (one measuring point in each of the up and downstream pipes, 985mm from the manhole centre line, see Figure 2.8), it was assumed that the hydraulic gradient within the pipes either side of the manhole section was the same as that observed within the straight pipe study. From the pressure readings before and after the manhole section, an extrapolation of the assumed hydraulic gradient was projected to the centre line of the manhole (See Figure 3.2 (a) and (c)). The difference in the offset between these assumed hydraulic gradients was again taken to be the total headloss due to the manhole. The assumption that the hydraulic gradients within the pipes either side of the manhole being the same as that measured within a single straight pipe concurs with the findings of Archer, Bettess and Colyer (1978). However, the transition of the hydraulic gradient from the manhole to the downstream pipe is not instantaneous. A non-linear variation will be observed in the pipe downstream of the manhole for at least 70 pipe diameters (Archer et al (1978)). Within this distance, the hydraulic gradient will asymptotically approach the gradient observed within a single straight pipe.

Due to spatial restrictions within the test facility, the provision of a pressure tapping at an adequate distance downstream was unfeasible. Measurements of the downstream pressure therefore include an unavoidable error, which will be included in the assumed hydraulic gradient (See Figure 3.2 (a) and (d)). Variations in headloss with surcharge for each chamber diameter can be seen in Figures 2.22, 2.26, 2.30 and 2.34. These results show that over the range of surcharges tested, at any one discharge, there are only minor fluctuations in the headloss. For most discharges, the magnitude of headloss shows a slight increase towards the lower surcharges.

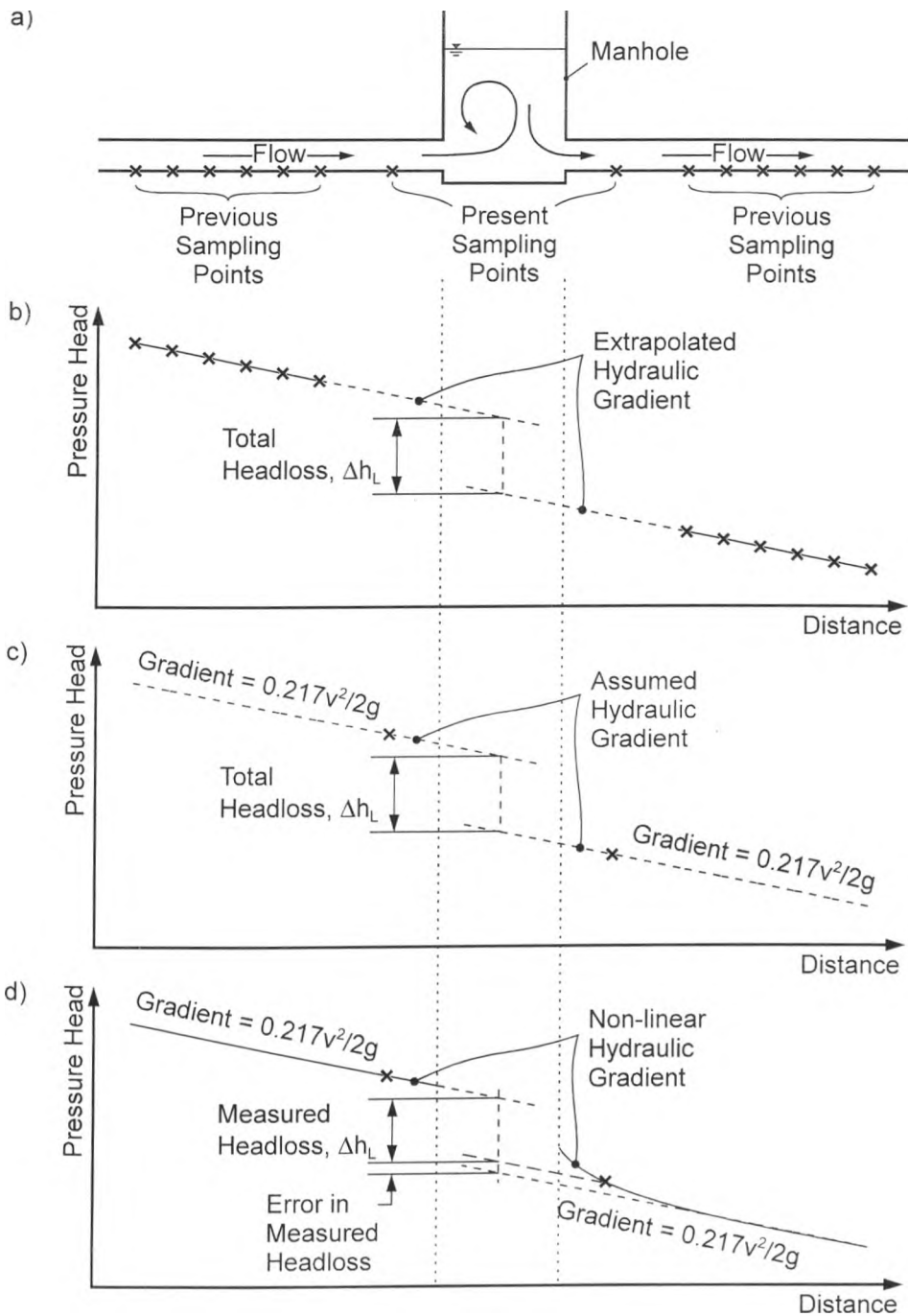


Figure 3.2 Measurements of the hydraulic gradient

- (a) Location of pressure tapplings for previous and present study
- (b) Method of determining hydraulic gradient from previous studies
- (c) Method of determining hydraulic gradient within the present study
- (d) Possible source of errors within present study.

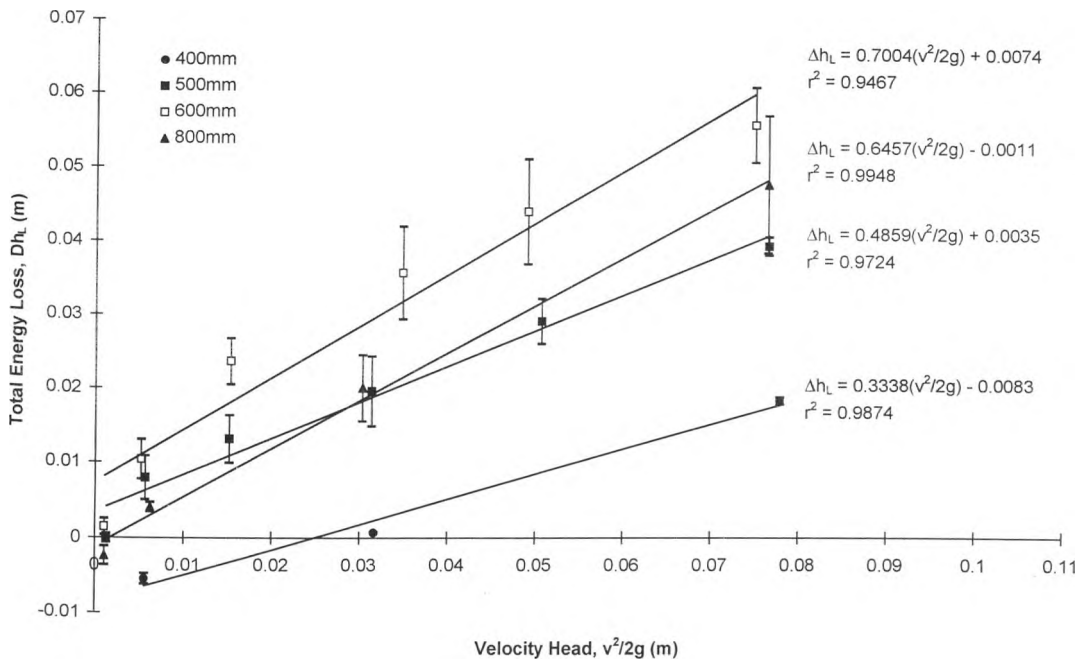


Figure 3.3 Variations in total headloss with velocity head for different chamber diameters

Observations made during testing programme showed that the water surface within the manhole chamber was greatly disturbed at these lower surcharges. Also evident was the formation of a small “standing wave” above the outlet pipe. As the surcharge was increased, these disturbances appeared to become dampened. Consequently it is concluded that the increase in turbulence at the lower surcharges leads to the increase in headloss through an increased energy dissipation. Similar observations were made by Archer, Bettess and Colyer (1978), in which it was concluded that for practical purposes, a general relationship between the headloss and velocity head could be assumed. Consequently any variation in headloss with surcharge within the present study shall be ignored, and variation in headloss with mean flow velocity shall be assumed to be the dominant mechanism.

The results in Figure 3.3 show surcharge averaged headlosses for each chamber diameter, where each headloss used to calculate the surcharge average is itself the temporal average of five, 300 second, test runs. Linear regressions through the results of each chamber show comparatively large variations in both slope and intercept. In some cases, the regression through the data can be seen to have a negative intercept. Previous studies have shown a relationship whereby a linear regression through the headloss data intercepts with the origin (Marsalek (1984), Pedersen & Mark (1990), Archer, Bettess & Colyer(1978)). Through

applications of Bernoulli, this would be expected. If there was no discharge, the study would become purely hydrostatic, hence the headloss would also be zero. Clearly, with the present data, if the linear regressions were adjusted to pass through the origin there would be a reduction in the correlation between the regression line and the data. However, as has been previously stated, the present data could, by some degree, be in error. There is also possibility that the pressure transducers themselves may have deviated from their initial calibration throughout the testing programme. Impurities within the test system, such as sediments and algae (which were both observed on occasions) could have impeded the pressure tappings, thus leading to errors in the measurements.

In an attempt to rectify the errors incurred in all the test runs, it is assumed that the source of the errors has only affected the intercept of the headloss / velocity head data. Moreover, if the gradient were affected, it would be impossible to quantify the magnitude of the error. Therefore, only the gradients of the measured headlosses are to be investigated further, thus assuming that the intercept of the regressions through each individual data set, passes through the origin.

To enable a direct comparison with previous studies, the results of headloss coefficient have been shown varying with the ratio of manhole diameter to the outlet pipe diameter (D_M/D_P).

In addition to the present study, Figure 3.4 also shows results found by Marsalek (1984) for both square and round un-benched manhole chambers, Johnston and Volker (1990) for square chambers, Hare (1983) and Pedersen and Mark (1990) for round manhole chambers.

The results suggest a similarity between the present study and its predecessors. Rather than supplying individual results, Pedersen and Mark (1990) suggested the gradient of a trend line that passes through the origin, shown as a dashed line in Figure 3.4. The gradient of this line was dependant on the chamber design, which, in terms of the present study, yields a value of 0.12. However, this result was only validated for values of $D_M/D_P \leq 4$. A equivalent regression through the present data set yields a gradient of 0.0820. From Figure 3.4, it is evident that there are similar trends in the results of the present study and those carried out previously. The greatest departure of the present study from any of its predecessors is seen in the results of Pedersen and Mark (1990). There is the possibility that these discrepancies could be accounted for by the limitations in the test facility that have previously been highlighted. However, the present study reflects results that are beyond the valid application of predictions

made by Pedersen and Mark (1990), and greater than any of the other previous studies cited. It is therefore concluded that although there is a relatively low correlation for a linear regression fitted to the present data (0.6133), trends within the present study are an accurate representation of manholes with a chamber diameter / pipe diameter ratio greater than four.

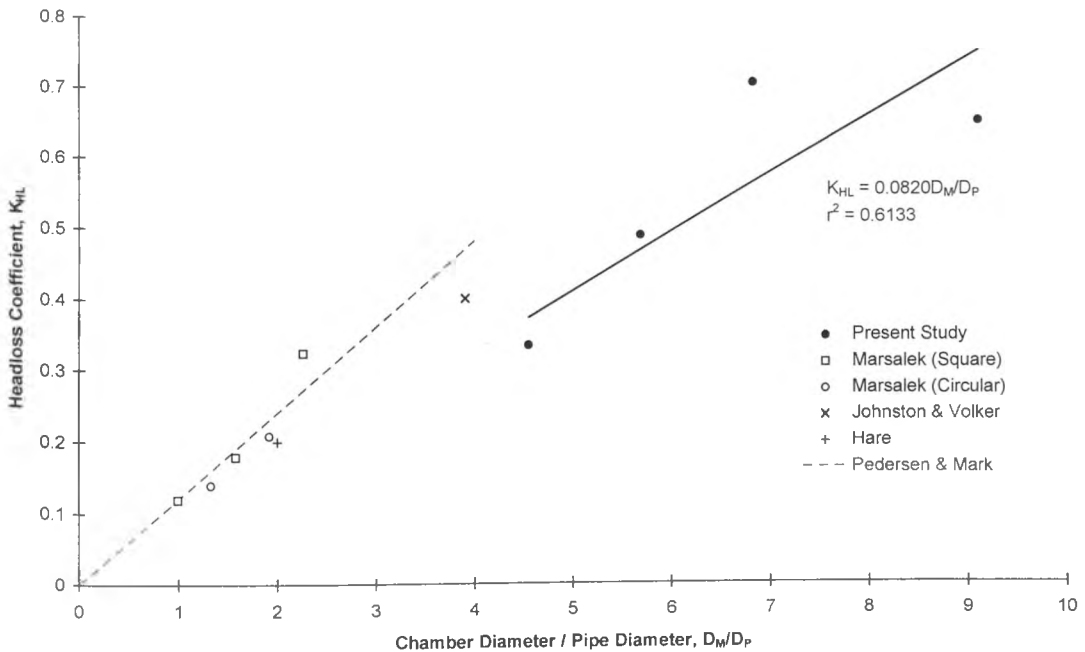


Figure 3.4 Comparison of present headloss data with previous studies.

In contrast to the observations made by Marsalek (1994) (regarding the findings of Sangster, Wood, Smerdan & Bossy (1958)) who stated "... Junctions wider than 2.26D were not studied, because Sangster et al found only minor increases in the loss coefficient for manholes wider than 2D and no change for widths greater than 2.5D. ...", where D represents the inlet pipe diameter, it is evident that there is an increase in the headloss coefficient values of D_M/D_P greater than 2.5. Although there is only limited data available, Sangster et al (1958) did actually predict these increases in the headloss for straight flow through chambers, but the analysis was not pursued.

3.2 Results to the Advective Dispersion Model

3.2.1 Straight Pipe

As with the findings of Taylor (1953 and 1954), an increase in the rate of change in the second moments, and consequently the dispersion coefficient, K , was observed with the increase in the discharge (Figure 3.5). However, the error bars (which show ± 1 standard deviation about the mean sample) suggest that there is also an increasing uncertainty in the results with the increasing discharge. The increase in the magnitude of the error bars could be a reflection of problems that were encountered in the analysis of data for higher discharges. Due to the relatively short temporal duration of the data at the higher discharges, errors made in determining the length of the tailing leg of the data lead to increasing percentage errors in the overall temporal distribution (Figure 2.10). This error is further heightened because a second temporal moment is used when calculating a dispersion coefficient (equation 1.44), thus squaring any temporal errors.

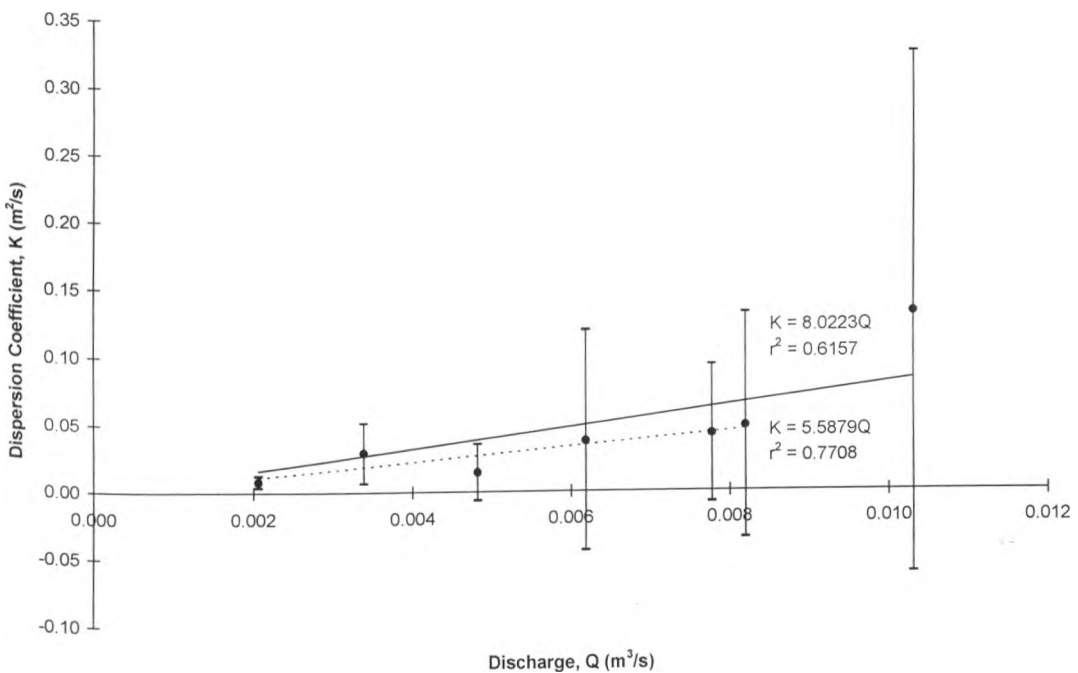


Figure 3.5 Variation of dispersion coefficient with discharge.

A linear regression through the entire straight pipe data set and passing through the origin yields a linear relationship between the dispersion coefficient and discharge, with a constant of

proportionality of $8.02m^{-1}$. It is possible to compare the present study to that performed by Taylor (1954). Taylor predicted that for turbulent flow in a straight pipe, a dispersion coefficient, K (equation 1.40), could be predicted from the pipe diameter (r) and the shear velocity (u^*).

$$K = 10.1ru^* \quad (1.40)$$

A value for the shear velocity can be determined from the boundary shear stress by applying the equation,

$$u^* = \sqrt{\frac{\tau_0}{\rho}} \quad (3.5)$$

where -

τ_0 = Shear stress (Nm^{-2}),

ρ = Density (kgm^{-3}).

Whilst the shear stress can be calculated from the change in peizometric pressure between two points along the length of the pipe,

$$\tau_0 = m \frac{dP^*}{dx} \quad (3.6)$$

where -

m = Mean hydraulic radius (m),

dP^*/dx = Rate of change in streamwise peizometric pressure (Nm^{-2} per m).

By implementation of the above equations (Douglas, Gasiorek & Swaffield (1987)) and the measured headlosses presented in Section 3.1.3, a prediction for the variation of dispersion coefficient with discharge can be found.

$$K = 3.59Q \quad (3.7)$$

where -

Q = Mean discharge (m^3s^{-1}),

The value 3.59 in equation 3.7 is comparable to the gradient of the linear regression through the dispersion coefficient / discharge data (solid line, Figure 3.5), which has a value of 8.02. From this result, it can be seen that Taylor method of predicting a dispersion coefficient (equation 1.40), results in a value that is less than half that measured in the present study. One possible reason for this deviation is the previously observed increase in uncertainty in the results as the discharge increases. If a linear regression is passed through all but the last data point in Figure 3.5 (dashed line), the gradient of the regression reduces to 5.59, whilst the correlation coefficient increases to 0.77. This is clearly closer to Taylor's prediction, however with the lack of any additional results on which to base the removal of this data point, there is little justification in making this amendment.

There is also the possibility that the measured dispersion coefficient was consistently greater than that predicted by Taylor due to limitations in the test facility. To enable a true calculation of the dispersion coefficient, it is necessary to determine an accurate area mean concentration. Although the modification to the fluorometers allows them to be mounted onto the test facility, it is not precisely known whether the full cross section of the pipe has been illuminated, or if the illumination is uniform across the cross section. Both of these scenarios can lead to tracer concentration / time profiles that may differ from previous studies. This could result in different levels of dispersion being predicted by different studies.

3.2.2 Manholes

From the results of the variation in dispersion coefficient with surcharge, for the range of discharges tested, several observations can be made between the different chamber diameters (Figures 2.16, 2.19, 2.23, 2.27 and 2.30). The most evident of which is a "plateau" region within the dispersion coefficients at low surcharges. Within this region, relatively low values of dispersion coefficient are measured in comparison to the results beyond the plateau. With the 400mm data (Figure 2.16) this region is scarcely evident, but becomes more pronounced as the diameter of the manhole increases. The results of the 800mm manhole (Figure 2.27) suggest that almost all the data acquired for this diameter lies within the plateau region.

Figure 3.6 shows the variation of a discharge averaged dispersion coefficient with surcharge. The data presented within this figure is the average result for all the discharges tested for each chamber. The data has been further averaged for each 25mm step in the surcharge. The error bars indicate ± 1 standard deviation in the data about the mean sample. Within the plateau region, the data shows little fluctuation, and remains relatively constant in relation to the data that follows the plateau. The error bars indicate that there is less spread in the data within the plateau region, after which a greater spread is seen due to the data's dependency on discharge.

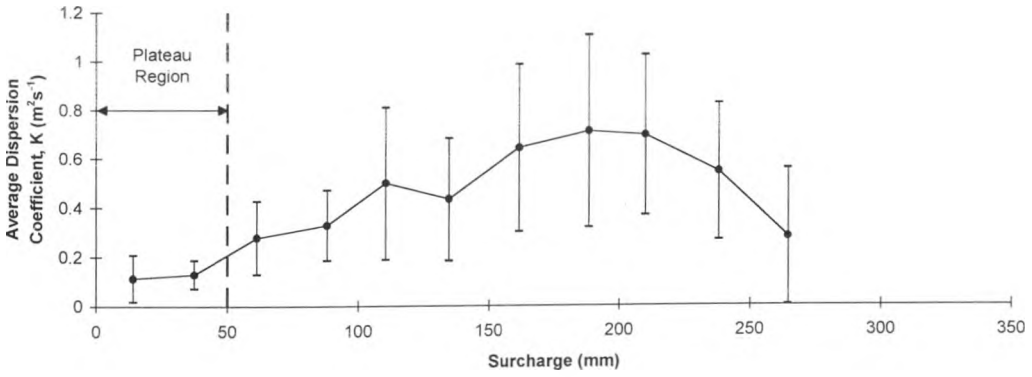
From these observations, it can be seen that there is a threshold level to the surcharge. Prior to this threshold, dispersion is relatively low, and because there is little fluctuation in this data, this suggests that it is independent of surcharge. There is however some evidence of a dependency on the discharge prior to the threshold (Figures 2.16, 2.19, 2.23, 2.27 and 2.31). The data appears to be stratified with the level of dispersion increasing with discharge, however the magnitude of the dispersion prior to the threshold is much less than that seen afterward.

Figure 3.6 illustrates how the threshold level in the surcharge increases with the increase in the chamber diameter. The dashed line indicates the approximate location of the surcharge threshold. With the 400mm diameter chamber (Figure 3.6 (a)), the threshold can be seen to be approximately 50mm. For each 100mm increase in the chamber diameter, the level of the surcharge threshold increases by approximately 50mm, until, with the 800mm diameter chamber (Figure 3.6 (d)) it has increased to 250mm. From these observations an approximate, linear relationship can be made between the level of the surcharge threshold and the manhole chamber diameter.

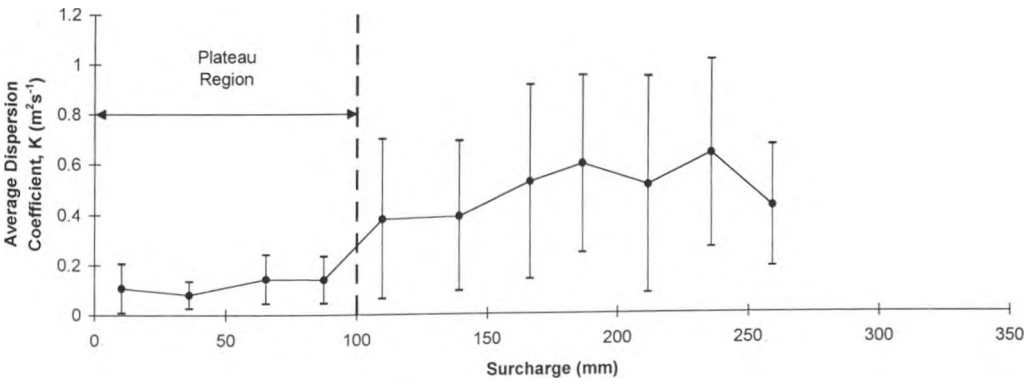
$$\text{Surcharge Threshold(m)} = 0.5 \times \text{Chamber Diameter(m)} - 0.15 \quad (3.8)$$

As with previous studies carried out on manhole designs (assessing alternative manhole parameters), it is probable that the surcharge threshold level will be proportional to the ratio of chamber diameter to the pipe diameter, but the lack of data within the present study makes this observation nothing more than speculation.

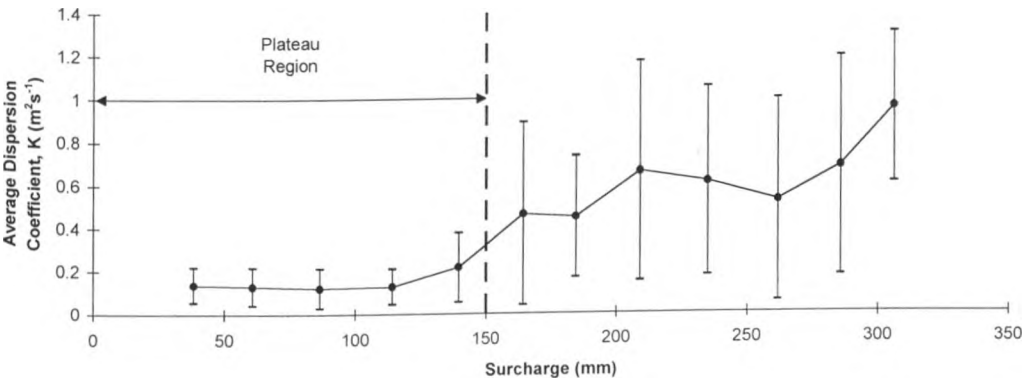
a)



b)



c)



d)

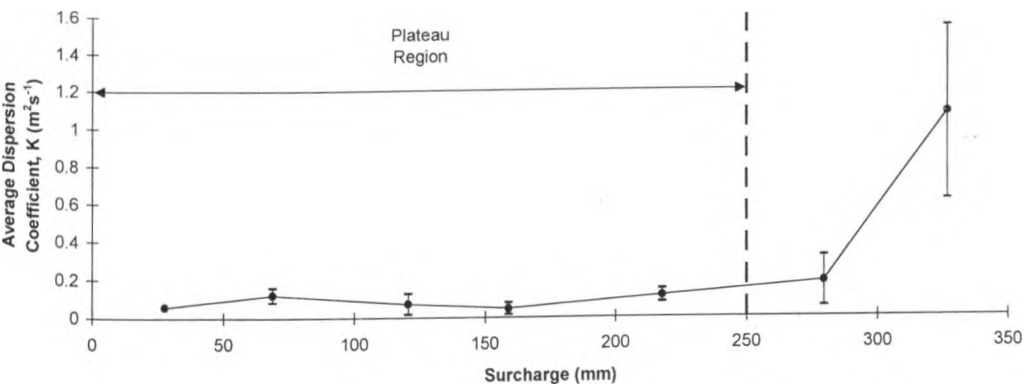


Figure 3.6 Increase in surcharge threshold with chamber diameter.

a) 400mm chamber, b) 500mm chamber, c) 600mm chamber, d) 800mm chamber.

Beyond the surcharge threshold the level of dispersion rises rapidly. Although a pronounced second plateau in the dispersion coefficient is not seen to be attained after the threshold, the results do show a tendency to level out (Figures 3.6, 2.16, 2.19, 2.23, 2.27 and 2.31). It is evident that there are fluctuations within the data that could be attributed to variations in the surcharge, however, the discharge is by far the most influential factor effecting the magnitude of the dispersion. This observation is endorsed by the general segregation within the data that clearly illustrates an increase in the dispersion coefficient with discharge. In some cases there is evidence of a lower discharge yielding a dispersion coefficient that is greater than a neighbouring higher discharge, and vice versa. But this is only seen in isolated cases, and with the large scatter in the data (denoted by large error bars), this is to be expected.

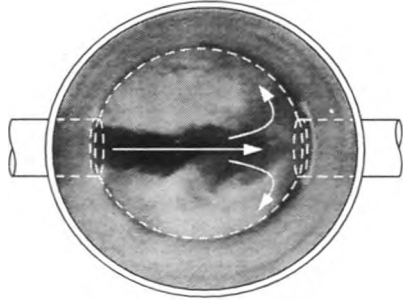
Another trend that is evident throughout the data is the increase in the error bars at the higher discharges (and subsequently the higher dispersion coefficients). As with the straight pipe study, this increase in the error bars is assumed to be the product of the increased difficulty in accurately determining the duration of the temporal distribution at higher discharges. Although the error bars are excessive, it is felt that there are obvious trends within the data that maintain its validity. As has been previously stated, due to the method of determining the error bars for the dispersion coefficient data, they should only be used as an indication of the data accuracy, and not an absolute measure.

The data suggests that for both pre and post threshold dispersion, the magnitude of the dispersion is primarily dependant on the discharge. The level of surcharge will dictate whether the data is influenced by a pre or post threshold dispersion coefficient. The difference in the magnitude of the pre and post threshold dispersion is due to different modes of mixing within the manhole chamber. Figure 3.7 is a composite image of a manhole chamber with a pre threshold surcharge. The image of the flow within the manhole was captured by video, and the main paths of a tracer within the chamber have been highlighted.

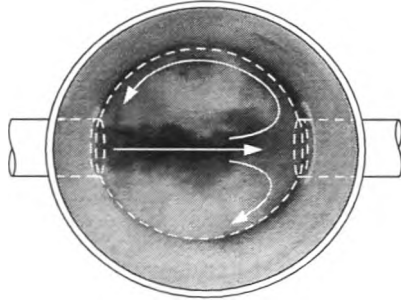
Within the views depicting the elevation of the manhole, the tracer appears consistently more concentrated towards the water surface. This is because the tracer was being fluoresced from a light source above the manhole chamber. The light source is attenuated as it passes through the tracer, thus giving the appearance of a greater concentration at the surface. However these images are still useful in determining the path taken by the tracer, and thus the mode of mixing. Figure 3.7(a) shows a tracer cloud entering the manhole chamber from the

left. The path of the tracer illustrates the submerged jet that Pedersen and Mark (1990) use to account for headlosses. As the tracer passes through the manhole, it is seen to recirculate on plan. By 9 seconds (Figure 3.7(c)) the tracer has become almost uniformly mixed within the chamber. The recirculating regions either side of the main flow (on plan) entrap the tracer, and allow it to only bleed back into the main flow. After 15 seconds another submerged jet is evident within the chamber. This time the jet consists of clear water entering into the manhole chamber after the tracer slug has passed. As a conclusion, it can be seen that within manhole with a pre threshold surcharge, the dominant mode of the mixing occurs on plan.

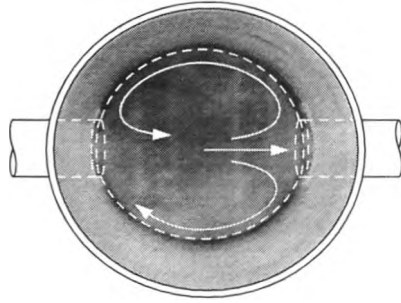
As a contrast Figure 3.8 illustrates the dispersive mechanisms within a manhole that has a post threshold surcharge. Again after 3 seconds the submerged jet is again evident within the manhole. However, rather than the recirculation occurring on plan, the tracer is seen to rise up above the outlet pipe towards the waters surface. Figure 3.8(b) and (c) show that a homogeneous blanket of tracer follows the water surface in the opposite direction to the main flow. The bulk of the tracer that has left the main flow through this process is entrapped in the large, surcharged body of water. Tracer will very slowly be re-entrained from this body of water back into the main flow. After 40 seconds the second submerged jet of clear water is only just visible through the tracer stored within the surcharged body of water. In contrast to the pre threshold case, the post threshold mixing predominantly occurs on elevation. This enables the tracer to become increasingly divorced from the main flow, in a body of water that is much larger than that available in pre threshold mixing. This results in a greater magnitude of dispersion being attained within a chamber that has a post threshold surcharge.



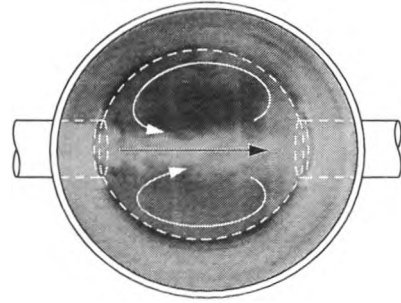
3 Seconds after entry into manhole chamber.



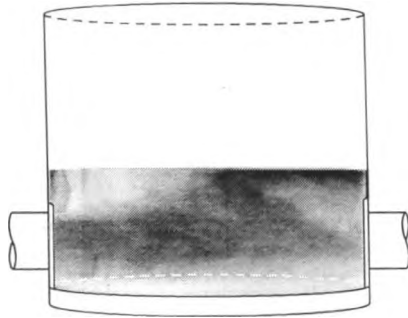
6 Seconds after entry into manhole chamber.



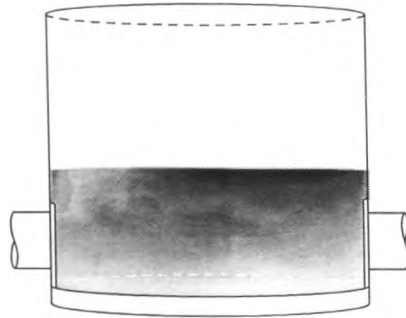
9 Seconds after entry into manhole chamber.



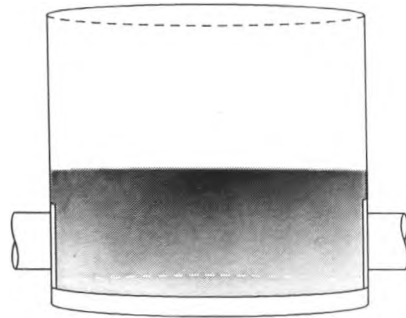
15 Seconds after entry into manhole chamber.



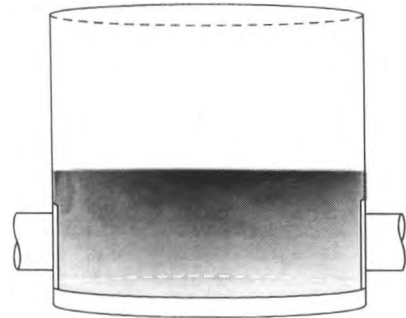
(a)



(b)



(c)



(d)

Figure 3.7 Composite image of dispersive mechanisms in a pre threshold surcharged manhole (Discharge = $2.10 \times 10^{-3} \text{m}^3 \text{s}^{-1}$, Surchage = 37.4mm)

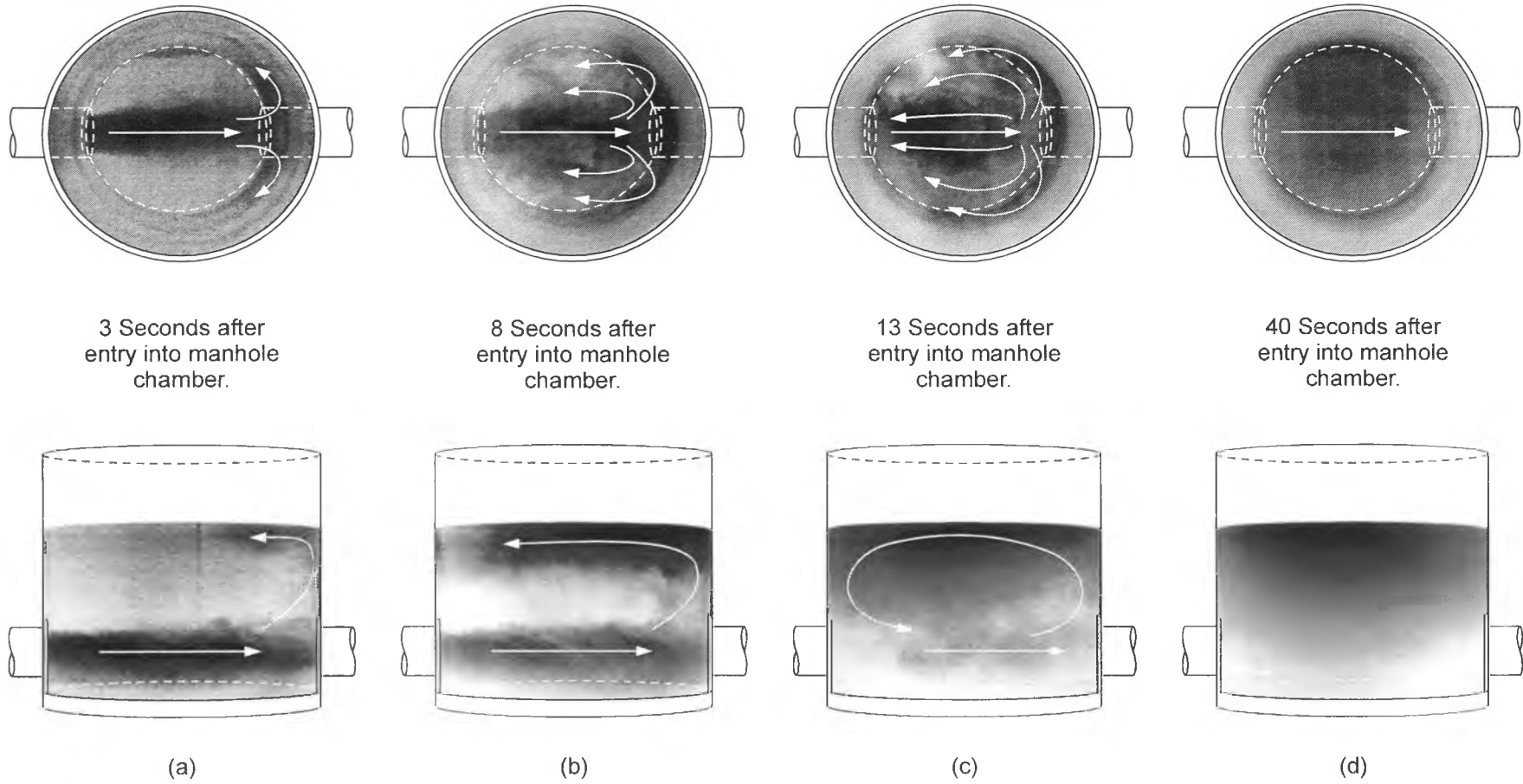


Figure 3.8 Composite image of dispersive mechanisms in a post threshold surcharged manhole
(Discharge = $2.06 \times 10^{-3} \text{m}^3 \text{s}^{-1}$, Surchage = 134.3mm)

As previously stated, the trends within the data, before and after the surcharge threshold exhibit a primary dependency on the discharge and not the surcharge. Consequently, surcharge averaged data can be examined for each of the manhole configurations. The data has been separated into results that are greater than or less than the surcharge threshold. As with the straight pipe, a dispersion coefficient due to the turbulent dispersion is under scrutiny. To determine the magnitude of the dispersion coefficient a linear regression that passes through the origin has been fitted to the data. This assumption is obviously not totally correct. Even if there was no flow, the tracer would still spread under molecular diffusion, thus causing an intercept with the y-axis that would be greater than zero. However, dispersion due to shear flow is several orders of magnitude greater than molecular diffusion (molecular diffusion within water ranges from 0.5×10^{-9} to $2.0 \times 10^{-9} \text{ m}^2 \text{ s}^{-1}$, Rutherford (1994)), thus any errors incurred due to this approximation will be negligible.

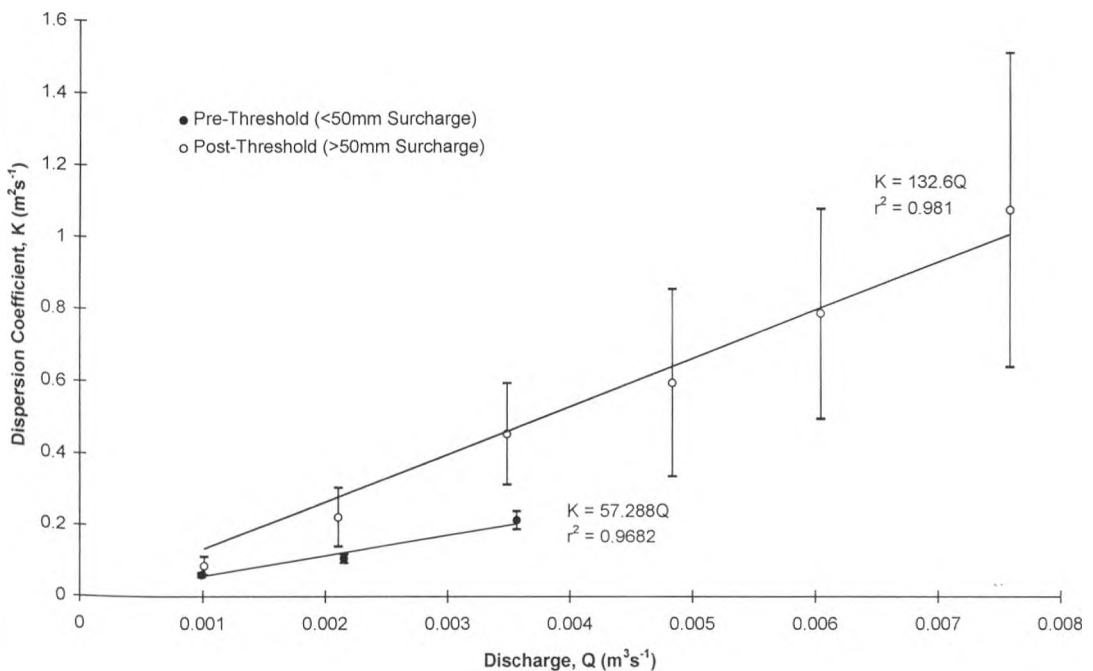


Figure 3.9 Dispersion coefficient for 400mm diameter chamber, before and after surcharge threshold.

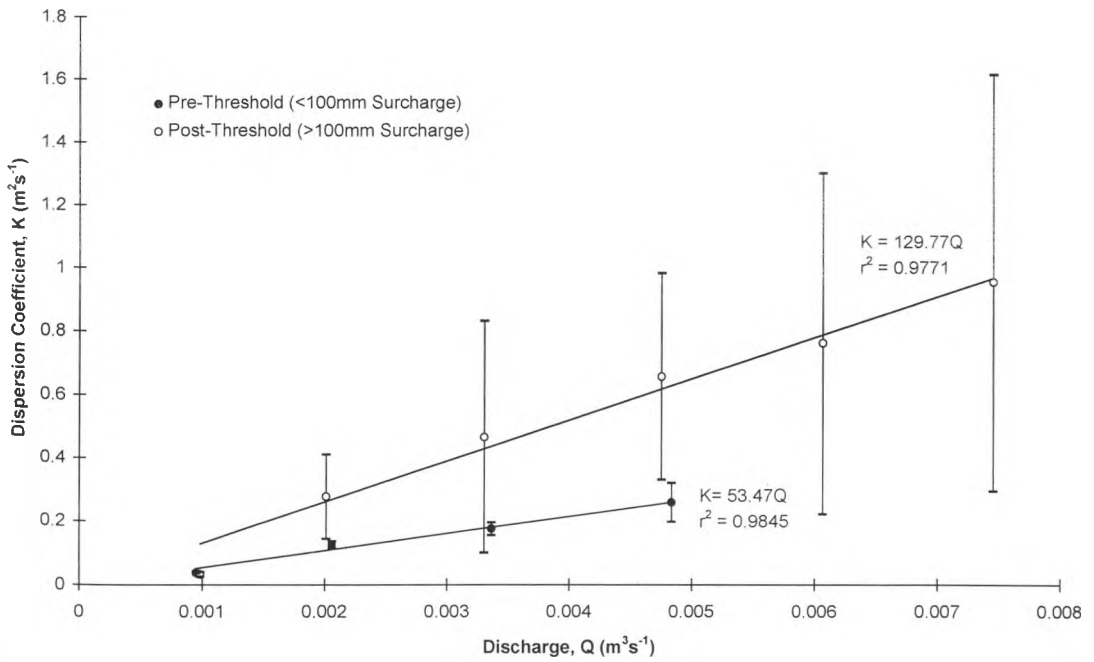


Figure 3.10 Dispersion coefficient for 500mm diameter chamber, before and after surcharge threshold.

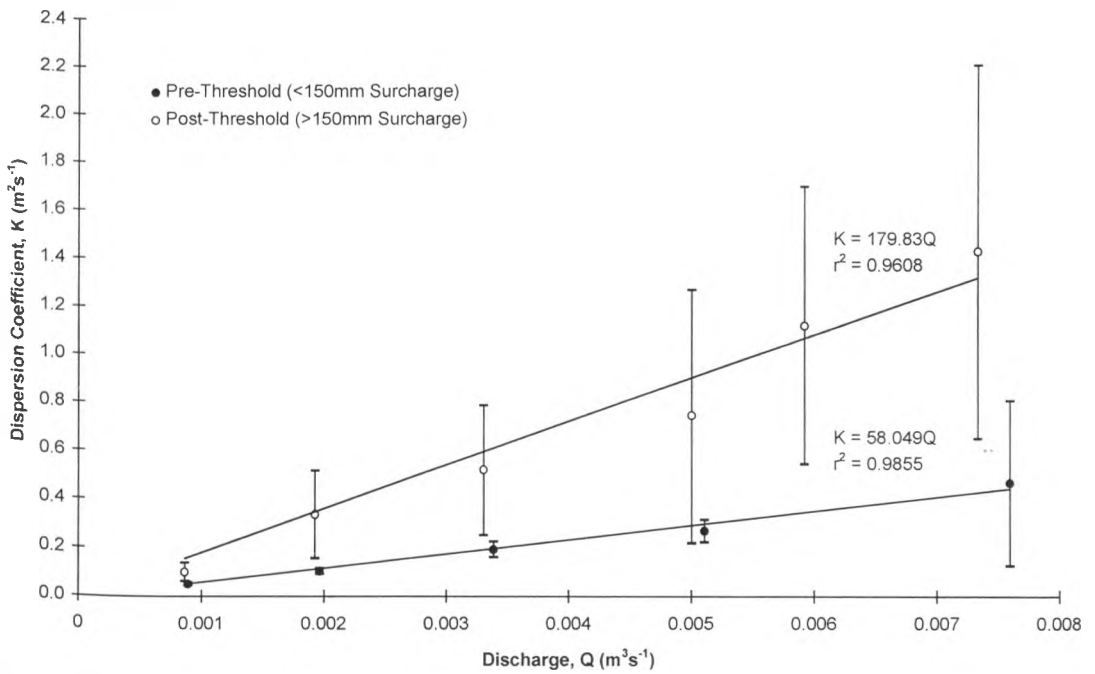


Figure 3.11 Dispersion coefficient for 600mm diameter chamber, before and after surcharge threshold.

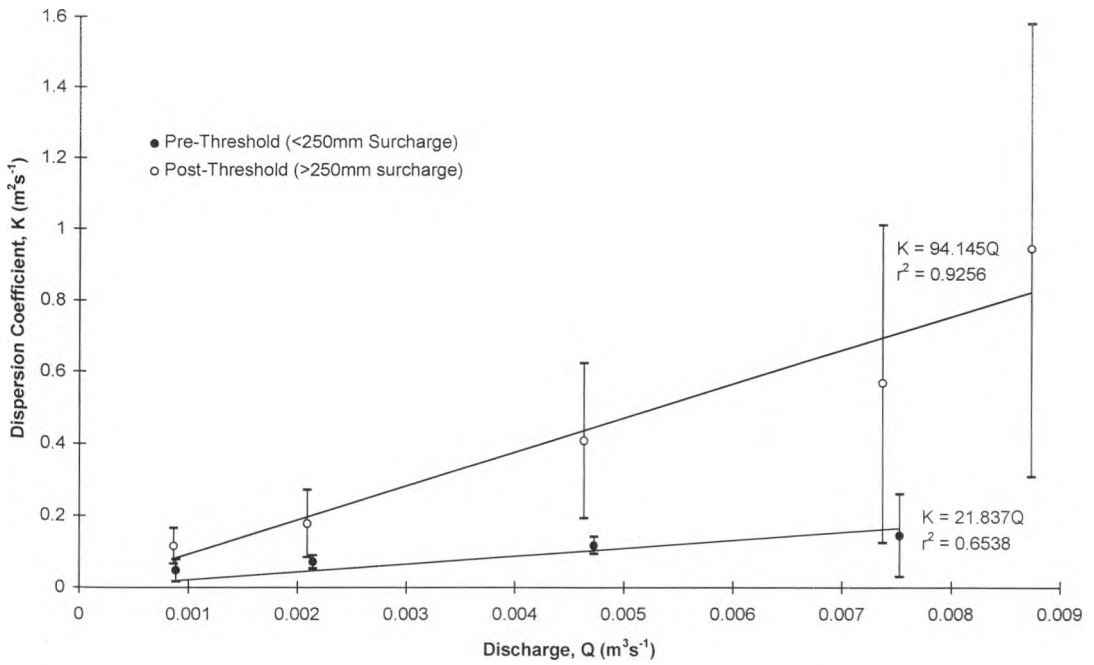


Figure 3.12 Dispersion coefficient for 800mm diameter chamber, before and after surcharge threshold.

From observing the variation of the dispersion coefficient with discharge (Figures 3.9, 3.10, 3.11 and 3.12), trends can be seen between the different chamber diameters. In the case of pre-threshold dispersion (indicated by the solid circles), it is evident that the magnitude of the dispersion is less than that found in post-threshold cases (indicated by hollow circles), for all chambers tested. As has been previously stated, there are fewer pre-threshold results for the 400mm chamber (Figure 2.16 and 3.6(a)) than any other chamber due to the low value of the surcharge threshold. This however, does not seem to have had an influential effect on the results. A possible reason for this is because within the pre-threshold dispersion coefficient, there is very little fluctuation in the results over the range of surcharges examined. Therefore, although there are few results for the 400mm chamber, the results that were obtained lie close to the average value that would be expected.

Data from the pre-threshold 800mm chamber is seen to give consistently lower results than all other chambers tested (Figure 3.13). Nevertheless, more pre-threshold tests were carried out on this chamber than any other. However it can also be seen from Figure 3.12, the regression

through the pre-threshold data predicts the lowest correlation coefficient out of all the manholes tested. This is due to the fact that the regression line has been fitted through the origin. If instead the regression is allowed to intercept with the y-axis, the correlation coefficient increases to 0.977. This indicates two possibilities, either that there are limitations within the test facility and sampling equipment as previously postulated in Section 3.2.1, or that the mechanisms of mixing within the manhole have differed from all the previous cases. The latter would be the case if the diameter of the manhole were great enough to allow the submerged jet seen in Figures 3.7 and 3.8 to decay totally within the chamber. This would initially become evident at the lower discharges due to the lower momentum of the jet. As a result, there would be an increase in the magnitude of the dispersion at the lower discharges. Thus a linear regression through the data would tend to result in an intercept with the y-axis that is greater than zero. More accurately, as the discharge approaches zero, the magnitude of the dispersion will become governed by molecular diffusion. As previously stated, this will mean that the spread of the tracer will tend towards 0.5×10^{-9} to $2.0 \times 10^{-9} \text{m}^2 \text{s}^{-1}$ as the discharge tends towards zero.

In comparison, the results of the post-threshold dispersion coefficients for the 800mm chamber (Figure 3.12) are also relatively low in comparison to all other chambers tested (Figures 3.9, 3.10 and 3.11). However, as illustrated by Figures 2.27 and 3.6, there is only a small data set on which to base this assumption. Moreover, a comparison between the results found for the 800mm chamber (Figure 2.27) with those found for all other chambers (Figures 2.16 2.19 2.23 and 2.31) suggests that the former has yet to reach a peak in the magnitude of the dispersion. It is therefore probable that the dispersion coefficient is still in the process of rising. Due to constraints within the test facility, it was impossible to test higher surcharges, therefore it was impossible to verify this claim.

From the evidence it can be seen that the results of the dispersion coefficient for the 800mm chamber, with a post threshold surcharge, are lower than the results for all other chambers. It has also been elucidated that this data may not be fully representative of the maximum magnitude in dispersion coefficient available within the chamber. As a conclusion, it is deemed unwise to include the 800mm post threshold results when calculating an expression for an average dispersion coefficient for all the chambers.

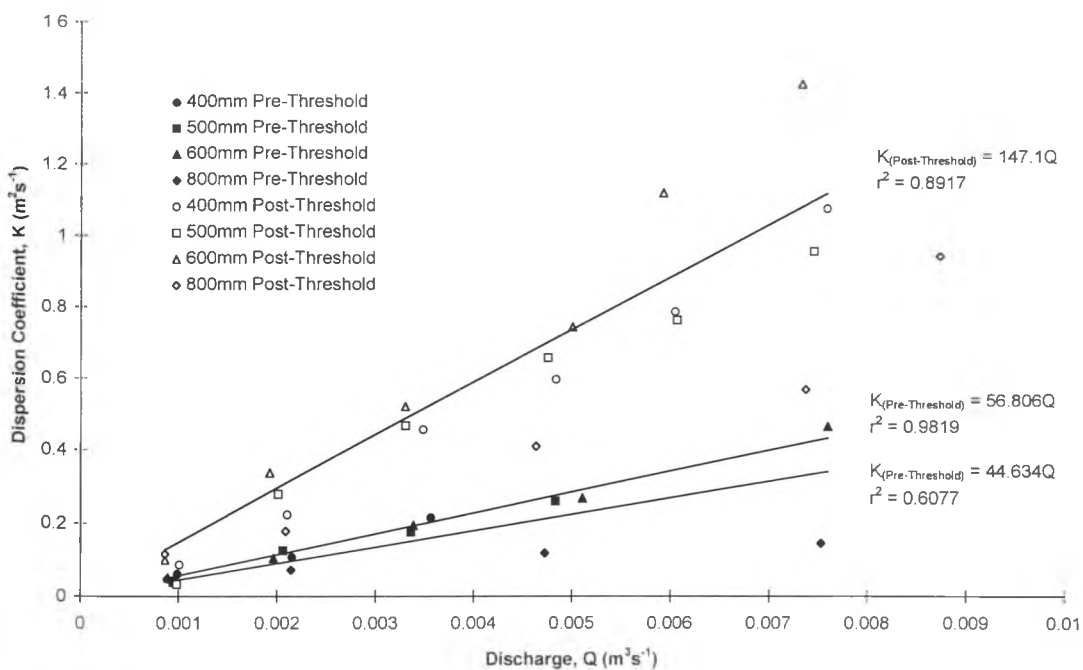


Figure 3.13 Summary of dispersion coefficients for all chamber diameters.

A general predictive formula for the dispersion coefficient as a function of discharge and independent of chamber diameter can be developed for both the pre and post-threshold surcharges. Figure 3.13 depicts a summary of all the pre and post threshold data. A linear regression through all but 800mm pre-threshold data results in the following relationship.

$$K_{(\text{Pre-threshold})} = 56.8Q \quad (3.9)$$

Where -

K = Dispersion coefficient (m^2s^{-1}),

Q = Discharge (m^3s^{-1}),

The correlation coefficient between this prediction, and the measured data is 0.982. If the 800mm pre-threshold data is included in the determination of the regression then the relationship between the dispersion coefficient and discharge is as follows.

$$K_{(\text{Pre-threshold})} = 44.6Q \quad (3.10)$$

As can be seen, the effect of including this data has lowered the constant of proportionality of the prediction. However, the correlation coefficient has also reduced to 0.608. It is therefore assumed that equation 3.9 provides a more robust solution when predicting pre-threshold dispersion coefficients.

For the post-threshold dispersion coefficient, reason has already been given for the exclusion of the 800mm data. Thus a linear regression through the remaining data sets yields the relationship,

$$K_{(\text{Post-threshold})} = 147.1Q \quad (3.11)$$

which has a correlation coefficient of 0.892.

Using equation 3.8 to determine the threshold level, and equations 3.9 and 3.11, it is possible to determine an approximate value for Taylor's dispersion coefficient.

3.3 Results to the Aggregated Dead Zone Model

3.3.1 Straight Pipe

In contrast to the Taylor's advective dispersion equation (ADE), the aggregated dead zone (ADZ) model (Section 1.3.2) does not owe its evolution to pipeline flow. Designed as a practical solution to the riverine transport of a solute, it is intended to compensate for the failings of the Taylor approach by accommodating for irregularities in the flow regime.

Although no direct comparison is made between the ADZ results for a straight pipe and a manhole chamber, the straight pipe results will be used in a comparison between the ADZ and the ADE (Section 3.4).

From Figure 3.14, it can be seen that two different forms of regression have been fitted to the data sets. The power relationship is depicted by the solid line, whilst the dashed line represents an exponential regression. From application in previous riverine studies, the power law is commonly used to formulate the regression through sampled data (Wallis, Young & Beven (1987)). Although the power relationship provides an adequate fit to the data, it does

not necessarily hold that it is a valid relationship for the manhole chambers. An exponential regression has therefore also been fitted to all of the data. Clearly this regression line will only provide an approximation because rather than tending towards infinity as the discharge tends towards zero, this regression line will intercept with the y-axis. However the exponential regression does provide an adequate representation of the data within the range of discharges tested.

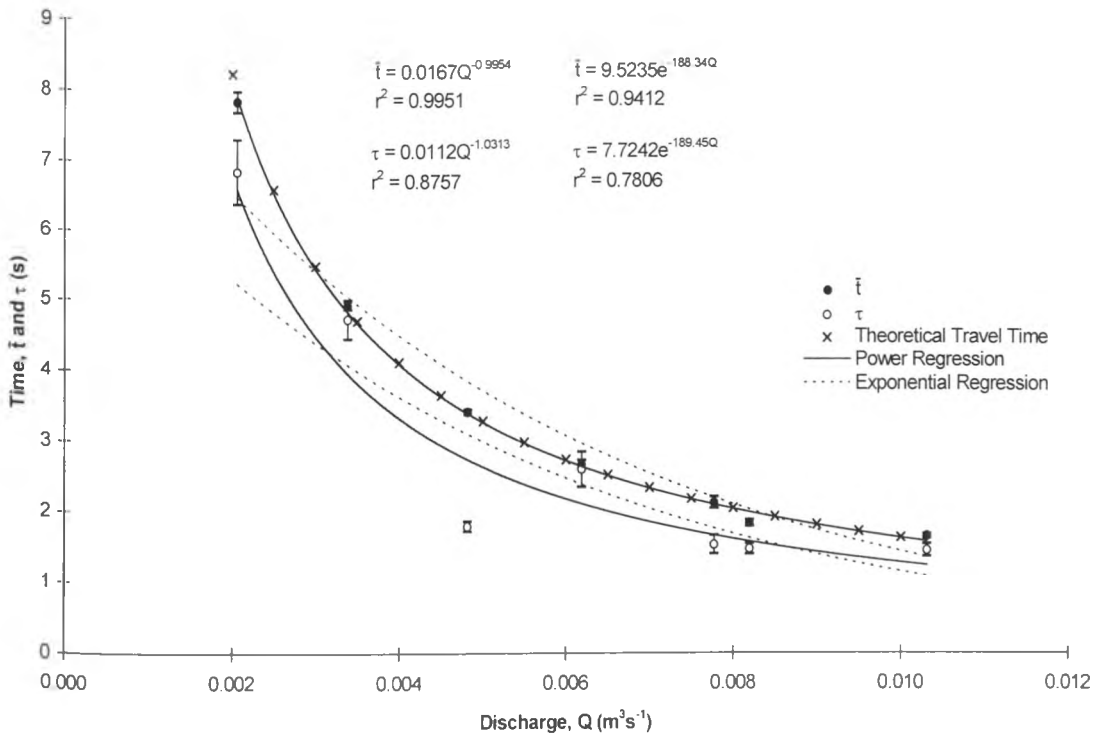


Figure 3.14 ADZ Coefficients, travel time (\bar{t}) and delay time (τ) for a straight pipe

Within any straight pipe study, the travel time (\bar{t}) should, theoretically be directly proportional to the inverse of the discharge. As can be seen in Figure 3.14, the power regression shows this to almost be the case.

3.3.2 Manhole

Through examination of the results for the travel time, \bar{t} (Figures 2.17, 2.20, 2.24 and 2.28), and delay time, τ (Figures 2.18, 2.21, 2.25 and 2.29) for a dispersing tracer, it can be seen that there are some deviations from the trends observed with the Taylor's dispersion

coefficient. The main difference is the lack of a definite threshold level in the surcharge. As the manhole diameter increases a step in the travel time starts to make itself evident in the lower discharges, but with the increase in discharge, this step diminishes. The observation of the step has not been reflected in the delay times, apart from possibly the lowest discharge through the 800mm diameter chamber (Figure 2.29). Consequently, the present study will pursue an analysis that is only dependant on discharge and independent of surcharge.

In contrast to the results of dispersion coefficient, the error bars associated with the travel time and delay time are relatively small. This would imply that even though the results appear to contain an element of scatter, each data point has a reasonable high level of confidence. This would be expected because both parameters are of first order, thus, there should be a reduction in the relative errors in comparison to those seen through the application of second moments.

To draw any relationship between the varying chamber diameters it is first necessary to determine what the relationship is between the ADZ parameters and discharge, thus eradicating all surcharge dependency from the results. As with the ADE data, this is done by determining the average values for all surcharges measured at any one discharge.

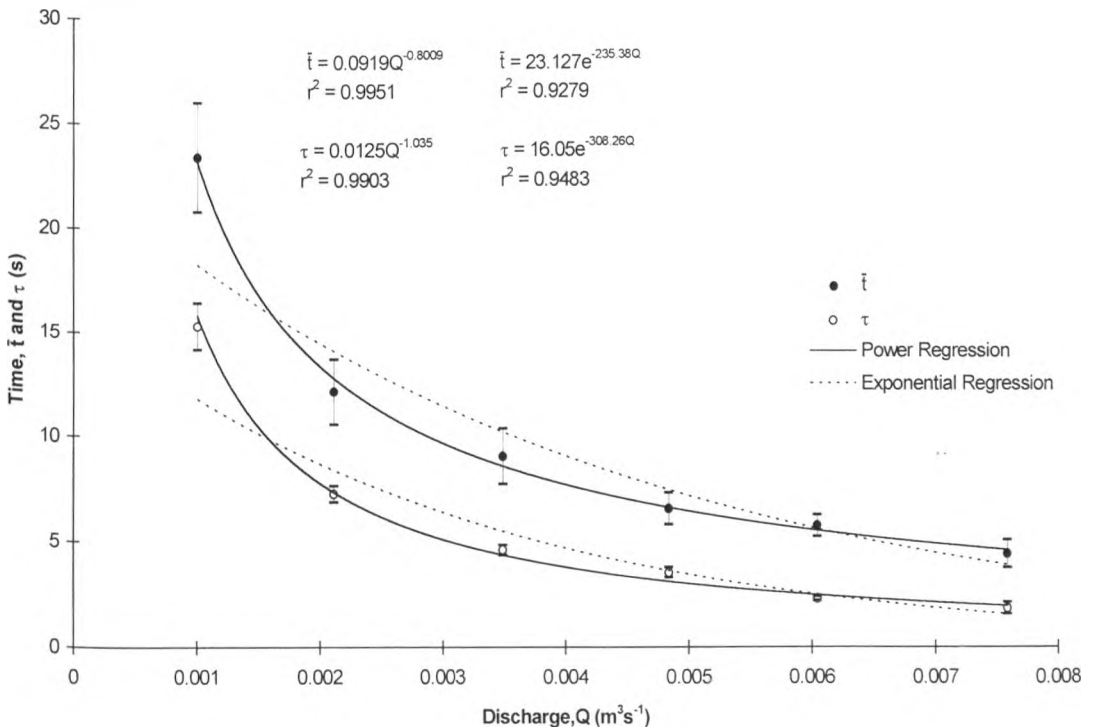


Figure 3.15 ADZ Coefficients, travel time (\bar{t}) and delay time (τ) for the 400mm chamber

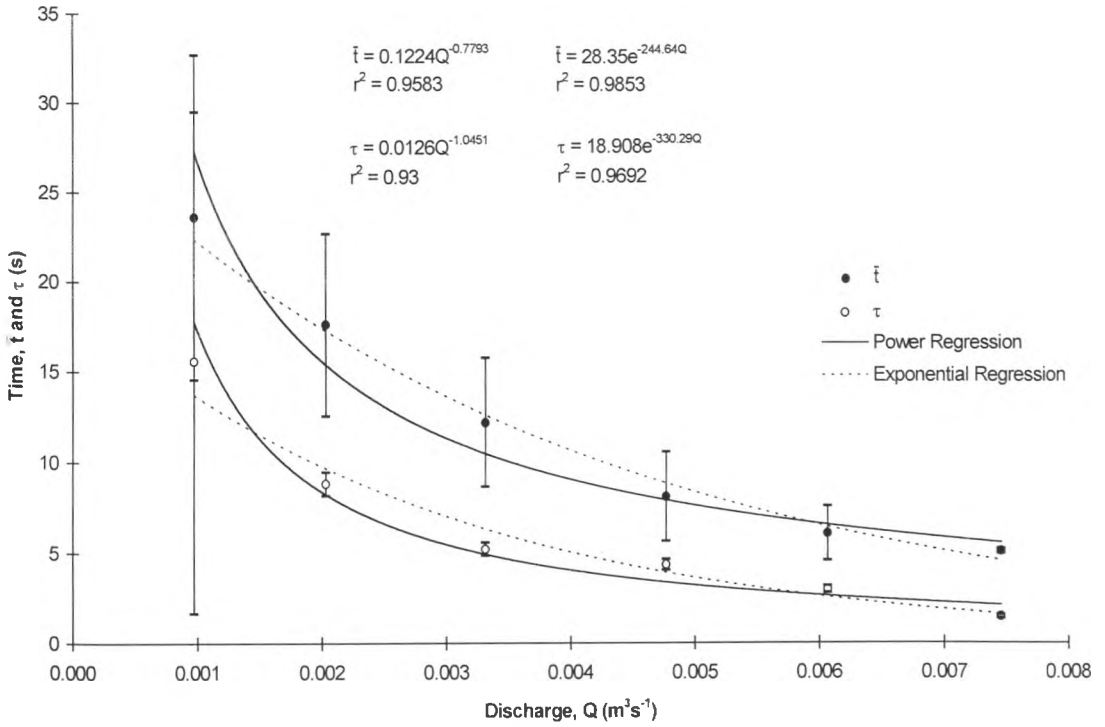


Figure 3.16 ADZ Coefficients, travel time (\bar{t}) and delay time (τ) for the 500mm chamber

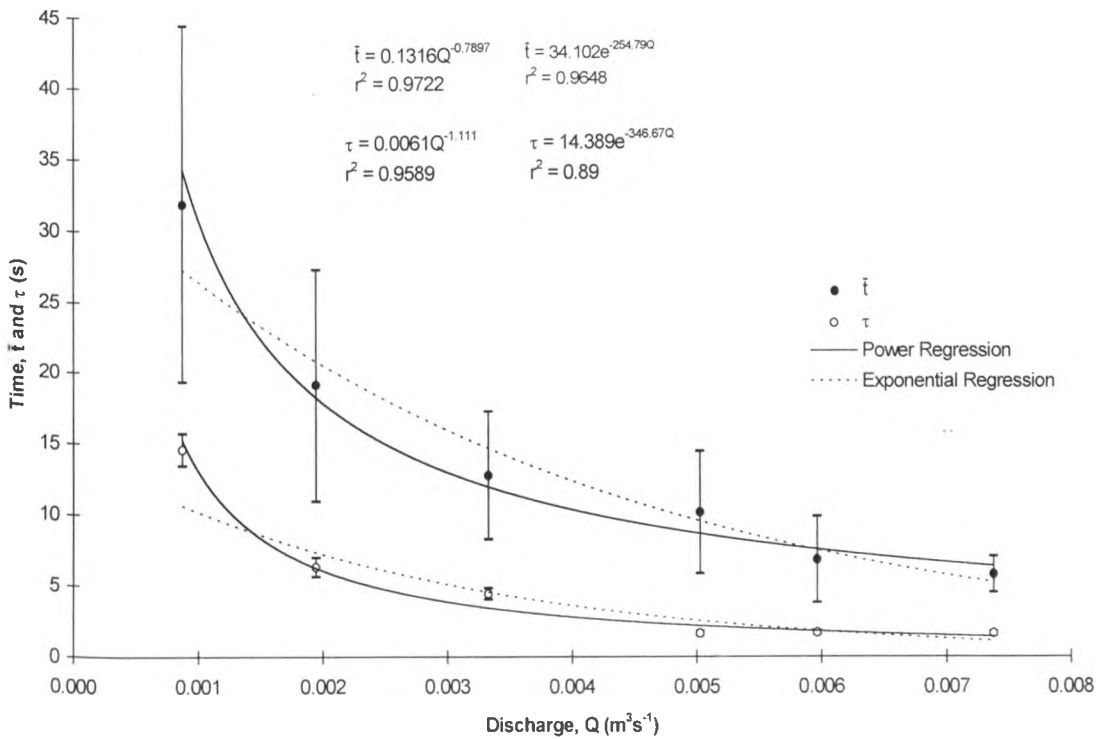


Figure 3.17 ADZ Coefficients, travel time (\bar{t}) and delay time (τ) for the 600mm chamber

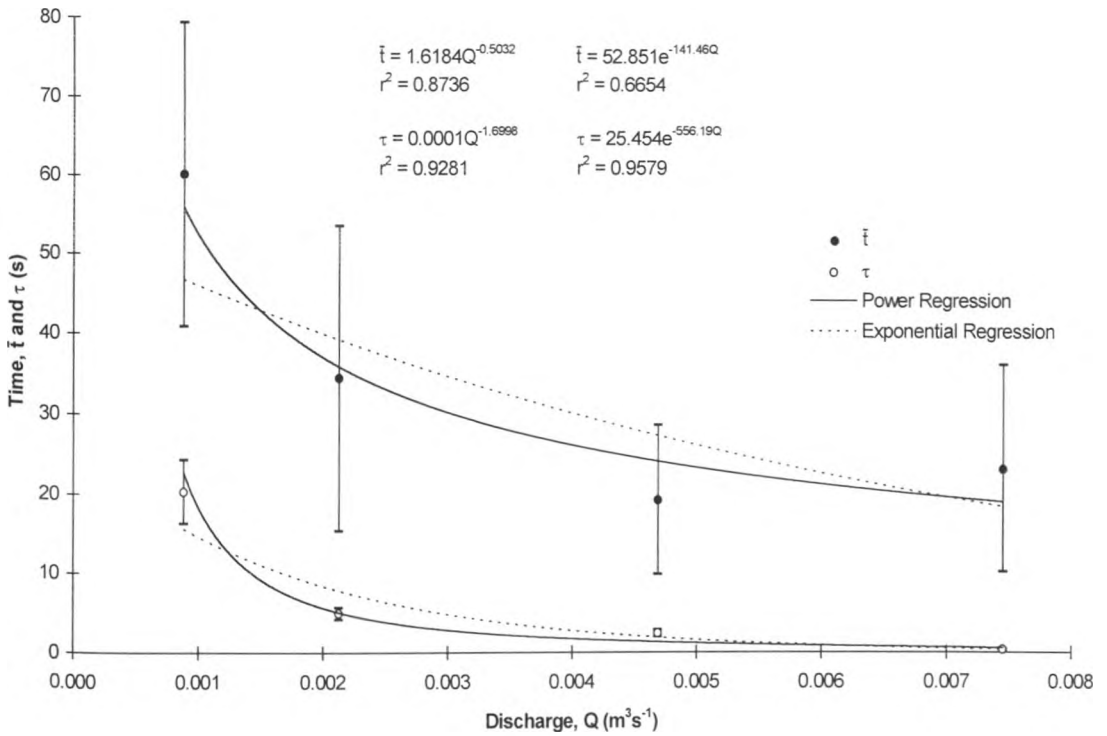


Figure 3.18 ADZ Coefficients, travel time (\bar{t}) and delay time (τ) for the 800mm chamber

From Figures 3.15 to 3.18, it can be seen that the power relationship provides an adequate approximation to the observations. However this relationship becomes more tenuous as the chamber diameter is increased.

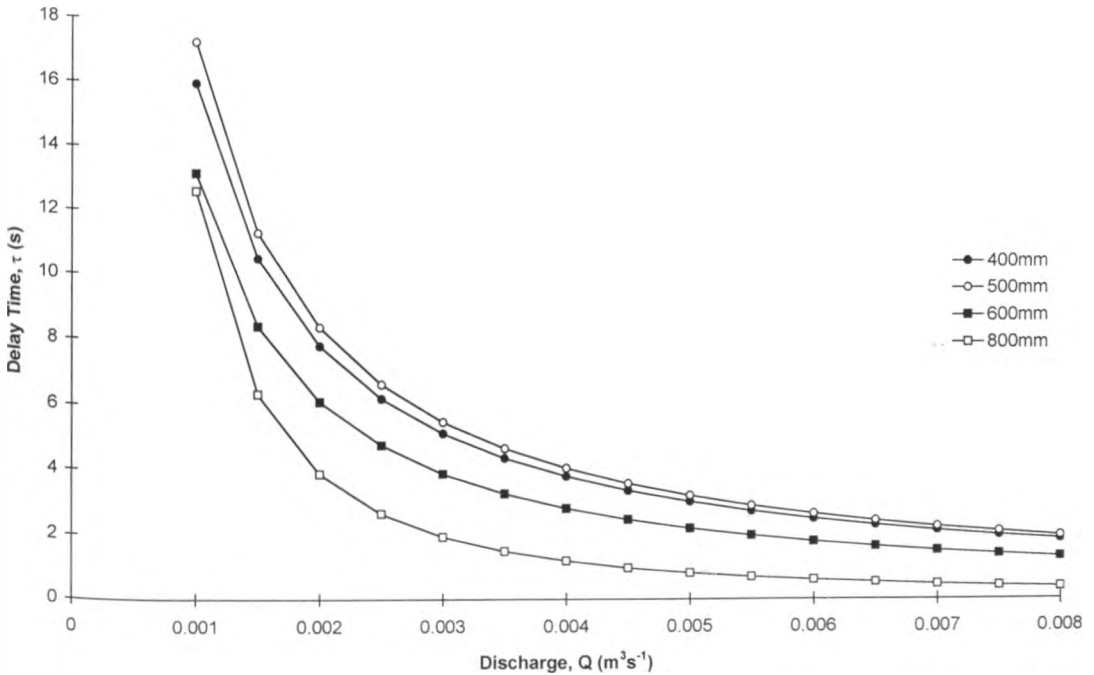


Figure 3.19 Variation of predicted delay time with discharge.

A comparison of the power relationships for the chambers tested (figures 3.19 and 3.20) show that the delay time has only minor fluctuations with the changes in the chamber diameter, whilst, the travel time is rapidly seen to increase.

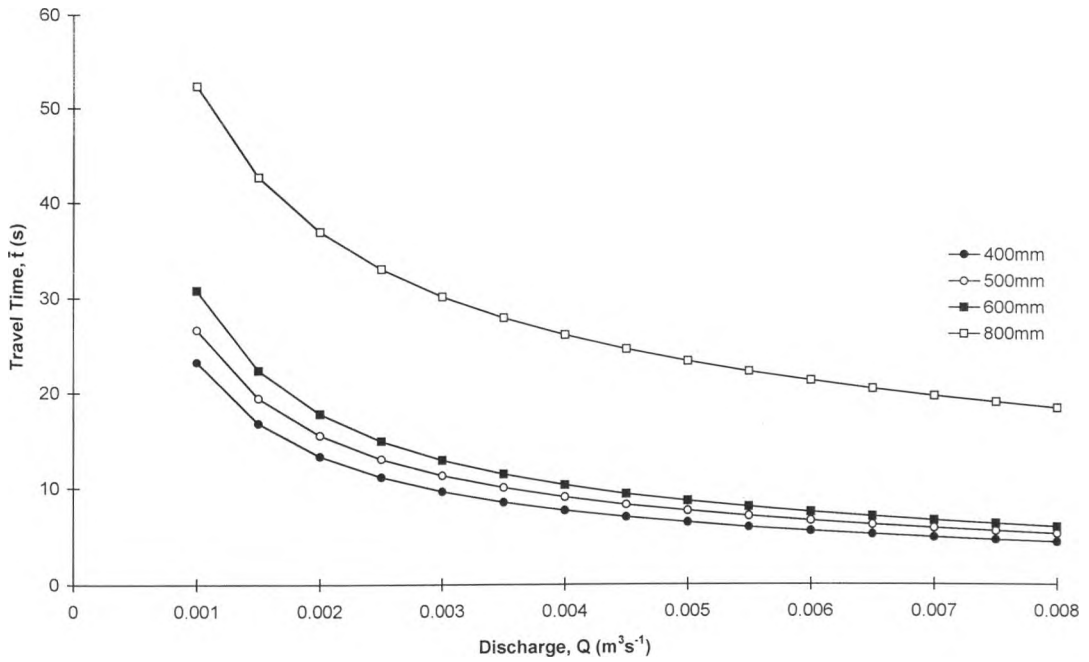


Figure 3.20 Variation of predicted travel time with discharge.

This would indicate that in general, the delay time is dependant on the discharge whilst showing an independence to the chamber diameter. This would concur with the findings of Pedersen et al (1990) who discuss a submerged jet travelling through the manhole, resulting from a proportion of the main flow that remains unimpeded as it passes through the manhole chamber. In contrast, the travel time can be seen to increase with the larger chamber diameters, whilst still exhibiting a dependency on the discharge. The increase in the travel time could be the result of the large storage volume causing a retardation in the bulk of the dispersing solute.

To unify the results from the different chamber diameters, it is possible to use an approach often used in riverine studies to compare reaches. A term known as the "dispersive fraction" is calculated for each chamber diameter (Wallis, Young & Beven (1987)). The dispersive fraction is the non dimensional ratio of the residence time (delay time (τ) minus travel time (\bar{t})) to the travel time (\bar{t}), and signifies the time spent by a tracer dispersing within a reach compared with the time the tracer has taken to pass through the reach (see Figure 1.7 and equation 1.56)

$$\gamma = \frac{T}{\bar{t}} \quad (3.12)$$

where -

γ = Dispersive fraction (-),

T = Residence time (s),

\bar{t} = Travel time (s).

By applying equation 3.12 to the results of Figures 3.15 to 3.18, a comparison of the ADZ results for the different chamber diameters can be resolved.

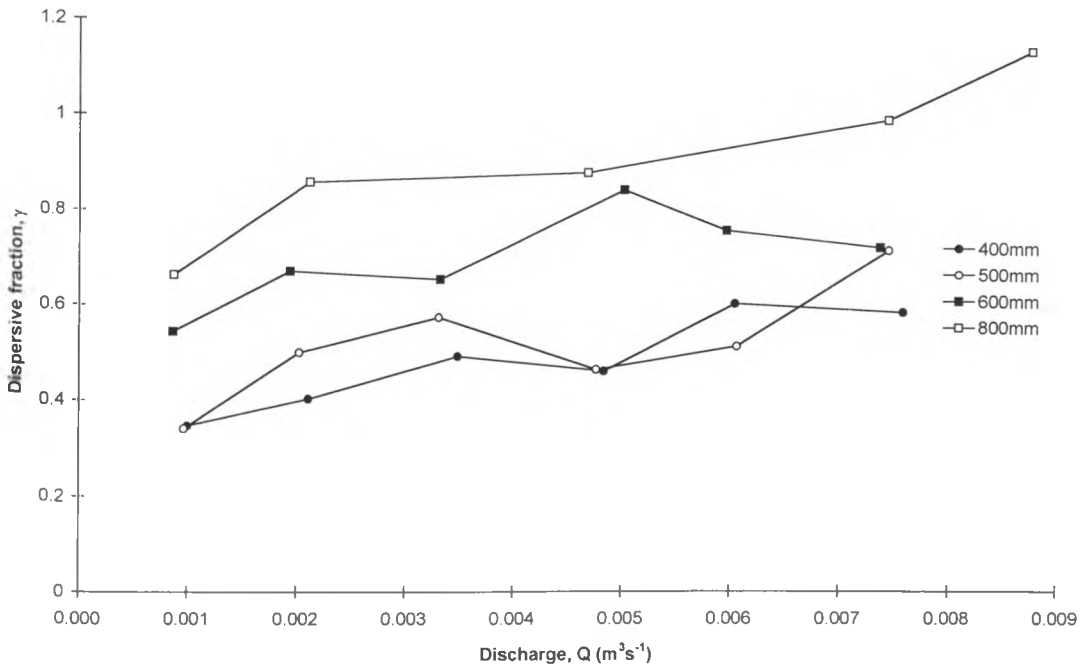


Figure 3.21 Variation of dispersive fraction (γ) with discharge for all chamber diameters

Although slightly ambiguous, there is a general increase in the dispersive fraction with the diameter of the manhole. In contrast to riverine studies, where the dispersive fraction is assumed to be constant for any single reach, Figure 3.21 suggests that there is an increase in the value at higher discharges.

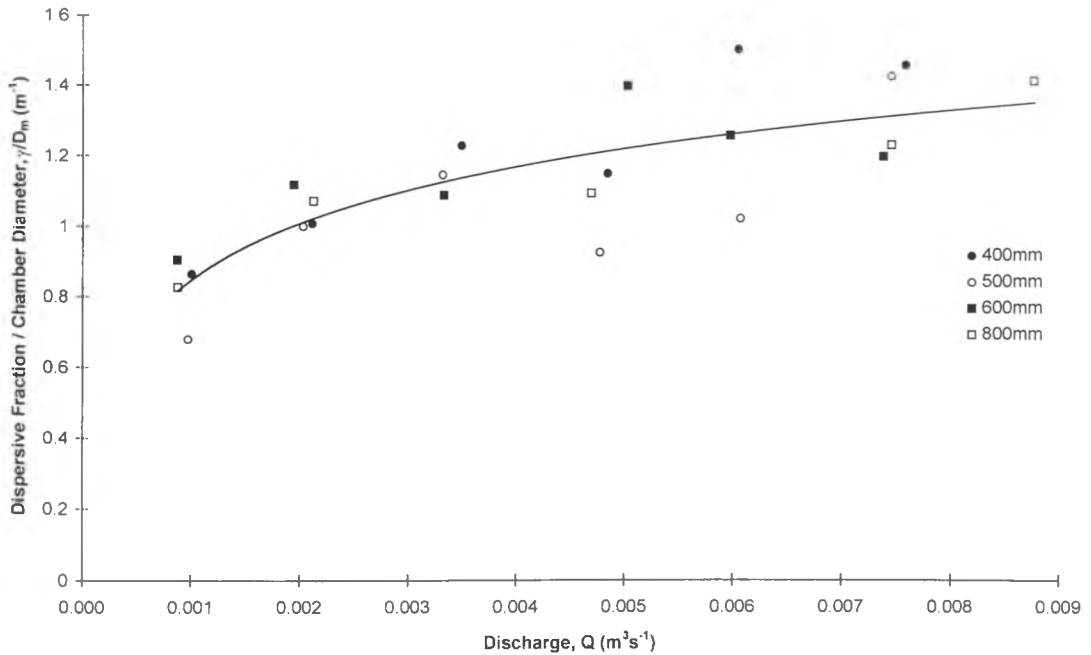


Figure 3.22 Variation of unified dispersive fraction with discharge

To account for the increase in the dispersive fraction with discharge and chamber diameter, it is desirable to form a general governing equation. An examination of the average dispersive fraction for each manhole chamber indicates that the dispersive fraction is proportional to the chamber diameter. Therefore a unified dispersive fraction (Figure 3.22) can be found by dividing the values found in Figure 3.21 by their associated chamber diameters.

From the regression through the data seen in Figure 3.22, an empirical expression for a unified dispersive fraction can be found.

$$\frac{\gamma}{D_m} = 0.2304 \log_e Q + 2.4393 \quad (3.13)$$

where -

γ = Dispersive fraction (-),

D_m = Manhole chamber diameter (m),

Q = Discharge ($m^3 s^{-1}$).

Although the correlation coefficient for the equation is only 0.6511, it is felt that this might be a product of the lack of data points. It is considered that a more in-depth study with the sole aim of formulating a more accurate unified dispersive fraction would develop a similar equation.

With the lack of data to prove otherwise, the above equation shall be assumed to yield a good approximation of a unified dispersive fraction.

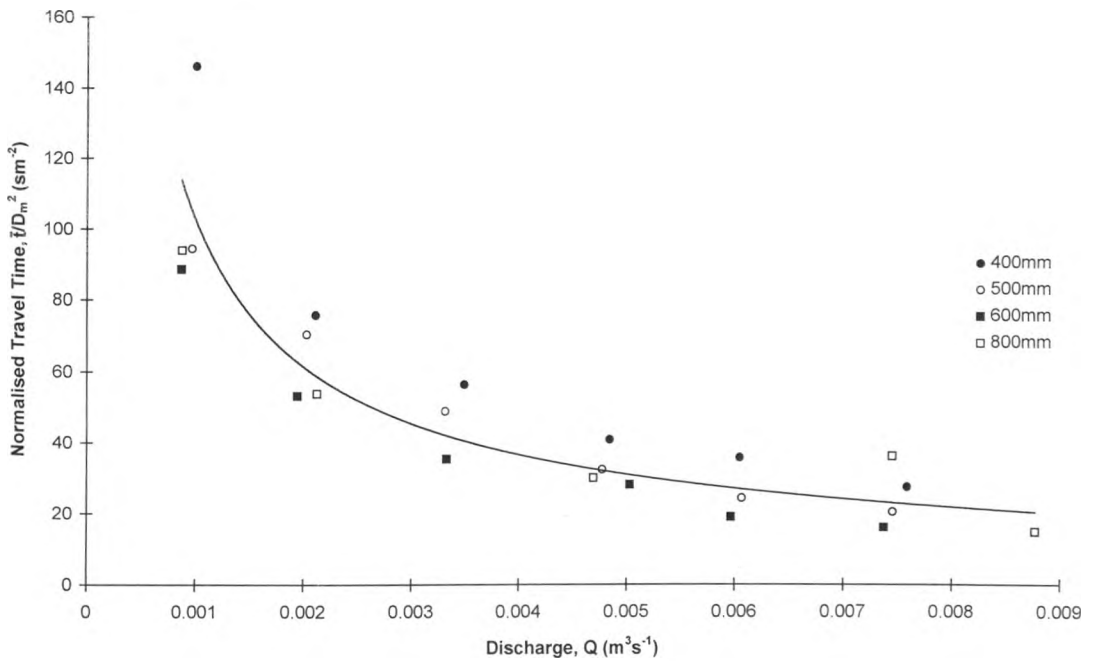


Figure 3.23 Variation of normalised travel time (\bar{t}/D_m^2) with discharge

For a prediction to be made solely from an upstream trace, there is also the need to be able to predict the travel time of a tracer as it passes downstream. As previously stated, the travel time appears to be dependant of both the chamber diameter and discharge. More accurately the travel time will be proportional to the chamber volume, however it has been illustrated that the surcharge is not a major influence on the travel times acquired from test data. As a result, the travel time is seen to be proportional to the discharge and the plan area of the manhole, which in itself is proportional to the square of the chamber diameter. Figure 3.23 illustrates the variation of a normalised travel time with discharge. The travel time has been normalised by dividing it by the square of the chamber diameter.

The regression through Figure 3.23 yields an equation that predicts the change in travel time with discharge for any chamber diameter.

$$\frac{\bar{t}}{D_m^2} = 0.5948Q^{-0.7459} \quad (3.14)$$

Through the implementation of equations 3.13 and 3.14 a prediction of a temporal concentration profile can be routed through a manhole chamber of any diameter. The only

information required to enable this prediction is the chamber diameter, the discharge and a temporal concentration profile upstream of the manhole.

3.4 Alternative Analysis – Optimal Iteration Study

3.4.1 Analysis Technique

All analysis techniques used within the current research until this section have been the application of techniques that have been implemented in previous studies. However these techniques have never previously been applied in the context of urban drainage schemes. As has been previously stated, the advective dispersion equation (ADE) technique was originally deduced to predict the dispersion of a solute flowing through a straight pipe. Likewise, the aggregated dead zone (ADZ) approach to dispersion modelling was developed to predict the spread of a tracer in natural water courses. Both of these techniques implement formulae developed to determine coefficients that are used within such modelling tools. However, these formulae owe much of their derivation to the historic development of the predictive tools themselves. It would therefore be true to say that the chance of these formulae accurately determining the coefficients required to model a drainage systems (and more notably within manhole chambers) is very slight.

The alternative methods described within this section will continue to utilise both the ADE and ADZ modelling techniques. However, this analysis will initially assume that the coefficients used within such models (i.e. travel time, \bar{t} , delay time, τ , and dispersion coefficient, K) are independent of the flow and chamber geometry. Instead of implementing any pre-determined tools or techniques to describe the modelling coefficients, they will be determined through an iterative process.

Predictions of the downstream distribution, calculated using both the ADE and ADZ techniques, shall be performed by an iterative computer program. This program will coarsely step through a broad range of modelling parameters (i.e. \bar{t} , τ and K), treating each parameter as an independent variable, and predict a downstream distribution for each step. Subsequently the predicted traces can be compared with the measured downstream profile,

and, through observing the 'best fit' between the measured and predicted data, the optimal modelling parameters can be determined. After determining an initial (rough) set of modelling parameters, the step size within the iteration can then be refined, and the data within the vicinity of the 'best fit' prediction, re-analysed. This refining process has been undertaken a further three times for each individual test performed on the manhole chambers, and each time the step size has been reduced. Analysing the data in this fashion has enabled a high level of accuracy to be attained in calculating the modelling parameters, whilst minimising the time required to undertake the analysis.

To enable the 'best fit' comparison between the measured data and the predictions found by implementing both the advective dispersion equation and the aggregated dead zone, a correlation coefficient has been determined. This correlation coefficient, often referred to as the coefficient of determination (Young, Jakeman & McMurtire (1980)), is proportional to the difference between the observed and predicted data (known as the residual) and independent of the x-axis. When calculating the coefficient of determination, neither the observed data or the predicted results are considered within a temporal frame of reference. Instead, the data is deemed to be located at integer reference locations along a non-dimensionalised x-axis.

$$R_T^2 = 1 - \frac{J_0}{\sum_{k=1}^N y_k^2} \quad (3.15)$$

where -

- R_T^2 = Coefficient of determination,
- J_0 = Sum of the squares of the residual non dimensional concentration,
- y_k = Observed non dimensional concentration at dimensionless time k.

The results of the coefficient of determination are a normalised measure of the degree to which the model explains the data. For a value of $R_T^2 = 1$, a model would predict a perfect match to the observed data. However a value of $R_T^2 \leq 0$ would indicate that a model had failed to describe the observed data.

It should be noted that the data analysed within this section is exactly the same as that examined in previous sections. Thus each data trace is actually the average of 5 individual

traces. After the current analysis was undertaken it was found that the results obtained for the 800mm manhole chamber did not concur with the results found for any of the other chambers. Indeed, for a majority of the 800mm data analysed, the coefficient of determination (R_T^2) was markedly below 0.9. Consequently, although the 800mm data has been included in representations of the results, it has not been used to elucidate any of the predictive formula for either the ADE or ADZ.

The data obtained for the straight pipe has not been re-analysed within this optimal iteration study. This is because the ADE already provides an adequate description of this scenario.

3.4.2 Optimal Iterative ADE Analysis

It should be noted that error bars have been deliberately omitted from all results plots within this study. The magnitude of these error bars (one standard deviation of the 5 data sets used to form the final temporal profiles) have already been depicted in section 2.6.

To aid in the determination of trends within the data, the previously determined 'surcharge threshold' has been superimposed onto each of the travel time / surcharge plots. It should be noted however that the value of the surcharge threshold is only an approximation rather than an absolute figure.

Some travel time plots depict a greater number of data points than their associated dispersion coefficient data sets. While undertaking the analysis it was noted that slight inaccuracies in the temporal results made little differences in the overall profiles predicted. However, any inaccuracies in the values of the dispersion coefficients manifested themselves in wildly inaccurate concentration profiles. Consequently it has been deemed that the use of travel time parameters associated with R_T^2 values as low as 0.8 are unlikely to be the cause of the inaccurate prediction in comparison to the dispersion coefficients. Thus additional temporal parameters have been included to obtain a better view of how these parameters vary with both surcharge and discharge.

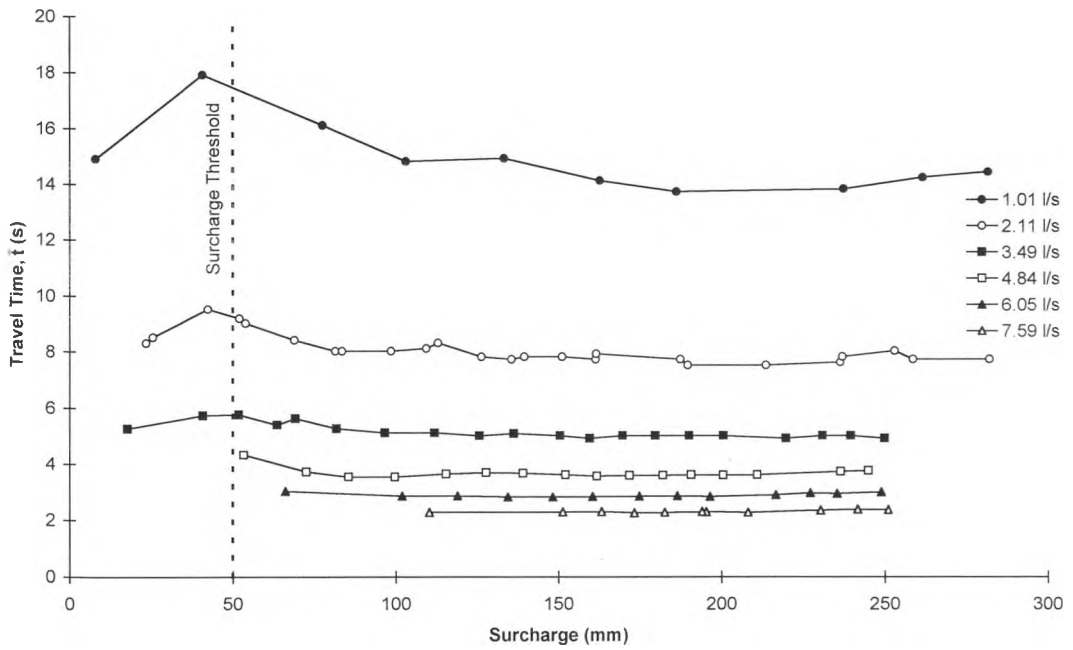


Figure 3.24 Variation in optimised travel time with surcharge for the 400mm chamber diameter.

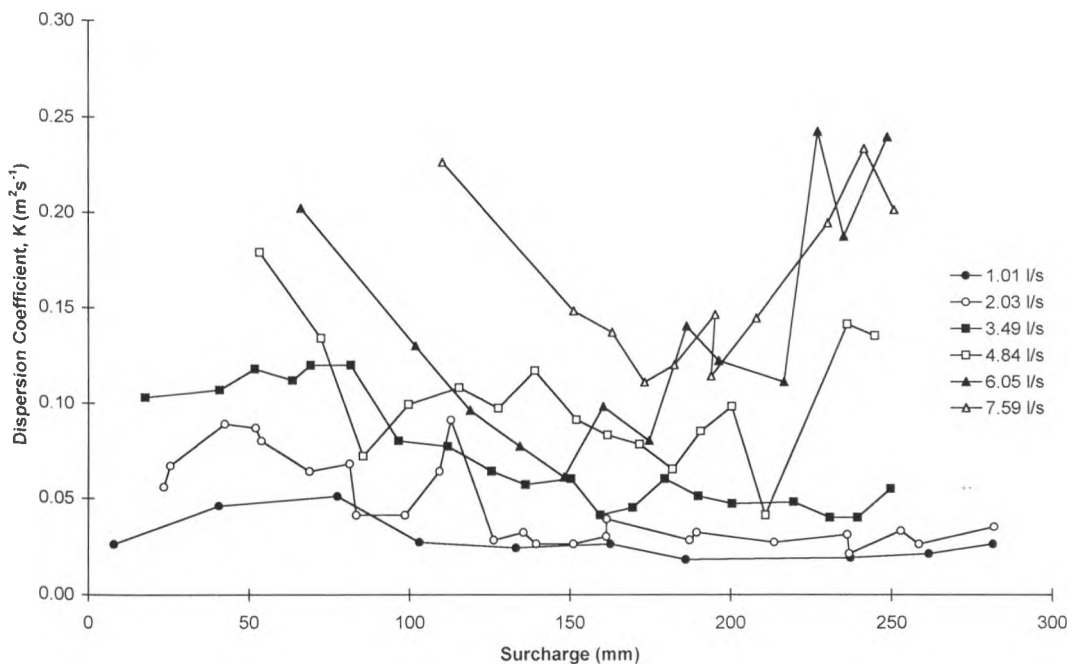


Figure 3.25 Variation in optimised dispersion coefficient with surcharge for the 400mm chamber diameter.

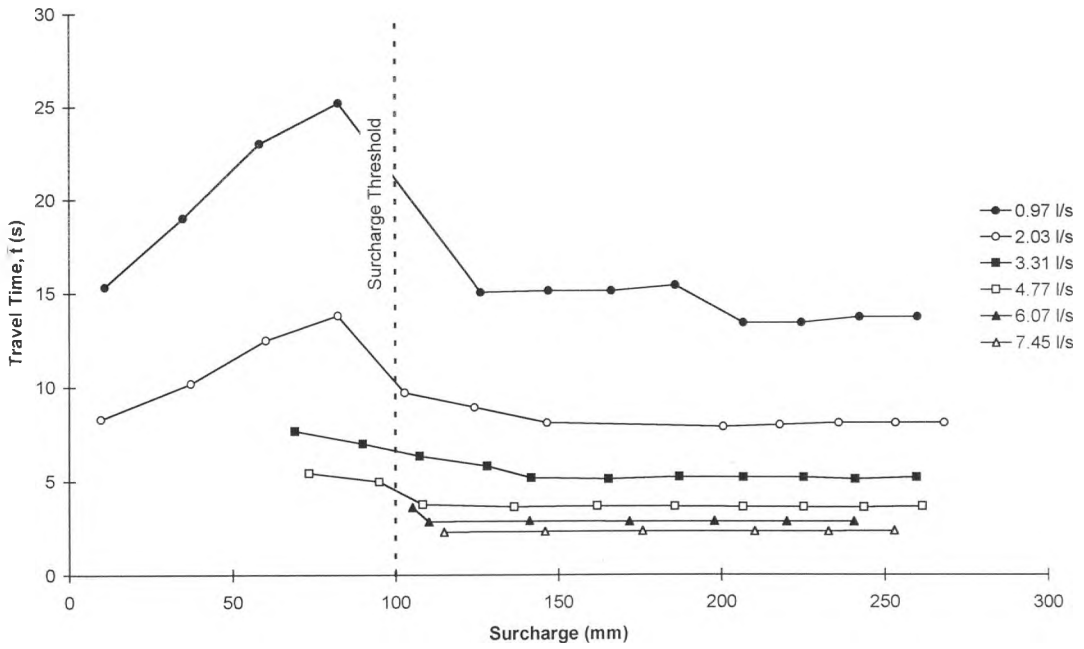


Figure 3.26 Variation in optimised travel time with surcharge for the 500mm chamber diameter.

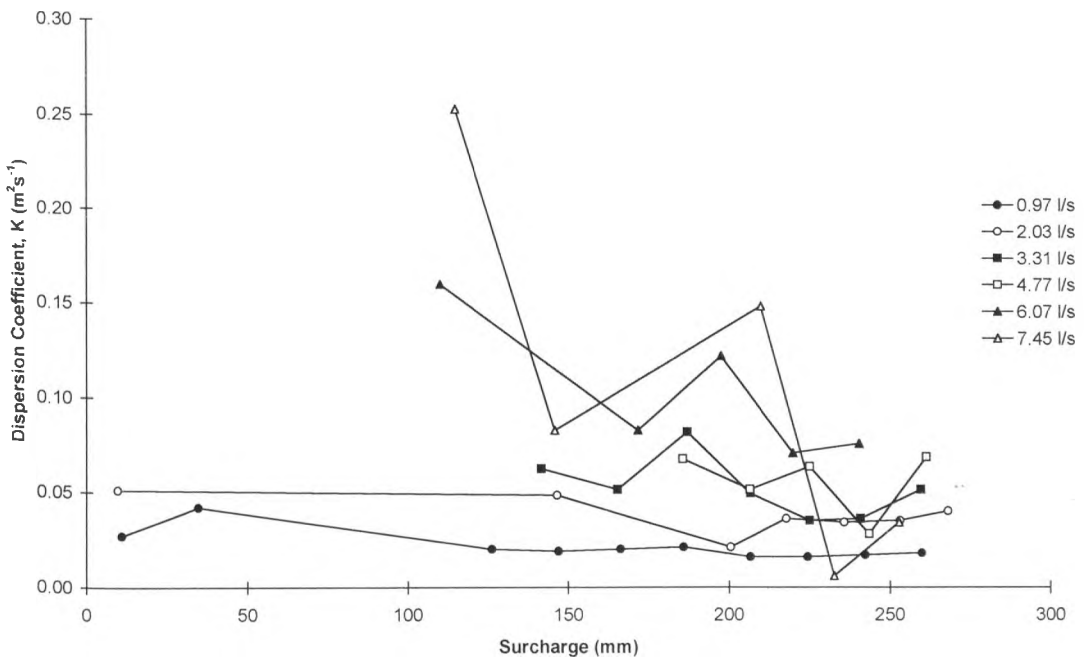


Figure 3.27 Variation in optimised dispersion coefficient with surcharge for the 500mm chamber diameter.

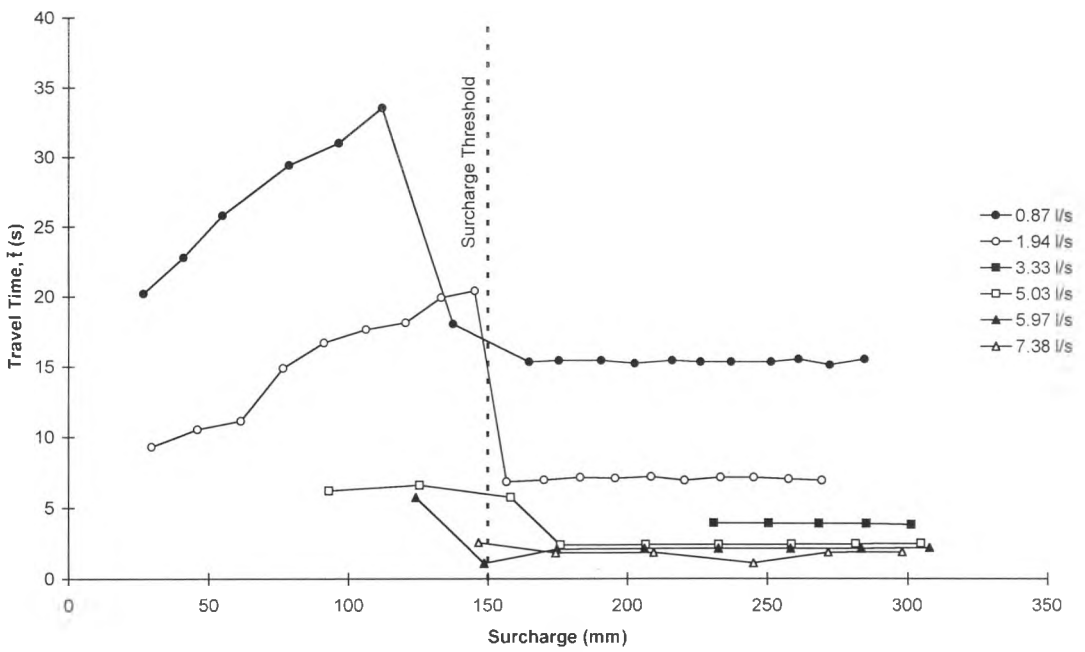


Figure 3.28 Variation in optimised travel time with surcharge for the 600mm chamber diameter.

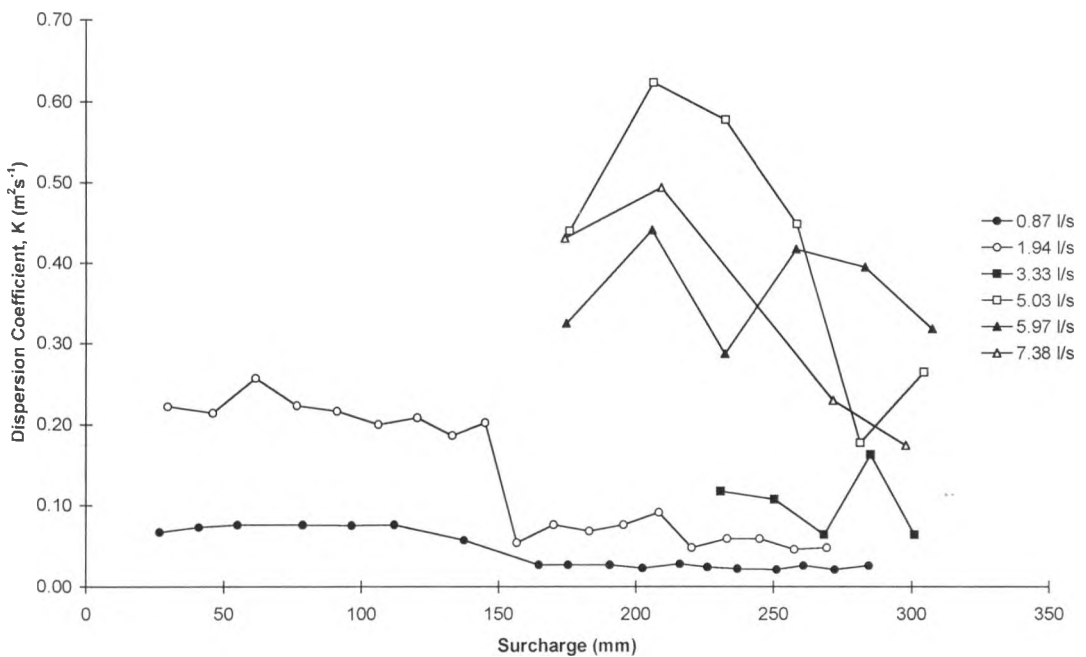


Figure 3.29 Variation in optimised dispersion coefficient with surcharge for the 600mm chamber diameter.

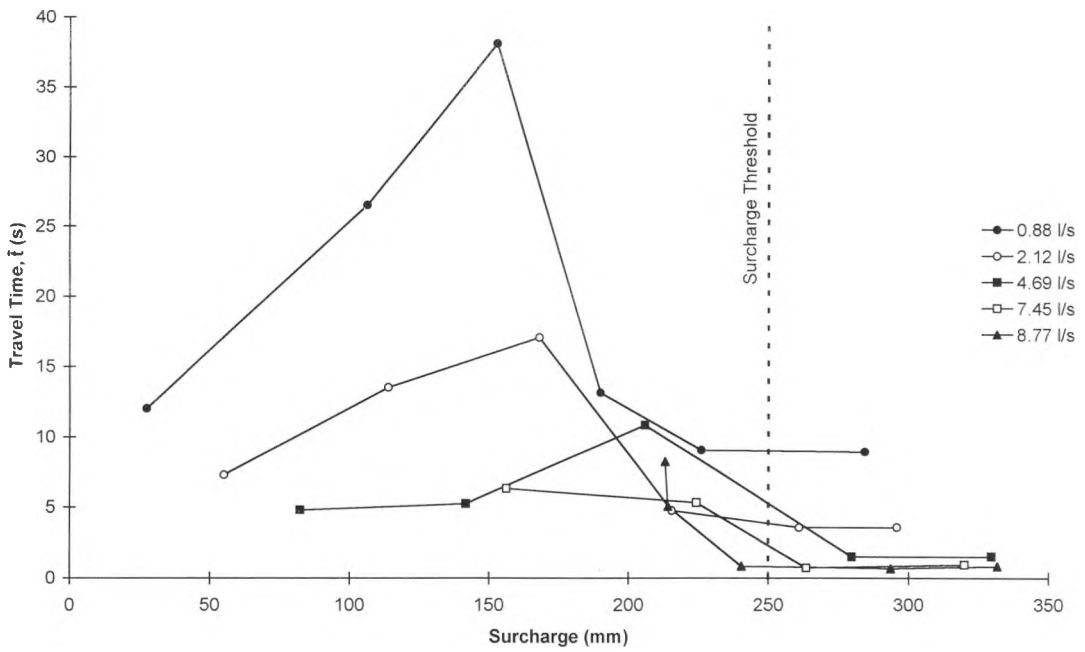


Figure 3.30 Variation in optimised travel time with surcharge for the 800mm chamber diameter.

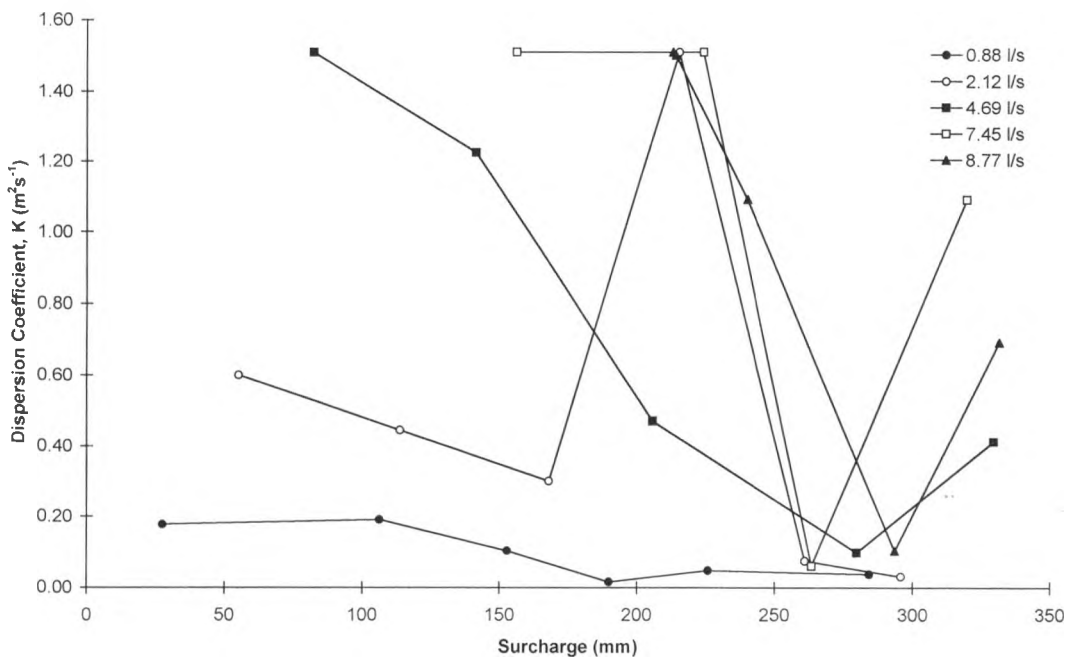


Figure 3.31 Variation in optimised dispersion coefficient with surcharge for the 800mm chamber diameter.

A general perusal of the results highlights several departures from the standard ADE analysis. With respect to the dispersion coefficients, the data is unfortunately not sufficiently detailed in surcharge intervals to conclude if the threshold level coincides with any major fluctuations in these results (Note: Data with unrepresentative R_T^2 values lower than 0.8 have been omitted). In contrast, with the standard ADE analysis, there was a strong indication that the threshold level corresponded to a substantial increase in the dispersion coefficient.

The optimal travel times determined through the iterative analysis exhibit a radical change within the vicinity of the of the threshold level. Prior to the threshold the travel times appear to increase proportionally with the surcharge. However, once the threshold limit has been attained the travel time rapidly declines to a plateau after which there is little fluctuation. Unfortunately there is little information on which to base a conclusive study of the pre-threshold travel times. For the case of this study, because a linear variation of the travel time has been observed with respect to surcharge, a surcharge averaged travel time will be assumed to provide an adequate mean travel time. Averaging the data in this fashion will incur undesirable errors in calculating travel time for the lower surcharges, however, to enable further analysis within the current work and eventually a general predictive tool, this step is deemed necessary due to the lack of quantifiable data.

Consequently, as with the standard ADE study, the travel time and dispersion coefficient data are averaged over each surcharge to enable a more general description of the data to be produced. However, in contrast to the standard ADE study, the present study therefore assumes that the dispersion coefficient is completely independent of surcharge. Two predictions are made to depict the variations of travel time with discharge, depending on whether the surcharge is above or below the surcharge threshold. It should be noted that within the optimal iteration study, the travel time corresponds purely to the temporal transport of the dispersing pollutant which is not necessarily proportional to the mean discharge through test facility (as would be expected in a straight pipe).

From Figure 3.32 it can be observed that all travel time data (with the exception of the 800mm diameter data) follow similar trends in their inverse proportionality to discharge. However in each case, there is an observed offset between the results for each chamber diameter. Allowing for fluctuations between different test scenarios, these offsets are seen to be almost linear between each chamber diameter.

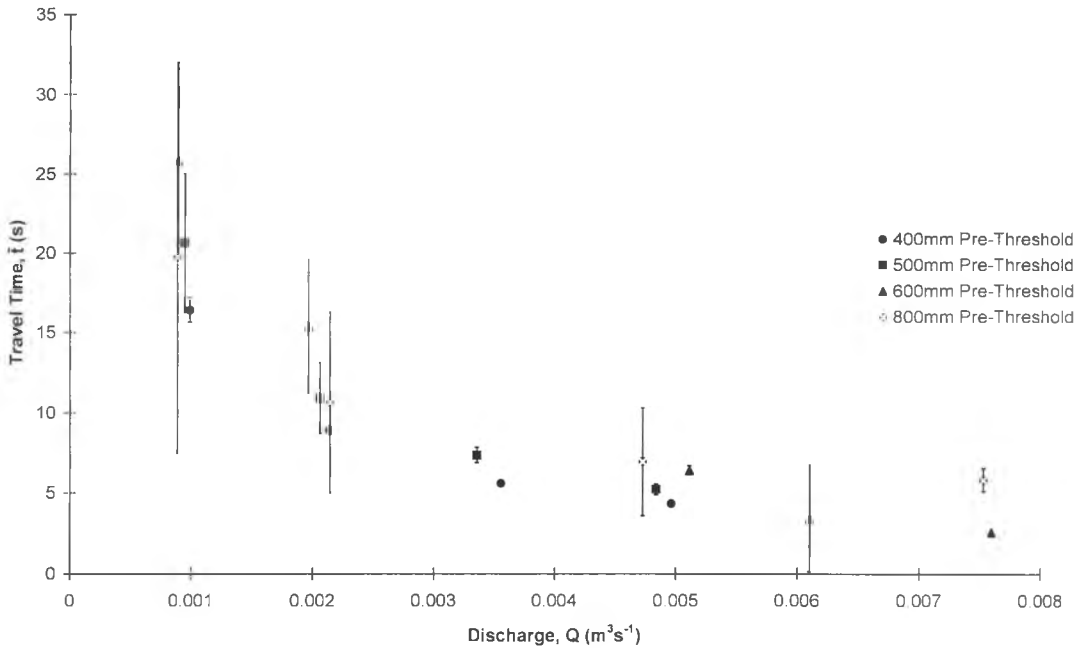


Figure 3.32 Surcharge averaged travel time prior to surcharge threshold.

To unify these results so that a single predictive equation can be formed, the data is normalised by dividing the travel by the manhole chamber diameter. The result, Figure 3.33, illustrates that this will indeed group the data, allowing a single, accurate regression to be fitted.

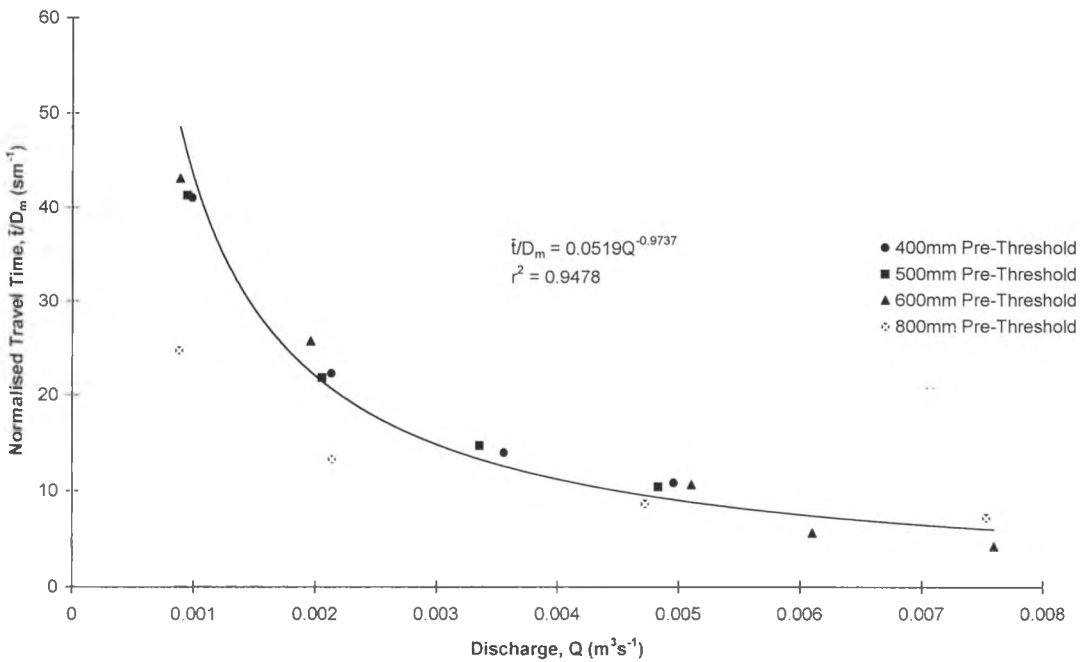


Figure 3.33 Normalised surcharge averaged travel time prior to surcharge threshold.

With regards to the post-threshold travel time, no obvious distribution, with respect to chamber diameter, is observed. Consequently, a predictive representation of this data has been formed by fitting a regression line directly to the observed data.

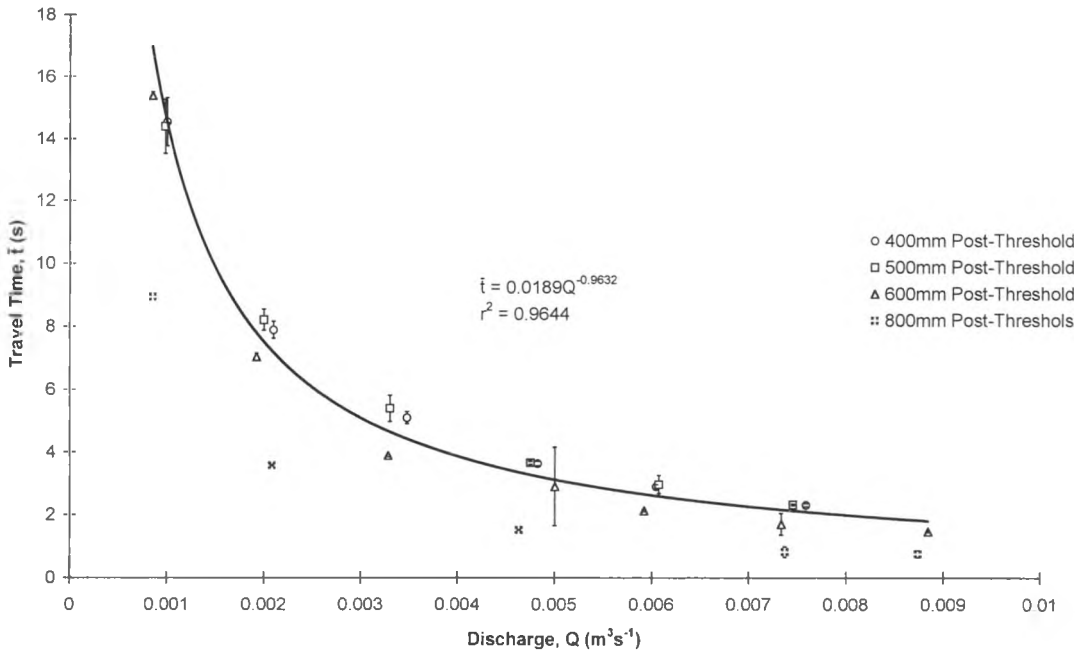


Figure 3.34 Surcharge averaged travel time after the surcharge threshold has been reached.

Figure 3.35 illustrates how the dispersion coefficient varies with discharge. As has been previously stated, minor fluctuations in the dispersion coefficient were observed to affect the shape of a prediction far greater than fluctuation in the travel time. Consequently, to endeavour to obtain a more accurate description of this relationship, only data that produced a correlation coefficient greater than 0.9 has been used to describe the dispersion coefficient results (0.85 in the case of the 800mm chamber results).

Although the results for the 800mm chamber are not being used to formulate any predictive equations, the above data encourages the view that more than one equation is required to summarise the effects of dispersion in all manhole chambers. A similarity may readily be drawn between both the 400mm and 500mm data sets. Likewise between the 600mm and 800mm data. Without further study of intermediate chamber diameters, it is impossible to say whether there is a gradual transition between chambers, or if there is a critical diameter at which the characteristics change.

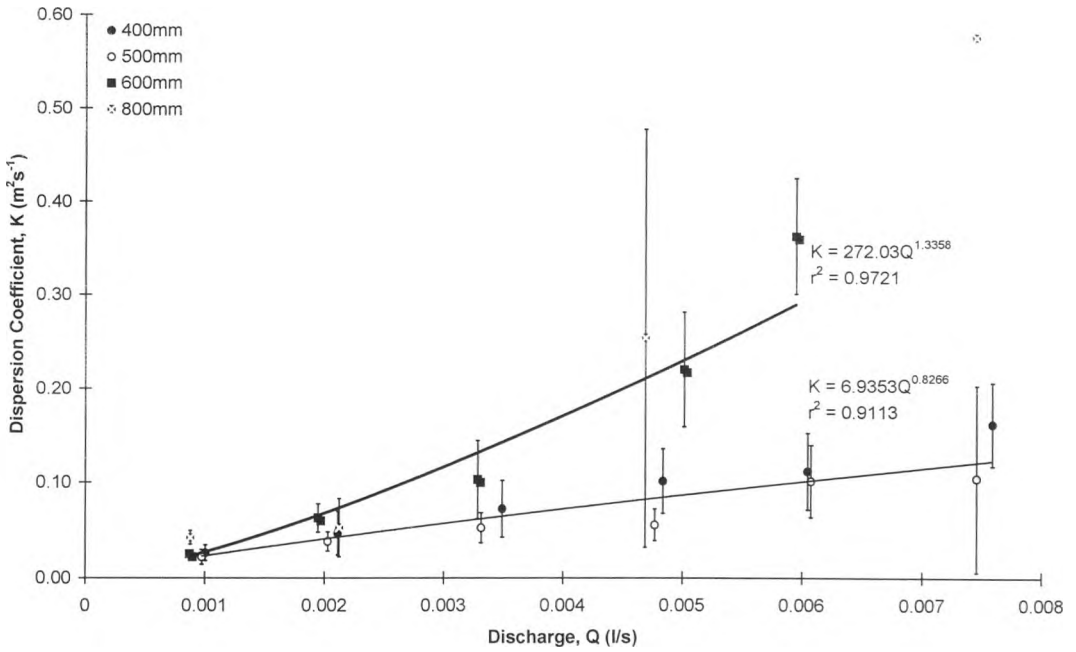


Figure 3.35 Variation of dispersion coefficient with discharge.

One possibility for the increased value of dispersion coefficient with increased chamber diameter could be the total decay of a submerged jet, from the inlet, within the body of the chamber (Pedersen and Mark, 1990). This would imply that the transition would not only be dependant in chamber diameter, but also the inlet pipe diameter and the discharge. However, for this study it shall be assumed that the pairing of the data for the smaller and larger chamber diameters yield unique dispersion coefficients.

Consequently, from this optimal iteration study of the advective dispersion equation, the following equations have been formulated to describe the change in a pollutant profile as it passes through a manhole chamber.

Pre-threshold travel time,

$$\frac{\bar{t}}{D_m} = 0.0519Q^{-0.9737} \quad (3.16)$$

Post-threshold travel time,

$$\bar{t} = 0.0189Q^{-0.9632} \quad (3.17)$$

where

D_m = Internal diameter of manhole chamber, (m),

\bar{t} = Travel time, (s),

Q = Discharge, (m^3s^{-1}).

Dispersion coefficient, K (m^2s^{-1}), for the 400mm and 500mm internal diameter chambers,

$$K = 6.9353Q^{0.8266} \quad (3.18)$$

Dispersion coefficient, K (m^2s^{-1}), for the 600mm (and approximate 800mm) internal diameter chambers,

$$K = 272.03Q^{1.3358} \quad (3.19)$$

3.4.3 Optimal Iterative ADZ Analysis

As with the optimal iterative ADE analysis, error bars have been excluded from all result plots within the current study. Furthermore, although data obtained from 800mm diameter chamber has been included throughout this section, this data has not be used to develop any predictive equations. The reasons for this are the same as those give in the previous section.

Again, two parameters are being determined through the optimal iterative analysis of the aggregated dead zone technique. These parameters are Travel Time, \bar{t} , and Delay Time, τ . The reason for re-establishing travel time values is because the iterative ADE analysis would have placed a dependency between the travel time and the dispersion coefficient. As a result both parameters will influence each other implying that the results found via this approach are unique to the analysis technique (i.e. the parameters found through iterative optimisation are not mutually exclusive). Hence the ADZ parameters that will be determined in this section will have a direct correlation with each other and no correlation with the optimal ADE analysis (although similarities will be seen in the results).

Again the surcharge threshold has been included in all the optimal iterative ADZ result plots. Clearly there is change in the characteristics of travel time within the vicinity of the threshold level. Such behaviour is a departure from that observed when undertaking the standard ADZ analysis, where no threshold was observed. In comparison to the optimal iterative ADE analysis, ADZ predicts a greater peak to the travel time data.

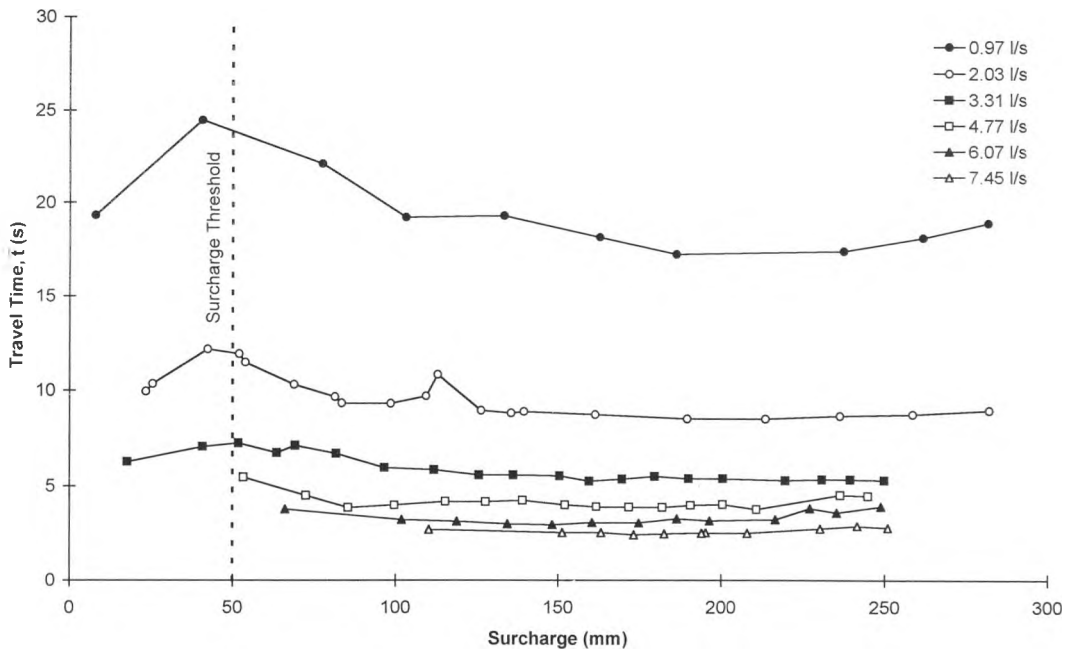


Figure 3.36 Variation in travel time with surcharge for the 400mm diameter chamber.

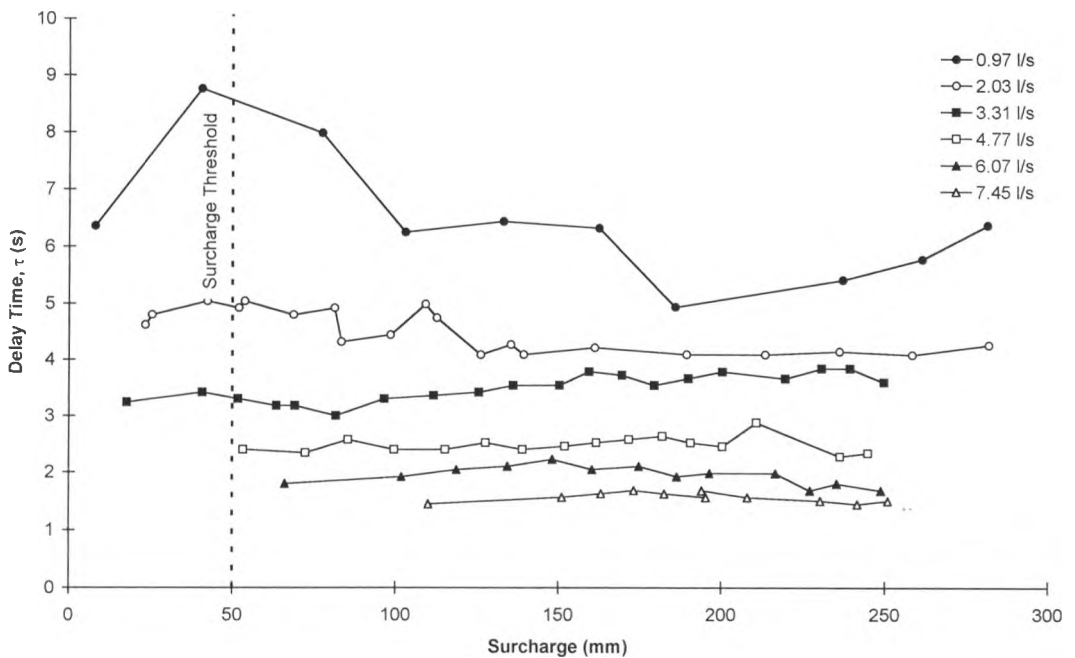


Figure 3.37 Variation in delay time with surcharge for the 400mm diameter chamber.

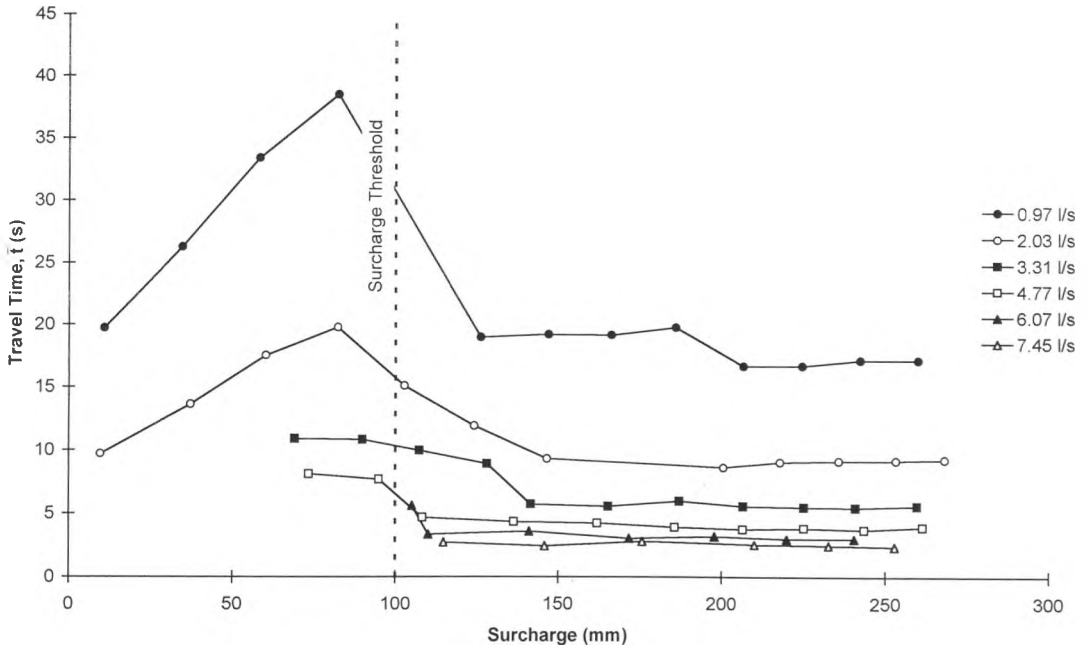


Figure 3.38 Variation in travel time with surcharge for the 500mm diameter chamber.

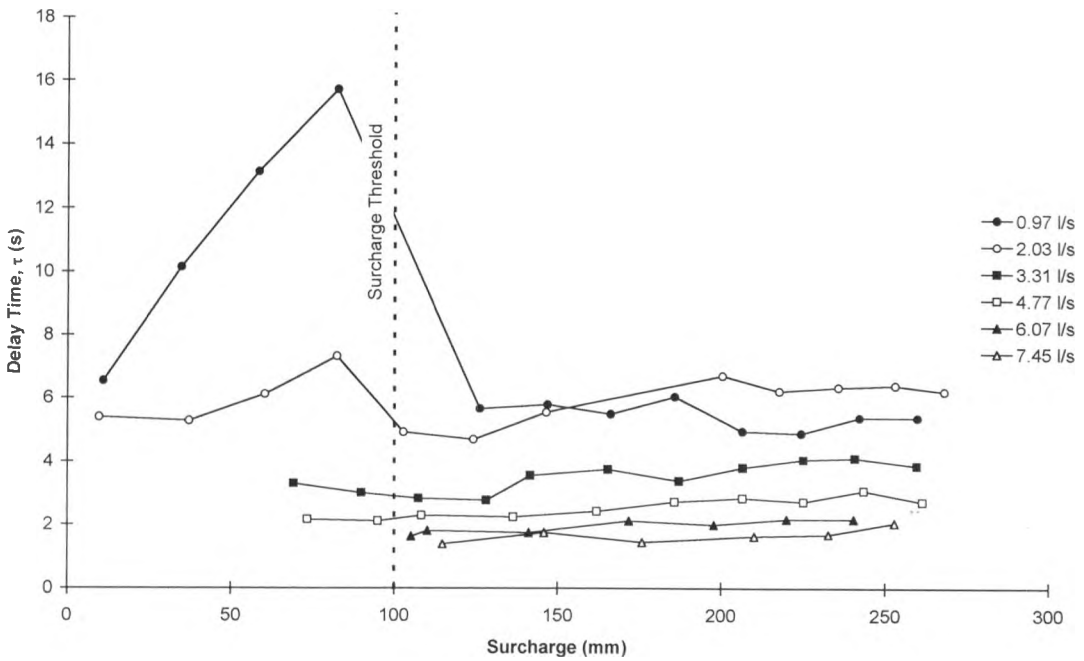


Figure 3.39 Variation in delay time with surcharge for the 500mm diameter chamber.

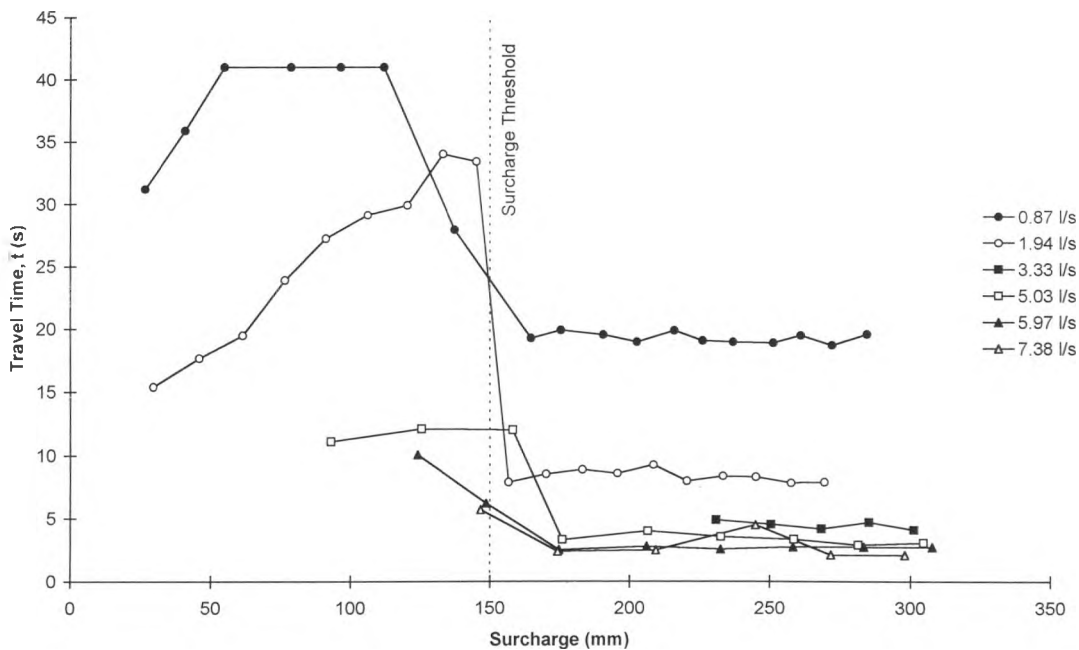


Figure 3.40 Variation in travel time with surcharge for the 600mm diameter chamber.

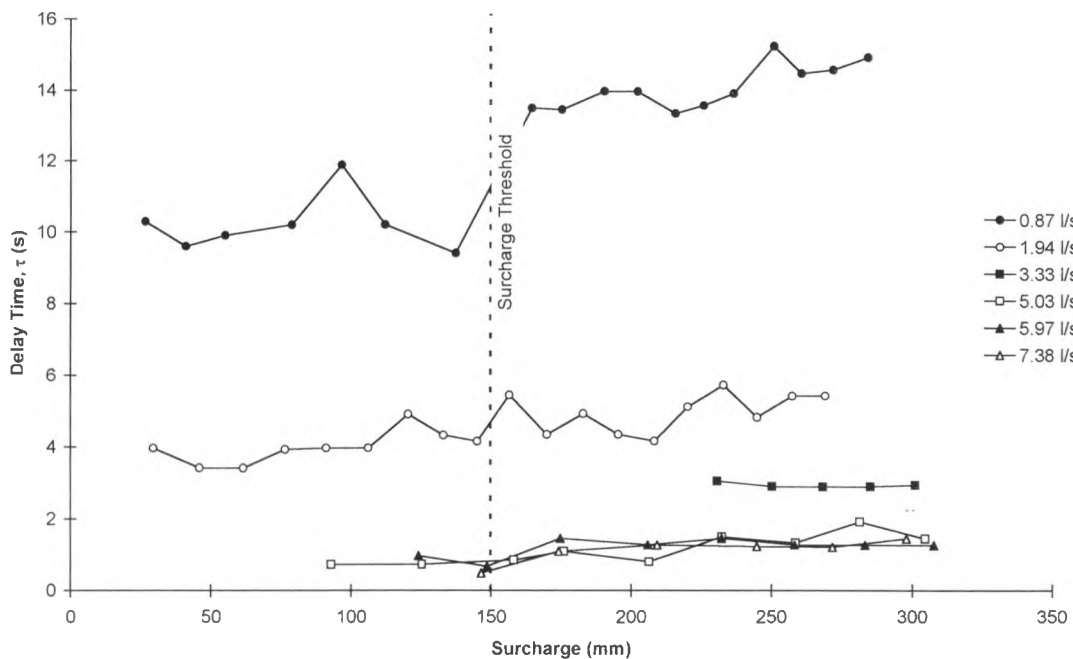


Figure 3.41 Variation in delay time with surcharge for the 600mm diameter chamber.

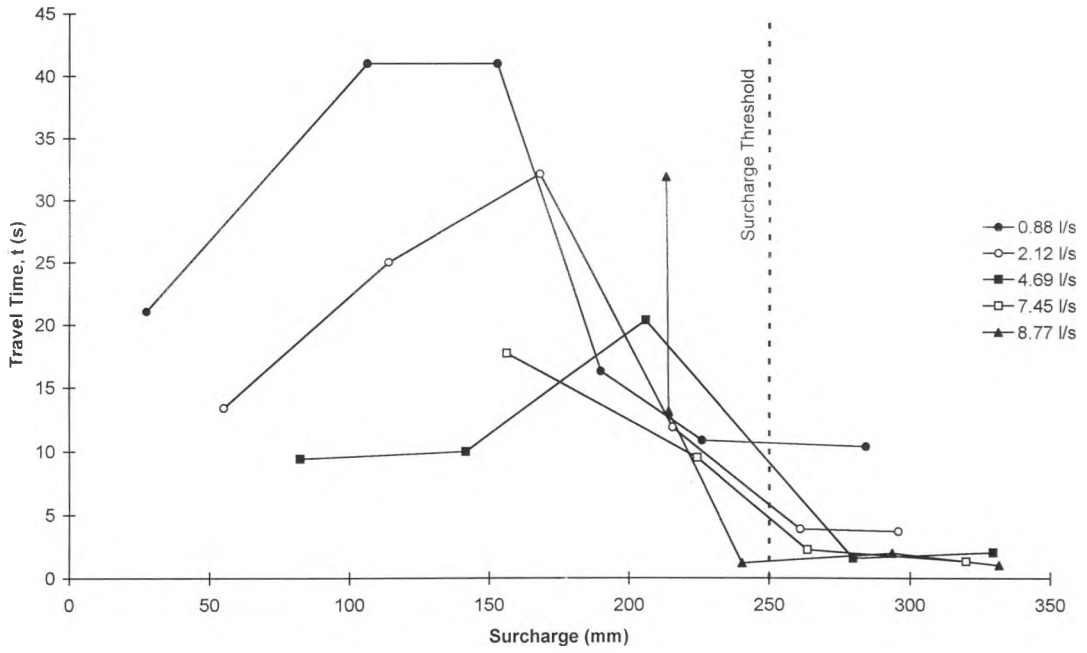


Figure 3.42 Variation in travel time with surcharge for the 800mm diameter chamber.

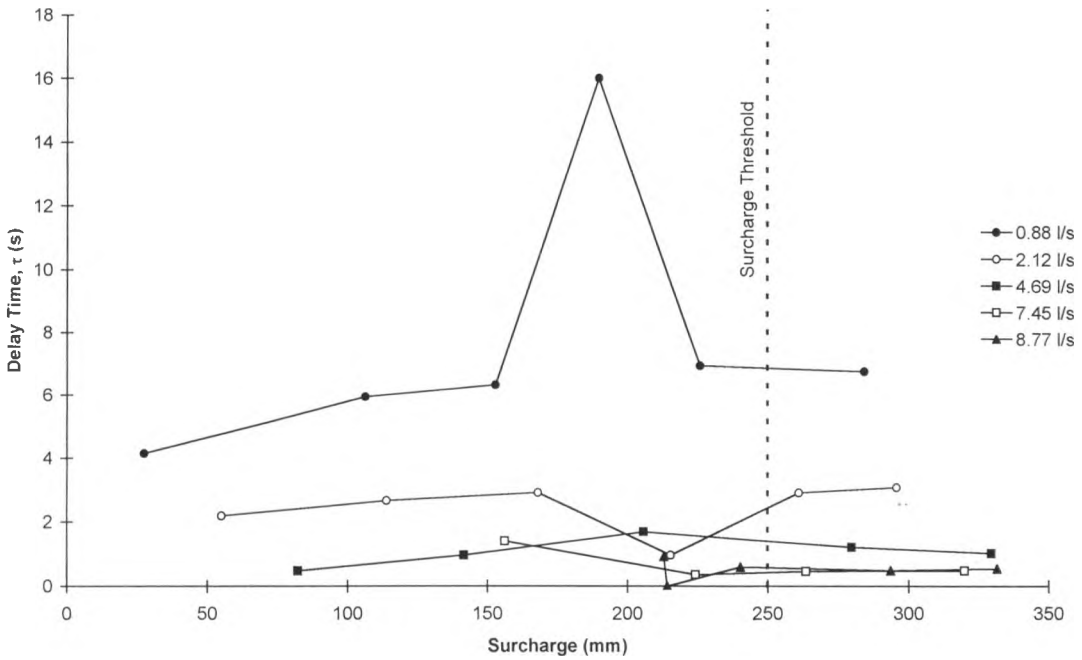


Figure 3.43 Variation in delay time with surcharge for the 800mm diameter chamber.

After the surcharge threshold has been obtained all data tends towards a plateau. As would be expected, the level of this plateau (with respect to travel time) is seen to decrease with the increase in discharge. While the surcharge is less than the threshold level, the travel time is also seen to increase with the increase in surcharge. However, due to the lack of reliable data within this region no attempt is to be made to describe this proportionality. Instead the travel time is averaged over the surcharge before and after the threshold levels. As was stated in Section 3.4.2, this will incur a degree of error in the pre-threshold travel times.

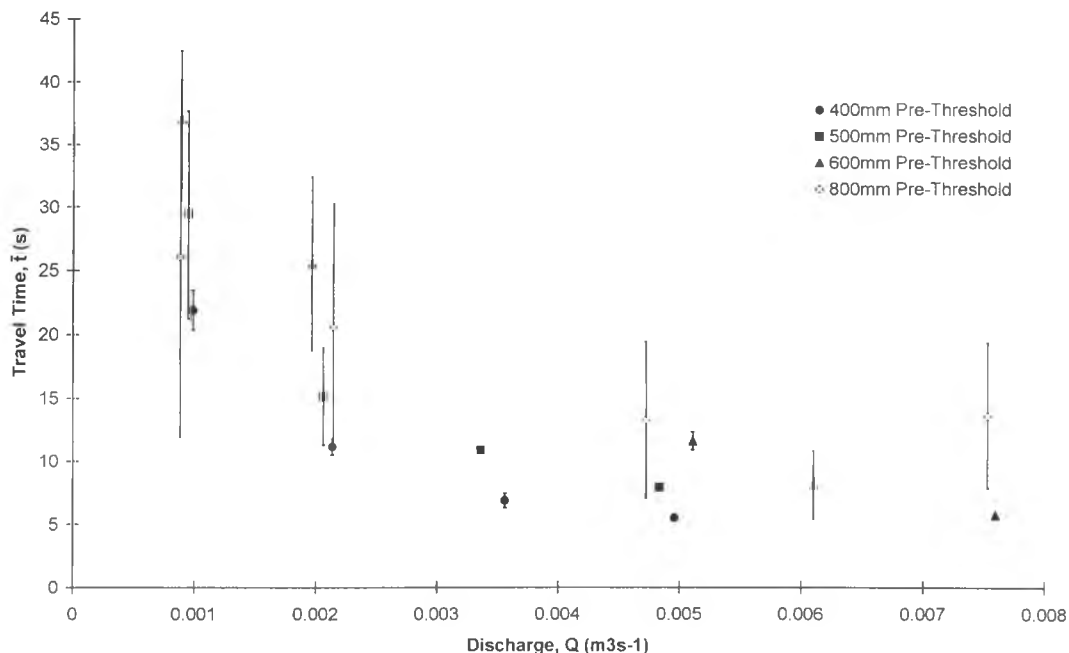


Figure 3.44 Surcharge averaged travel time prior to the surcharge threshold.

As seen with the iterative ADE analysis, the surcharge averaged pre-threshold travel time increases proportionally with the increase in chamber diameters. However the above figure also illustrates a departure from the previous ADE analysis, with all the observed travel times being approximately 50 per-cent greater than those calculated. To unify these results the travel time is again normalised by dividing each result by the associated internal diameter on the manhole chambers (D_m).

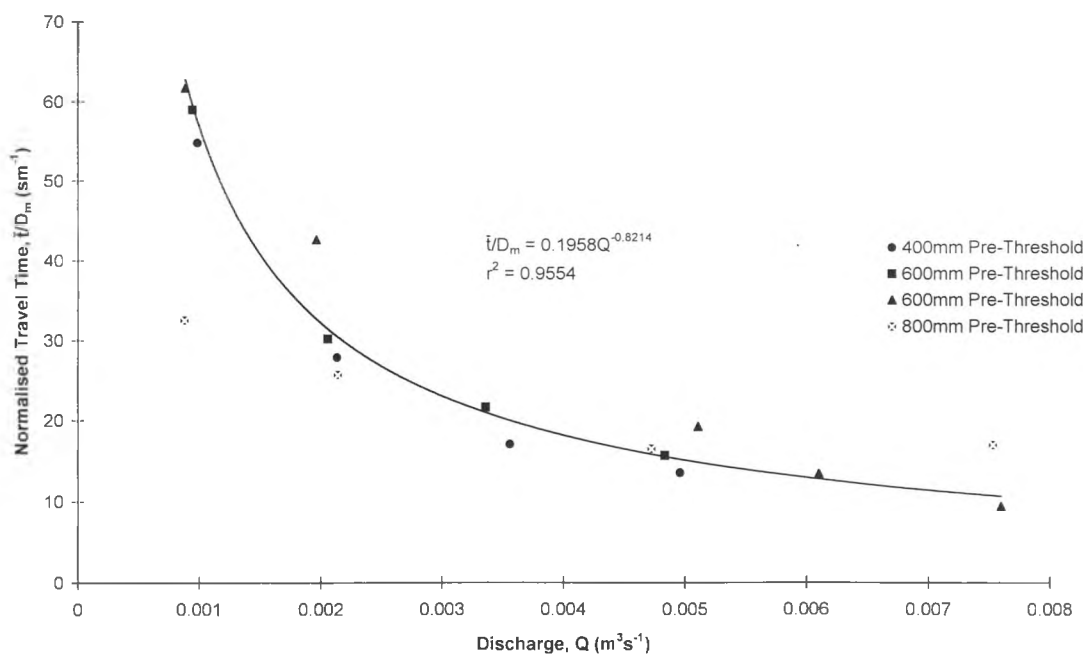


Figure 3.45 Normalised surcharge averaged travel time prior to the surcharge threshold.

Figure 3.45 clearly illustrates the departure of the 800mm chamber data from all other chambers tested. For this reason and the poor correlation coefficient that were obtained during the analysis of the 800mm data, none of the predictive formulae derived within this section shall be based on these results.

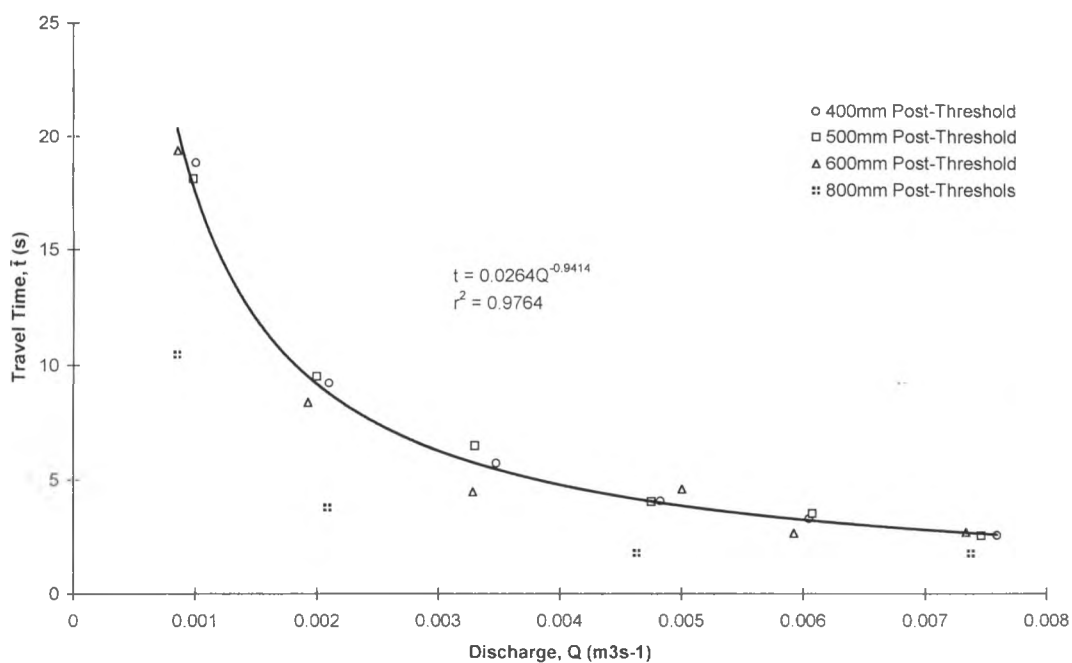


Figure 3.46 Surcharge averaged travel time after the surcharge threshold has been reached.

In contrast to the travel time, the delay time has not been sub-divided into pre and post-threshold surcharges. Although some results depict a dependency on the surcharge threshold, these dependencies are far from common throughout all the data sets.

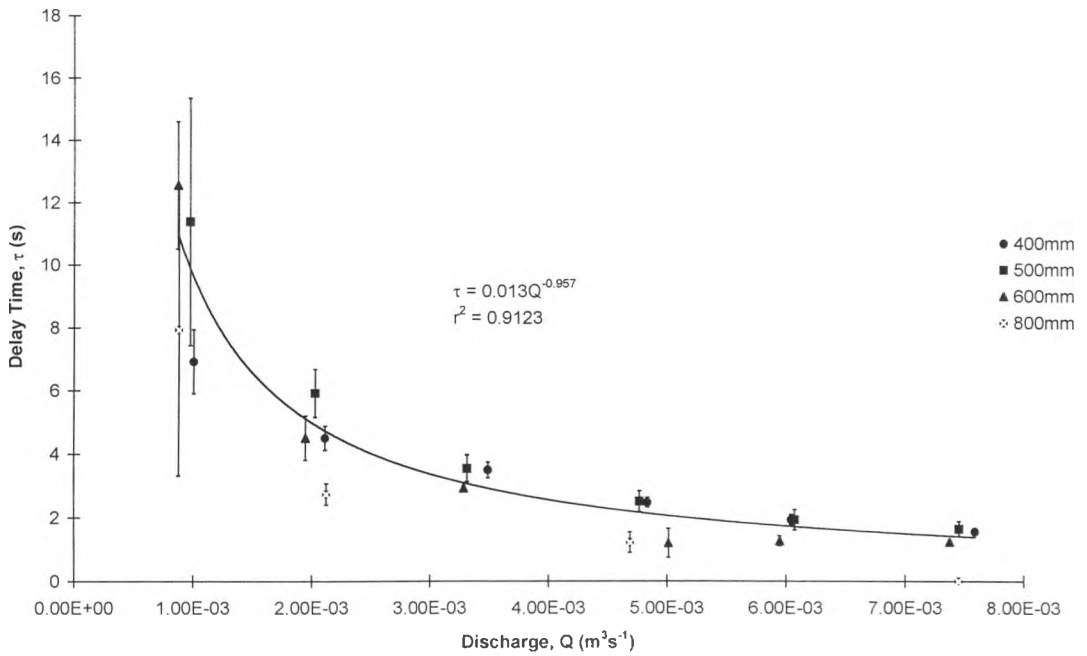


Figure 3.47 Surcharge averaged delay time.

When considering the differences between travel time and delay time, it is relatively easy to postulate why the travel time should be dependant on the surcharge (in relation to the surcharge threshold) whilst the delay time remains independent. The travel time is essentially the average time taken for a pollutant to travel from a location upstream of the manhole to one downstream. As the volume of water retained within the manhole increases both the storage and flow mechanisms within the manhole will undergo change. The fact that the travel time tends to decrease once the threshold has been attained suggests that a larger proportion of the pollutant is passing directly through the chamber. This is possibly due to a reduction in energy dissipation which gives rise to the uneven water surface within the chamber at low surcharges. Conversely, the delay time (or first arrival time as it is sometimes called) will be governed by the peak velocity profile travelling through the manhole system. Provided that the submerged jet generated within the manhole (Pedersen et. al., 1990) does not totally decay before exiting the chamber, the delay time will always remain proportional (approximately) to the mean discharge.

As a result of the optimal iterative study applied in conjunction with the aggregated dead zone technique, the following predictive equations have been formulated to predict dispersion within a manhole system.

Pre-threshold travel time,

$$\frac{\bar{t}}{D_m} = 0.1958Q^{-0.8214} \quad (3.20)$$

Post-threshold travel time,

$$\bar{t} = 0.0264Q^{-0.9414} \quad (3.21)$$

Delay time,

$$\tau = 0.013Q^{-0.957} \quad (3.22)$$

where -

D_m = Internal diameter of manhole chamber, (m),

\bar{t} = Travel time, (s),

τ = Delay time, (s),

Q = Discharge, (m^3s^{-1}).

Chapter 4

Comparison Between Observed and Predicted Data

4.1 Data Selection

Within the previous chapter several equations were developed to describe coefficients that can be used in conjunction with either the advective dispersion equation (ADE) or the aggregated dead zone (ADZ) modelling techniques. These coefficients include the standard ADE dispersion coefficient, K (equations 3.8, 3.9 and 3.11) and the standard ADZ dispersive fraction and travel time (equation 3.13 and 3.14), as well as optimal ADE dispersion coefficient and travel time parameters (equations 3.16, 3.17, 3.18 and 3.19) and, optimal ADZ travel and delay times (equations 3.20, 3.21 and 3.22). From this multitude of modelling coefficients, it is now possible to draw a comparison between all of these predictive methods.

To enable this comparison, test data from each of the chamber diameters and the straight pipe (in the case of the standard modelling coefficients) will be used.

For each chamber diameter, the data utilised within the comparison has an associated discharge of approximately 3.5×10^{-3} to $4.5 \times 10^{-3} \text{m}^3 \text{s}^{-1}$. This correlates to the average discharge for which data was acquired. Moreover, for each manhole configuration both a pre and post-threshold surcharge has been examined[†].

In addition, two further discharges have been regarded for the 600mm diameter chamber (the average chamber diameter tested), representing discharges greater than and less than the average discharge.

With the straight pipe, the test data used within the comparison is that resulting from a discharge of $6.19 \times 10^{-3} \text{m}^3 \text{s}^{-1}$, the average discharge tested.

By utilising both the aggregated dead zone (equation 1.54) and the frozen cloud approximation (equation 1.39), a comparison between each predictive method and the actual downstream profile can be observed.

[†] Note: For clarity, standard and optimised results have been presented in separate (adjacent) figures.

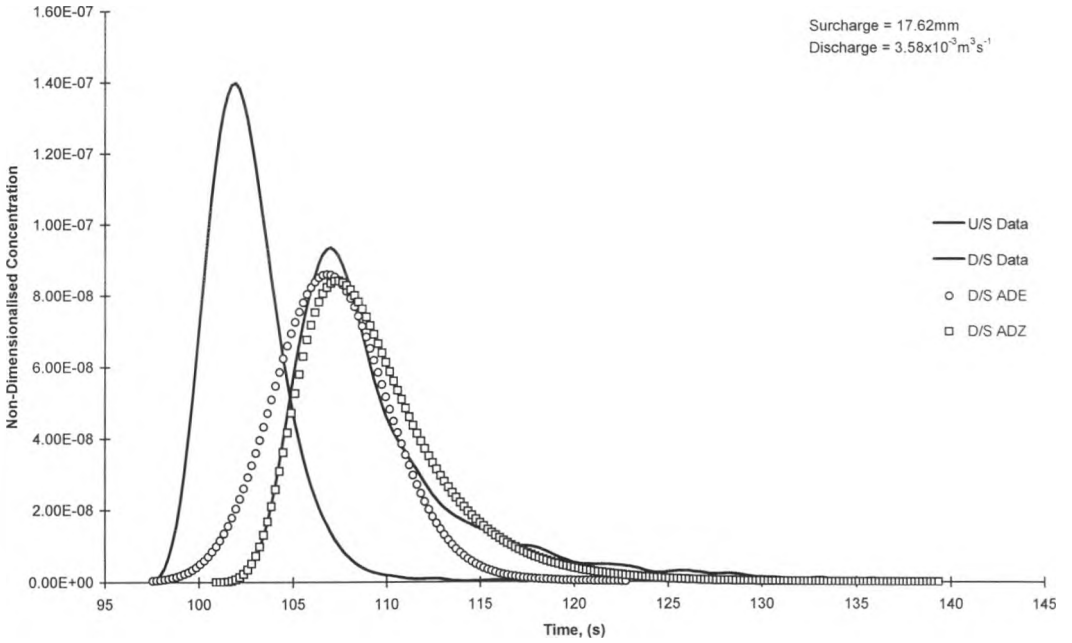


Figure 4.1 Standard ADE and ADZ predictions for a 400mm chamber with a pre-threshold surcharge presented with measured data.

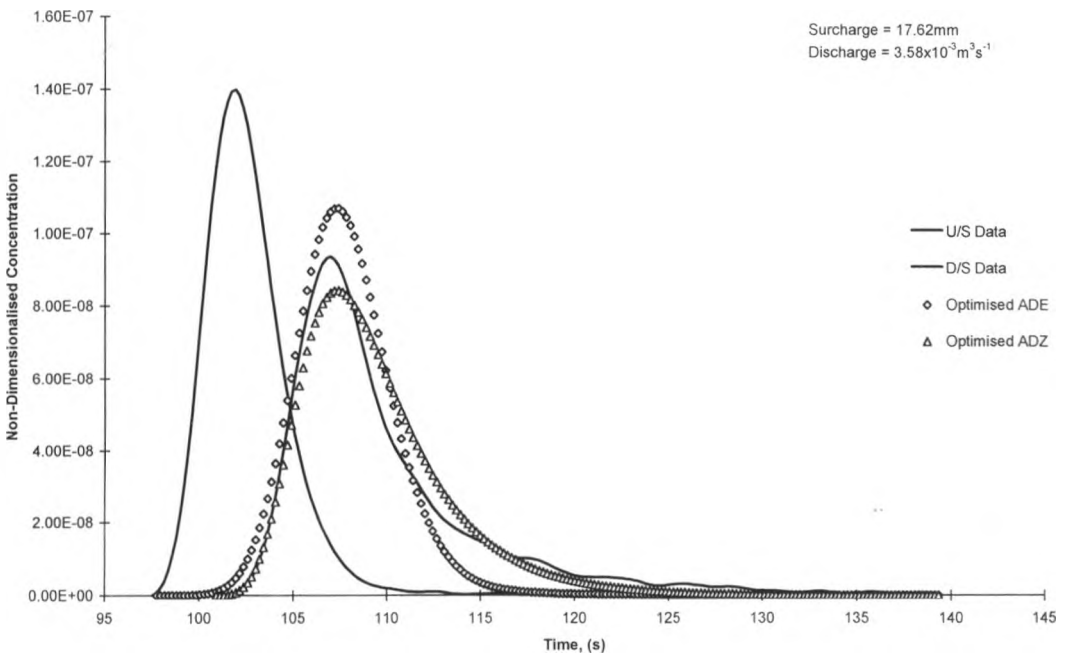


Figure 4.2 Optimised ADE and ADZ predictions for a 400mm chamber with a pre-threshold surcharge, presented with measured data.

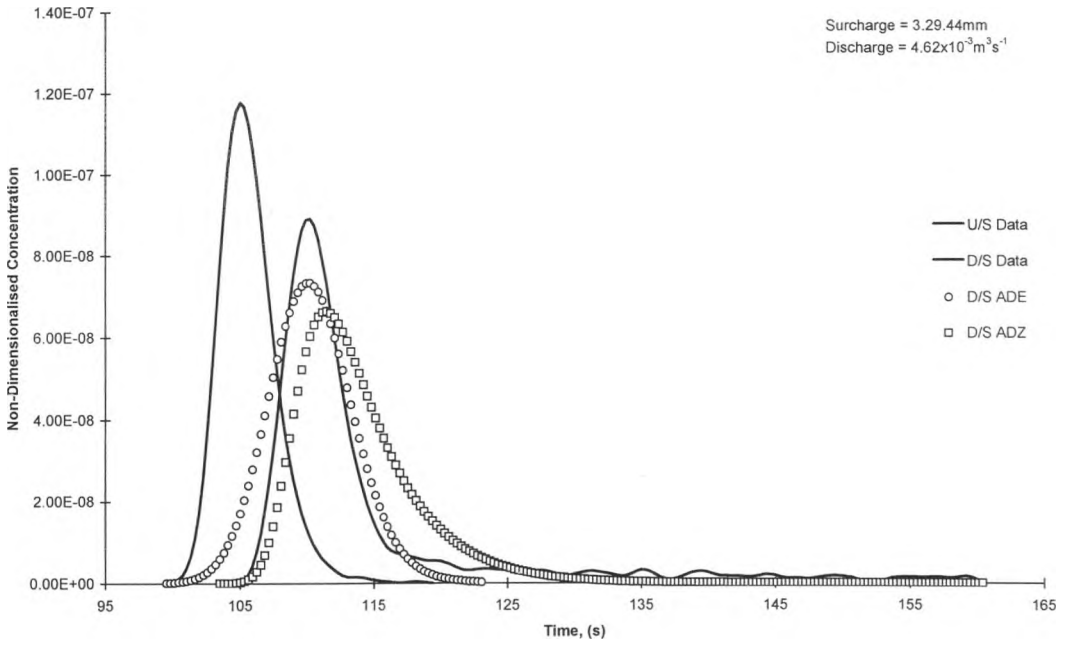


Figure 4.3 Standard ADE and ADZ predictions for a 400mm chamber with a post-threshold surcharge, presented with measured data.

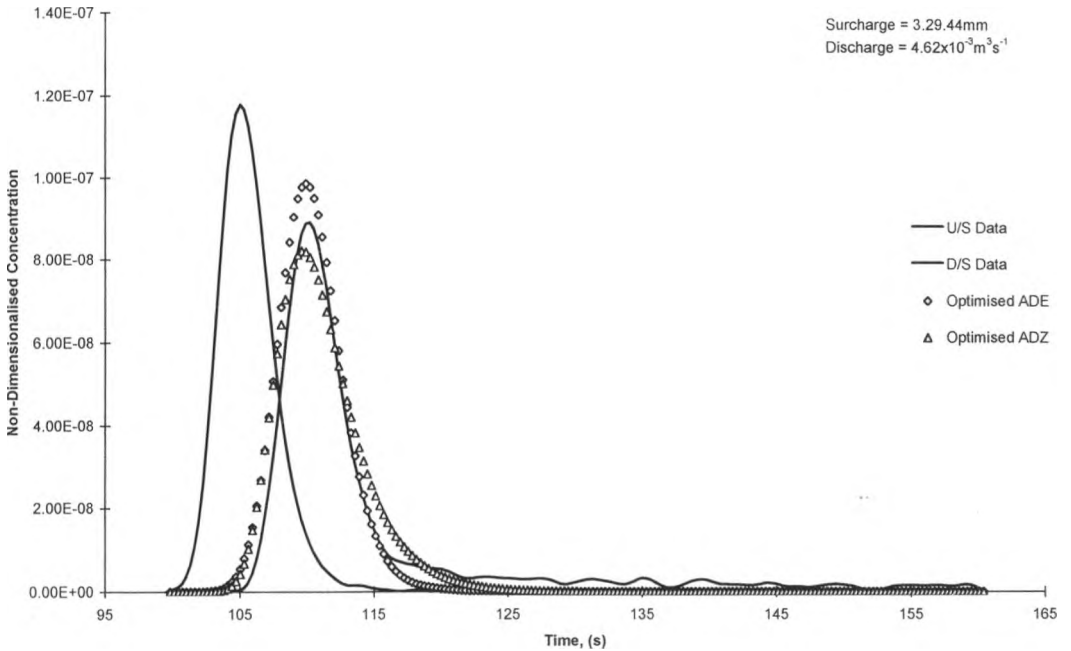


Figure 4.4 Optimised ADE and ADZ predictions for a 400mm chamber with a post-threshold surcharge, presented with measured data.

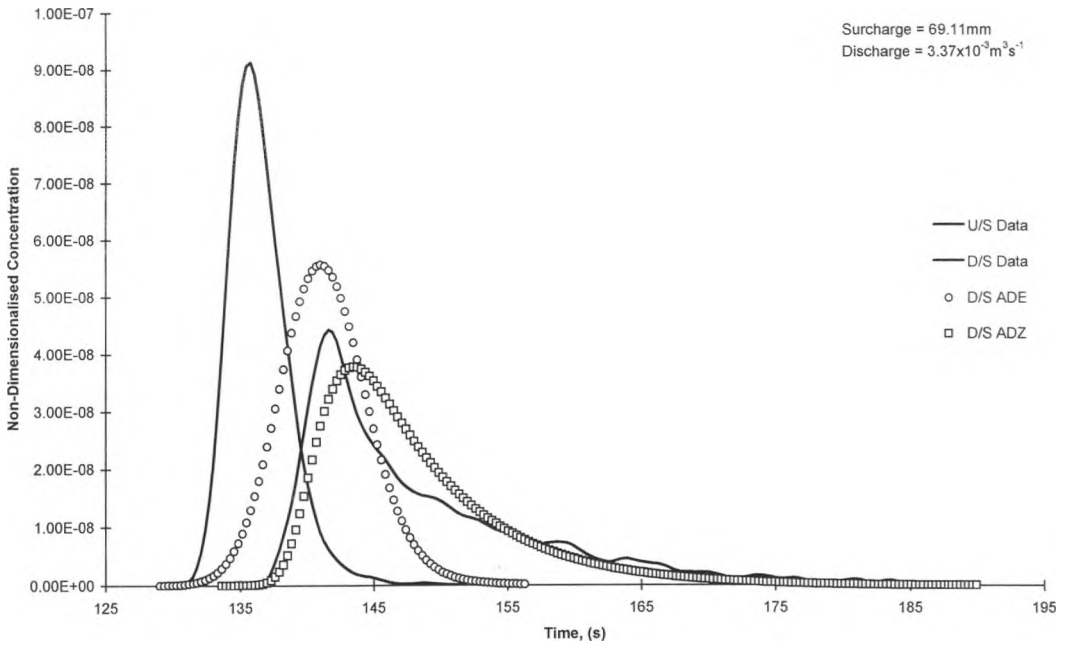


Figure 4.5 Standard ADE and ADZ predictions for a 500mm chamber with a pre-threshold surcharge, presented with measured data.

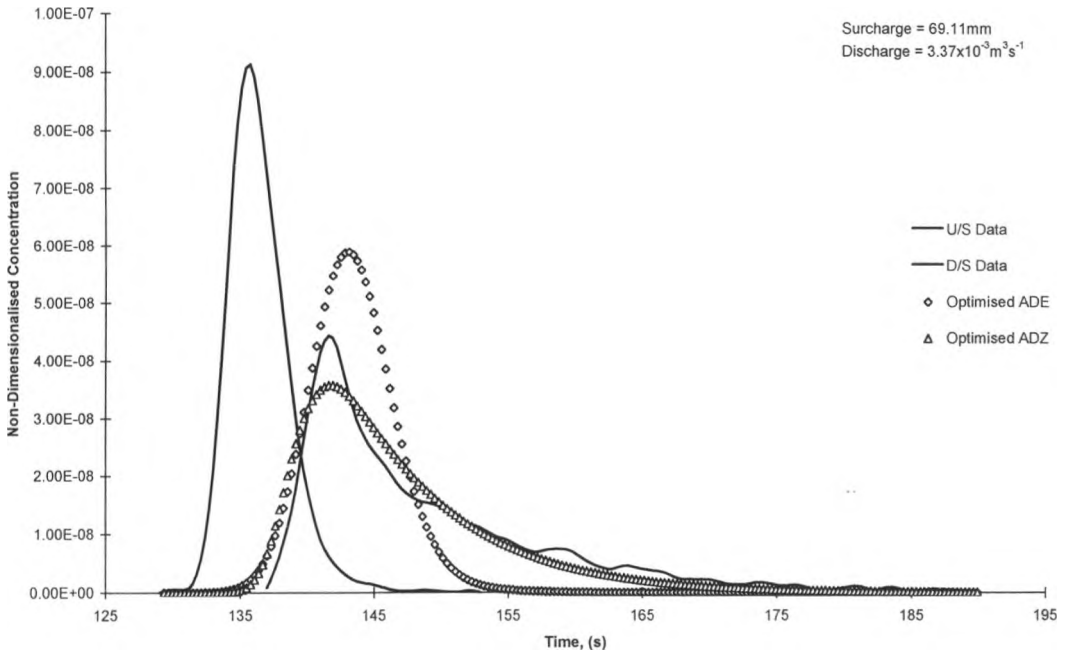


Figure 4.6 Optimised ADE and ADZ predictions for a 500mm chamber with a pre-threshold surcharge, presented with measured data.

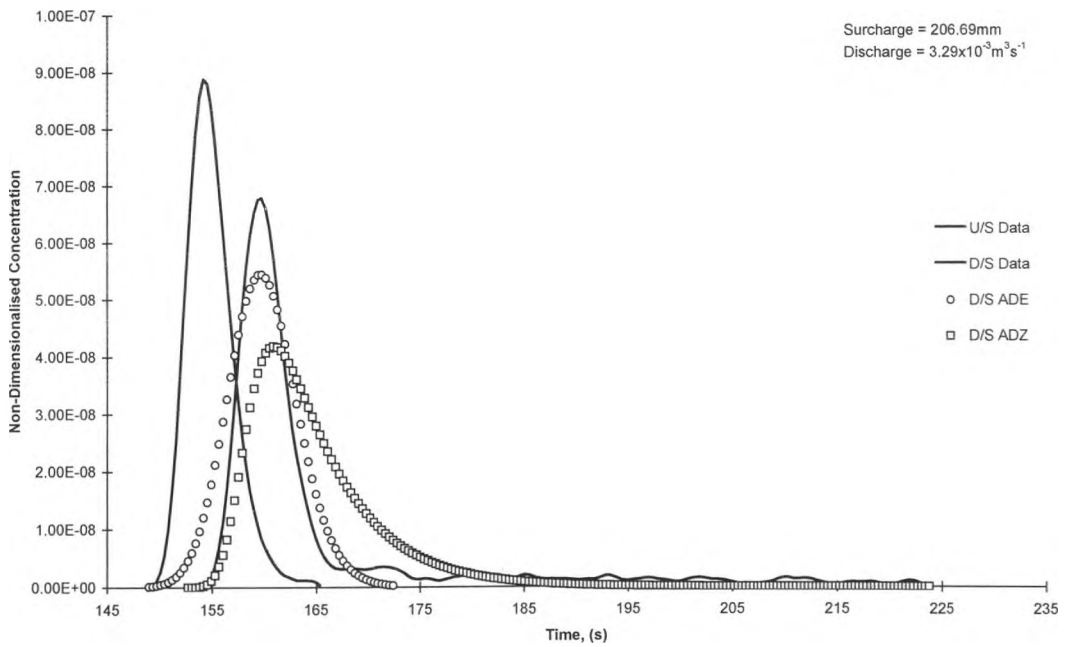


Figure 4.7 Standard ADE and ADZ predictions for a 500mm chamber with a post-threshold surcharge, presented with measured data.

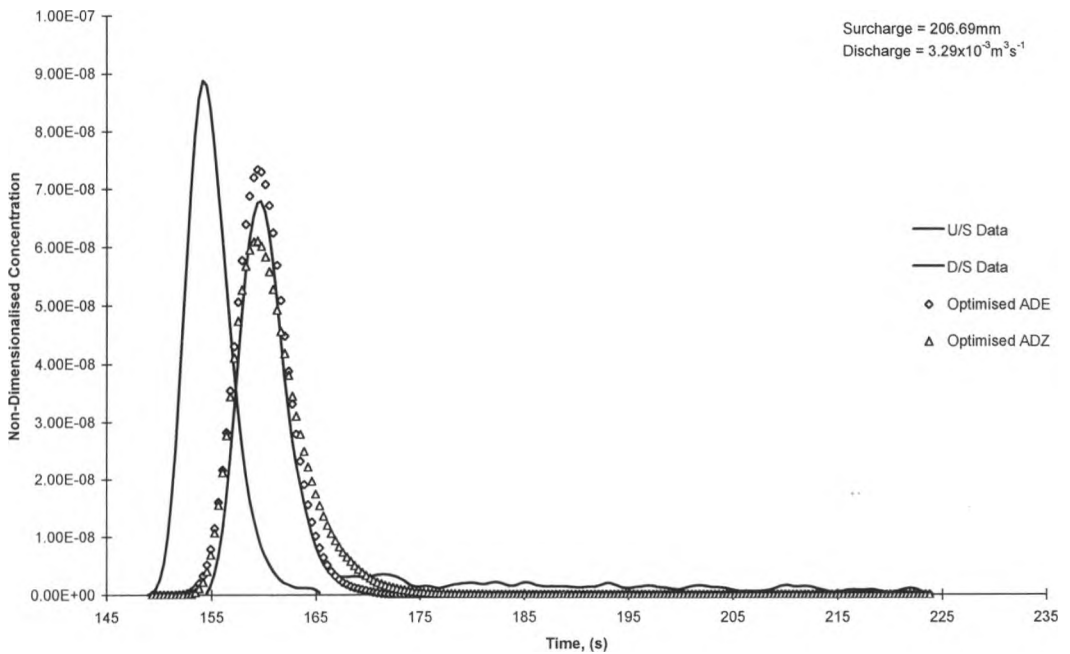


Figure 4.8 Optimised ADE and ADZ predictions for a 500mm chamber with a post-threshold surcharge, presented with measured data.

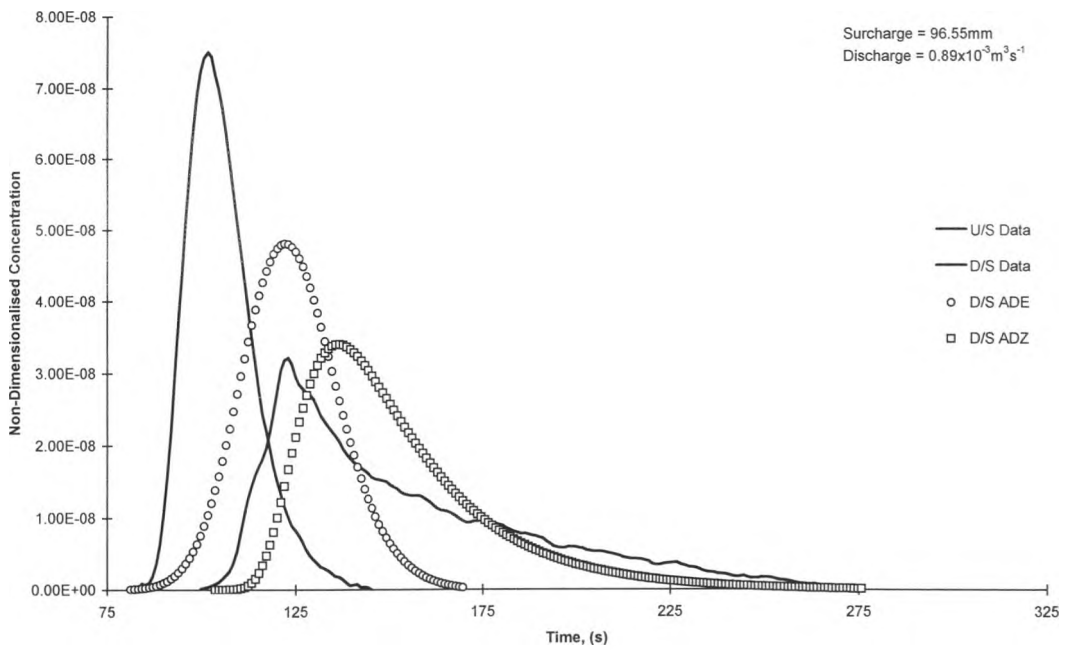


Figure 4.9 Standard ADE and ADZ predictions for a 600mm chamber with a pre-threshold surcharge, presented with measured data.

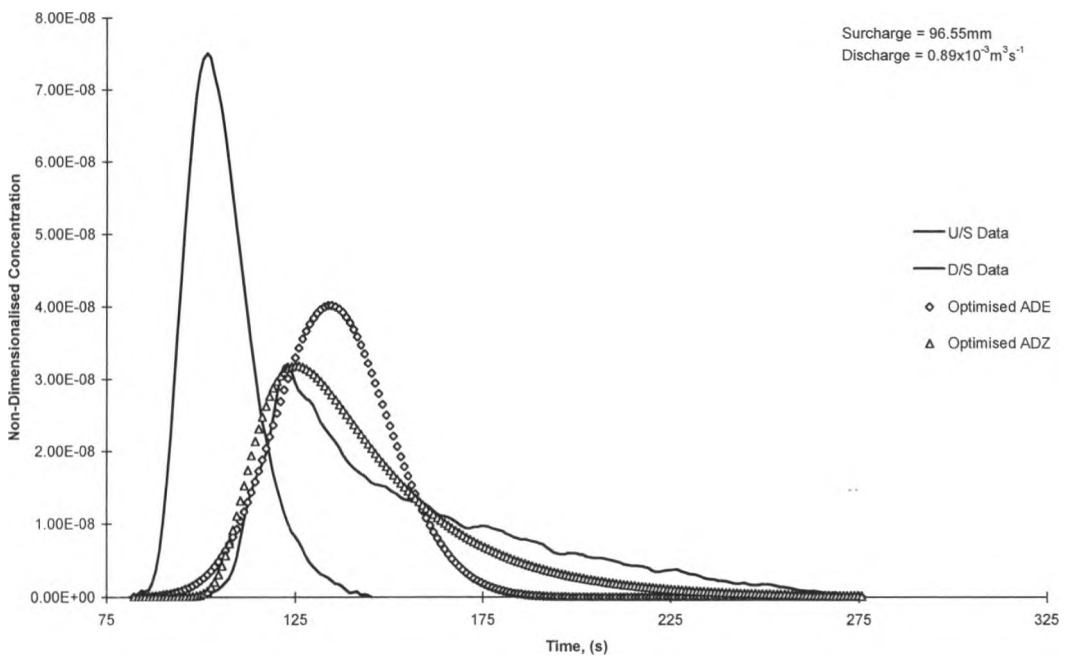


Figure 4.10 Optimised ADE and ADZ predictions for a 600mm chamber with a pre-threshold surcharge, presented with measured data.

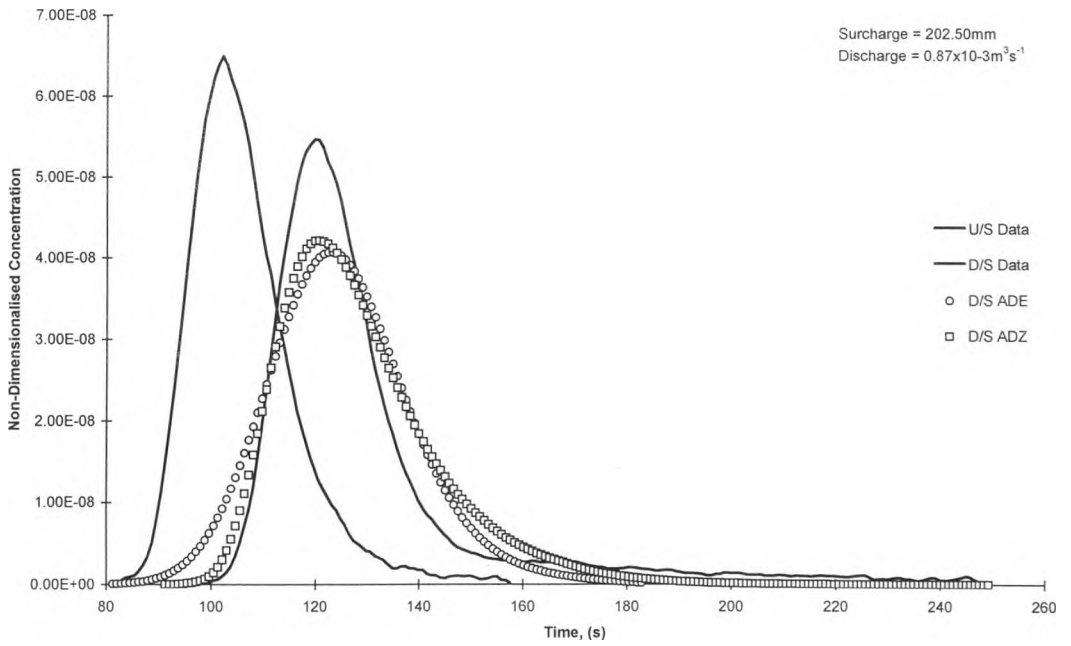


Figure 4.11 Standard ADE and ADZ predictions for a 600mm chamber with a post-threshold surcharge, presented with measured data.

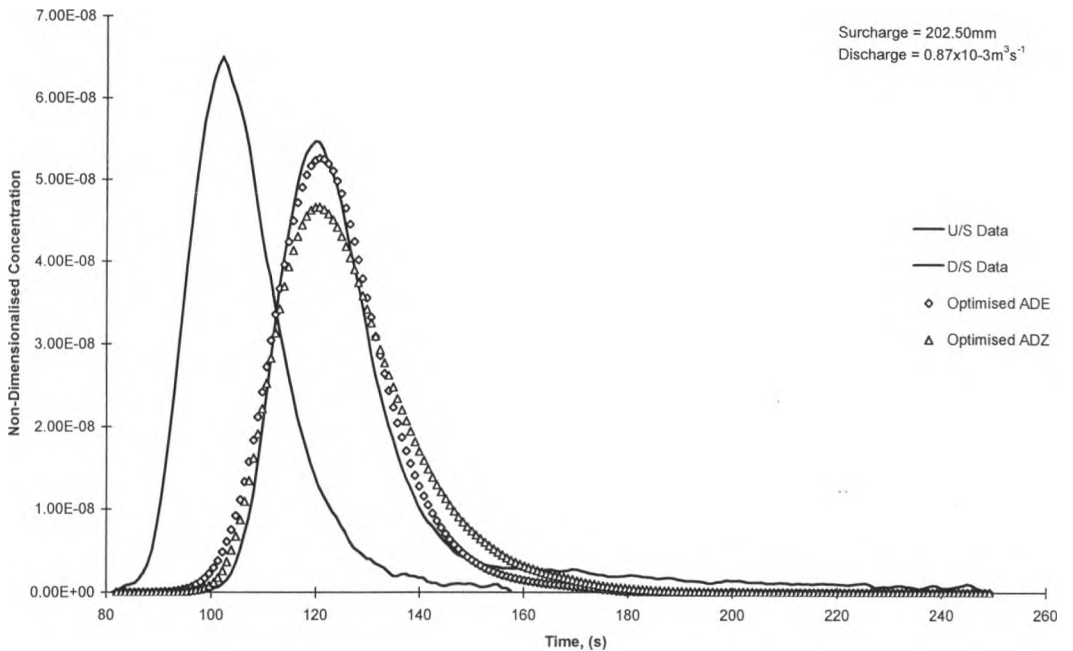


Figure 4.12 Optimised ADE and ADZ predictions for a 600mm chamber with a post-threshold surcharge, presented with measured data.

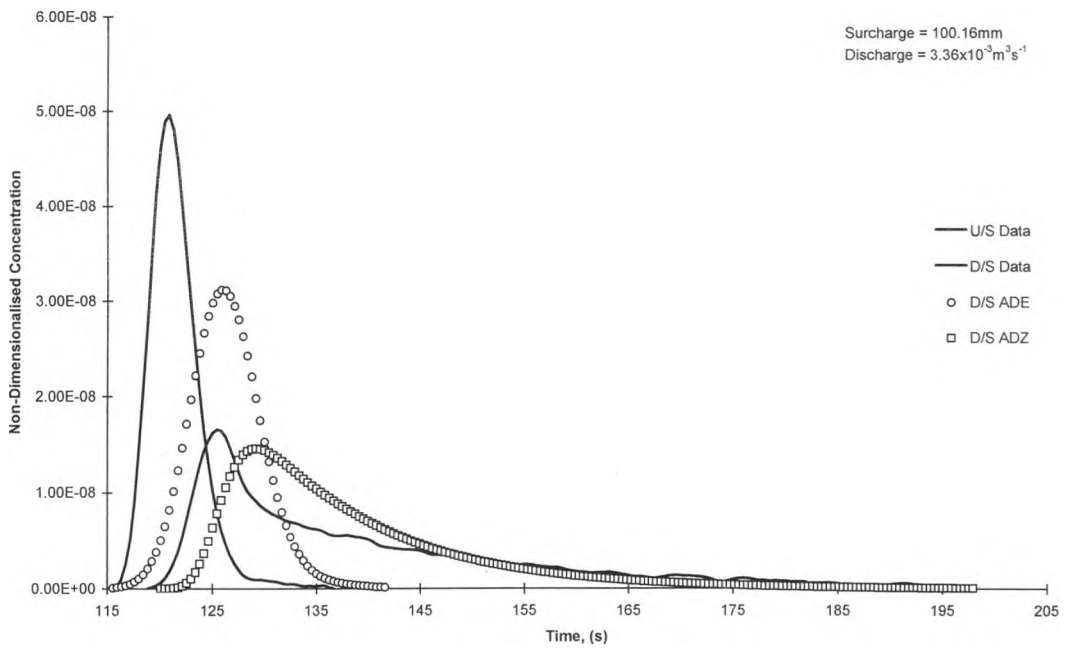


Figure 4.13 Standard ADE and ADZ predictions for a 600mm chamber with a pre-threshold surcharge, presented with measured data.

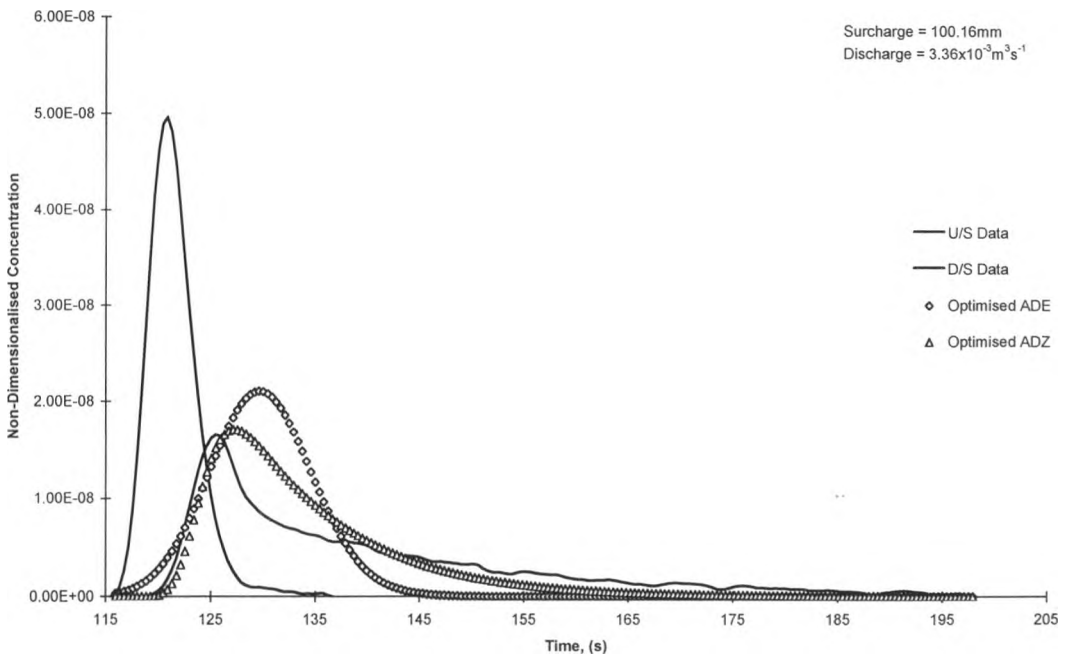


Figure 4.14 Optimised ADE and ADZ predictions for a 600mm chamber with a pre-threshold surcharge, presented with measured data.

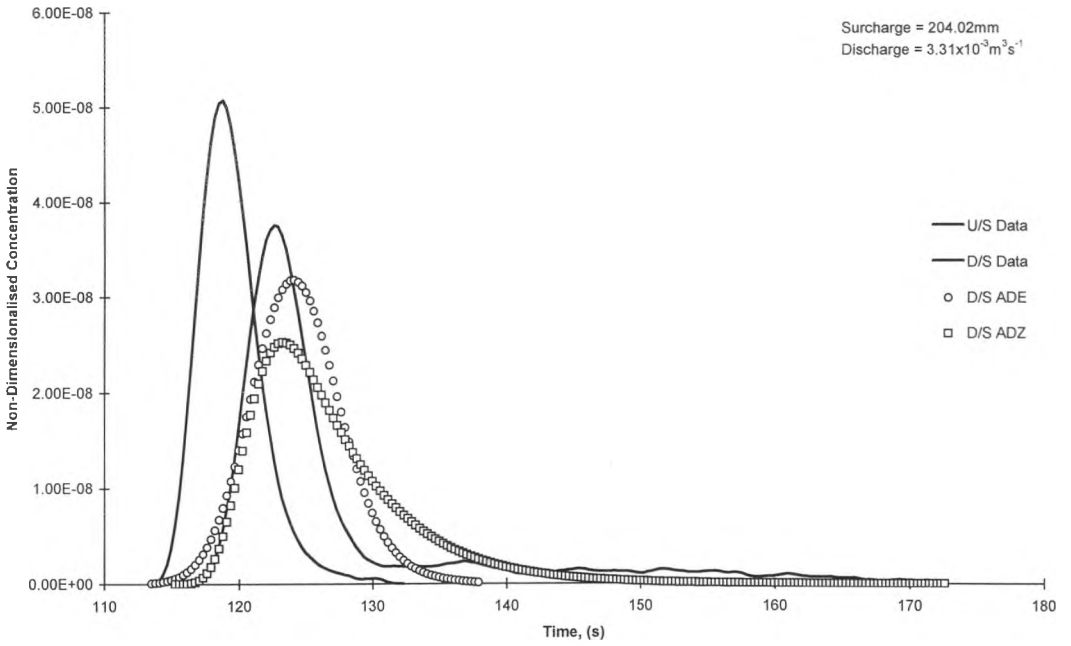


Figure 4.15 Standard ADE and ADZ predictions for a 600mm chamber with a post-threshold surcharge, presented with measured data.

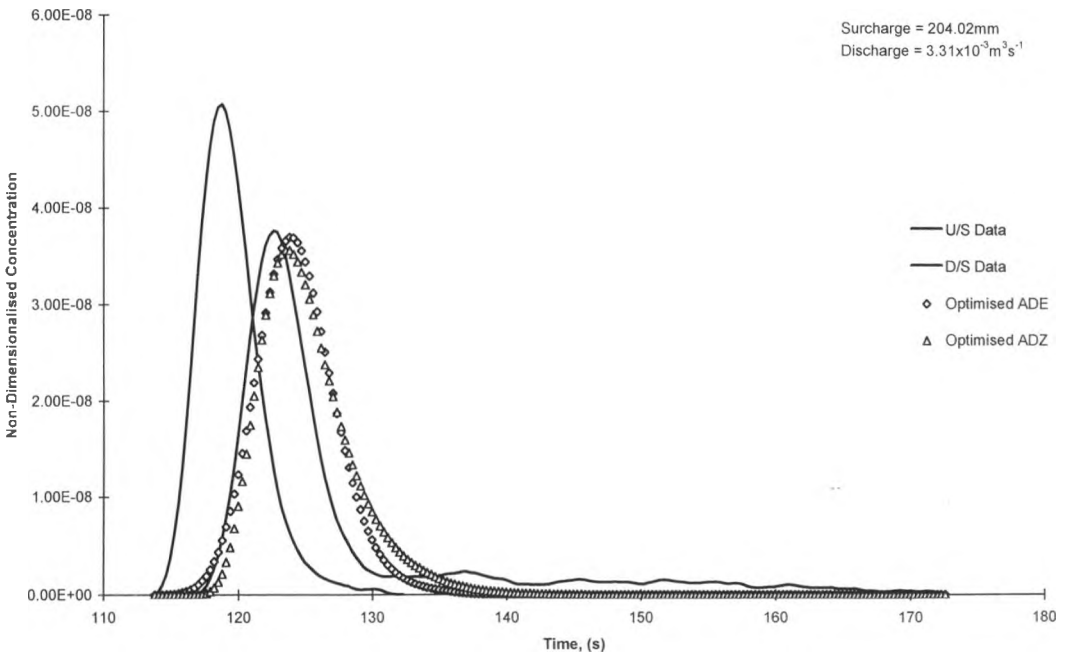


Figure 4.16 Optimised ADE and ADZ predictions for a 600mm chamber with a post-threshold surcharge, presented with measured data.

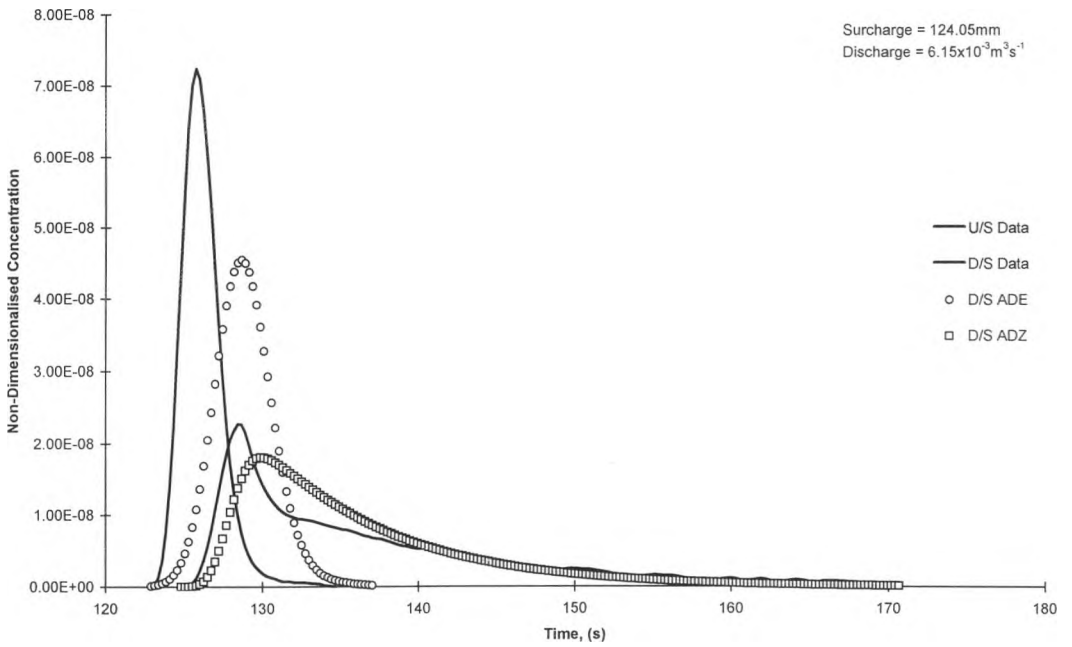


Figure 4.17 Standard ADE and ADZ predictions for a 600mm chamber with a pre-threshold surcharge, presented with measured data.

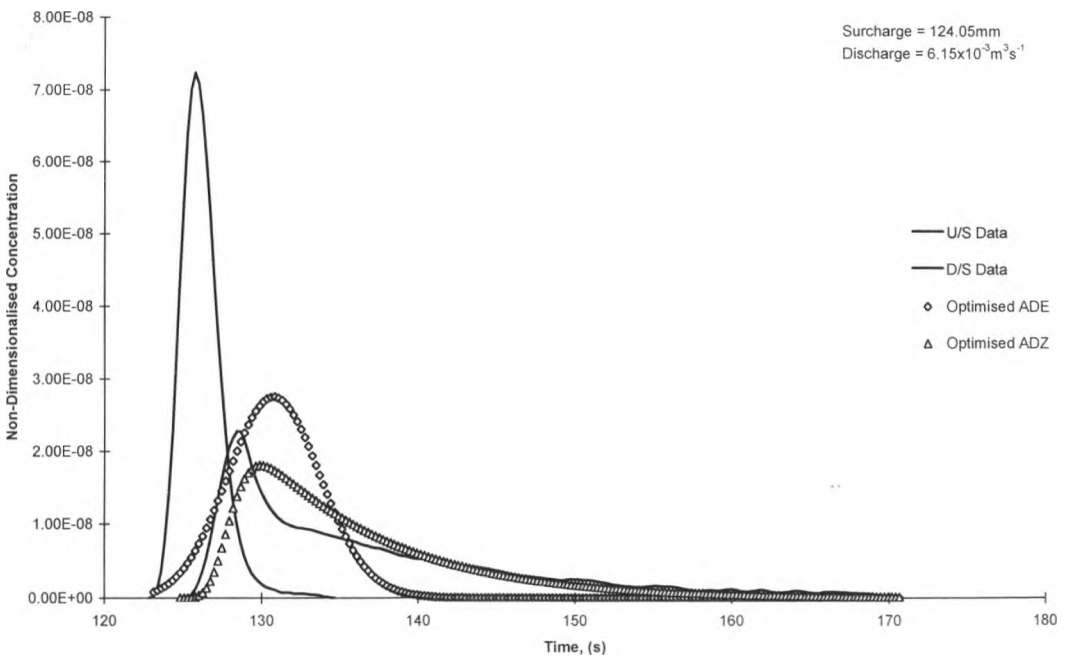


Figure 4.18 Optimised ADE and ADZ predictions for a 600mm chamber with a pre-threshold surcharge, presented with measured data.

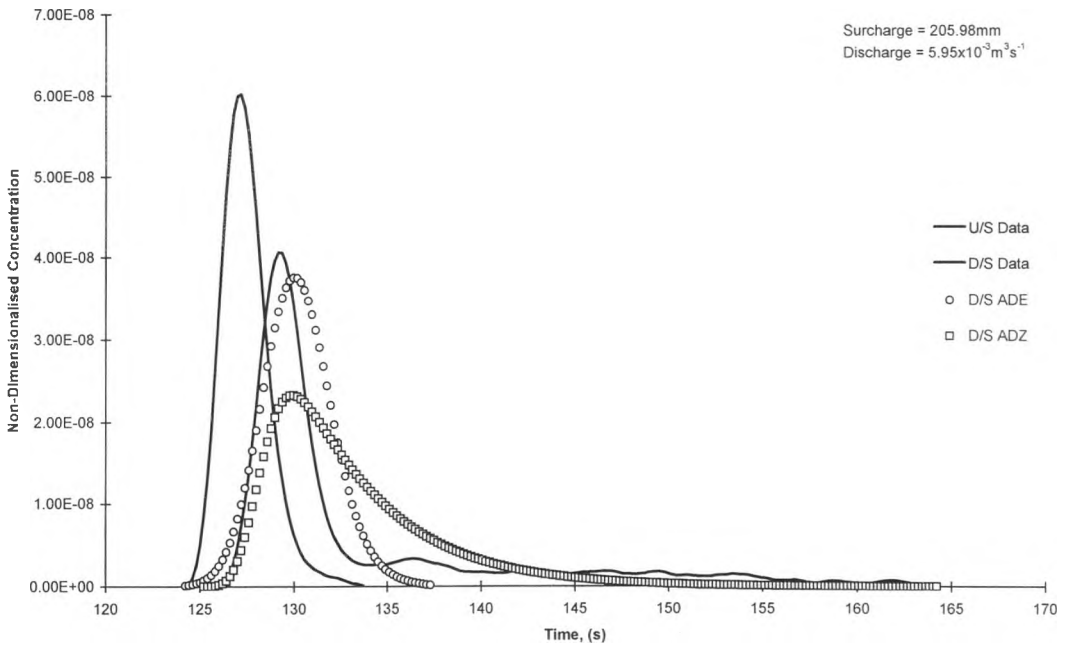


Figure 4.19 Standard ADE and ADZ predictions for a 600mm chamber with a post-threshold surcharge, presented with measured data.

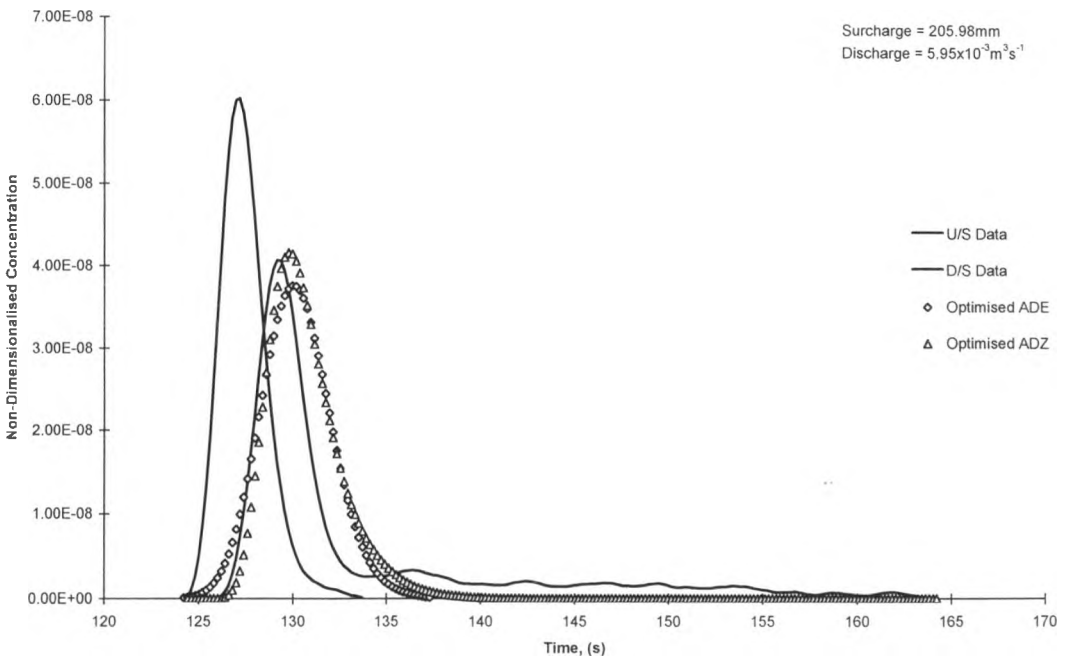


Figure 4.20 Optimised ADE and ADZ predictions for a 600mm chamber with a post-threshold surcharge, presented with measured data.

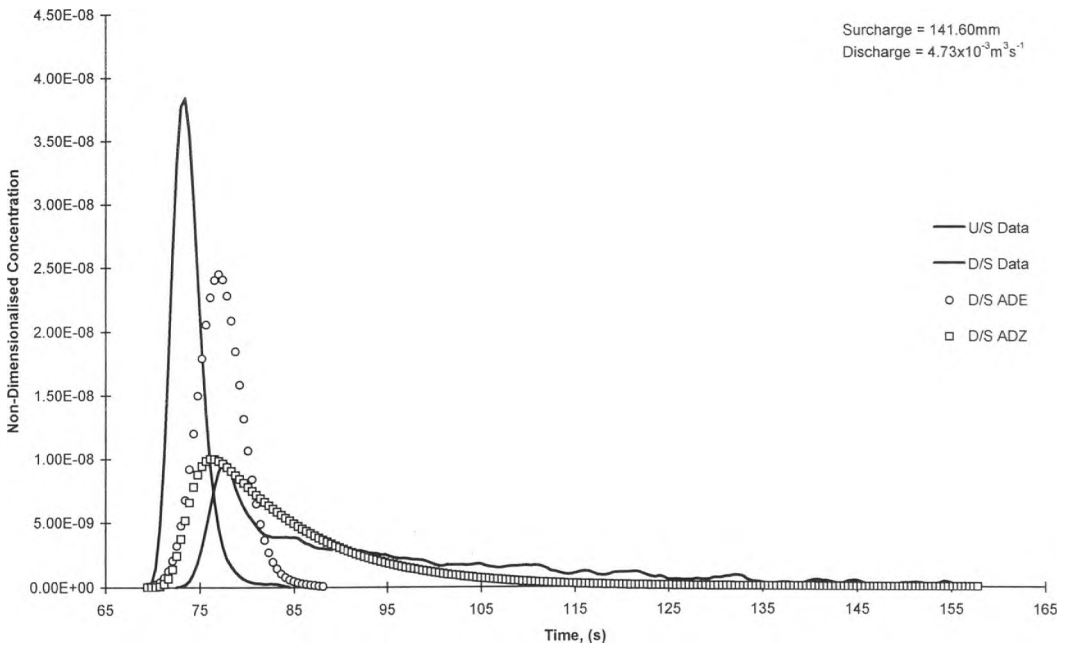


Figure 4.21 Standard ADE and ADZ predictions for a 800mm chamber with a pre-threshold surcharge, presented with measured data.

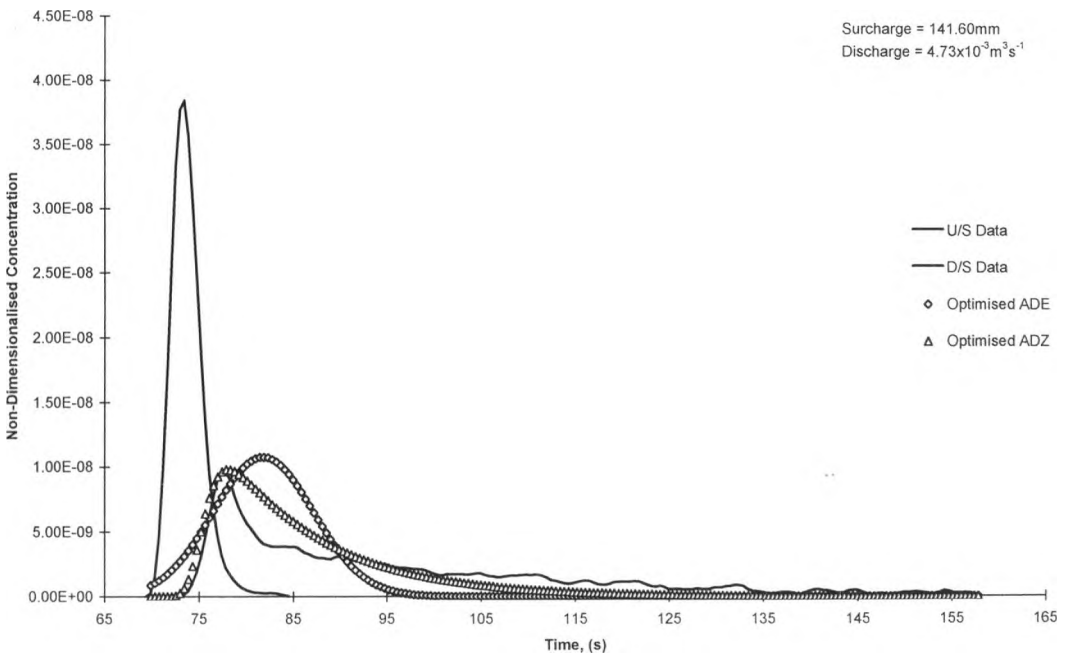


Figure 4.22 Optimised ADE and ADZ predictions for a 800mm chamber with a pre-threshold surcharge, presented with measured data.

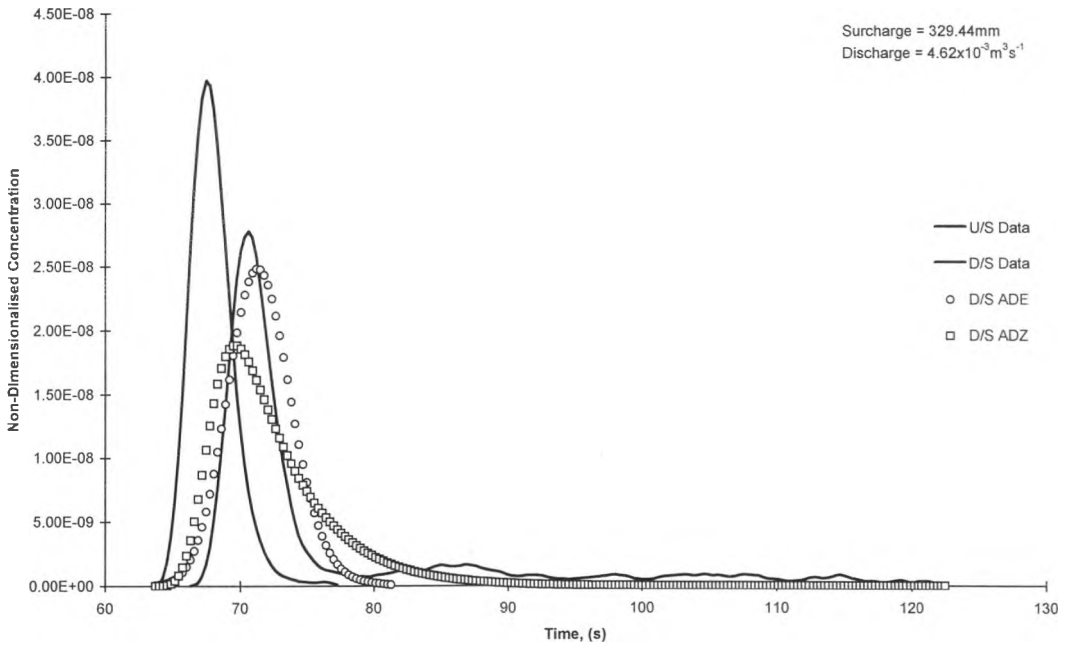


Figure 4.23 Standard ADE and ADZ predictions for a 800mm chamber with a post-threshold surcharge, presented with measured data.

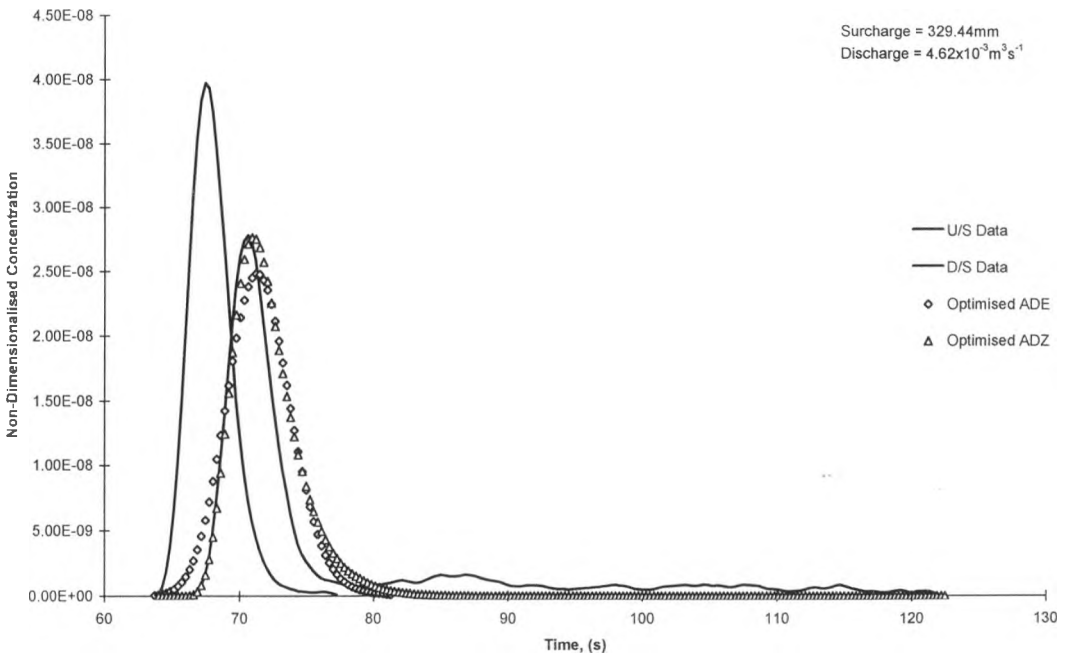


Figure 4.24 Optimised ADE and ADZ predictions for a 800mm chamber with a post-threshold surcharge, presented with measured data.

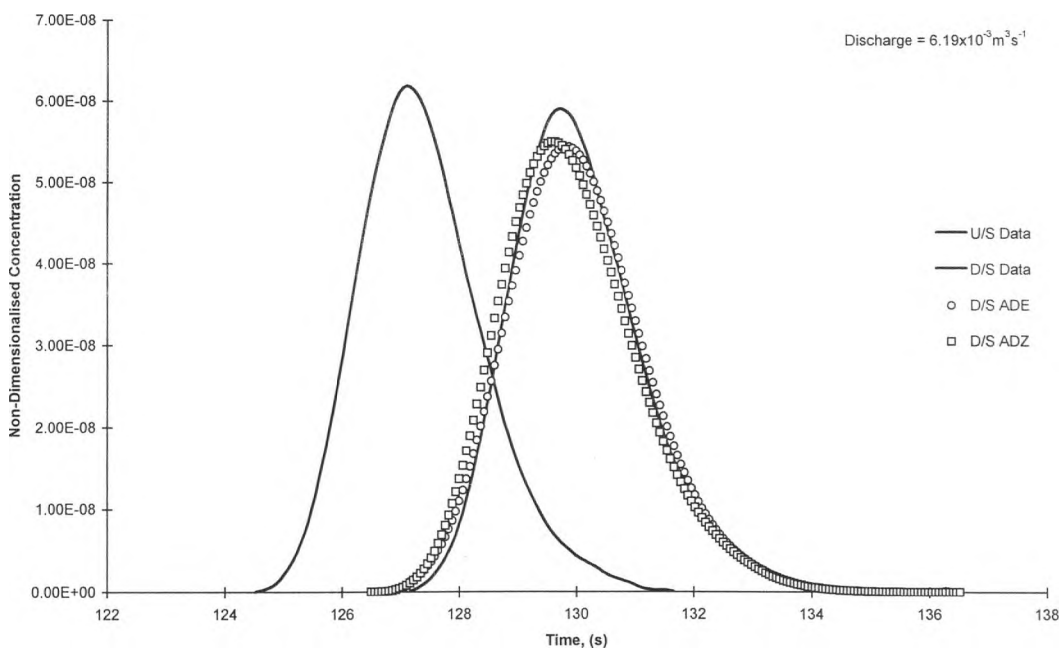


Figure 4.25 Observed and predicted data for a straight pipe with an average discharge.

The results of the predictions seen in Figures 4.1 to 4.25 have been summarised in Table 4.1. 'ADE R_T^{21} ' and 'Optimised ADE R_T^{21} ' represent the coefficient of determination for the standard, and optimised advective dispersion equation respectively, whilst 'ADZ R_T^{21} ' and 'Optimised ADZ R_T^{21} ' represent the standard and optimised aggregated dead zone.

4.2 Summary of Standard ADE and ADZ Predictions for all Manhole Diameters

Scrutiny of the standard results for the different manhole configurations (Figures 4.1, 4.3, 4.5, 4.7, 4.9, 4.11, 4.13, 4.15, 4.17, 4.19, 4.21, 4.23 and Table 4.1) can be divided into two separate categories, either pre or post-threshold surcharges. The main reason to adopt this approach is due to the obvious differences in the measured downstream profiles. In the case on the pre-threshold measurements, the downstream profile adopts a 'wedge' shaped appearance (e.g. Figure 4.1).

Test Configuration	Figure No.	Surcharge (mm)	Pre/Post-Threshold Surcharge	Discharge (m ³ s ⁻¹)	ADE R _T ²	ADZ R _T ²	Optimised ADE R _T ²	Optimised ADZ R _T ²
400mm Chamber	4.1 / 4.2	17.62	Pre	3.58x10 ⁻³	0.911	0.974	0.936	0.974
400mm Chamber	4.3 / 4.4	179.62	Post	3.50x10 ⁻³	0.918	0.784	0.950	0.958
500mm Chamber	4.5 / 4.6	69.11	Pre	3.37x10 ⁻³	0.512	0.887	0.656	0.958
500mm Chamber	4.7 / 4.8	206.69	Post	3.29x10 ⁻³	0.910	0.726	0.961	0.956
600mm Chamber	4.9 / 4.10	96.55	Pre	0.89x10 ⁻³	0.338	0.684	0.644	0.934
600mm Chamber	4.11 / 4.12	202.50	Post	0.87x10 ⁻³	0.916	0.943	0.984	0.970
600mm Chamber	4.13 / 4.14	100.16	Pre	3.36x10 ⁻³	0.012	0.673	0.407	0.829
600mm Chamber	4.15 / 4.16	204.02	Post	3.31x10 ⁻³	0.858	0.836	0.868	0.857
600mm Chamber	4.17 / 4.18	124.05	Pre	6.15x10 ⁻³	-0.225	0.838	0.430	0.838
600mm Chamber	4.19 / 4.20	205.98	Post	5.95x10 ⁻³	0.810	0.717	0.810	0.806
800mm Chamber	4.21 / 4.22	141.60	Pre	4.73x10 ⁻³	-1.421	0.671	0.325	0.816
800mm Chamber	4.23 / 4.24	329.44	Post	4.62x10 ⁻³	0.878	0.801	0.878	0.899
Straight Pipe	4.25	-	-	6.19x10 ⁻³	0.995	0.988	-	-
Mean Results (Pre)	-	-	Pre	-	0.021	0.788	0.566	0.892
Mean Results (Post)	-	-	Post	-	0.882	0.801	0.908	0.908
Mean Results	-	-	-	-	0.493	0.810	0.737	0.900

Note: Table represents a summary of Figures 4.1 to 4.25.

Table 4.1 Summary of ADE and ADZ predictions.

In contrast, when observing the post-threshold measurements, a majority of the data is seen to adopt an almost gaussian profile, followed by a relatively long, and low lying tail (e.g. Figure 4.3).

For the pre-threshold prediction of the 400mm chamber, both the ADE and the ADZ supply an accurate representation of the observed data (R_T^2 values of 0.911 and 0.974 respectively). Both predictions estimate peak concentrations within 10 per-cent of the observed value. Although the ADE has a similar R_T^2 value to the ADZ, observation of the predictions (Figure 4.1) show that the origin of the rising limb of the ADE is noticeably early in comparison to the measured data. Moreover, the ADE has failed to predict the elongated tail of the distribution. This, however has had only a minor effect on the R_T^2 value because the data within the tail constitutes only a small proportion of the entire downstream distribution.

As the chamber diameter is increased, the ADE predictions are seen to progressively worsen. The reason for the degradation between the predicted and observed data is due to both the ADE's nature of generating Gaussian distributions, and the increasing departure of the observed data from this state. While the peak concentration of the ADE predictions increases to as much as 250 per-cent of the measured peak concentration (Figure 4.21), the R_T^2 value is seen to drop below zero. This signifies that the ADE has failed to describe the observed data. The cause of the decay in the R_T^2 value is a combination of both the increase in the over estimation of the peak concentration and the fact that an increasing proportion of the overall concentration distribution lies within the elongated tail of the distribution.

Conversely, the ADZ predictions generally provide a more accurate description of the pre-threshold data. This is reflected in the R_T^2 values given in Table 4.1. Even though there is an increasing deviation between the measured peak concentration and that predicted by the ADZ (falling to 60 per-cent of the observed peak concentration in the case of the 800mm chamber), an average R_T^2 value of 0.788 is obtained (in comparison to 0.021 for the ADE prediction). In general the ADZ technique provides more accurate pre-threshold prediction than the ADE because of its ability to represent the tail of the distribution (rather than the peak value), which, as the chamber diameter is increased accounts for a larger proportion of the entire distribution.

When examining the post-threshold results (Figures 4.3, 4.7, 4.11, 4.15, 4.19, 4.23 and Table 4.1), the ability of the ADE and ADZ, to describe the observed data is seen to be the reverse of the pre-threshold findings. In this case, almost all of the R_T^2 values for the ADE are greater than that of the ADZ (as reflected in the average values). The ADE also consistently predicts a peak concentration within 20 per-cent of the observed value. However, in all cases, due to the nature of its Gaussian predictions, the ADE fails to describe the long tail seen in the observed downstream distributions. This failure to describe the tail data is not reflected in the R_T^2 values because of the relatively low proportion of data found within the tail.

The overall reason for the relatively low R_T^2 values recorded for the ADZ predictions can generally be attributed to a poor representation of the measured data. This has manifested itself in two ways, either a temporal shift (positive or negative) in predicted profile, displacing it from the measured data (e.g. Figure 4.13), or an insufficient representation of the peak concentration, consequently resulting in high tail concentrations (e.g. Figure 4.19). The probable cause of this misrepresentation is the use of inappropriate coefficients used within the ADZ model. With the value of the coefficients being based totally on discharge, and bearing no relation to the pre or post-threshold surcharges, the downstream predictions will tend to form similar shaped profiles. However, observation of the measured results presented in Section 4.1 show that this is not the case.

4.3 Summary of Optimised ADE and ADZ Predictions for all Manhole Diameters

When comparing the optimised predictions with those of the standard analysis, it can be seen that in a majority of cases a distinct improvement has been attained in the R_T^2 values (Table 4.1). However, for some cases it can be observed that the standard ADE and ADZ have managed to determine the optimum solutions, prior to the alternative analysis (i.e. The ADE predictions within Figures 4.20 and 4.24, and the ADZ predictions in 4.2 and 4.18). The reason for the apparent success of the standard analysis over the optimised study is unclear, however, in all but the ADZ results depicted within Figure 4.2, the R_T^2 values are all relatively low, thus indicating a level of uncertainty within these predictions. A possible reason for the

success of the ADZ prediction within Figure 4.2 could be the relatively low distortion of the measured downstream trace (the trace depicts neither the excessive tail or peaked first impulse portrayed in the results of other chambers). It should be noted however that, although the standard approach has predicted these few optimum solutions, it has proved not to be reliable consistent for all other cases.

As with Section 4.2, a closer inspection of the results shall be divided into pre and post-threshold predictions. When comparing the optimised pre-threshold ADE predictions with the measured data (Figures 4.2, 4.6, 4.10, 4.14, 4.18, 4.22 and Table 4.1), the following observations can be made. Although the R_T^2 values start off as being adequate (0.936 for the 400mm chamber), they soon deteriorate as the manhole chamber increases in diameter. Observation of Figure 4.2, and all other subsequent plots of the pre-threshold predictions, shows that, due to its gaussian nature, the ADE has actually failed to predict the tail of the measured downstream data. The apparent success of the prediction for the 400mm chamber comes as a result of the relatively small diameter. When a tracer enters the chamber, a large proportion of the mass passes straight through, thus maintaining the gaussian nature of the upstream profile in the downstream trace. As the chamber diameter is increases, so more of the tracer mass is shifted from the initial impulse into the tail region of the trace (due to retention of the tracer within the volume of the manhole), placing it outside the predictive capabilities of the ADE. Consequently the coefficient of determination drops to 0.325 for the 800mm diameter chamber (Figure 4.22 and Table 4.1).

In contrast to the pre-threshold ADE results, nearly all the post-threshold predictions result in high coefficients of determination (Table 4.1). Again, if the predicted profiles are compared to the observed data (Figures 4.4, 4.8, 4.12, 4.16, 4.20 and 4.24) in can be seen that the ADE still fails to predict the tail (as expected) in the downstream profile. However, the consistently high R_T^2 's result from the fact that, for these traces, the tail forms only a small proportion of the overall mass of tracer. Furthermore, the bulk of the tracer that initially passes through the manhole chamber retains its approximate gaussian distribution, which is ideally suited to an ADE prediction.

All predictions made using the optimised ADZ technique (either pre or post-threshold), provide good estimations of the measured downstream profiles. These predictions may not always

supply the greatest R_T^2 values (when compared to the results of other predictions), but the modelling technique is consistent through all surcharges and discharges examined.

A closer inspection of optimised pre-threshold ADZ profiles (Figures 4.2, 4.6, 4.10, 4.14, 4.18 and 4.22), highlights similarities between the optimised and standard ADZ approaches. Although the predictions do not simulate the peaked nature of the initial impulse of the downstream profile, they make a reasonably good approximation of the tail. As previously stated, within pre-threshold distributions, the tail accounts for a large proportion of the overall mass of the downstream data. Thus, all of the pre-threshold ADZ predictions provide good R_T^2 values.

When observing the R_T^2 values for the post-threshold ADZ predictions (Table 4.1) it can be seen that all values are relatively high (producing an average of 0.908). Scrutiny of these profiles provides an explanation why these predictions result in consistently high coefficients of determination. Within these profiles, it is the region of the peak concentration that describes a majority of the mass of the tracer. The accurate representation of this portion of the data (as seen with the post-threshold ADZ predictions) will result in a high R_T^2 . Furthermore, this predictive technique also manages to predict a proportion of the extended tail. Although this particular region of the prediction has not been too successful due to the extreme length of the low lying tail, however in attempting to predict even part of this tail will result in an improve R_T^2 . A major improvement observed within the optimised ADZ predictions over those made using all other modelling techniques is the accuracy within the temporal domain. All other modelling techniques have shown limitation in predicting the temporal location of the downstream profile. The standard ADE is seen predicts profiles that both start and finish too early. Whilst the optimised ADE has corrected for the failure to predict the correct start time, inevitably the finish time of the prediction is incorrect due to the inability to fit a gaussian profile to the measured data. Likewise, the standard ADZ has also displayed limitations. Although the ADZ technique is capable of predicting distributions of temporal duration's seen within the measured data, it is evident from the predictions depicted in Section 4.1 that the technique is inaccurate in its predictions of the start of the profile, and indeed the location of the peak concentration. As previously suggested, these errors could result from inappropriate modelling parameters.

In studying the optimised ADZ predictions it can be observed that in all cases the start and peak times of the predicted profile closely resemble the measured data. Although the finish times of the pre-threshold predictions is ambiguous (due to tail being represented by an exponential decay) it can be observed that a majority of the data within the tail region has been accounted for. The only perceived shortcoming of the optimised ADZ is seen in its inability to predict the tail region within post-threshold distributions. However it should be noted that a majority of the data in these cases is held within the initial impulse of the downstream profile (within the vicinity of the peak concentration), which is accurately being portrayed by these predictions.

4.4 Summary of ADE and ADZ Predictions for the Straight Pipe

For the straight pipe, both the advective dispersion and aggregated dead zone predictions (Figure 4.25) show an accurate representation of the observed data. This accuracy is reflected in the R_T^2 values of 0.995 and 0.988 for the ADE and ADZ predictions respectively (Table 4.1). According to the coefficients of determination, the ADE provides a slightly more accurate description of the observed data than the ADZ. It is not surprising that this is the case, the ADE was originally developed to model straight pipes (Taylor (1953 and 1954)), and has been proven to provide an accurate solution. Discrepancies between the observed data and the predictions are the result of inaccuracies in the dispersion coefficient used with the ADE, and the travel and delay times used with the ADZ. Within Section 3.2.1 a relationship between the ADE dispersion coefficient and the discharge was observed (Figure 3.5). Likewise, Section 3.3.1 developed a relationship between the ADZ travel and delay times with discharge (Figure 3.14).

In both cases, predictive formula were developed to determine the coefficients to be used within either the ADE or ADZ. However the empirical nature of these equations leads towards a measure of uncertainty in the coefficients that they predict. The uncertainty in the prediction of these coefficients is reflected in the deviation of both the ADE and ADZ predictions from the observed data.

Chapter 5

Conclusions

5.1 Introduction

In studying the modelling parameters determined within Chapter 3, and predictions made within Chapter 4 several distinguishing features can be observed, both between different predictions, and between the predictions and measured data. To assist in the comparison between the different analysis techniques, the terms 'pre-' and 'post-threshold surcharge', described within Chapter 3, and quantified within Equation 3.8 shall be widely used throughout the conclusions.

5.2 Standard ADE and ADZ Predictions

With regards to the standard analysis of the advective dispersion equation (ADE) and aggregated dead zone (ADZ), a departure between the predictions made using each technique can be observed. Both techniques provide an adequate prediction for the 400mm diameter chamber with respect to the coefficient of determination, R_T^2 (Section 3.4.1 and Equation 3.15) under both pre and post-threshold surcharges. However, as the chamber diameter is increased, so a discrepancy between each analysis technique arises. In general, it has been observed that whilst the ADZ produces more accurate pre-threshold predictions, the ADE is seen to predict better post-threshold cases. Observation of pre-threshold data (Section 4.1, e.g. Figure 4.1) has shown that for all chamber diameters, the downstream profile is of a 'wedge' shaped distribution, although the initial impulse of the downstream distribution is seen to become more peaked within the larger chamber diameters. The probable cause of the increase in peaked nature of the data is the time taken for the tracer to re-circulate within the surcharged volume of the manhole. For pre-threshold surcharges, this re-circulation occurs on plan (Figure 3.7), which would therefore imply, that the larger the manhole diameter, the greater time lag in the downstream profile before the tail data becomes evident. Whilst the

ADZ attains a good representation of this profile, albeit without predicting the peaked nature, the ADE, due to its Gaussian nature fails to describe this distribution.

In contrast to the pre-threshold results, those attained for the post-threshold, as previously stated, depict a reversal in the predictive accuracy of both the ADE and ADZ. Under these surcharged conditions the measured data can be seen to adopt a profile where the initial impulse of the downstream distribution is almost Gaussian, followed by a long, low lying tail (Section 4.1, e.g. Figure 4.3). The ADE predictions for this data show a good correlation with the initial impulse, however they fail to predict the observed tail. The apparent success of these predictions (with respect to R_T^2) arises due to the fact that such a small percentage of the overall mass of the downstream distribution is accounted for by the tail region. When observing the ADZ predictions for the post-threshold results it can be seen that there is an underestimate in the peak concentration, whilst the magnitude of data within the tail region has been over calculated. Consequently, the post-threshold ADZ predictions are similar in appearance to those predicted for the pre-threshold surcharges. This clearly illustrates that the modelling parameters derived within Chapter 3 are not sufficiently accurate in their description of the observed data to account for the dramatic change in the measured profiles. Unlike the ADE, no dependencies were made between the predictions and the surcharge level (with respect to the surcharge threshold). Subsequently, at a single discharge, no deviation is made within the predicted ADZ modelling parameters over the range of surcharges.

5.3 Optimised ADE and ADZ Predictions

In considering the predictions made for the optimised ADE and ADZ, it should be noted that, as well as determining the optimum solution for the modelling parameters, the numerical models constructed to predict the parameters for each modelling technique have also increased in complexity. With regards to the ADE, two equations were developed to determine the dispersion coefficient, K , depending on the chamber diameter (i.e. 400-500mm or 600-800mm). Similarly the travel time parameter used within the ADZ technique (as well as the ADE) has included a dependency on level of surcharge by having different equations for the pre or post-threshold cases.

In a general comparison between the standard and optimised studies (Table 4.1) it can be seen that the optimised predictions tend to produce a higher level of accuracy (with relation to R_T^2). However it is also evident, as with the standard predictions, that the ADE is still incapable of accurately predicting the pre-threshold profiles. The reason for this failure is unchanged from the standard study. Basically the measured data is too far removed from a Gaussian profile for the ADE to make an accurate representation. From studying the profiles of the ADE predictions for the post-threshold results it can again be seen that the process has, unsurprisingly also failed to reproduce the observed tail within the data. Again the cause of this failure is due to the ADE's inability to predict profiles that deviate from a Gaussian profile. However, although this tail portion of the prediction has been omitted, the post-threshold predictions still produce high R_T^2 values. This result is identical to the findings of the standard study. The apparent success of the post-threshold ADE predictions is a result of the initial impulse of the downstream profile behaving in a Gaussian manner. The optimised predictions attain a higher level of accuracy than the standard approach, by not overestimating the spread of the initial impulse. Instead of basing the value of the coefficient on the rate of change in the second moments, the optimised study has used coefficients that generate the most accurate prediction (i.e. R_T^2 tends towards unity).

Finally, in studying the results for the optimised ADZ (Table 4.1) it is clear that this form of prediction consistently attains high R_T^2 value for both the pre and post-threshold predictions. Although a few of the predictions result in lower R_T^2 values than those obtained through previously discussed analysis techniques, an average of 0.9 has been obtained over the range of configurations tested within Chapter 4 (Table 4.1).

The main factor in favour of this analysis technique is the fact that it provides an accurate, generalised approach to the modelling of manhole chambers. On closer inspection of optimised ADZ predictions for pre-threshold surcharges, the most noticeable feature is the temporal location of the predicted profile. With all other analysis techniques, either a temporal shift can be observed within the prediction (in either the start time of the profile, or in the location of the peak concentration), or an inaccurate calculation of the end time of the prediction (evident in all pre-threshold ADE predictions). However, although the shape of the optimised pre-threshold ADZ profile may not exactly match that of the measured data, the prediction accurately determines the start, peak and end times. In comparing the shape of the

ADZ prediction with that of the pre-threshold data, it again becomes evident that the ADZ is incapable of modelling the peaked nature within the initial impulse of the downstream distribution (as observed with the standard ADZ). In fact it will always be impossible for the ADZ technique to reproduce this initial peaked impulse. This is because the predicted downstream distribution consists of a transposition of the upstream measured profile, and thus, must be of the same general distribution.

On closer inspection of the post-threshold distribution, it is again evident, as with the standard and optimised ADE, that the temporal location of the predicted distribution closely matches the measured data for at least the majority of the overall mass. However as with all ADE predictions, the post-threshold ADZ fails to predict the elongated, low lying tail observed within the measured data. This is again due to the fact that the downstream prediction is made through a transposition of the upstream profile. However, because the main bulk of the data has been accurately represented a high R_T^2 has been attained.

5.4 Synopsis

Clearly, from the investigation of the analysis techniques used within the current study, the optimised ADZ provides the most conclusive solution. Through the application of this single analysis technique, it has been shown that it is possible to make an accurate prediction of the magnitude of the downstream profile of a dispersed solute based on discharge, surcharge, geometry (of the manhole chamber) and an upstream concentration profile. The following formula derived within Chapter 3, may be used to express the ADZ parameters required to make a prediction. Firstly, it must be determined whether the surcharge within the chamber is above the surcharge threshold defined for the specified chamber diameter.

$$\text{Surcharge Threshold(m)} = 0.5 \times \text{Chamber Diameter(m)} - 0.15 \quad (3.8)$$

Dependant on whether a pre or post-threshold surcharge exists, the relevant travel time, \bar{t} , for the dispersing solute can be determined. If pre-threshold conditions exist, the travel time can be deduced as follows:

$$\frac{\bar{t}}{D_m} = 0.0519Q^{-0.9737} \quad (3.16)$$

Otherwise, for a post-threshold surcharge, the travel time should be taken as:

$$\bar{t} = 0.0189Q^{-0.9632} \quad (3.17)$$

Finally, a delay time, τ , which is independent of all but the mean discharge must be calculated:

$$\tau = 0.013Q^{-0.957} \quad (3.22)$$

where -

D_m = Internal diameter of manhole chamber, (m),

Q = Discharge, ($m^3 s^{-1}$).

Once all the above ADZ parameters have been determined, they may be applied in conjunction with the standard ADZ equation to determine the predicted downstream concentration profile.

$$c_{2,k} = -ac_{2,k-1} + bc_{1,k-\delta} \quad (1.54)$$

where,

$c_{1,i}$ and $c_{2,i}$ = Input and output concentrations at discrete time step i , respectively,

k = Discretised time interval,

where $k = t / \Delta t$,

t = time,

and Δt = Measured time step.

δ = Discretised advective time delay,

where $\delta = \tau / \Delta t$.

$a = -\exp(\Delta t / (\bar{t} - \tau))$

$b = 1+a$

Finally, to elucidate the net effect of the manhole chamber within an urban drainage system, the results of the dispersion due to the manhole chamber will be compared with those of the

straight pipe. Within Section 3.3.1 the following relationships were observed between the discharge, Q , and the travel and delay times, \bar{t} and τ .

$$\bar{t} = 0.0167Q^{-0.9954} \quad (5.1)$$

$$\tau = 0.0112Q^{-1.0313} \quad (5.2)$$

[Note: Within Chapter 3 equations 5.1 and 5.2 were portrayed in Figure 3.14]

If these straight pipe equations are compared with the optimised results determined within equations 3.16, 3.17 and 3.22, assuming a discharge of 10 l/s, the result for the pre-threshold travel time through the 800mm diameter manhole is 2.25 times greater than that for the straight pipe. However the travel time through the manhole is seen to decrease to the same value as the straight pipe once the surcharge exceeds the threshold level. The delay times (whose value is calculated irrespective of the manhole chamber diameter or surcharge), for the same discharge is only 0.8 times that seen in the straight pipe, implying that the leading edge of a tracer travels faster through the manhole chamber than it could travel through the same length of pipe. One possible cause of the reduction in delay time to below that of the straight pipe is the reduction in friction across the diameter of the manhole chamber.

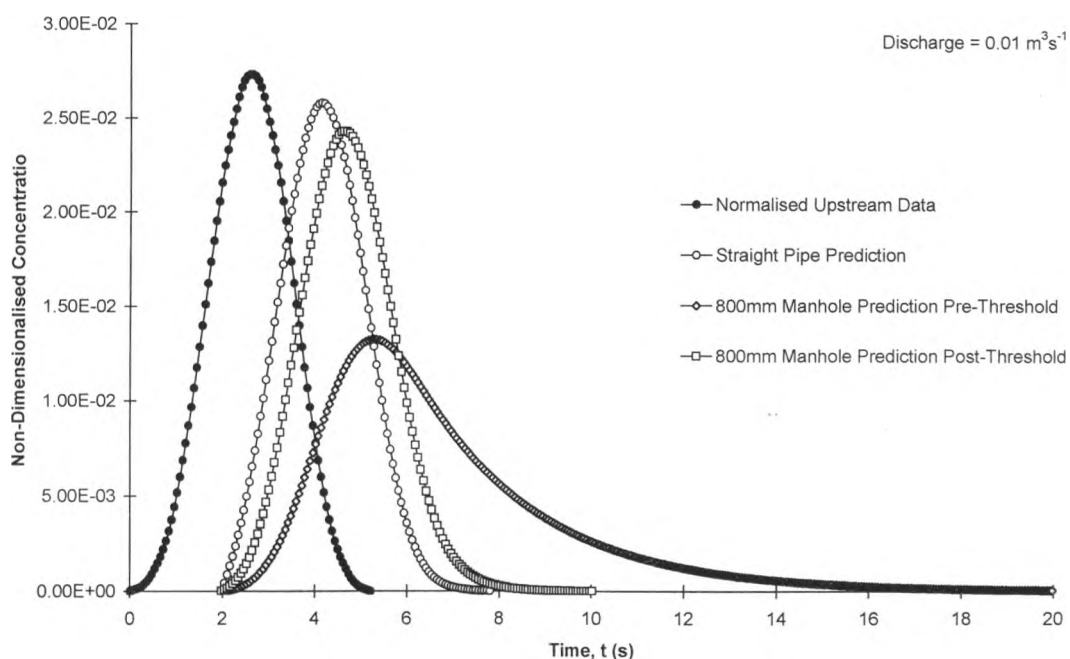


Figure 5.1 Comparison between spread of a tracer traveling through a straight pipe and an 800mm manhole chamber.

Figure 5.1 illustrates the differences between ADZ predictions for the straight pipe and the largest manhole chamber tested. Using Figure 5.1 as an approximate measure of the temporal spread caused by the presence of a manhole chamber, it can be deduced that the chamber will increase to temporal spread of a solute between 1 and 3.5 times that observed within a straight pipe. Thus the bulk of the dispersing solute will be distributed over a much greater duration.

References

- Archer, B., Bettes, F. & Colyer, P. J. (1978). 'Head Losses and Air Entrainment at Surcharged Manholes.' Hydraulic Research Station, Wallingford, Oxon, Report No. IT 185, November.
- Aris, R. (1956). 'On the Dispersion of a Solute in a Fluid Flowing through a Tube.' Proceedings of the Royal Society, London, Series A, Vol. 235, pp 67-77.
- Barnett, A. G. (1983). 'Exact and Approximate Solutions of the Advective-Diffusion Equation.' Proc. XXth I.A.H.R. Congress, Moscow, Hydro. Tech. Inst., Moscow, 5-9 September, Vol. 3, pp 180-190.
- Beck, M. B., Adeloje, A. J., Lessard, P., Finney, B. A. & Simon, L. (1988). 'Stormwater Overflows: Modelling Impacts on the Receiving Waters and the Treatment Plants.' Urban Discharge and Receiving Water Quality Impacts, Proc. I.A.W.P.R.C. 14th Biennial Conf., Brighton, U.K., 18-21 July, pp 87-105.
- Beer, T. & Young, P. C. (1983). 'Longitudinal Dispersion in Natural Streams.' A.S.C.E. Journal of Environmental Engineering, Vol. 109, No. 5, October, pp1049-1067.
- Chatwin, P. C. (1980). 'Presentation of Longitudinal Dispersion Data.' A.S.C.E. Journal of the Hydraulic Division, Vol. 106, No, HY 1, January, pp 71-83.
- Council of the European Communities (1991). 'Directive Concerning Urban Waste Water Treatment.' (91/271/EEC), Official Journal L135, 30 May.
- Crabtree, B., Gent, R. & Garsdal, H. (1994). 'Sewer Simulation.' Surveyor, 7 July.
- Douglas, J. F., Gasiorek, J. M. & Swaffield, J. A. (1987). 'Fluid Mechanics.' Longman Scientific & Technical, ISBN 0-582-98861-6.

-
- Field, R. & Struzeski, E. J. (1972). 'Management and Control of Combined Sewer Overflows.' Jour. Water Pollution Control Federation, Vol. 44, No. 7, July, pp 1393-1415.
- Fischer, H. B. (1966). 'A Note on the One-Dimensional Dispersion Model.' Air & Wat. Pollut. Int. Jour. Vol. 10, pp 443-452.
- Fischer, H. B. (1968). 'Dispersion Predictions in Natural Streams.' A.S.C.E. Journal of the Sanitary Engineering Division, Vol. 94, No. SA 5, October, pp 927-943.
- Foundation for Water Research (1994). 'Urban Pollution Management Manual.' FR/CL 0002, ISBN 0 9521712 1 X, November.
- French, R. H. (1986). 'Open Channel Hydraulics.' McGraw-Hill, ISBN 0-07-Y66342-4.
- Green, H. M., Beven, K. J., Buckley, K. & Young, P. C. (1994). 'Pollution Incident Prediction with Uncertainty.' Mixing and Transport in the Environment, K. J. Beven, P. C. Chatwin, & J. H. Millbank, eds., John Wiley & Sons, pp 113-137.
- Gupta, K., Saul, A. J. (1996). 'Specific Relationships for the First Flush Load in Combined Sewer Flows.' Water Research, Vol. 30, No. 5, May, pp 1244-1252
- Guymer, I., O'Brien, R. & Harrison, C. (1996). 'Representation of Solute Transport and Mixing within a Surcharged Benched Manhole using an Aggregated Dead Zone (ADZ) Technique.' Wat. Sci. Tech., Vol. 34, No. 3-4, pp 95-101.
- Guymer, I., O'Brien, R., Mark, O. & Dennis, P. (1997). 'An investigation of Fine Sediment Mixing within Free-Flowing and Surcharged Manholes.' The Sewer as a Physical, Chemical and Biological Reactor, Aalborg University, Denmark, 25-28 May.

- Hogland, W., Berndtsson, R. & Larson, M. (1984) 'Estimation of Quality and Pollution Load of Combined Sewer Overflow Discharge' Proc. Third Int. Conf. Urban Storm Drainage, Göteborg, Sweden, 4-8 June, pp 841-850.
- Holley, E. R. (1969). 'Unified View of Diffusion and Dispersion.' A.S.C.E. Journal of the Hydraulics Division, Vol. 95, No. HY 2, March, pp 621-631.
- Johnston, A. J. & Volker, R.E. (1990). 'Head Losses at Junction Boxes.' A.S.C.E. Journal of Hydraulic Engineering, Vol. 116, No. 3, March, pp 326-341.
- Larson, M., Berndtsson, R., Hogland, W., Spångberg, Å., & Bennerstedt, K. (1990). 'Field Measurements and Mathematical Modeling of Pollution Build-Up and Pipe-Deposit Wash-Out in Combined Sewers.' 5th International Conference on Urban Storm Drainage, Osaka, Japan, pp 325-332.
- Liu, H. & Cheng, H. D. (1980). 'Modified Fickian Model for Predicting Dispersion.' A.S.C.E. Journal of the Hydraulics Division, Vol. 106, No. HY 6, June, pp 1021-1040.
- Marsalek, J. (1984). 'Head Losses at Sewer Junction Manholes.' A.S.C.E. Journal of Hydraulic Engineering, Vol. 110, No. 8, August, pp 1150-1154.
- Metcalf and Eddy, Inc. (1991). 'Waste Water Engineering: Treatment, Disposal and Reuse.' International Edition, McGraw-Hill, ISBN 0-07-100824-1.
- Microsoft Corporation (1992). 'Microsoft Excel User's Guide 2.' Microsoft Corporation.
- National Rivers Authority (1993). 'Guidelines for AMP2. Periodic Review, Version 2.' Approved by Quadripartite Meeting, 14 December.
- Nordin, C. F. & Sabol, G.V.(1974). 'Empirical Data on Longitudinal Dispersion in Rivers.' U.S. Geological Survey, Water Resources Investigation.

Nordin, C. F. & Troutman, B. M. (1980). 'Longitudinal Dispersion in Rivers: The Persistence of Skewness in Observed Data.' *Water Resources Research*, Vol. 16, No. 1, February, pp 123-128.

O'Brien, R. (1993). 'Longitudinal Dispersion of Solutes in Urban Drainage Systems.' Abstracts from the 4th European Postgraduate Workshop on Urban Runoff - Sewer Systems. Treatment Plants and Receiving waters, Aalborg University, Denmark, 5-9 July.

Payne, J. A., Moys, G. D., Hutchings, C. J. & Henderson, R. J. (1989). 'Development, Calibration and Further Data Requirements of the Sewer Flow Quality Model MOSQUITO.' *Urban Storm Water Quality and Ecological Effects Upon Receiving Waters*, Proceedings of the 2nd Wageningen Conference, 20-22 September.

Pedersen, F. B. & Mark, O. (1990). 'Head Losses in Storm Sewer Manholes: Submerged Jet Theory.' *A.S.C.E. Journal of Hydraulic Engineering*, Vol. 116, No. 11, November, pp 1317-1328.

Pedersen, F. B. (1977). 'Prediction of Longitudinal Dispersion in Natural Streams. Institut of Hydrodynamics and Hydraulic Engineering, Technical University of Denmark, Series Paper No. 14, February.

Prosig (1994) 'Dats Plus 2: Spreadsheet Signal Processing Environment.' Prosig Computer Consultants Ltd., Hampshire, UK.

Rutherford, J. C. (1994). 'River Mixing.' John Wiley & Sons Ltd., England, ISBN 0-471-94282-0.

Sangster, W. M., Wood, H. W., Smerdon, E. T. & Bossy, H. G. (1958). 'Pressure Changes at Storm Drain Junctions.' *Engineering Series Bulletin No. 41*, Engineering Experiment Station, University of Missouri, Columbia.

-
- Saul, A. J. & Thornton, R. C. (1989). 'Hydraulic Performance and Control of Pollutants Discharged from a Combined Sewer Storage Overflow.' *Water Science & Technology*, Vol. 21, No. 8/9.
- Smart, P. L. & Laidlaw, I. M. S. (1977). 'An Evaluation of Some Fluorescent Dyes for Water Tracing' *Water Resources Research*, Vol. 13, No. 3, February, pp 15-33.
- Stefan, H. G. & Demetrapoulos, A. (1981). 'Cells-in-Series Simulation of Riverine Transport.' *A.S.C.E. Journal of the Hydraulics Division*, Vol. 107, No. HY 6, June, pp 675-697.
- Taylor, G. (1953). 'Dispersion of Soluble Matter in Solvent Flowing Slowly Through a Tube.' *Proceedings of the Royal Society, London, Series A*, Vol. 219, 25 August, pp 186-203.
- Taylor, G. (1954). 'The Dispersion of Matter in Turbulent Flow Through a Pipe.' *Proceedings of the Royal Society, London, Series A*, Vol. 223, 20 May, pp 446-468.
- Thackston, E. L. & Schnelle, K. B. (1970). 'Predicting the Effects of Dead Zones on Stream Mixing.' *A.S.C.E. Journal of the Sanitary Engineering Division*, Vol. 96, No. SA 2, April, pp 319-331.
- Turner Designs (1981). 'Operating & Service Manual: Model 10 Series Fluorometer.' Turner Designs, 845 W. Maude Avenue, Sunnyvale, California, 94086.
- Turner Designs (1981). 'Filter Selection Guide, 998-0005 (Ver2).' Turner Designs, 845 W. Maude Avenue, Sunnyvale, California, 94086.
- Valentine, E. M. & Wood, I. R. (1977). 'Longitudinal Dispersion with Dead Zones.' *A.S.C.E. Journal of the Hydraulics Division*, Vol. 103, No. HY 9, September, pp 975-990.

Wallis, S. G., Guymer, I. & Bilgi, A. (1989). 'A Practical Engineering Approach to Modelling Longitudinal Dispersion.' Hydraulic and Environmental Modelling of Coastal, Estuarine and River Waters, R. A. Falconer, P. Goodwin & R. G. S. Matthew. eds., University of Bradford, UK, 19-21 September, pp 291-300.

Wallis, S. G., Young, P. C. & Beven, K. J. (1989). 'Experimental Investigation of the Aggregated Dead Zone Model for Longitudinal Solute Transport in Stream Channels.' Proceedings of the Institute of Civil Engineers, Vol. 87, Pt 2, March, pp1-22.

Young, P., Jakeman, A. & McMurtrie, R. (1980). 'An Instrument Variable Method for Model Order Identification.' Automatica, Vol. 16, pp281-294.